UNIVERSITY OF SOUTHAMPTON

Faculty of Engineering and Physical Sciences
School of Engineering

Impact of Pressure Gradient History on Smooth and Rough Wall Turbulent Boundary Layers

by

Thomas Preskett

MEng

ORCiD: 0000-0001-9203-1266

A thesis for the degree of
Doctor of Philosophy

March 2026

University of Southampton

Abstract

Faculty of Engineering and Physical Sciences
School of Engineering

Doctor of Philosophy

Impact of Pressure Gradient History on Smooth and Rough Wall Turbulent Boundary Layers

by Thomas Preskett

Turbulent boundary layers often occur over surfaces which are considered rough, often with external conditions which influence the development of the boundary layer. One of the most common influences is external streamwise pressure gradients. The combination of roughness and pressure gradients exists in many common engineering applications, including on a ship's hull, turbine blades and leading edges of aerofoils due to icing. This work experimentally explores the effect of the pressure gradients on smooth and rough wall turbulent boundary layers at high Reynolds numbers. There are three main subsections focusing on the mean flow, the turbulence statistics and the structures within the flow.

Experiments are carried out in the University of Southampton's 12 m boundary layer wind tunnel. A NACA 0012 aerofoil of 1.25 m chord mounted in the freestream to impose pressure gradients onto the developing turbulent boundary layer. Flow measurements are initially taken at a single point, one chord downstream of the trailing edge of the aerofoil, using hot wire anemometry. Combined with independent skin friction measurements, this allows the effect of pressure gradient history on the roughness constant to be examined. The effect of pressure gradient history and the differences between smooth and rough walls are also examined using the pre-multiplied energy spectra.

Particle image velocimetry is used to obtain the flow development under different pressure gradient histories. The types of events and variation in flow structures with different pressure gradient histories are examined, as well as the differences between smooth and rough walls. Throughout this work, an integral pressure gradient parameter, $\Delta\beta$, is defined to quantify the upstream pressure gradient history. Based on this parameter, a predictive model for the skin friction variation in the flow due to the pressure gradient history is developed. This is initially done based on a single point measurement before being further developed for the entire flow field.

Contents

List of Figures

List of Tables

Declaration of Authorship

I declare that this thesis and the work presented in it is my own and has been generated by me as the result of my own original research.

I confirm that:

1. This work was done wholly or mainly while in candidature for a research degree at this University;
2. Where any part of this thesis has previously been submitted for a degree or any other qualification at this University or any other institution, this has been clearly stated;
3. Where I have consulted the published work of others, this is always clearly attributed;
4. Where I have quoted from the work of others, the source is always given. With the exception of such quotations, this thesis is entirely my own work;
5. I have acknowledged all main sources of help;
6. Where the thesis is based on work done by myself jointly with others, I have made clear exactly what was done by others and what I have contributed myself;
7. Parts of this work have been published as: T. Preskett, M. Virgilio, P. Jaiswal, and B. Ganapathisubramani. Effects of pressure-gradient histories on skin friction and mean flow of high reynolds number turbulent boundary layers over smooth and rough walls. *Journal of Fluid Mechanics*, 1010:A30, 2025
   T. Preskett and B. Ganapathisubramani. The impact of pressure gradient history on flow structures in high reynolds number rough wall turbulence. *International Journal of Heat and Fluid Flow*, 116:109942, 2025
   T. Preskett, M. Virgilio, P. Jaiswal, and B. Ganapathisubramani. Effect of pressure gradient histories on turbulence characteristics of turbulent boundary layers over smooth and rough walls. *Physical Review Fluids*, 11(1):014603, 2026

Signed: Date:

Acknowledgements

Thank you to my supervisor, Prof. Bharathram Ganapathisubramani, for his guidance and support during this research.

Thank you to all the past and present members of *bgroup* for their help and support over the past four years. In particular, I am grateful to Dr Dea Wangsawijaya, Dr Marco Virgilio, and Dr Prateek Jaiswal for their support and collaboration during our collaborative experimental campaigns.

Finally, I am grateful to my family for their support throughout my PhD.

I gratefully acknowledge the financial support from the following sources:

Engineering and Physical Sciences Research Council (EPSRC) (Grant Ref no: EP/W026090/1)

European Office for Aerospace Research and Development (Grant No: FA8655-22-1-7163, Programme Manager: Dr. Doug Smith).

Definitions and Abbreviations

Coordinate System and Dimensions

c	Aerofoil chord (m)
l	Hot Wire Probe Sensing Length (m)
x	Streamwise coordinate (m)
y	Wall normal coordinate (m)

Velocity Parameters

u	Instantaneous streamwise velocity (m/s)
u'	Streamwise velocity fluctuation given by $u' = u - U$ (m/s)
U	Mean streamwise velocity (m/s)
v	Instantaneous wall normal velocity (m/s)
v'	Wall normal velocity fluctuation given by $v' = v - V$ (m/s)
V	Mean wall normal velocity (m/s)

Freestream and Pressure Parameters

$Cp = \frac{P - P_\infty}{\frac{1}{2}\rho \mathrm{U}_\infty^2}$	Pressure Coefficient
$K = \frac{\nu}{\mathrm{U}_1^2}\frac{d\mathrm{U}_1}{dx}$	Acceleration parameter
P	Static pressure (Pa)
P_0	Total pressure (Pa)
P_a	Atmospheric Pressure (Pa)
P_∞	Reference static pressure (Pa)
q	Dynamic Pressure (Pa)
T_a	Atmospheric Temperature (°C)
U_∞	Freestream velocity (m/s)
$\beta = \frac{\delta^*}{\tau_0}\frac{dP}{dx}$	Clauser pressure gradient parameter

ν	Kinematic viscosity of fluid (m^2/s)
ρ	Density of fluid (kg/m^3)

Boundary Layer Parameters

$C_f = \frac{\tau_0}{\frac{1}{2}\rho U_\infty^2} = 2\frac{U_\tau^2}{U_\infty^2}$	Friction coefficient
d	Zero plane displacement of roughness (m)
k_s	Equivalent sand grain roughness (m)
U_{99}	Boundary layer edge velocity (m/s)
$U_\tau = \sqrt{\frac{\tau_0}{\rho}}$	Friction velocity (m/s)
y_0	Roughness length (m)
$y^+ = \frac{yU_\tau}{\nu}$	Inner scaled wall normal position
δ	Boundary layer thickness (m)
$\delta^* = \int_0^\delta (1 - \frac{U}{U_{99}})dy$	Displacement thickness (m)
$\Delta\Pi = \Pi_{PG} - \Pi_{ZPG}$	Change in wake strength from ZPG value
ΔU^+	Roughness function
Π	Wake strength parameter
τ_0	Wall shear stress (Pa)
$\theta = \int_0^\delta \frac{U}{U_{99}}(1 - \frac{U}{U_{99}})dy$	Momentum thickness (m)

Reynolds Numbers

$k^+ = \frac{kU_\tau}{\nu}$	Roughness Reynolds number
$Re_x = \frac{U_\infty x}{\nu}$	Reynolds number
$Re_\theta = \frac{U_\infty \theta}{\nu}$	Momentum thickness Reynolds number
$Re_\tau = \delta^+ = \frac{U_\tau \delta}{\nu}$	Friction Reynolds number

Roughness Shape Parameters

A_f	Frontal projected area of roughness element (m^2)
A_p	Plan area of roughness elements (m^2)
A_t	Total plan area (m^2)
$ES_x = \frac{1}{A_t}\int \lvert\frac{\partial h'}{\partial x}\rvert dA$	Effective Slope
$ES_y = \frac{1}{A_t}\int \lvert\frac{\partial h'}{\partial y}\rvert dA$	Effective Slope
$Fl = (\frac{1}{A_t}\int h'^4 dA)/k_{rms}^4$	Flatness
h'	Variation in roughness elevation above mean (m)

k	Peak to trough roughness height (m)
$k_a = \frac{1}{A_t}\int \lvert h' \rvert dA$	Average roughness height (m)
$k_{rms} = \sqrt{\frac{1}{A_t}\int h'^2 dA}$	Root mean square roughness height (m)
$Sk = (\frac{1}{A_t}\int h'^3 dA)/k_{rms}^3$	Skewness
$\lambda_f = \frac{A_f}{A_t}$	Frontal Solidity
$\lambda_p = \frac{A_p}{A_t}$	Plan Solidity

Abbreviations

A/D	Analogue to Digital Converter
APG	Adverse pressure gradient
A-FPG	Adverse-favourable pressure gradient
BLWT	Boundary layer wind tunnel
CAD	Computer Aided Design
CFD	Computational Fluid Dynamics
CTA	Constant Temperature Anemometry
DAQ	Data acquisition
DNS	Direct Numerical Simulation
EXP	Experimental
FOV	Field of View
FPG	Favourable Pressure gradient
F-APG	Favourable-adverse pressure gradient
HWA	Hot-Wire Anemometry
IL	Internal Layer
LES	Large Eddy Simulation
LSM	Large scale motions
Loc.	Location
Meas.	Measured Value
PG	Pressure Gradient
PID	Proportional Integral Derivative
PIV	Particle Image Velocimetry
PM	Panel Method
Pred.	Predicted Value
PTU	Programmable Timing Unit
RMS	Root-mean-square
RW	Rough Wall
SW	Smooth Wall
TBL	Turbulent boundary layer
VLSM	Very large scale motions
ZPG	Zero pressure gradient

Chapter 1

Introduction

In engineering applications, most surfaces are not smooth and have surface defects and features that result in them being rough. Extensive previous research, a detailed summary is provided in chapter 2, has shown that roughness modifies the near-wall turbulence mechanisms. This results in higher skin friction and, therefore, higher drag for rough walls than smooth walls. Previous studies have examined turbulent boundary layers (TBLs) over smooth and rough walls, predominantly under zero pressure gradient (ZPG) conditions. While these studies give a fundamental understanding of the effect of roughness, their practical applications are often limited when applied to real-world problems due to other external conditions.

Climate change and the impact of carbon emissions are high on the political agenda. A recent report, H.M. Goverment (2021), outlined the UK response to the impact of carbon emissions and the policy changes required to reduce their impact. The impact of climate change in the UK has resulted in extreme weather events, whether that be prolonged periods of hot weather or torrential downpours, causing flash flooding (H.M. Goverment, 2021). Transport systems and power generation are two key areas identified in this report where emissions must be reduced. Global shipping contributes 3% of the global carbon emissions, often from burning low-quality fuel oils (Deng and Mi 2023). Figure 1.1a shows a typical sample of bio-fouling, formed by marine organisms attaching to the hull. Monty et al. (2016) presented an extensive look at the effect of bio-fouling on the drag on a frigate. They showed that even for a realistic, sparse tube worm surface, a frigate-sized ship had a 23% drag penalty, increasing to 34% for a larger vessel such as an aircraft carrier. These drag penalties result in large increases in fuel consumption and, therefore, carbon emissions.

Another source of emissions, as shown in H.M. Goverment (2021), is power generation, which is responsible for 11% of the UK's total greenhouse emissions. Steam turbines operate in extreme conditions due to high temperature and humidity, which can cause pitting due to corrosion. Figure 1.1b shows a typical turbine blade where the

(A) Bio-fouling on a marine vehicle (Wildlife and Welfare n.d.)

(B) Pitting on turbine blades (Epri Journal 2015)

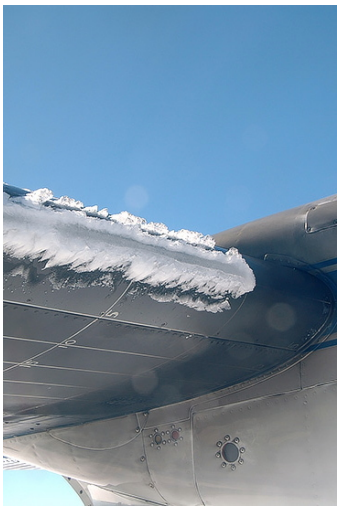

(C) Leading edge wing icing (Flight Safety Foundation 2017)

surfaces are damaged due to corrosion. Yun et al. (2005) reported that for a single-axis turbine, there is a 19% reduction in the turbine efficiency due to the roughness. When considering roughness, it is not just the impact on the environment where an impact is felt; roughness introduces safety issues. The formation of ice on the leading edge of a wing reduces the maximum lift that a wing produces (Cao et al. 2015). As seen in figure 1.1c, the build-up of icing changes the aerofoil's shape and surface properties. Therefore, understanding the formation of ice and how the TBLs over the wing are affected is important.

The previous examples all experience roughness; however, it is also combined with pressure gradients (PG). In all cases shown, the PG comes from the shape of the surface upon which the roughness occurs. Much previous research has focused on individual effects of roughness and pressure gradients; however, few have looked at the combined effects of roughness and pressure gradients. Understanding the combined effects is important when trying to make operational decisions. Take the hull of a ship; there is a need to balance the out-of-service time to clean the hull with the extra fuel burn and associated emissions, which the bio-fouling will result in. This requires knowledge of how roughness changes the flow and development of models to predict the change in the surface for a prescribed set of conditions.

1.1 Thesis outline

This thesis explores the effect of different PG histories on high Reynolds number TBLs through a series of experiments. This data is used to develop models and correlations which can be used to predict the effect of different PG histories. The analysis is divided

into three sections: the mean flow, turbulence statistics and the variation of the structures within the flow. A detailed look at the previous literature is presented in chapter 2, which concludes with the overall aim and objectives of the thesis based upon the open questions from past literature. Chapter 3 outlines the experimental techniques used to obtain the data for analysis. This includes hot wire anemometry, particle image velocimetry and wall shear stress measurements using a drag balance and oil film interferometry. Also presented is an estimation of the uncertainty of properties measured. Chapter 4 looks at the mean flow statistics at a single point, including the variation in skin friction and the effect on the mean velocity profile from hot wire anemometry. Chapter 5 extends the analysis to look at how the turbulence statistics are affected by different PG histories before looking for correlations in the turbulence statistics. Chapters 6 and 7 look at the streamwise development of the flow over both smooth and rough walls, respectively. The variation of the boundary layer structure and the coherent structures within the flow, with chapter 7 focusing on how the surface affects the flow response to different PG histories. The work is concluded in chapter 8 along with recommendations for future research.

1.2 Author contributions

The following works have been published or are under review in the following journals. Where these works form the basis of all or part of a chapter, it is stated in the footnote on the first page of the corresponding chapter.

T. Preskett, M. Virgilio, P. Jaiswal, and B. Ganapathisubramani. Effects of pressure-gradient histories on skin friction and mean flow of high reynolds number turbulent boundary layers over smooth and rough walls. *Journal of Fluid Mechanics*, 1010:A30, 2025

T. Preskett and B. Ganapathisubramani. The impact of pressure gradient history on flow structures in high reynolds number rough wall turbulence. *International Journal of Heat and Fluid Flow*, 116:109942, 2025

T. Preskett, M. Virgilio, P. Jaiswal, and B. Ganapathisubramani. Effect of pressure gradient histories on turbulence characteristics of turbulent boundary layers over smooth and rough walls. *Physical Review Fluids*, 11(1):014603, 2026

The following work has been published by another author using data obtained during collaborative experimental campaigns.

M. Virgilio, T. Preskett, P. Jaiswal, and B. Ganapathisubramani. Pressure gradient history effects on integral quantities of turbulent boundary layers: experiments and data-driven models. *Journal of Fluid Mechanics*, 1014:A2, 2025

noindent Parts of this work have been used at the following conferences.

T. Preskett and B. Ganapathisubramani. Effects of pressure gradient history on rough-wall turbulent boundary layers. *UK Fluids Conference 2022*, Sheffield, UK, September 6-8, 2022

T. Preskett and B. Ganapathisubramani. Reynolds number and pressure gradient history effects on rough-wall turbulent boundary layers. *75th Annual Meeting of APS Division of Fluid Dynamics*, Indianapolis, Indiana, USA, November 20-22, 2022

T. Preskett and B. Ganapathisubramani. Effect of pressure gradient history on rough-wall turbulent boundary layers. *The 14th International ERCOFTAC Symposium on Engineering Turbulence Modelling and Measurements (ETMM-14)*, Barcelona, Spain, September 6-8, 2023

T. Preskett and B. Ganapathisubramani. Streamwise development of boundary layer properties over a rough wall turbulent boundary layer with pressure gradients. *76th Annual Meeting of APS Division of Fluid Dynamics*, Washington, DC, USA, November 19-21, 2023

T. Preskett and B. Ganapathisubramani. Boundary layer development under streamwise pressure gradients at high Reynolds numbers over rough walls. *The 13th International Symposium on Turbulence and Shear Flow Phenomena (TSFP- 13)*, Montréal, Canada, June 25-28, 2024

T. Preskett and B. Ganapathisubramani. High Reynolds number smooth wall turbulent boundary layers with streamwise pressure gradients. *UK Fluids Conference 2024*, Swansea, UK, September 9-11, 2024

1.3 Data availability

The data used in this thesis is available from the University of Southampton repository and is split into three datasets:

- The smooth and rough wall hot wire anemometry dataset, including the mean pressure gradient history associated with this study, is available at DOI: 10.5258/SOTON/D3829.
- The smooth wall PIV dataset associated with this study is available at DOI: 10.5258/SOTON/D3822.
- The rough wall PIV dataset associated with this study is available at DOI: 10.5258/SOTON/D3828.

Chapter 2

Background

This chapter looks at the previous studies upon which this thesis builds. The first part of the chapter explores the fundamentals of a TBL with details of the scaling laws present within a TBL. The mean flow, representing the overall properties and shape of the boundary layer, is assessed for both smooth and rough walls before examining the effects of different PG histories. The next section first looks at turbulence statistics within a TBL for a ZPG over smooth and rough walls before extending this to include the effect of different PG histories. The final review section looks at the different coherent structures present within a TBL and how these are affected by the PG history. This chapter concludes with the aim and objectives based on the gaps identified in previous literature.

2.1 Smooth wall turbulent boundary layer

The smooth wall TBL under ZPG conditions has been extensively studied. The review of Smits et al. (2011) highlights many previous studies. A turbulent boundary layer can typically be divided into two regions: the inner and outer regions. The viscosity of the near-wall flow dominates the inner region of the flow. This region is characterised by structures the size of the viscous length scale, ν/U_τ, where ν is the kinematic viscosity of the flow and U_τ is the friction velocity defined by

$$U_\tau = \sqrt{\frac{\tau_0}{\rho}}, \tag{2.1}$$

where τ_0 is the wall shear stress and ρ is the fluid density. Using these scaling parameters, Prandtl (1925), defined the law of the wall given by

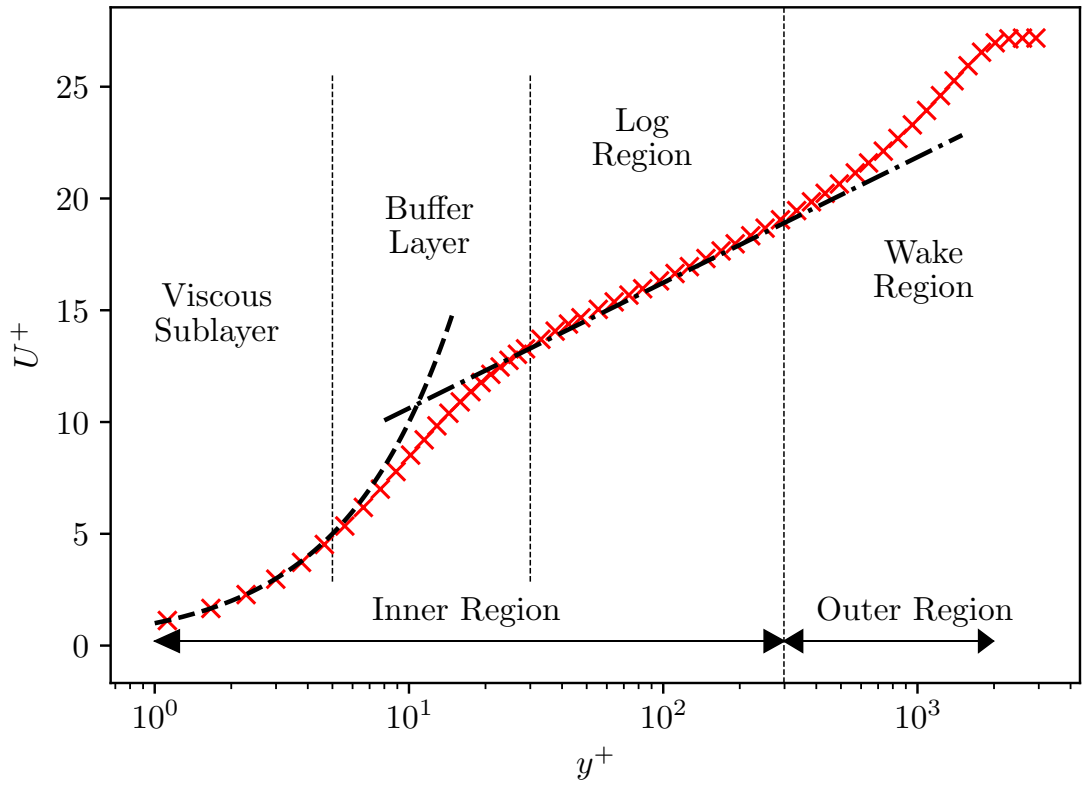

FIGURE 2.1: Smooth wall boundary layer velocity profile showing classical regions. Adapted from Castro and Vanderwel (2021) using DNS data at $Re_\tau = 1989$ from Borrell et al. (2013). The classic viscous sublayer, $U^+ = y^+$, is shown by (- - -) in the viscous sublayer region. The log-law, $U^+ = \frac{1}{\kappa} \ln y^+ + B$, is shown by (—·—)

$$\frac{U}{U_\tau} = f\left(\frac{yU_\tau}{\nu}\right), \tag{2.2}$$

where U is the mean streamwise velocity. The outer region of the flow is dominated by structures of the $\mathcal{O}(\delta)$, where δ is the boundary layer thickness. The relevant velocity scale in this region is U_{99}, the boundary layer edge velocity. U_{99} is defined as the point at which a ZPG TBL reaches 99% of the freestream velocity. The boundary layer thickness is defined for a ZPG TBL as the distance from the wall where $U \geq U_{99}$. In this region, the scaling is defined by the velocity defect law given by

$$\frac{U_{99} - U}{U_\tau} = g\left(\frac{y}{\delta}\right) \tag{2.3}$$

Figure 2.1 shows the various regions of a typical smooth wall boundary layer. It can be seen that the inner region typically consists of three sub-regions. The first is a viscous sublayer that can accurately be described by

$$U^+ = y^+, \tag{2.4}$$

where the superscript $^+$ denotes scaling with inner units and $y^+ = yU_\tau/\nu$. The buffer layer is the next region up from the wall, which is classically considered $5 \leq y^+ \leq 30$ (Castro and Vanderwel 2021). In Pope (2000), it is reported as $5 \leq y^+ \leq 50$, showing some debate over its extent. The flow is more complicated in this region, and as such, there is no classical velocity profile in this region. Attempts, however, have been made to define the flow in this region, such as Musker (1979). When considering boundary layer flows, scale separation defines the ratio between the inner and outer length scales. The scale separation is often quantified using the Re_τ, also known as δ^+, defined by

$$Re_\tau = \frac{\delta U_\tau}{\nu} \tag{2.5}$$

If there is a large enough scale separation, there is a region overlapping the inner and outer regions known as the logarithmic region. In this region, inner and outer scaling are assumed to be valid. The velocity in this region can be described by the log law defined by

$$\mathrm{U}^+ = \frac{1}{\kappa} \ln y^+ + B, \tag{2.6}$$

where κ is the von Kármán constant and B is the smooth wall intercept. The logarithmic region for a smooth wall TBL is typically assumed to extend from $30\nu/U_\tau < y \leq 0.15\delta$ (Jiménez 2004; Smits et al. 2011; Romero et al. 2022). For a boundary layer, κ is taken at 0.39, and B is 4.3 as given by Marusic et al. (2013). As reported by Marusic et al. (2010b) and Smits et al. (2011), the value of these constants is dependent on the flow facility (channel flow, wind tunnel or pipe flow). The final part of a turbulent boundary layer to consider is the wake region, first characterised by Coles (1956). The composite profile describes both the logarithmic region and the wake region. The resulting compositing profile is considered valid for $y^+ \geq 50$ (Jiménez 2004). The resulting velocity distribution defined by Coles (1956) as

$$U^+_{smooth} = \frac{1}{\kappa} ln(y^+) + B + \frac{\Pi}{\kappa} W(\eta), \text{with}, \eta = \frac{y}{\delta}, \tag{2.7}$$

where Π is Cole's wake parameter and W is wake function. Cole's wake parameter can be seen as a measure of the deviation of the velocity profile from the log law. Since the wake function is normalised such that $W(0) = 0$ and $W(1) = 2$ and therefore the maximum deviation is given by $2\Pi/\kappa$ (Pope 2000 and Castro and Vanderwel (2021)). The wake function can take various forms; the classical function arising from Coles (1956) is $W(\eta) = 2\sin^2((\pi/2)\eta)$ (Pope 2000). Another wake function is a fourth-order polynomial from Lewkowicz (1982) given by

$$W(\eta) = 2\eta^2(3-2\eta) - \frac{1}{\Pi}\eta^2(1-\eta)(1-2\eta) \tag{2.8}$$

When considering a TBL, it is possible to define the boundary layer thickness in several ways. The most common has already been introduced, which is the boundary layer thickness, δ. The second is the displacement thickness, which is defined as the distance the wall would need to be moved inwards to maintain the same flow rates as if the flow were inviscid. The displacement thickness, δ^*, can be calculated from

$$\delta^* = \int_0^\delta \left(1 - \frac{U}{U_{99}}\right) dy \tag{2.9}$$

The final measurement of boundary layer thickness is the momentum thickness, θ. Defined as the distance the wall would need to be moved inwards to maintain the same momentum flow rate if the fluid were inviscid, and is defined by

$$\theta = \int_0^\delta \frac{U}{U_{99}}\left(1 - \frac{U}{U_{99}}\right) dy \tag{2.10}$$

The displacement and momentum thickness are often combined into the boundary layer shape factor, H. This is a non-dimensional parameter given by

$$H = \frac{\delta^*}{\theta} \tag{2.11}$$

2.2 Rough wall turbulent boundary layer

The majority of real-life engineering applications experience some form of surface roughness. Extensive reviews of rough wall TBL can be found in past literature, including those of Raupach et al. (1991), Jiménez (2004) and more recently Chung et al. (2021). Any roughness with a height, k, greater than a few wall units will modify the boundary layer (Jiménez 2004). The extent to which roughness modifies a TBL depends on the relative size and type of roughness (Castro 2007; Flack et al. 2007). The overall structure of a rough wall TBL differs from that of a smooth wall due to the roughness sublayer. This region replaces the viscous sublayer seen in smooth wall flows and is thought to extend approximately $5k$ above the wall (Raupach et al. 1991; Schultz and Flack 2007).

Roughness increases the thickness of the boundary layer compared to that of a smooth wall. The addition of the roughness leads to an increase in the skin friction coefficients, C_f, defined by

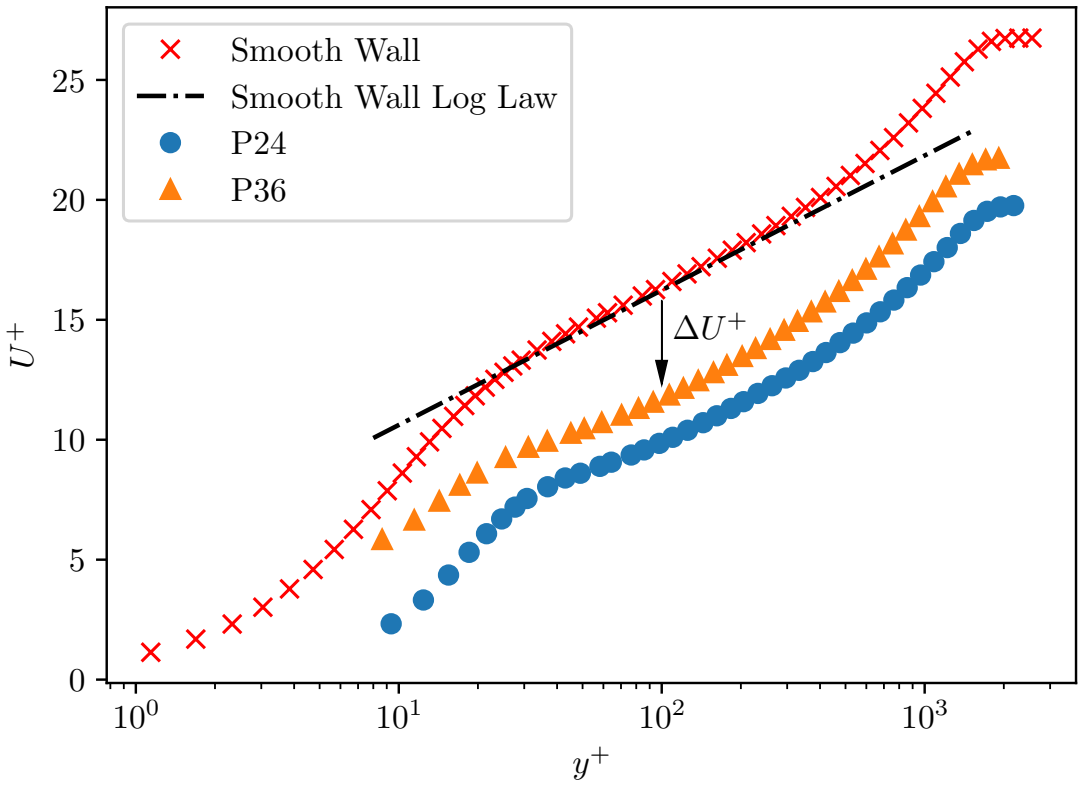

FIGURE 2.2: Inner scaled boundary layer profiles for smooth and rough walls showing the downward shift in the profile due to the roughness known as the roughness function, ΔU^+. Smooth wall DNS data at $Re_\tau = 1704$ from Borrell et al. (2013). Sandpaper data from Gul and Ganapathisubramani (2021), P24 sandpaper data at $Re_\tau = 1834$ and P36 sandpaper data at $Re_\tau = 1617$.

$$C_f = \frac{\tau_0}{\frac{1}{2}\rho U_{99}^2} = 2\left(\frac{U_\tau}{U_{99}}\right)^2 \tag{2.12}$$

The works of Clauser (1954) and Hama (1954) independently observed that both a smooth and rough wall velocity profile have a similar shape. However, it was noted that there was a downward shift in the velocity profile in the log region, as shown in figure 2.2. The addition of the roughness function, ΔU^+, commonly models this downward shift, which represents the momentum deficit due to a given roughness (Clauser 1954; Wu and Piomelli 2018; Chung et al. 2021). The resulting log law profile for a rough wall is given by

$$\mathrm{U}^+ = \frac{1}{\kappa}\ln\left((y-d)^+\right) + B - \Delta U^+, \tag{2.13}$$

where d is the zero plane displacement. As reported by Chung et al. (2021), the zero plane displacement is the position at which the outer region of the flow perceives the wall to lie. Typically, d is assumed to be between the underlying wall and the crest of

the roughness elements. For a ZPG flow, d is typically assumed to equal $k/2$ (Squire et al. 2016). The gradient of the log law region (κ) is assumed to be independent of the surface under zero pressure gradient conditions (Clauser 1954; Jiménez 2004).

Prediction of the roughness function

While equation 2.13 provides a way of modelling the velocity profile over a rough wall, it requires prior knowledge of the roughness function. Therefore, a method of predicting the roughness function is required. The pioneering experiments of Nikuradse (1933) conducted uniform sand grain roughness experiments in a pipe flow facility. Schlichting (1937) introduced the concept of the equivalent sand grain roughness, k_s. Defined as the size of closely packed uniform sand grains from Nikuradse (1933) that results in the same drag as a given surface (Chung et al. 2021). The roughness function is related to the equivalent sand grain roughness (Flack and Schultz 2010) as

$$\Delta U^+ = \frac{1}{\kappa} \ln k_s^+ + B - 8.5 \tag{2.14}$$

While equation 2.14 may seem to offer the solution for predicting the roughness function, it has some limitations. Firstly, equation 2.14 is only valid in the fully rough regime (see section 2.2). Secondly, it requires knowledge of a given surface's k_s value. It is currently impossible to reliably determine k_s from physical measurements of a surface. Instead, hydrodynamic experiments must be performed in the fully rough regime to determine the value of k_s (Flack and Schultz 2014). This is a problem as experiments are expensive, time-consuming and often impractical. The works of Flack and Schultz (2010) and Chung et al. (2021) provide comprehensive reviews of the current research on the relationships between surface properties and the corresponding values of k_s. Chung et al. (2021) lists the need for three parameters: a roughness height (k_a, k_{rms} etc), either a frontal solidity (λ_f), effective slope (ES) or roughness density parameter (λ_s) and finally a planar solidity (λ_p), skewness (S_k) or solid volume fraction (ϕ). The problem is that while these surface properties are relatively easy to find for a given surface, the relationships currently proposed by Flack and Schultz (2010) and Chung et al. (2021) are often only valid for limited ranges of surface parameters. There is no universal law, which is well summed up in the words of Chung et al. (2021) *'an all-encompassing equation relating k_s to topography remains elusive'*.

Roughness flow regimes

Different flow regimes can be defined using the equivalent sand grain roughness. Rough wall flows can be divided into three regions: the hydraulically smooth region, the transitionally rough regime and the fully rough regime (Flack and Schultz 2010). Historically, a surface is smooth when $k_s^+ < 5$ and fully rough when $k_s^+ > 70$. If the value of k_s^+ is in between, the surface is said to be transitionally rough. However, these can only be considered guidelines and have been seen to vary depending on the surface type (Flack and Schultz 2010).

For a surface to be considered hydraulically smooth, the roughness height must be less than a few wall units (Jiménez 2004). In this regime, the fluid viscosity damps out any perturbations caused by the roughness. This means there is no additional drag due to the roughness and $\Delta U^+ = 0$ Flack and Schultz (2010). In the transitionally rough regime, the vortices generated by the roughness are no longer damped by the fluid's viscosity. In this region, both the form drag of the elements and the viscous drag result in the overall drag of the surface (Flack and Schultz 2010).

A flow can be considered fully rough when C_f is independent of the Reynolds number. For a given surface, the flow can be considered fully rough when the roughness function reaches a linear asymptote at large values of k^+. k^+ is the roughness Reynolds number given by $k^+ = kU_\tau/\nu$. In the fully rough regime, it is possible to represent the effect of roughness using the roughness length, y_0. The relationship between y_0 and k_s (Chung et al. 2021) is given by

$$y_0 = k_s e^{\kappa B} \tag{2.15}$$

Combining equations 2.13 and 2.15, the composite velocity profile for a rough wall can be defined by

$$U^+_{rough} = \frac{1}{\kappa} ln\left(\frac{y-d}{y_0}\right) + \frac{\Pi}{\kappa} W(\eta) \text{ with}, \eta = \frac{y-d}{\delta - d} \tag{2.16}$$

Outer layer similarity

Building on the observations of Hama (1954) on flow universality, Townsend (1976) proposed the Reynolds number similarity hypothesis and later expanded by Raupach et al. (1991). The hypothesis states that the turbulent motions outside the roughness sublayer are independent of the surface for a sufficiently high Reynolds number. The surface only influences the outer layer velocity (U_{99}) and length scale (δ) (Flack and Schultz 2014; Chung et al. 2021). The two assumptions for this hypothesis are that the

Reynolds number is sufficiently high, ensuring suitable scale separation. The second is that the roughness height relative to the boundary layer thickness is small. This hypothesis leads to the scaling that the outer region is independent of a surface in deficit form as given by equation 2.3.

Jiménez (2004) suggested that $\delta/k > 40$ ensures the roughness effects are less than half the thickness of the log region. However, for the mean flow, similarity has been seen for much larger values up to $\delta/k = 5$ in Castro (2007). Similarly, Flack and Schultz (2014) saw a collapse in the outer region for $\delta/k = 16$. However, this view is not universally accepted, as differences in the outer region have been reported in studies such as Krogstad et al. (1992) and Tachie et al. (2002), which observed variations in the mean velocity deficit profile.

For a given surface, it is possible, using equation 2.16, to write the deficit profile for any surface as

$$\frac{U_{99} - U}{U_\tau} = -\frac{1}{\kappa} ln\left(\frac{y-d}{\delta-d}\right) + \frac{\Pi}{\kappa}\left[2 - W\left(\frac{y-d}{\delta-d}\right)\right] \tag{2.17}$$

As seen in equation 2.17, there is no dependence on any roughness parameters. The same equation can be derived for a smooth wall using equation 2.7 with d equal to zero.

2.3 Effect of pressure gradient history on mean flow

Having examined the mean flow of a ZPG TBL for smooth and rough walls, the effect of PGs on the mean flow is now considered. First, the parameters used to define different PG histories are introduced before examining their effect on smooth and rough walls.

Defining a pressure gradient

The definitions of the adverse pressure gradient (APG) and favourable pressure gradient (FPG) are well-known when considering PGs. An FPG is one where the pressure decreases in the streamwise flow direction, resulting in $dp/dx < 0$, where dp/dx is the streamwise pressure gradient. An FPG results in an accelerating freestream flow. The opposite is true for an APG where $dp/dx > 0$ and the freestream flow decelerates in the streamwise flow direction.

A concept often used in the study of boundary layer development is that of the self-similar boundary layer, also known as the self-preserving boundary layer or equilibrium boundary layer. As defined by Townsend (1956), this is a boundary layer in which

the mean velocity profile and flow statistics, such as Reynolds shear stress and turbulence intensities, are invariant with respect to streamwise coordinates when scaled with the correct local velocity and length scales. The smooth and rough wall boundary layers in sections 2.1 and 2.2 do not meet this requirement. This is because the velocity distribution of the boundary layer requires both inner and outer scaling to normalise the profile. Townsend (1956) and later Rotta (1962) showed that the only wall-bounded flow over a smooth wall satisfying this strict definition is a sink flow. Coles (1956) further found that sink flows over a smooth wall have a wake strength factor, $\Pi = 0$, and are considered a pure wall flow; this work was later supported by the work of Marusic et al. (2010b).

Due to the strict nature of Townsend (1956) definition of self-similar flows, other definitions are used for a near-equilibrium boundary layer. One such definition used by Marusic et al. (2010b) is that at a high enough Reynolds number, the flow can be considered in near equilibrium if outer layer similarity is seen with streamwise development.

When considering pressure gradient flows, both near-equilibrium and non-equilibrium flows have been considered. The work of Bobke et al. (2017) and Monty et al. (2011) showed that the velocity distribution should follow a power law in the freestream to achieve this near-equilibrium state. When studying these near-equilibrium flows, a key parameter is the Clauser pressure gradient parameter, β, first proposed by Clauser (1954), defined by

$$\beta = \frac{\delta^*}{\tau_0}\frac{dP}{dx} \tag{2.18}$$

The β parameter is crucial to the study of the near-equilibrium boundary layer, especially for adverse pressure gradients, since, as reported by Monty et al. (2011), a constant β is a necessary condition for a near-equilibrium boundary layer, supporting the same conclusion made by Rotta (1962) and Mellor and Gibson (1966). For a ZPG flow, β will be zero, thus in near equilibrium. More recently, the work of Ghanadi and Djenidi (2022) suggests that the self-preserving state of the turbulent boundary layer is dependent on the external pressure gradient. In contrast, Bobke et al. (2017) saw a similar lack of collapse for different pressure gradients in turbulence intensity profiles. This conclusion was drawn from the lack of collapse of the mean velocity profiles. However, as noted above, the definition of near equilibrium comes from the collapse of the mean velocity deficit. A non-equilibrium boundary layer can be defined as one in which $\beta \neq const$, and as such, no outer layer similarity is seen.

When defining the strength of the pressure gradient, the acceleration parameter K, first proposed by Launder (1964), is often used for favourable pressure gradients given by

$$K = \frac{\nu}{U_{99}^2}\frac{dU_{99}}{dx}, \tag{2.19}$$

where dU_{99}/dx is the local freestream velocity gradient. As noted by Monty et al. (2011), K can be used to uniquely characterise an equilibrium boundary layer since for these flows $\beta = const$.

Effect of pressure gradient history on the mean flow

To examine how roughness effects vary with different PG histories, one needs to decouple the effect of PG and roughness. Therefore, work studying the effect of PG on rough wall flows often also considers smooth wall flows under similar PGs.

Extensive studies on smooth and rough walls have shown that PG history affects C_f. Extensive studies over smooth walls, including Spalart and Watmuff (1993), Krogstad and Skåre (1995) and Volino (2020), have shown a reduction in C_f with APGs. Similar results have been seen for rough wall flows in Shin and Song (2015a), Ghanadi and Djenidi (2022) and Volino and Schultz (2023), amongst many others. In all these experiments, U_τ has been derived from the velocity profile and not directly measured, introducing increased uncertainty into the results. The effect of skin friction under an FPG flow is more complicated. The LES simulations of Piomelli et al. (2000) showed for low Reynolds number smooth wall flow (Re_θ Spalart (1986)) that an FPG initially increases C_f before decreasing as the flow relaminarise. Relaminarisation only occurs under strong FPG and leads to a breakdown of the classical log law region (Warnack and Fernholz 1998). At higher Reynolds numbers, relaminarisation does not occur, and the C_f increases as shown by Volino (2020) and Ghanadi and Djenidi (2022). The addition of roughness to a flow means the flow cannot relaminarise. FPGs lead to an increase in the wall shear stress, which in turn leads to an increase in k^+, which further increases the skin friction (Cal et al. 2006, Shin and Song 2015b and Tay et al. 2009a).

The effect of the PG history on the mean velocity profile is seen in figure 2.3. The clearest difference between the different profiles is seen in the wake region of the flow. APG has been shown to increase the wake strength, leading to a thicker boundary layer compared to a ZPG flow (Samuel and Joubert 1974; Aubertine and Eaton 2005; Monty et al. 2011). This effect is also seen for rough wall flows, including that of Tsikata and Tachie (2013). Particle image velocimetry (PIV) measurements of rough walls in a diffuser by Tay et al. (2009b) concluded that the effect on the wake is larger for a smooth wall than a rough wall. An FPG has the opposite effect on the wake strength, leading to a reduction compared to ZPG flows on both smooth and rough wall flows (Tay et al. 2009a; Volino 2020; Volino and Schultz 2023). This results in a thinner boundary layer compared to a ZPG flow. These changes in the wake region result in variations in the

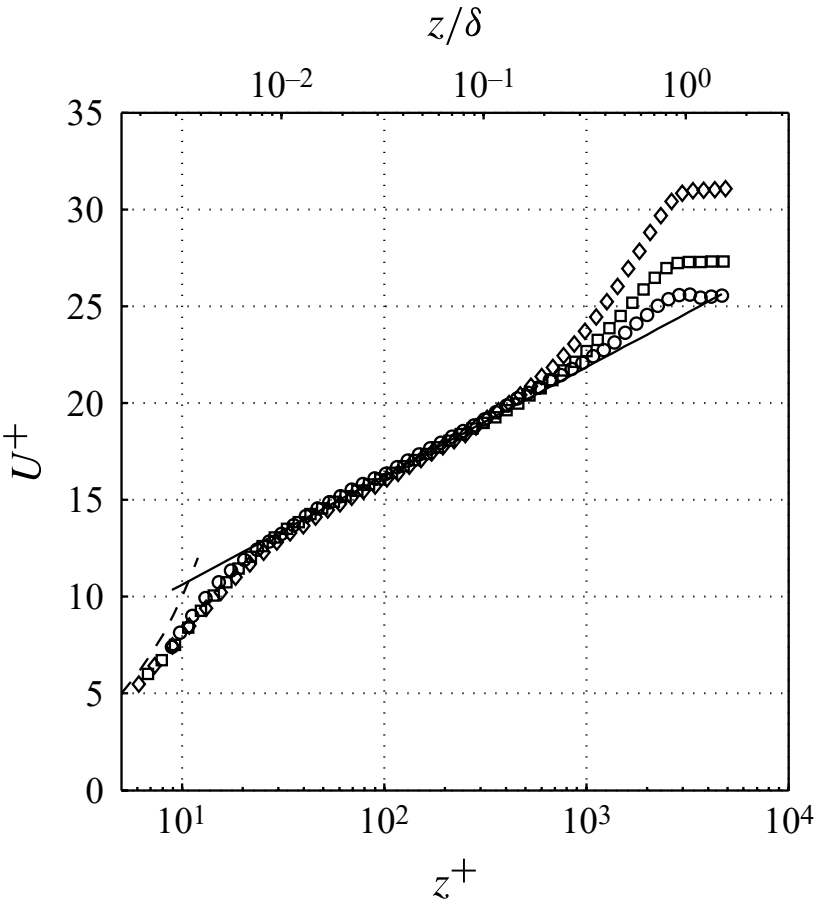

FIGURE 2.3: Mean inner scaled boundary layer velocity profiles over a smooth wall for $Re_\tau \approx 3000$: ◊ for APG, □ for ZPG and ○ for FPG. Adapted from Harun et al. (2013).

boundary layer shape factor. At constant Re_τ, the work of Monty et al. (2011) showed that the boundary layer shape factor increases with APG strength. For a smooth wall flow, they concluded that the shape factor decreases with the Reynolds number, as is seen for ZPG flows. These conclusions are supported by the work of Shin and Song (2015a) and Spalart and Watmuff (1993), who further concluded that both δ^* and θ increase with APG. The opposite results have been seen over a smooth and rough wall for an FPG in Volino (2020) and Volino and Schultz (2023) with a reduction in the shape factor.

The changes to the wake region are accompanied by changes to the log region depending on the PG type. Nagano et al. (1998), Lee and Sung (2009), Monty et al. (2011) and Tsikata and Tachie (2013) have all shown that the wake region starts nearer the wall under APG conditions, for both smooth and rough wall flows. For an FPG, the opposite effect is seen where the log region extends further away from the wall compared to the ZPG flow (Spalart and Watmuff 1993; Shin and Song 2015b). Evidence also shows that the log law gradient, κ, is not constant. The smooth wall study of Spalart and Watmuff (1993) and more recently Knopp et al. (2021) have suggested that κ decreases

when the flow is exposed to an APG. The simulations of Piomelli et al. (2000) suggested that under mild FPG conditions, the slope of the log law was reduced, consistent with an increase in κ. These results suggest that the assumption in sections 2.1 and 2.2 that κ is constant may not be valid and is indeed dependent on the local flow condition. Further work is, however, required before conclusions can be made on the value of κ for a given PG history. The work of Tay et al. (2009b) also suggested changes in the near-wall region with APG, with a thickening of the roughness sublayer by a factor of three.

The log law of a rough wall is not only described by log law constants but also by the roughness function. As previously described, modelling the roughness function requires k_s (or y_0). However, the effect of PGs on this is uncertain. Some of the earliest experiments on the effect of APG were carried out by Perry and Joubert (1963), which concluded that the roughness function was independent of the PG the flow experienced. This would imply, as is currently done for CFD simulations, that the ZPG equivalent sand grain roughness can be used regardless of the pressure gradient applied. More recently, this assumption has been challenged. The experiments of Pailhas et al. (2008) concluded that an APG did affect the value of k_s. A similar conclusion was reached by Tsikata and Tachie (2013) and Tay et al. (2009b) that APG leads to an increase in the value of k_s. The work of Fritsch et al. (2022) and Vishwanathan et al. (2023), as well as Volino and Schultz (2023), demonstrated the variation in k_s under different pressure gradients. These studies had contrasting conclusions with Vishwanathan et al. (2023) suggesting that k_s is independent of pressure gradient histories (although the values of β explored were not very strong and the variance in k_s was as much as 50% across cases, but without any specific trends with pressure gradient). In contrast, Volino and Schultz (2023) suggests a weak trend that k_s increases with FPG and decreases with APG. Vishwanathan et al. (2023) suggested that the variation in k_s is due to the choice of extent of log region during the fitting process, which is necessary to determine k_s (or ΔU^+). Volino and Schultz (2023) also indicated a dependence of k_s on k/δ, suggesting that these results may reflect a lack of scale separation. It should be noted that all these studies have significant uncertainty in their results, also due to indirect wall shear stress measurements. Therefore, any fitting process and determination of parameters depend on the value of skin friction.

Formation of Internal Layer

Internal layers (ILs) are layers inside the main TBL in which there are increased vortices resulting in a region of strong shear stress (Wu and Squires 1998; Balin and Jansen 2021; Parthasarathy and Saxton-Fox 2023). The formation of ILs has been seen to occur with rapid changes in the boundary conditions of the flow. The first of these changes is changes in both the surface curvature or step changes in roughness (Antonia and

Luxton 1971, 1972; Baskaran et al. 1987; Wu and Squires 1998). The second reason for their formation, and the one applicable to this work, is that the switch from FPG to APG causes ILs to grow, as shown by Tsuji and Morikawa (1976) and more recently Parthasarathy and Saxton-Fox (2023). As noted by Wu and Squires (1998), these ILs form due to a rapid change in the skin friction, which, as noted in section 2.3, occurs due to different PG histories. Wu and Christensen (2006) extended this, suggesting that a region of stabilisation may need to follow the rapid change in the skin friction.

Smits and Wood (1985) presented evidence that ILs form since the inner and outer regions of the boundary layer adjust to the PG at different rates. The inner region reacts faster than the outer region to changes in PG history, supported by the later work of Baskaran et al. (1991). This later work further suggested a decoupling of the inner and outer regions of the boundary layer, with the outer region acting as a free shear region, and has since been supported by Balin and Jansen (2021). Internal layers are important when considering the turbulence statistics within a TBL since they result in inflection points within the Reynolds shear stress profiles, along with the increase in near-wall shear stress. The challenge when studying the effect of PG history on ILs is reliably identifying the edge of the internal layer. Parthasarathy and Saxton-Fox (2023) proposed a method which looks for changes in the slope of the mean velocity profile; however, this method is limited to flows with clear changes in the velocity profile slope.

Prediction of effects of pressure gradient history on mean flow

The review of the mean flow under the influence of PG shows a clear effect of the flow history on the mean velocity profile. Much of the previous modelling of boundary layers involves the von Kármán's integral momentum equation. Integration of the mean momentum equation across the boundary layer yields equation 2.20 (White and Majdalani 2021; Castro and Vanderwel 2021)

$$\frac{d\theta}{dx} + (2+H)\frac{\theta}{U_{99}}\frac{dU_{99}}{dx} = \frac{C_f}{2}, \tag{2.20}$$

where $d\theta/dx$ is the streamwise gradient of the momentum thickness. Equation 2.20 has three unknowns (θ, H and C_f) and therefore requires equations to relate variables in order to find a solution. As outlined in White and Majdalani (2021), one solution is to use the composite velocity profile (equation 2.7). However, this introduces another unknown, the wake strength, which, as has been seen, is a function of the local PG. Das (1987) proposed a relationship between the local β and the Π, based on previous data (White and Majdalani 2021). The relationship is a given by

$$\beta \approx -0.4 + 0.76\Pi + 0.42\Pi^2 \tag{2.21}$$

While this provides a closure to the momentum integral equation as seen in White and Majdalani (2021), the range of Π for a given β is large. This introduces uncertainty into the prediction, and thus, improvements are needed. A similar idea was proposed by Perry et al. (2002), who showed theoretical relationships between Π and β. The key parameter from this work is ζ, which is given by

$$\zeta = \frac{U_{99}}{U_\tau}\delta\frac{d\Pi}{dx}, \tag{2.22}$$

where $d\Pi/dx$ is the local streamwise gradient of the wake strength. Using this parameter, they define a relationship for β, given by

$$\beta = \begin{cases} -0.5 + 1.2\Pi^{\frac{4}{3}} + \zeta^2(1.10/\Pi^2) & \text{if } \zeta \geq 0 \\ -0.5 + 1.2\Pi^{\frac{4}{3}} + \zeta(0.62 + 0.25\Pi) & \text{if } \zeta < 0 \end{cases} \tag{2.23}$$

Equation 2.23 gives $\beta = f(\Pi, d\Pi/dx)$ that, for many flows, presents a problem since knowing $d\Pi/dx$ is often not practical or possible to predict. More recent work by Vinuesa et al. (2017) examined experimental and simulation APG data, including the LES of Bobke et al. (2017). This work aimed to capture the APG effects using $\overline{\beta}$, which is defined by

$$\overline{\beta}(Re_\theta) = \frac{1}{Re_\theta - Re_{\theta,0}}\int_{Re_{\theta,0}}^{Re_\theta}\overline{\beta}(Re_\theta)dRe_\theta, \tag{2.24}$$

where $Re_{\theta,0}$ is the initial Re_θ. Resulting in a relationship, which relates the change in C_f to the integral of the PG, is defined by

$$C_f^{APG} = \frac{C_f^{ZPG}}{H_{ZPG}^{\overline{\beta}/2}}, \tag{2.25}$$

where C_f^{APG} is defined at the point of evaluation of $\overline{\beta}$ and C_f^{ZPG} and H_{ZPG} are the ZPG values of at the same Re_θ. While good agreement with data is seen with equation 2.25, there is a requirement for β history at different streamwise stations. This requires data of both C_f and δ^* along with the local pressure gradient. Obtaining this data is costly, whether from experiments or simulations. Ideally, there would be a method which relates the PG history to the variation in the wake strength without the need for detailed measurements.

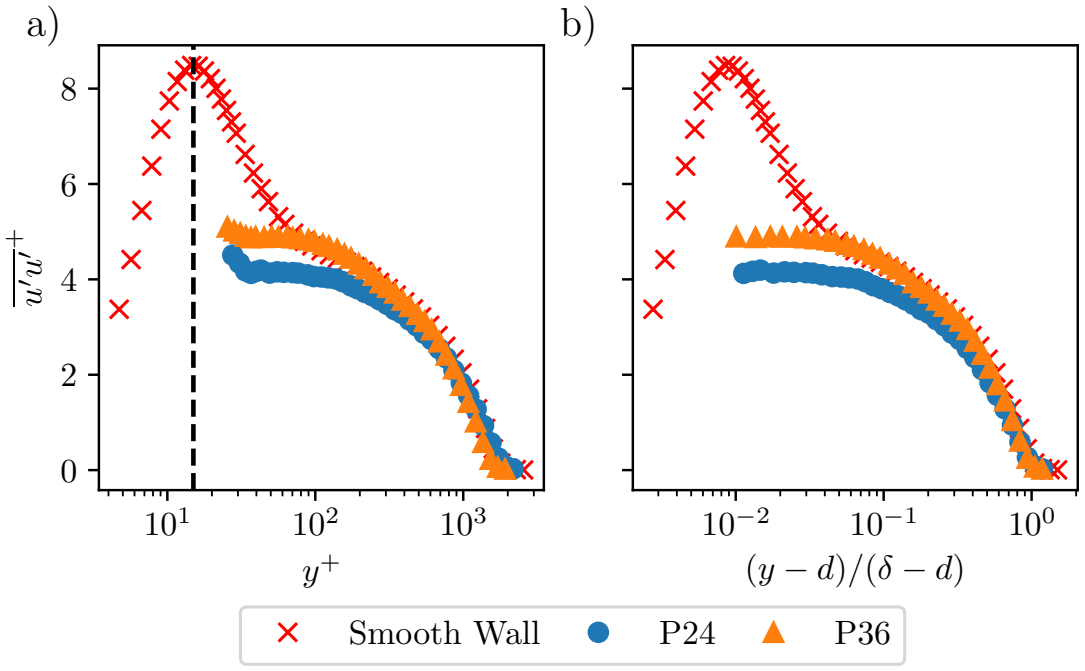

FIGURE 2.4: Streamwise Reynolds stress profiles for smooth and rough walls. Smooth wall DNS data at $Re_\tau = 1704$ from Borrell et al. (2013). Sandpaper data from Gul and Ganapathisubramani (2021), P24 sandpaper data at $Re_\tau = 1834$ and P36 sandpaper data at $Re_\tau = 1617$. *a* Inner scaled turbulence profiles as a function of y^+ with a vertical dashed line is plotted at $y^+ = 15$. *a* Inner scaled streamwise Reynolds stress as function of $(y-d)/(\delta-d)$.

2.4 Turbulence statistics in the turbulent boundary layer

The review of the mean flow has shown that the mean velocity profile differs due to PG history. This section examines turbulence statistics, focusing on how turbulence varies with the pressure gradient and how this affects the mean velocity profile. When considering the turbulence within a TBL, the most commonly considered parameter is the streamwise Reynolds stress, $\overline{u'u'}$. A direct numerical simulation (DNS) smooth wall streamwise Reynolds stress, $\overline{u'u'}^+ = \overline{u'u'}/U_\tau^2$, is shown in figure 2.4*a*. The most prominent feature is the inner peak at $y^+ = 15$ shown by the vertical dashed line in figure 2.4*a*. This inner peak location is considered to be universal, as shown by the works of Marusic et al. (2010a), Monty et al. (2011), Volino (2020) and Deshpande et al. (2023). While the inner peak location is independent of Re_τ, De Graaff and Eaton (2000) and Marusic et al. (2010a) among others have shown $\overline{u'u'}^+$ to be a function of Re_τ.

When studying turbulence, Taylor's hypothesis (Taylor 1938) is often used to convert temporal spectra, such as that from a hot wire probe, to a spatial one. It assumes a statistically stationary flow in which the flow statistics are invariant in time. Hence, it is also known as the frozen-turbulence approximation (Pope 2000). Scale decomposition of $\overline{u'u'}$ by Hutchins et al. (2009) and Marusic et al. (2010a) considered the

effect of Reynolds number on both the small ($\lambda < \delta$) and large scales ($\lambda \geq \delta$). The results showed that the small scales are invariant to Re_τ while the large-scale component increases with Re_τ. This increase in the large-scale structures happens at all wall-normal locations. Analysis of the pre-multiplied energy spectra of a smooth wall TBL by Hutchins and Marusic (2007a) identified two distinct peaks when sufficient scale separation exists ($Re_\tau > 1700$) Hutchins and Marusic (2007a). The first is the inner peak in the streamwise Reynolds stress. The second appears in the log region and is attributed to very large-scale motions (VLSMs) in the flow (see section 2.5). Hutchins and Marusic (2007b) showed that the magnitude of the peak increases with the Reynolds number, meaning more energised structures as the Reynolds number increases.

In section 2.2, outer layer similarity was introduced, demonstrating the collapse of the mean flow for ZPG rough and smooth wall flows in the outer region. The collapse in the outer region, however, is not limited to only the mean flow and is also seen in the turbulence statistics. As with the mean flow, outer layer similarity is seen when U_τ is used for the velocity scale and δ as the length scale for normalisation, as is seen in figure 2.4*b*. The inner peak in the smooth wall cases is not seen for a rough wall flow. The inner peak is disrupted by the roughness elements breaking the vortices near the wall (Schultz and Flack 2007). It is also possible to scale the streamwise Reynolds stress with U_{99}^2 (outer scaling), leading to different conclusions on the effect of roughness. Shin and Song (2015b) and Tay et al. (2009b) have shown that outer scaling results in the streamwise Reynolds stress of a rough wall being higher than that of a smooth wall throughout the boundary layer. Squire et al. (2016) examined the difference in pre-multiplied energy spectra between smooth and rough walls, showing a clear reduction in the energy of near-wall large structures. The magnitude of this reduction is seen to be dependent on k_s^+.

Effect of pressure gradient history on turbulence statistics

Scaling was seen to impact the conclusions drawn when assessing the impact of roughness on the turbulence statistics. Similar differences are seen with scaling when accessing the impact of PG history on turbulence statistics. Monty et al. (2011) and Harun et al. (2013) amongst others have shown APG to increase $\overline{u'u'}^+$ throughout a smooth wall TBL as shown in figure 2.5*a*. This increase in energy comes from an increase in both the small and large scales being energised with an increase in APG strength (Monty et al. 2011; Harun et al. 2013; Bobke et al. 2017). Recently Deshpande et al. (2023) showed that under APG conditions, the small-scale energy reduces as Re_τ increases. This differs from the large-scale energy, which Tanarro et al. (2020) showed to increase as Re_τ increases. APGs result in an outer peak as can be seen in figure 2.5*a*, which for sufficiently strong APGs has been seen to exceed the inner peak (Monty et al. 2011; Bobke et al. 2017). Monty et al. (2011) offers one possible explanation for this

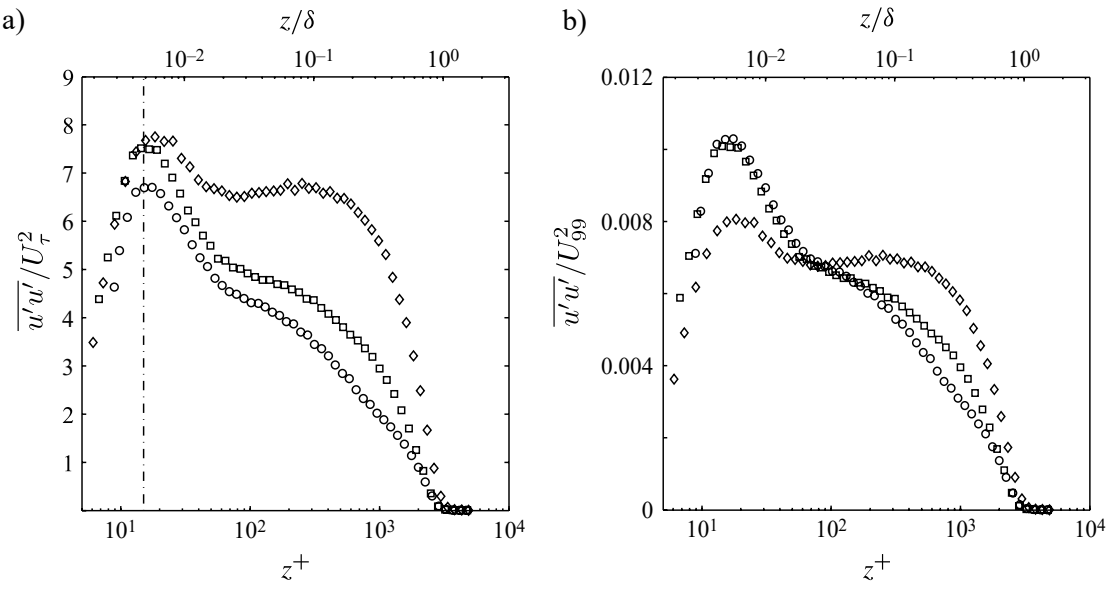

FIGURE 2.5: (*a*) Mean inner scaled streamwise Reynolds stress profiles and (*b*) Mean outer scaled streamwise Reynolds stress profiles over a smooth wall for $Re_\tau \approx 3000$: ◊ for APG, □ for ZPG and ○ for FPG. Adapted from Harun et al. (2013). Note that z^+ is the wall-normal position in the coordinate system of Harun et al. (2013).

peak, suggesting it is due to a relocation of dormant motions from the inner to outer region.

An FPG has the opposite effect to that of an APG, reducing $\overline{u'u'}^+$ throughout the boundary layer as seen in figure 2.5*a*. Spectral analysis by Harun et al. (2013) shows a reduction in both the small and large scales throughout the boundary layer. When outer scaling is used, these conclusions switch, that being that APG leads to a reduction in the near-wall turbulence, whereas FPG leads to an increase. These effects can be seen in figure 2.5*b*, where it is also seen that the trends in the outer region a independent of scaling (Monty et al. 2011; Harun et al. 2013).

The work of Tay et al. (2009b), Shin and Song (2015a), Ghanadi and Djenidi (2022), and Vishwanathan et al. (2023) has shown that the streamwise Reynolds stress in the outer region behaves similarly for smooth and rough walls. This holds for both APG and FPG cases, regardless of the scaling used. For a rough wall, Tay et al. (2009b) showed a reduction in near-wall turbulence with an APG, as is expected from the ZPG cases. Collapse in the outer region was also seen between the rough and smooth walls for the same PG history. This collapse in the outer region, however, is not universal since the same study showed that the collapse in the outer region disappears for a stronger roughness. Similarly, when going from ZPG to APG, Volino and Schultz (2023) saw no collapse between smooth and rough wall flows in the outer region. However, their work did see a collapse between the smooth and rough walls in the ZPG recovery section following an FPG. The pre-multiplied energy spectra presented by Ghanadi and Djenidi (2022) showed that the difference between PG and ZPG cases is similar

in the inner region, suggesting that energy distribution there is primarily influenced by roughness rather than the imposed PG. They also suggested that the effect of PG becomes more pronounced with increasing Reynolds number.

To conclude this part, the effect PG has on the effect of roughness is examined, considering both the mean flow and Reynolds shear stress. Tachie (2007) showed using boundary layer properties (δ, δ^* and θ) that roughness and APGs combined to increase these properties more than either individually. Questions, however, remain whether these properties alone are enough to draw conclusions. Tay et al. (2009b) reaches similar conclusions based on the mean velocity deficit and Reynolds shear stress. More recently, Shin and Song (2015a) concluded differently, based on the mean flow and turbulence statistics, that APGs suppress the effect of roughness. Cal et al. (2006) and Tay et al. (2009a) have both concluded that roughness effects are more dominant than FPG effects. Similarly, Tachie et al. (2007) concluded that FPGs have less effect as the flow transitions from transitional to fully rough. While Shin and Song (2015b) suggested that FPGs enhance the effect of roughness, the opposite of their findings for an APG in Shin and Song (2015a).

2.5 Coherent structures in turbulent boundary layers

Examination of the mean flow and turbulence statistics has shown variation in properties with both Reynolds number and PG history. As shown by the spectral analysis, these changes come from coherent structures with different wavelengths and positions within the flow. This section will explore these different types of structures within a TBL and how roughness and PG history affect them.

Marusic et al. (2010b) and Smits et al. (2011) both provide reviews of the different coherent structures within a ZPG smooth wall TBL. These coherent structures can be broken into four types, namely near-wall streaks, hairpin vortices, large-scale motions (LSMs) and very large-scale motions (VLSMs) (Smits et al. 2011). Near-wall streaks were first identified by Kline and Runstadler (1959) and further explored in their later work Kline et al. (1967). These streaks are regions of alternating high and low momentum typically spaced 100 viscous units apart in the spanwise direction, independent of Reynolds number (Kline et al. 1967; Smith and Metzler 1983). Figure 2.6*a* shows a visualisation of these near-wall streaks from Kline et al. (1967). Blackwelder and Eckelmann (1979) and Smith and Metzler (1983), among others, have shown streamwise lengths in excess of 1000 viscous units. These streaks are responsible for the high near-wall turbulence production found near the wall of a TBL through a process known as bursting (Kim et al. 1971). This process involves the streaks *lifting* away from the wall due to the streamwise vorticity until they reach a point where they become unstable. This is followed by rapid oscillations and breakup, throwing slow-moving fluid away from the

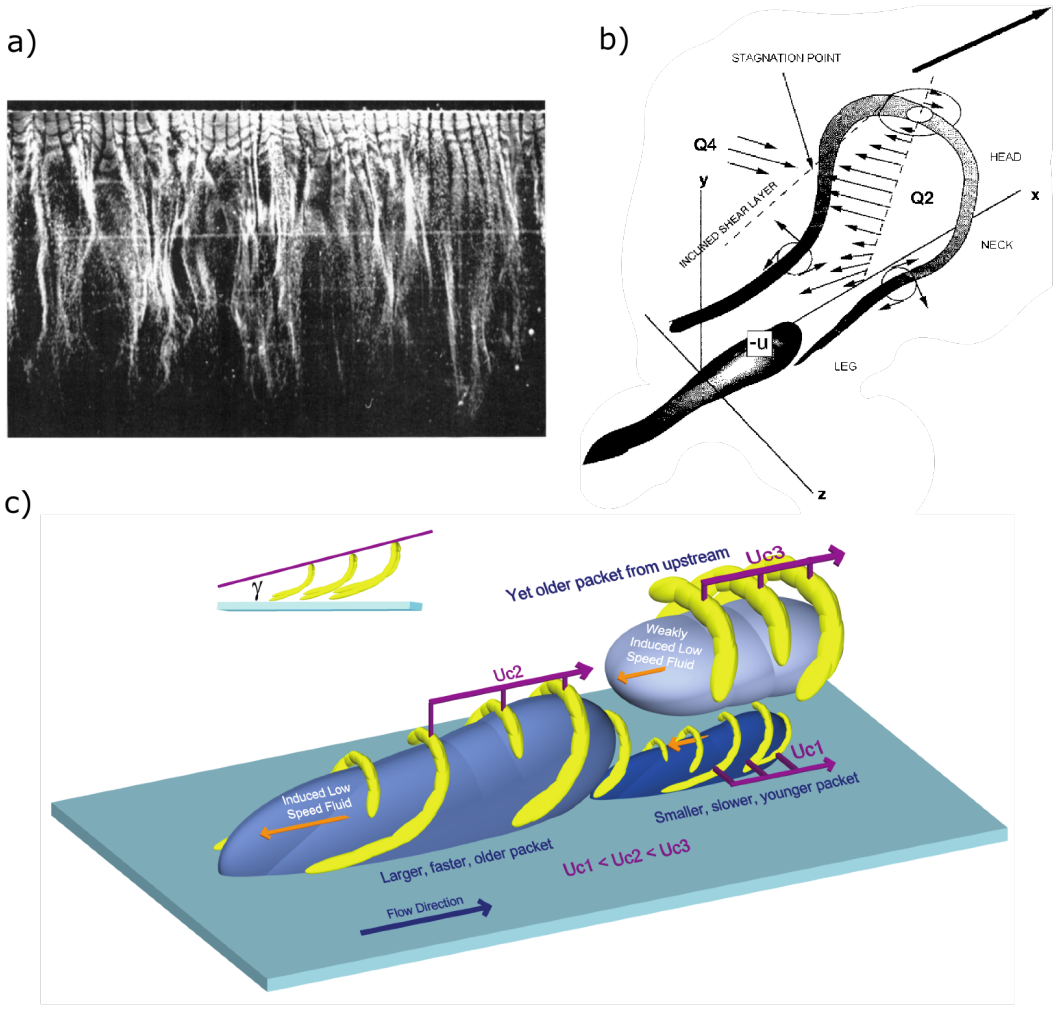

FIGURE 2.6: (*a*) Visualisation of near wall streaks at $y^+ = 2.5$ from Kline et al. (1967). (*b*) Diagram of hairpin vortex adapted from Adrian (2007). (*c*) Diagram of hairpin vortices packet adapted from Adrian (2007).

wall into the outer flow. These streaks are responsible for the inner wall peak seen in section 2.4, centred around $y^+ = 15$ (Marusic et al. 2010a). This process is known as an ejection event where $u' < 0$ and $v' > 0$, also known as a Q2 event in quadrant analysis. Due to mass continuity, these ejection events must be accompanied by fluid moving towards the wall (Pope 2000). The events first identified by Corino and Brodkey (1969) are known as sweep events or Q4 events with $u' > 0$ and $v' < 0$.

Theodorsen (1952) first proposed the presence of hairpin vortices in TBL, with experimental confirmation by Head and Bandyopadhyay (1981). These vortices have the shape shown in figure 2.6*b*. These structures consist of two long quasi-streamwise vortices connected by the hairpin head, which is inclined at 45° (Theodorsen 1952; Pope 2000; Castro and Vanderwel 2021). These vortices induce Q2 events in the flow encased by the head of the hairpin, with the flow around the hairpin being a Q4 event (Adrian 2007). These opposing events result in a stagnation point and hence high shear near the

head of the structure, responsible for significant Reynolds shear stress within the flow (Adrian 2007; Castro and Vanderwel 2021).

LSMs are thought to be created by multiple hairpin vortices aligning and travelling with the same convective velocity (Adrian et al. 2000; Ganapathisubramani et al. 2003; Adrian 2007; Smits et al. 2011). These structures only exist when there is a high enough scale separation. Detailed analysis of these structures is provided in Adrian et al. (2000). Figure 2.6*c* shows a diagram from Adrian (2007) showing these vortex packets, showing the aligned heads of the hairpins, which are inclined at around 12°. These packets consist of multiple layers of hairpin vortices and have been found to have a streamwise length of $2-3\delta$ (Adrian 2007). Much longer streamwise meandering structures around $10-15\delta$ in length have been observed; these are VLSMs (Hutchins and Marusic 2007b). As briefly touched on in section 2.4, these structures are responsible for the peak in the log region of turbulence spectra.

When considering TBLs, one of the key concepts is that of the attached eddy model. An extensive review of previous works on the attached eddy model is given by Marusic and Monty (2019). The initial model proposed by Townsend (1951, 1976) proposes that energy-containing coherent eddies extend to the wall and interact with it, influencing near-wall dynamics without necessarily being fully attached (Marusic and Monty 2019). This was later extended by Perry and Chong (1982) with the addition of attached eddies, which originate from the wall. More recently Perry and Marušić (1995) added both attached and detached eddies, where detached eddies are hairpin vortices that have become separated from the wall (Volino et al. 2007). These detached eddies are responsible for the outer layer flow structure (Smits et al. 2011). While this model suggests that the near-wall structures are independent of the outer region, this is only partial (Volino et al. 2007). This is due to the near-wall setting the boundary condition for the outer flow, which in turn influences the velocity profile and hence wall shear stress (Volino et al. 2007). The coupling between the near-wall and outer flows was investigated by Hutchins et al. (2009), showing that the LSMs in the outer region modulate the near-wall processes.

Section 2.4 showed that roughness reduces the inner-scaled near-wall turbulence. It has been seen in this section that near-wall streaks are responsible for the inner peak. For a sufficiently rough surface, the formation of these streaks will be interrupted, leading to the reduction seen in near-wall turbulence (Volino et al. 2007). Looking at near-wall Grass (1971) suggested that the region between roughness elements is the origin of ejection events in a rough wall. Further, it is concluded that these provide the momentum transport between a TBL's inner and outer layers, irrespective of the surface. Volino et al. (2007) showed that hairpin packets are present in rough wall flows similar to those seen in smooth wall flows.

Two-point spatial correlation is often used to represent the coherent structures in the flow field. Nakagawa and Hanratty (2001) suggested that the contours between a smooth and rough wall are similar in both streamwise extent and the inclination of the structures based on limited snapshots. Volino et al. (2007) similarly presented two-point correlation results; however, they concluded differently, with the rough wall having structures 10% to 20% smaller based on the correlation length.

Another method often used when examining flow structures is to look at the type of events present within the flow using quadrant analysis. Flack et al. (2005) showed the contribution of sweeps and ejections to the overall shear stress. They concluded that the roughness-induced changes are limited to the near-wall roughness sublayer. This result is not universal since Krogstad et al. (1992) showed an increase in the contribution of both sweeps and ejections well into the outer region of the flow. Flack et al. (2005) also showed that outside the roughness sublayer, both smooth and rough walls, ejection events have a significantly higher contribution to the Reynolds shear stress than sweep events. In these regions, both sweeps and ejections' contributions linearly decrease with distance from the wall. Comparing the ratio of ejections to sweep events, it is seen that, for both smooth and rough walls, ejection events increase in contribution with distance from the wall. In both Krogstad et al. (1992) and Flack et al. (2005), strong sweep events contribute more in the near-wall region of rough walls than ejection events in a smooth wall. Similar results are seen in Schultz and Flack (2007), although in the transitionally rough regime and not the fully rough regime of Flack et al. (2005).

Effect of pressure gradient on coherent structures

The effect of PG history on coherent structures is much less studied than the effect on the mean flow and turbulence statistics. Analysis by Lee and Sung (2009) of an APG smooth wall TBL obtained through DNS looked at the effect of APGs on coherent structures. Starting with the near-wall streaks Lee and Sung (2009) showed that the spacing between streaks increases by a factor of four compared to that of a ZPG TBL. Furthermore, it is seen that the streaks become more irregularly spaced. However, the width of the streaks remains unchanged with PG strength. The hairpin vortices are also seen to increase in strength with APGs, along with an increase in the inclination angle.

Several studies have considered the effect of APGs on streamwise structures. For mild APGs, both Lee and Sung (2009) and Harun et al. (2013) have seen longer coherent structures at the edge of the log law. However, for stronger APGs, Krogstad and Skåre (1995) determined that APGs reduced the streamwise correlation length using eight cross-wire HWA probes. Rahgozar and Maciel (2011) found similar results based on PIV measurements showing less frequent long structures under APG compared to ZPG. Investigating these differences Lee (2017) suggests that mild APGs increase the streamwise length of structures due to more merging of nearby structures. This occurs

because APGs lead to an increase in the spanwise length scale. For stronger APGs, they conclude that due to the suppression of the formation of hairpin vortices, LSMs are unable to concatenate to form VLSMS, resulting in reduced streamwise length. With APGs Lee (2017) reported higher amplitude modulation between the inner and outer region, which increases with APG strength.

Volino (2020) considered smooth wall TBLs under both FPG and APG with a recovery ZPG region in between. Examination of the flow structures using two-point correlations showed that FPGs increase both the spanwise and streamwise length of the structures relative to δ. It was seen that these changes are strongest near the wall and that, in the ZPG conditions, they return quickly to their initial condition. For an APG TBL, the effect on the length of the structure is the opposite of that seen for an FPG. Volino and Schultz (2023) used the same configurations as in Volino (2020) with a rough wall to examine the impact of roughness and PGs. Their work showed that the correlation lengths between rough and smooth walls showed no clear differences. Furthermore, the inclination of the structures for both rough and smooth walls were found to be similar. FPGs lead to a reduced inclination relative to the wall, while APGs increase the inclination of the structures.Volino and Schultz (2023) also noted that under APGs, the coherent structures appear to reach a maximum angle of 18°, which is unchanged with increasing APG strength. This angle is noted as the same maximum as seen in Lee and Sung (2009).

The final property to consider is the effect of PG on sweep and ejection events. Lee and Sung (2009) showed that due to the increased vortex spacing, as a result of APGs, there is a reduction in the frequency of ejections while the sweeps increase in duration. Volino (2020) showed that FPGs increase the significance of ejection events in the middle of the boundary layer. It was suggested that this is due to increased strain due to the acceleration of the TBL in the outer region, reducing the effect of sweep events. In the outer flow for an APG, sweeps are again seen to increase in significance compared to ejection events, resulting in a reduction of Q2/Q4 compared to a ZPG TBL. When comparing the ratio of ejections to sweeps (Q2/Q4), strong FPGs increase Q2/Q4 more for a rough wall compared to a smooth wall in the middle of the boundary layer (Volino and Schultz 2023). Volino and Schultz (2023) suggests this is due to the increased ejections generated by the roughness elements. However, as both APG and FPG strength reduce, the change from ZPG reduces to almost negligible (Volino and Schultz 2023).

2.6 Current challenges and open questions

The review of previous literature has shown that there are only a limited number of studies that have considered the effect of non-equilibrium PGs on smooth and rough

walls. The available studies are limited to relatively low Reynolds numbers and, therefore, the scale separation is small. Furthermore, these studies do not have independent skin friction measurements, meaning high uncertainty is seen in the conclusions. One of the areas of debate is whether the value of y_0 (or k_s) depends on PG history. The current assumption in modelling is that the value is constant and independent of the PG history; however, past research is inconclusive. Another challenge is whether it is possible to translate PG history effects from smooth wall to rough wall cases. While it is known that the roughness will modify the inner region of the flow, there is little on quantifying the effect of PG history on the outer region and how it compares to smooth wall flows. DNS is not possible at the high Reynolds numbers required to achieve high scale separation, and therefore, experiments are required to answer this question.

Past research on the turbulent pre-multiplied spectra is limited, often due to the measurement techniques not allowing for temporal data to be obtained. As noted above, previous research has looked at the effect of roughness on the pre-multiplied energy spectra; similar work is required to look at the effect of PG history. When considering roughness, one of the key modelling assumptions is outer layer similarity. It is well known that this assumption holds up under ZPG conditions; the collapse under different PGs is unclear, especially at high Reynolds numbers. Furthermore, no research currently quantifies how different PG histories affect the different regions of a turbulent spectrum.

There is a lack of past research on the effect of the PG histories on coherent structures at high Reynolds numbers, which is required for large-scale separation. With DNS not possible at these high Reynolds numbers, this requires large PIV fields of view in which the structures can be determined, which is often not available in previous data. Previous research has often focused on one region of the boundary layer, looking at how the coherent structures in different regions of the boundary layer respond to different PGs would deepen the understanding of how TBLs respond to PGs.

2.7 Aims and objectives

Building on the issues raised in section 2.6, the aims and objectives can be defined. The overall aim of this thesis can be summarised by the following -

To investigate the influence of non-equilibrium pressure gradient history on high Reynolds number turbulent boundary layers over smooth and rough walls, focusing on the evolution of mean flow properties, turbulence statistics, and coherent flow structures.

To explore this aim, the thesis is split into sub-sections exploring the effect of PG history on the mean flow, turbulence statistics and coherent flow structures, with the following objectives.

- Investigate the effect of non-equilibrium PG histories on the mean velocity profiles, including the effect on the roughness length scale using independent skin friction measurements.
- To develop and test predictive models for boundary layer properties based on limited measurements for smooth and rough walls.
- Investigate the effect of non-equilibrium PG histories on the turbulence with the TBLs and how the response differs between smooth and rough walls.
- Investigate the effect of non-equilibrium PG histories on different turbulent events and whether the surface affects the flow's response
- Investigate the effect of non-equilibrium PG histories on the coherent structures present within a TBL and how their responses vary with distance from the wall

Chapter 3

Methodology

This chapter outlines the measurement techniques and experimental setups used during the course of this work. Firstly, details of the boundary layer wind tunnel used for all experiments, along with the surfaces and pressure gradient setup. Details of each measurement technique are given, including data processing and uncertainty. Finally, the incoming ZPG boundary layer is quantified before any pressure gradient effects.

3.1 Facility

The 12 m closed-loop boundary layer wind tunnel at the University of Southampton was used for all experiments in this report. This tunnel consists of five interchangeable sections measuring 2.4x1x1.2 m (LxHxW) with an interchangeable floor depending on the application required, as shown in figure 3.1. For all floors, a ramp of $\approx 5^{\circ}$ is fitted at the start of the test section to remove the step up to the test surface. A 3D turbulator strip with a height of 0.5 mm is placed at the top of the ramp to trip the boundary layer.

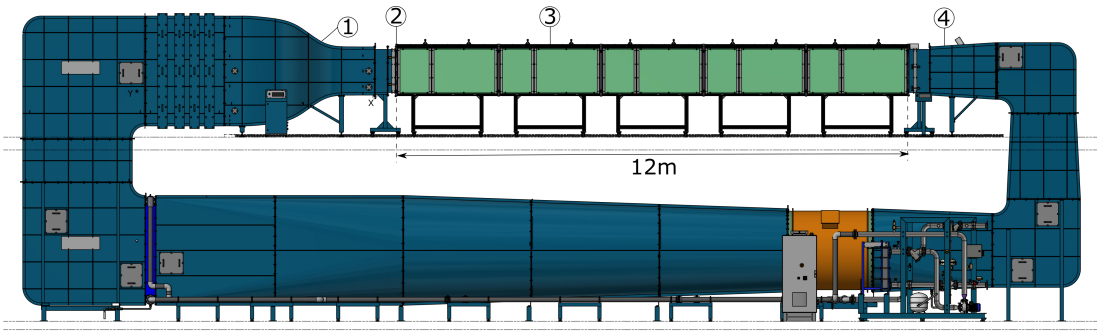

FIGURE 3.1: Diagram of boundary layer wind tunnel in which experiments were carried out, adapted from GUNT Gerätebau GmbH (2020a). ①: Wind tunnel contraction, ②: start of test section, ③: one of five sections make up the test section and ④ wind tunnel diffuser.

The tunnel can achieve flow speeds of up to 50 m/s in a clean configuration at maximum power. The flow is conditioned after leaving the return loop through a honeycomb section and three fine wire meshes of decreasing sizing before being accelerated through a contraction with a contraction ratio of six, resulting in a mean freestream turbulence intensity of 0.3% for the smooth wall and 0.6% for the rough wall.

Temperature and atmospheric pressure are measured using an RTD TST414 thermometer and a Setra 278 barometric pressure transducer. The tunnel temperature is maintained constantly using a chiller and heat exchanger on the tunnel return loop. The tunnel data is sampled, allowing the temperature and pressure to be recorded throughout each experiment.

3.1.1 Pressure gradient setup

To generate different PG histories, a NACA 0012 aerofoil is used, similar to previous works, including Fritsch et al. (2022) and Vishwanathan et al. (2023). The aerofoil has a chord of 1.25 m, 37% larger than seen in the previous works. This allows for PG histories over larger distances and at higher Reynolds numbers. The wing consists of a wooden core with a foam surface, which is then covered with fibreglass and varnish to give a smooth surface. The aerofoil is constructed to be 1 cm narrower than the wind tunnel span (1.2 m). The gap between the aerofoil and tunnel side walls is sealed with window draught seal to give an air-tight seal. Four actuators are mounted from the tunnel roof onto which the aerofoil is mounted as shown in figures 3.2*a* and *b*. The chord line in the full retracted state lies approximately 0.56 m above the tunnel floor. All mounting points are positioned on the top surface of the aerofoil to minimise any adverse effects on the flow below the aerofoil.

3.1.2 Surfaces

This experiment uses two different surface types: a smooth wall and a rough wall. The smooth wall is constructed from 26.5 mm aluminium honeycomb sandwich panels, and the top and bottom sheets are 1.25 mm thick. Figure 3.3*a* shows the smooth wall construction. To ensure the maximum possible smoothness of the wall, scratches are removed until they cannot be felt. The wall is then polished to a mirror finish. In the measurement region, the central two-thirds of the tunnel is replaced with 10 mm safety glass. This modification provides optical access and reduces conductivity for hot-wire measurements. Gaps between the panels are filled with plasticine to achieve the highest level of smoothness practically possible.

The second surface is the rough wall, the roughness being expanded steel mesh manufactured by Cadisch. Figure 3.3*b* shows the section of the steel mesh mounted

a)

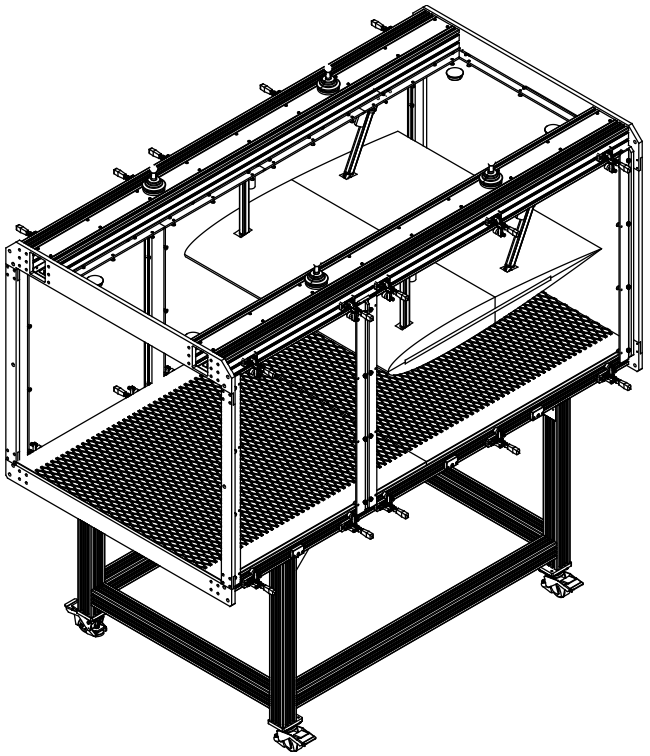

b)

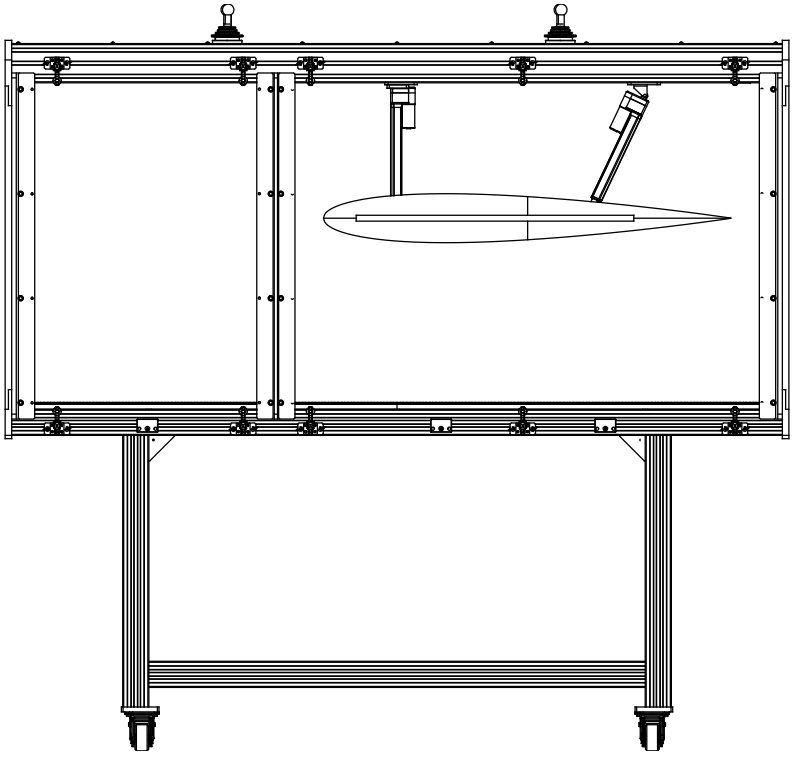

FIGURE 3.2: Diagrams of actuated NACA 0012 aerofoil in its full retracted position, inside one of the five interchangeable wind tunnel sections of the 12 m boundary layer wind tunnel adapted from GUNT Gerätebau GmbH (2020b). (*a*) Isometric view and (*b*) Side on view

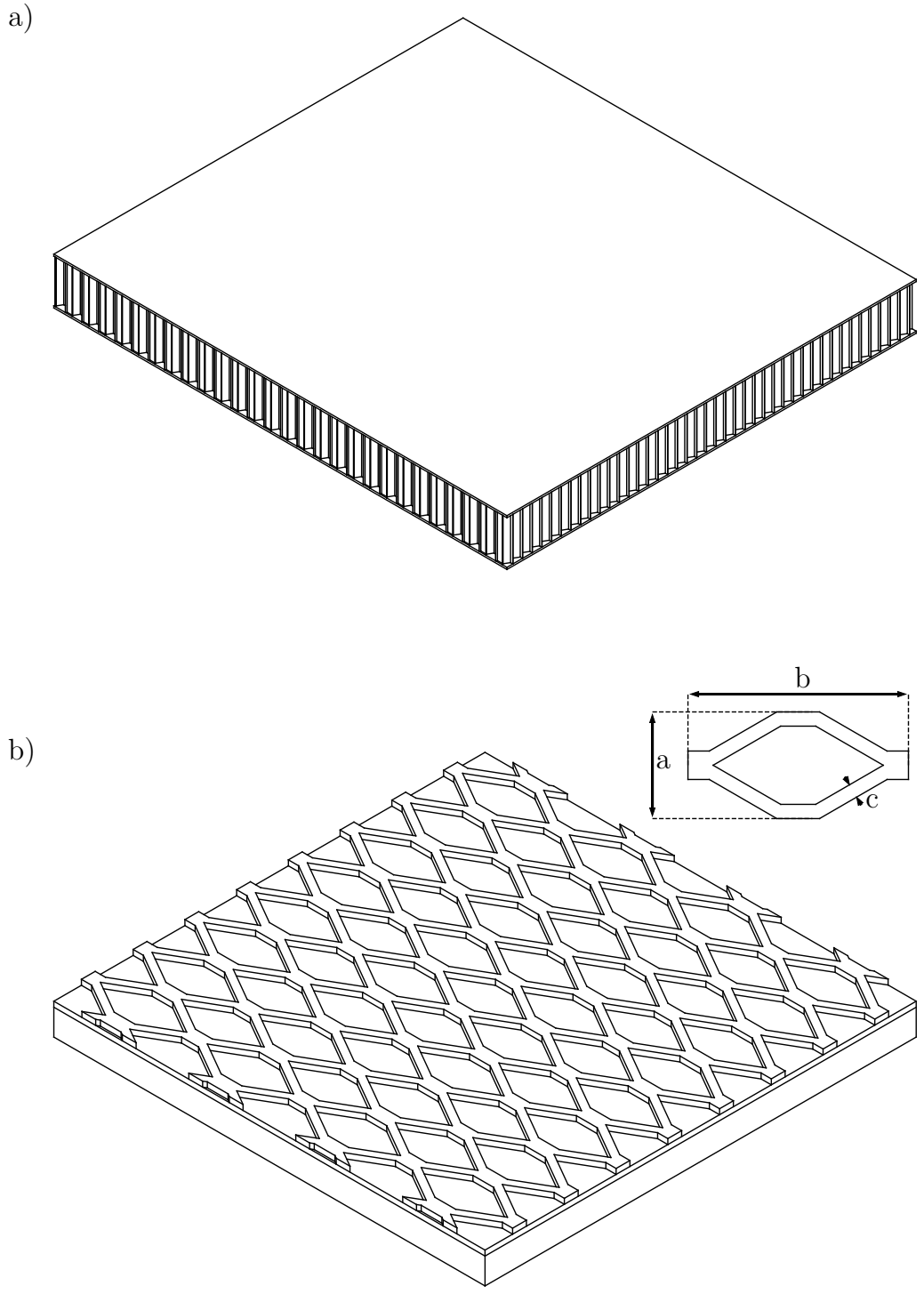

FIGURE 3.3: 250 x 250 mm sections of the floor of the wind tunnel for (*a*) Smooth wall honeycomb 26.5 mm thick honeycomb (*b*) Rough wall constructed of 15 mm plywood, 3 mm acrylic upon which the 3 mm roughness mesh is mounted. Cutout in the top right corner shows the dimensions of each roughness element, *a*: 30 mm, *b*: 62 mm, *c*: 4 mm.

λ_f	λ_p	k (mm)	k_a (mm)	ES_x	ES_y	Sk	Fl
0.10	0.27	3	0.88	0.31	0.14	0.91	1.82

TABLE 3.1: Estimation of different roughness parameters, definitions as given in section 5

upon a baseboard consisting of 15 mm plywood topped with 3 mm acrylic. Figure 3.3*b* also shows the dimensions of each roughness element; they have a spanwise width of 62 mm, a streamwise length of 30 mm and a thickness of 3 mm. These dimensions result in an open area for the roughness of 73%.

Different parameters are used to quantify roughness, a detailed look at which can be found in Chung et al. (2021). Utilising the simplified CAD model shown in figure 3.3*b*, it is possible to estimate some of the more common properties. The CAD model has limitations, as the small chamfers on the edges of each element are not accounted for. Hence, λ_p is taken from Cadisch Precision Meshes (n.d.). Table 3.1 summarises these properties, and the definitions are given in section 5.

3.2 Velocity Measurements - Pitot Tube

This section looks at the workings and limitations of a pitot tube used to set and record the velocity of the wind tunnel.

3.2.1 Principle of operation

A pitot tube uses Bernoulli's equation, which relates total pressure, static pressure and flow velocity, to calculate the incoming flow velocity given by

$$P_0 = P + \frac{1}{2}\rho U^2, \tag{3.1}$$

where P_0 is the total pressure of the flow, P is the local static pressure and U is mean streamwise velocity. Figure 3.4 shows a cross-section of a pitot tube, the inner tube used to measure the total pressure where the flow enters the tube and is then slowed to zero velocity. Holes in the outer tube are used to measure the static pressure of the flow. The two pressure ports are then connected to a digital manometer, a Furness FCO560 digital manometer, to measure dynamic pressure, which is the difference between total and static pressure. Using the equation 3.1, it is possible to calculate the flow velocity using the density calculated from the pressure and temperature recorded from the tunnel.

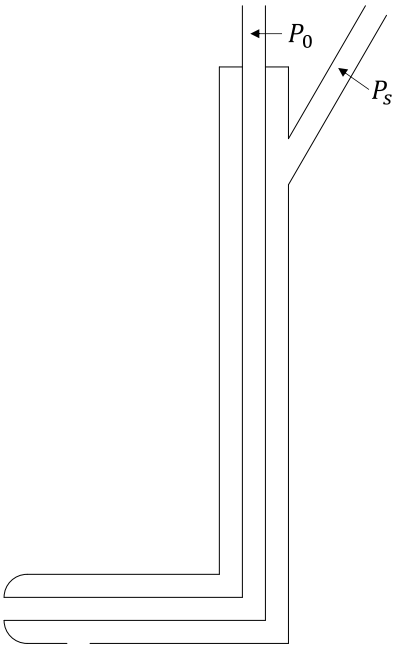

FIGURE 3.4: Diagram showing the cross-section of a pitot tube used to measure mean flow speeds inside the wind tunnel

3.2.2 Limitations and uncertainty

A pitot tube is limited to measuring only the mean velocity of a flow due to the system's slow response time. The method outline previously only holds for low turbulence intensity flow regions; corrections are needed in high turbulence intensity regions (Perry et al. 2001). Uncertainty is introduced to the measurement due to the angle of the pitot tube to the flow; therefore, care must be taken when positioning the pitot. When calculating the velocity with a pitot tube, uncertainty is also introduced from the sensors measuring temperatures and pressures within the tunnel. A typical uncertainty budget for a pitot tube measurement is given in table 3.2. It can be seen that the statistical uncertainty is also included; to calculate this, the standard error of the mean is used, given by

$$\sigma_U = \frac{\sigma}{\sqrt{n}}, \tag{3.2}$$

where σ_U is the standard error in the mean for U, σ is the standard deviation of the U and n is the number of samples (Kirkup and Frenkel 2006). The main contribution to uncertainty in pitot tube measurements by an order of magnitude is the uncertainty in the dynamic pressure. The uncertainty value of ± 0.10 m/s is for a 95% confidence interval. Since the dynamic pressure varies with tunnel speed, the uncertainty in the velocity measurement will also vary. For a 10 m/s measurement, the uncertainty is ± 0.19 m/s while at 30 m/s it is ± 0.07 m/s.

Variable	Typ. value	Accuracy Value	Unit	p.d.f	Sensitivty Coefficent	Standard Uncertainty Value (m/s)
q	228.3	2.03	Pa	rect.	$\sqrt{\frac{R(T+273.15)}{2qP_a}}$	0.050
P_a	102242	30	Pa	rect.	$-\sqrt{\frac{qR(T+273.15)}{2P_a^3}}$	-0.0016
T	21.8	0.1	°C	rect.	$\sqrt{\frac{qR}{2(T+273.15)P_a}}$	0.0037
E	1.1	0.0003	V	rect.	$\sqrt{\frac{R(T+273.15)}{2(200*E)P_a}}$	0.0015
σ_{U_∞}	0.005	0.0008	m/s	norm	1	0.0008
					Combined Expanded Uncertainty:	0.10 m/s

TABLE 3.2: Uncertainty Budget of a typical pitot tube measurement at 20 m/s. The dynamic pressure, q, has uncertainty due to both the sensor and the A/D converter, given by E.

3.3 Wall pressure measurements

Measurements of the wall pressure are required to know the strength of the PG that the flow is experiencing. Pressure taps are fitted to the wind tunnel floor to measure the wall pressure. For the smooth wall, twenty tubes with an inner diameter of 0.6 mm are fitted to the floor space, 0.24 m apart. For rough wall measurements, sixteen pressure taps of 0.5 mm inner diameter were used, spaced approximately 0.265 m apart. The taps' position relative to the aerofoil's leading edge are given in tables 3.3 and 3.3 for the smooth and rough wall. The taps are located 0.25 m from the tunnel's side walls, outside any effect of the side wall boundary layer. The size of the pressure tap will affect the measurement; however, this is the same for a given surface and similar between the two surfaces, and therefore the error introduced is minimised. The effect of the tap on the flow is further minimised but ensuring the taps are flush-mounted to the wall of the tunnel and there are no sharp edges inside the tap. The tube length from the pressure transducer to the taps varies depending on the tap; longer tubes will result in some small viscous loss, however, this effect compared to the overall pressure is minimal. The region of interest focuses from one chord upstream of the aerofoil leading edge to one chord downstream of the leading edge. This is based on panel method simulations, details of which are given in appendix A, showing that the influence of an aerofoil is limited to approximately one chord upstream and downstream. There are some limitations to using a panel method simulation since they are based on inviscid flow. Therefore, there are boundary layers on the wind tunnel walls and aerofoil surface, not present in a panel method simulation. These will lead to an overestimate of the pressure distribution given by the panel method compared to the actual experiment.

The pressures are recorded relative to the pressure outside the tunnel using a ZOC 33/64 Px attached to Rad Base 3200. The pressure coefficients are calculated using

Tap No.	1	2	3	4	5	6	7	8	9	10
$\Delta x/c$	-1.29	-1.10	-0.90	-0.71	-0.52	-0.33	-0.14	0.06	0.25	0.44
Tap No.	11	12	13	14	15	16	17	18	19	20
$\Delta x/c$	0.63	0.82	1.02	1.21	1.40	1.60	1.78	1.98	2.17	2.36

TABLE 3.3: Location of pressure taps relative to the leading edge of aerofoil for the smooth wall turbulent boundary layer measurements

Tap No.	1	2	3	4	5	6	7	8
$\Delta x/c$	-1.10	-0.88	-0.67	-0.46	-0.25	-0.03	0.20	0.39
Tap No.	9	10	11	12	13	14	15	16
$\Delta x/c$	0.62	0.83	1.02	1.24	1.45	1.68	1.90	2.08

TABLE 3.4: Location of pressure taps relative to the leading edge of aerofoil for the rough wall turbulent boundary layer measurements

Variable	Typ. value	Accuracy Value	Unit	p.d.f	Sensitivty Coefficent	Standard Uncertainty Value (m/s)
P	-92.0	3.75	Pa	rect.	$\frac{1}{q}$	0.0091
P_s	-3.9	3.75	Pa	rect.	$-\frac{1}{q}$	-0.0091
q	238.2	2.03	Pa	rect.	$\frac{-C_p}{q}$	0.0046
σ_{C_p}	0.0025	0.00019	-	norm	1	0.00024
					Combined Expanded Uncertainty:	0.027

TABLE 3.5: Uncertainty Budget of a typical wall pressure measurement taken at 20 m/s for the smooth wall setup.

$$C_p = \frac{P - P_\infty}{\frac{1}{2}\rho U_\infty^2}, \tag{3.3}$$

where C_p is the pressure coefficents, and P_s is the reference static pressure. The reference static pressure is interpolated to be one chord in front of the leading edge. While this will introduce some uncertainty in the result, this region is near ZPG, so any error will be negligible. This position is the same streamwise position as the reference pitot used for setting U_∞.

3.3.1 Uncertainty

The main sources of error must be identified to consider the uncertainty of wall pressure measurements. These are the transducer errors of the pressure scanner and the digital manometer. The repeatability in C_p due to the wall pressure measurements is also taken into account. The statistical uncertainty of the dynamic pressure is negligible, as shown in table 3.2. These values result in the uncertainty budget shown in table 3.5 for a smooth wall for the -8° case at $x/c = 0.25$. The uncertainty in C_p varies

with velocity due to the variation in the dynamic pressure, resulting in an uncertainty of ± 0.027 at 20 m/s. At 10 m/s, the uncertainty is ± 0.11, while at 30 m/s, the value is much smaller at ± 0.012. These values are calculated with a coverage factor of 2, giving a confidence interval of 95%. Once again, the statistical uncertainty of C_p is negligible compared to the measurement errors in dynamic and wall pressure. The uncertainty of rough wall measurements is very similar since the setup uses the same equipment.

3.4 Single streamwise location velocity measurements - Hot Wire Anemometry

This section explores the measurement technique of hot wire anemometry used to obtain time-resolved boundary layer velocity profiles at a single streamwise location. Firstly, the principle of operation of Hot Wire Anemometry (HWA) is explored before looking at the experimental setup used to obtain velocity profiles. Finally, the uncertainty of a typical hot wire measurement is explored.

3.4.1 Principle of operation

A hot wire is used to gain time-resolved velocity measurements at a given location based on the change in resistance with temperature. The probe consists of a heated wire whose resistance varies with changes in flow velocity due to heat transfer. A single in-house wire probe similar to the Dantec 55P05 probe is used for hot wire measurements, consisting of a $5\mu m$ tungsten wire. This is coated with copper, leaving a sensing length, l, of 1 mm. This results in a length-to-diameter ratio of 200, which meets the requirement in Ligrani and Bradshaw (1987) that l/d should not be less than 200 to prevent the conduction of the supports affecting the result. The dimensionless wire length l^+ given by (lU_τ/ν) varies between $21 < l^+ < 74$ for the smooth wall and between $33 < l^+ < 140$ for the rough wall cases. In using a single sensing wire, it is assumed that $U >> V$ since it cannot distinguish between the two components.

The wire temperature was controlled using a Dantec Streamline Pro CTA, allowing control of the wire parameters. For a CTA system, the wires' temperature is kept constant, with varying current as the temperature changes. The key parameter in defining the wire's temperature is the overheat ratio given

$$a = \frac{R_w - R_0}{R_0}, \tag{3.4}$$

where a is the overheat ratio, R_w is the resistance of the wire at operating temperature, and R_0 is the resistance at ambient temperature (Jørgensen 2001). For this experiment, the overheat ratio is set to 0.8.

The probe's resistance forms part of a Wheatstone bridge arrangement, with the voltage across the bridge used to represent the resistance of the wire (Tropea et al. 2007). The streamline pro system conditions the signal by applying the chosen gain and offset. These are varied based on the flow speed to maximise the range of voltages. The output of the streamline is digitised via a NI USB-6212 16-bit DAQ. The frequency of acquisition of the hot wire signal is 30 KHz for the rough wall and 24 Khz for the smooth wall. The acquisition time is calculated to ensure at least 20,000 boundary layer turnovers. The time the signal needs to be acquired, t_{samp}, is calculated by

$$t_{samp} = \frac{N_{TO}\delta}{U_{99}}, \tag{3.5}$$

where t_{samp} is the sampling time of the hot wire, N_{TO} is the number of turnovers, U_{99} is the boundary layer edge velocity and δ is the boundary layer thickness. The tunnel control system ensures the temperature is held within $\pm 0.3^{\circ}$C and the freestream velocity within ± 0.1 m/s during the long acquisition time.

The frequency response of the HWA system is estimated through a square-wave test. The Dantec Streamline Pro CTA has a built-in square-wave test, which defines the cut-off frequency as the frequency at which the fluctuation amplitude is reduced by a factor of two, also known as the -3 dB limit (Jørgensen 2001). For the probe used in this work, the cut-off frequency is found to be greater than 25.6 kHz. It is noted that, for flow speeds up to 100 m/s, damping occurs at roughly 30-50% of this value ($\sim 8 - 13$ kHz), meaning the usable frequency range of the HWA is somewhat lower than the cut-off frequency (Jørgensen 2001). This likely means that the cut-off frequency is slightly lower than the Nyquist frequency of 15 kHz. The CTA also features an analogue 10 kHz low-pass filter, which is applied to the signal. This means that measurement bandwidth is limited to below roughly 10 kHz when both the probe response and the analogue filter are considered.

3.4.2 Experimental setup

In order to obtain the velocity profile at a given streamwise distance, the hot wire probe is traversed through the boundary layer. The probe is traversed using an in-house traverse with an accuracy of 50 μm. The traverse has a slight backlash of < 1 mm every time it travels through the boundary layer. This was identified by checking the wall position before each run, so the wall position is reset each time to compensate. The initial wall position is set using a microscope digital camera to measure the distance

from the wall using a vertically mounted ruler in line with the wire. The wire is then moved down the distance measured to the initial starting position of the profile. This was nominally set to 0.4 mm for the smooth wall; however, it was noted after the experiments that the flow causes deflection of the hot wire probe support. Therefore, the smooth wall data wall position was corrected as detailed in appendix B based on the inner peak of the streamwise Reynolds stress at $y^+ = 15$. For the rough wall, the initial wire is level with the crest of the roughness elements at $y = 3$ mm. Since the roughness elements are large ($k = 3$ mm), the maximum deflection is less than 25% of the roughness height based on the smooth wall deflections. There is no reliable method for correcting this wall position for rough wall cases, since there is no known independent reference point, which introduces error in the wall position. It was not possible to use the smooth wall deflection either, since the velocity near the wall is different compared to the smooth wall. Since the boundary layer for a rough wall is thicker than that of a smooth wall, the relative error introduced by this deflection is less than for the smooth wall cases. Each profile has log spacing of points up to $\approx 0.8\delta$, then linearly spaced from here to the chosen end point in the freestream.

Calibration is carried out before (pre) and after (post) each profile is obtained. Each calibration consists of 14 points, ranging from zero to the maximum required velocity, ensuring that all fluctuations within the hot wire signal fall within the calibration range. During calibration, the mean voltage of the bridge and the velocity and reference pitot are recorded along with the standard flow parameters required (T, P_a, etc).

Rough wall ZPG measurements are taken in a clean, configured tunnel as described in section 3.1. A single pitot tube is mounted on the tunnel roof to record the tunnel speed. Figure 3.5 shows the ZPG rough wall measurements setup. The hot wire is positioned at $L = 9.03$ m, where $L = 0$ m is the start of the test section. This point is also $x/c = 2$ since x_0 is located at the leading edge of the aerofoil. This is the same location as the reference smooth wall data from Aguiar Ferreira et al. (2024). For PG measurements, the leading edge of the NACA 0012 aerofoil is mounted two chords upstream of the hot wire position. Figure 3.6 shows the position of the aerofoil relative to the hot wire. Also shown is the second pitot tube mounted on the traverse for calibration. For the smooth wall, this is 0.3 m above the floor, and 0.36 m for the rough wall. This is done to ensure the hot wire is between the boundary layer on the floor and away from the wake of the aerofoil. Calibration is carried out with the aerofoil fully retracted at 0° to ensure no effect of the wake on the calibration.

3.4.3 Data processing

After data has been acquired, processing of the signal is required. The first step is to correct the voltages for any small drifts in temperature ($< 5°C$). This requires the

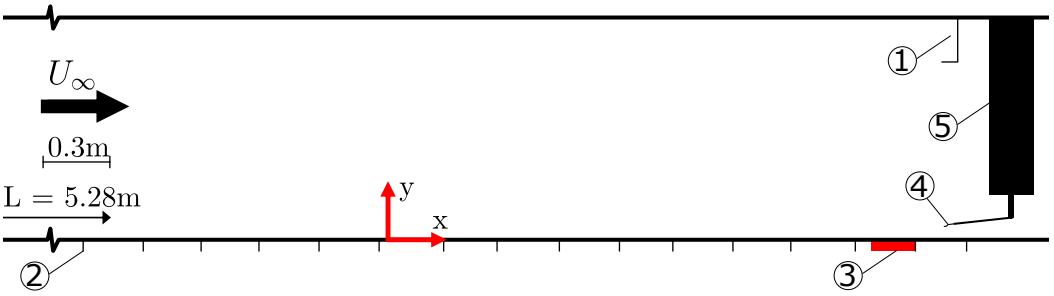

FIGURE 3.5: Diagram of experimental setup for ZPG rough wall measurements. ① Pitot tube used to set the freestream velocity, ② 16 pressure taps used for the rough wall setup, ③ Drag balance for rough wall skin friction measurements, ④ Hot wire probe located at 9.03 m from the test section start, mounted on ⑤ vertical traverse.

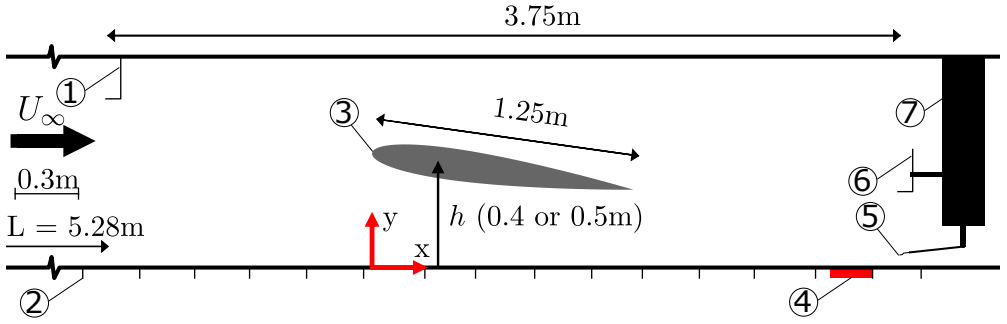

FIGURE 3.6: Diagram of experimental pressure gradient setup for smooth and rough wall measurements. ① Pitot tube used to set the freestream velocity, ② 16 pressure taps used for the rough wall setup, ③ NACA 0012 aerofoil used for generating pressure gradients, ④ Drag balance for rough wall skin friction measurements, ⑤ Hot wire probe located at 9.03 m from the test section start, ⑥ Pitot tube used for calibration, ⑦ Vertical traverse

operating temperature of the wire, T_w, to be known at the start of pre-calibration. This can be calculated by

$$T_w = T_0 + \frac{a}{\chi}, \tag{3.6}$$

where T_0 is the ambient temperature at the start of the measurement and χ is the sensing wire's temperature coefficient of resistance (Jørgensen 2001). Before applying corrections for any temperature variation, the signal must be rescaled to remove the offset of the signal. Due to the temperature-controlled wind tunnel, the correction factor will be small, as the tunnel is maintained within $\pm 0.3°$C of the mean temperature. The bridge voltage is corrected using

$$E_{corr} = E_{measured} \cdot \left(\frac{T_w - T_0}{T_w - T_a} \right)^{0.5}, \tag{3.7}$$

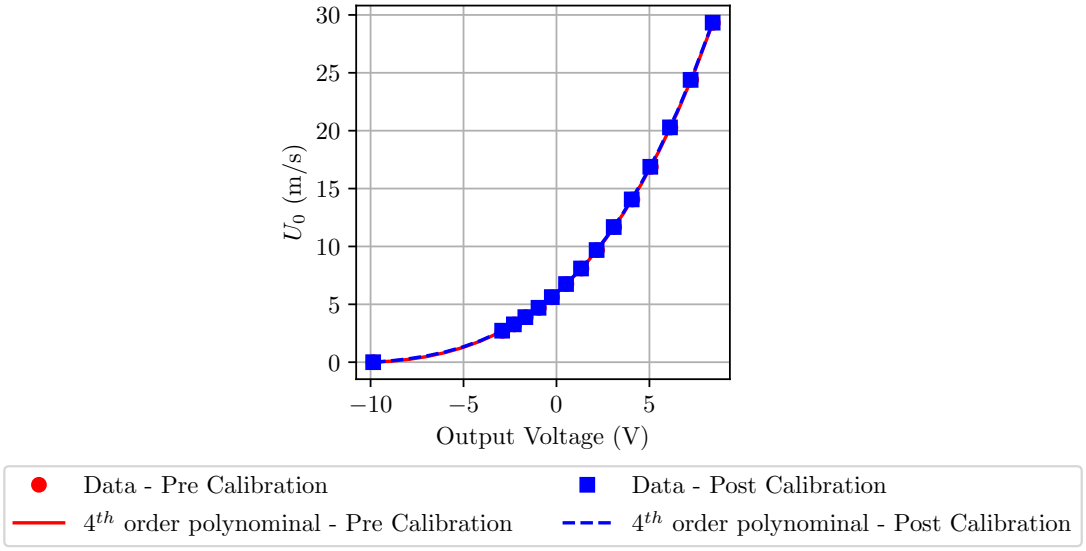

FIGURE 3.7: Example calibration plot showing pre and post calibrations with 4^{th} order polynomial best fit curves. The data is taken from the rough wall $-8°$ case at 20 m/s.

where E_{corr} is the temperature-corrected voltage, $E_{measured}$ is the measured voltage, T_w is the wire temperature, T_0 is the ambient temperature at the start of calibration, and T_a is the ambient temperature at the point of measurement.

The voltages must be converted to velocities once the data has been corrected for temperature variation. This requires a calibration function that maps corrected voltages to reference velocities from the reference pitot tube. Figure 3.7 taken at 20 m/s for the $-8°$ rough wall case is an example of the pre and post calibrations. Due to the signal range being between -10 and +10 V, a 4^{th} order polynomial is chosen as the calibration function instead of the commonly used King's Law. The resulting best fit of the polynomial is seen in figure 3.7. It can also be seen that pre- and post-calibration functions are very similar, meaning a very small drift in the response of the wire. This is despite the 4.5 hr between the two different calibrations. The resulting calibration function allows the signal at each point of the corresponding boundary layer profile to be converted to velocities. From this signal, the mean, variance, and spectra can be calculated as required.

3.4.4 Uncertainty

The uncertainty of a single point in a velocity profile has several sources of error, as shown in table 3.6. The first is $\epsilon_{calibration}$, which is the error due to the calibration process, from Jørgensen (2001); this is taken to be $0.02U$. As seen in table 3.6, this is by far the largest contribution to the uncertainty of a given velocity point. The second error is due to the fitting error in the calibration function, which is quantified by the root mean square of the errors in the fit. The error due to the bit error of the A/D converter is

Variable	Typ. value	Accuracy Value	Unit	p.d.f	Sensitivty Coefficent	Standard Uncertainty Value (m/s)
$\epsilon_{calibration}$	-	0.18	m/s	norm.	1	0.18
$\epsilon_{linearisation}$	-	0.0072	m/s	norm.	1	0.0072
E	1.8	0.00031	V	rect.	$\frac{\partial U}{\partial E}$	0.00033
T_a (Overheat)	22.3	0.19	°C	rect.	$2U(1+\frac{A}{B}\frac{1}{\sqrt{U}})\frac{1}{T_w-T_a}$	0.013
T_a (ρ)	22.3	0.19	°C	rect.	$\frac{U}{T_a}$	0.0034
T_a (ν)	22.3	0.19	°C	rect.	$0.5U\frac{T_a+3C}{T_a(T_a+C)}$	0.0027
P_a	101460	30.0	Pa	rect.	$U\frac{U}{P_a}$	0.0015
σ_U	2.4	0.021	m/s	Norm.	1	0.021
					Combined Expanded Uncertainty:	0.354 m/s

TABLE 3.6: Uncertainty budget for a velocity point taken from the rough wall velocity profile at $-8°$ with $h = 0.5$ m at 20 m/s. The data point is taken within the log law with U of 8.91 m/s. $\epsilon_{calibration}$ is the error due to the calibration process, and $\epsilon_{linearisation}$ is the error due to the fit of the calibration process. There are three contributions due to the error in the T_a, these are from the error due to the overheat ratio, the density and the viscosity (Jørgensen 2001).

seen to be negligible. The error due to the measured temperature is broken down into three different sources: error due to the overheat ratio, error due to the density and error due to the viscosity. The overheat ratio is the second largest contribution to the overall error. The sensitivity coefficients for the overheat ratio include variables A and B, which are given by equations 3.8 and 3.9 as given in Tropea et al. (2016).

$$A = 0.39\frac{\pi l k_a}{\chi R_0} \tag{3.8}$$

$$B = 0.51\frac{\pi l k_a}{\chi R_0}\sqrt{\frac{\rho d}{\mu}} \tag{3.9}$$

where k_a is the thermal conductivity of air taken as 0.0257 W m^{-1} K^{-1} (Tropea et al. 2016), μ is the dynamic viscosity of air. Sutherland's law is used when estimating the variation in the viscosity with temperature given by

$$\frac{\mu}{\mu_0} = \left(\frac{T_a}{T_0}\right)^{\frac{3}{2}}\frac{T_0+C}{T_a+C}, \tag{3.10}$$

where μ_0 is the reference viscosity at T_0 and C is Sutherland's Constant taken to be 120 K. The three uncertainties related to T_a are added together before being used in the combined uncertainty as stated in Jørgensen (2001). The final measurement error comes from the measurement of the atmospheric pressure and is seen to be small. The statistical uncertainty is quantified using the standard error of the mean and is seen

to be negligible. Since the HWA measurements are correlated, the n used to calculate the standard error is the effective number of uncorrelated samples, n_{eff}. This can be calculated using

$$n_{eff} = \frac{t_{samp}}{2\tau_{int}}, \tag{3.11}$$

where τ_{int} is the integral timescale of the flow as calculated from the integral of the autocorrelation function up to the first zero crossing. This increases the standard error for the data point used here by a factor of 24; however, it remains negligible compared to the calibration error. The uncertainty budget is calculated for a point in the log law with a mean velocity of 8.91 m/s. The overall expanded uncertainty with a 95% confidence interval is $\pm$0.354 m/s. Due to the percentage uncertainty used for $\epsilon_{calibration}$, the largest uncertainty for a case at 20 m/s is found in the freestream with an error of $\pm$0.85 m/s; however, this uncertainty is less than 4% of U.

The above uncertainty is for the mean velocity; however, there is also an error in the streamwise Reynolds stress, $\overline{u'u'}$. To quantify the variance in $\overline{u'u'}$ the following equation from Benedict and Gould (1996) can be used,

$$\sigma^2_{\overline{u'u'}} = \frac{1}{n_{eff}} \left(\overline{u'^4} - (\overline{u'u'})^2 \right), \tag{3.12}$$

where n_{eff} is the number of uncorrelated samples as given by equation 3.11. The standard error can be evaluated using equation 3.12. This can be further supplied if a normal distribution for the velocity fluctuations is assumed, and the standard percentage uncertainty can be given by

$$\frac{\sigma_{\overline{u'u'}}}{\overline{u'u'}} = \sqrt{\frac{2}{n_{eff}}} \tag{3.13}$$

Taking equation 3.13 results in a standard percentage error in $\overline{u'u'}$ for the velocity point given in table 3.6 of 1.2%. This is five times larger than the standard percentage error of the mean velocity measurement. This is still negligible compared to the contribution from other sources, the main contributor of which is the calibration error.

3.5 Flow field measurements - Particle Image Velocity (PIV)

This section examines acquiring and processing the image pairs required for particle image velocity (PIV). Section 3.5.1 summarises the setups used, including details of the

cameras, lenses, and optics. Section 3.5.2 then details the pre-processing and processing steps taken to obtain the final flow fields.

3.5.1 Experimental setup

Employing PIV, the comprehensive evolution of the boundary layer over a given surface is captured. The region of interest spans from one chord upstream of the leading edge to one chord downstream of the aerofoil trailing edge. The pitot tube and aerofoil are set out in section 3.4.2 to set the inlet speed and generate pressure gradients. Seeding for the wind tunnel is provided using a Martin Magnum 1200 smoke machine using JEM PRO-FOG with an average particle size of $1 - 1.5\mu$m (Martin Professional n.d.). The light source chosen for carrying out PIV is a Litron Bernoulli 200-15 Nd:YAG laser with a beam of wavelength 523 nm.

The laser optics used differ depending on the surfaces. The laser is mounted under the wind tunnel for the smooth wall setup. The beam enters the tunnel through the floor via two mirrors, pointing upstream parallel to the flow. Separately mounted concave (-) and convex (+) spherical lenses are used to optimise the sheet thickness at the measurement position. These are mounted to the floor on optical posts. A -20 mm cylindrical lens is mounted after both the spherical lenses to generate the light sheet. A summary of the lenses used can be found in table 3.7. The concave lens is usually chosen such that it is half the strength of the concave lens. The rough wall's setup changes slightly, such that the laser beam enters the tunnel through the side wall. The optics consist of three mirrors to align the beam pointing downstream parallel with the flow. The final mirror is mounted on a strut from the wind tunnel roof with LaVision sheet optics mounted directly in front. This strut is positioned at least 0.7 m downstream of the measurement station, so as not to cause interference. The wall pressure distributions during each PIV run confirm that there are no significant changes in the measurement location due to the strut. A 20 mm lens generates the laser sheet for positions two to four. A -50 mm is used for the first case since the laser sheet has to travel further before measurements are taken. The position of the laser sheet relative to the camera positions and aerofoil can be seen in figure 3.8 for the smooth wall and figure 3.9 for the rough wall.

Triggering of the PIV system is controlled via the LaVision Davis software and a PTU X timing control system. The cameras and lenses used depend on the surface. A summary of the cameras and lenses used can be found in table 3.8. Four cameras are used for the smooth wall setup, while three are used for the rough wall. The overall field of view captured by all cameras at each position is similar in both cases. A summary of the average magnifications and field of views can be found in table 3.8. The Δt between frames is set, so the freestream has at least 10 pixels of movement. For all but one case, the time between images, Δt, is set to 55μs. The exception is the rough wall

	Surface	Concave lens (mm)	Convex lens (mm)	Cylindrical lens (mm)
Position 1	SW	-75	150	-20
Position 2	SW	-50	100	-20
Position 3	SW	-75	200	-20
Position 4	SW	-75	150	-20
Position 1	RW	-	-	-50
Position 2	RW	-	-	-20
Position 3	RW	-	-	-20
Position 4	RW	-	-	-20

TABLE 3.7: Lens configuration used to generate a laser sheet perpendicular to the wall for both smooth and rough walls.

Surface	Camera	Lens	Single Image Size (WxH) (pix)	Single Camera FOV (WxH) (m)	Average Magnification (pix/mm)
SW	4 x LaVision Imager US 25MP	Nikon 50 mm f1.8	5312x4600	0.31x0.27	17.3
RW	3 x LaVision ImagerProLX 16MP	Sigma 105 mm f2.8	4872x3248	0.44x0.30	10.9

TABLE 3.8: Summary of the cameras and lenses with camera field of views (FOV) and average magnification across all positions for a given surface.

-4° case at position four, where Δt is set to 50μs. For each case, at least 2000 image pairs are taken. The images are nominally triggered at 0.5Hz for the smooth wall and 0.6Hz for the rough wall cases. The laser is triggered at double the rate of the cameras since the beam power is optimum for frequencies ≥ 1. The write speed of the storage drives constrains the image frequency due to the large files being obtained.

The cameras for the smooth wall study capture images from the wall surface up to approximately 0.3 m. However, the rough wall study faces limitations due to the roughness's angular shape. This angular roughness reflects light, which, if not controlled, could damage the camera sensor. The cameras are set to image above the roughness elements to reduce risk. The camera heights are set such that the bottom of the image is at a maximum of $3.6k$, above the wall. Where possible, the cameras were placed lower depending on the laser power, which was done to ensure the cameras did not saturate. The range of heights is $2.2k$ to $3.6k$ with an average of $2.8k$, which is equivalent to 3% of the ZPG boundary layer thickness. Therefore, the majority of the log region is captured. The wall position for the smooth wall is set from the position of the laser reflection on the surface of the glass. For the rough wall calibration, images are taken with a vertically mounted ruler to obtain the position relative to the wall.

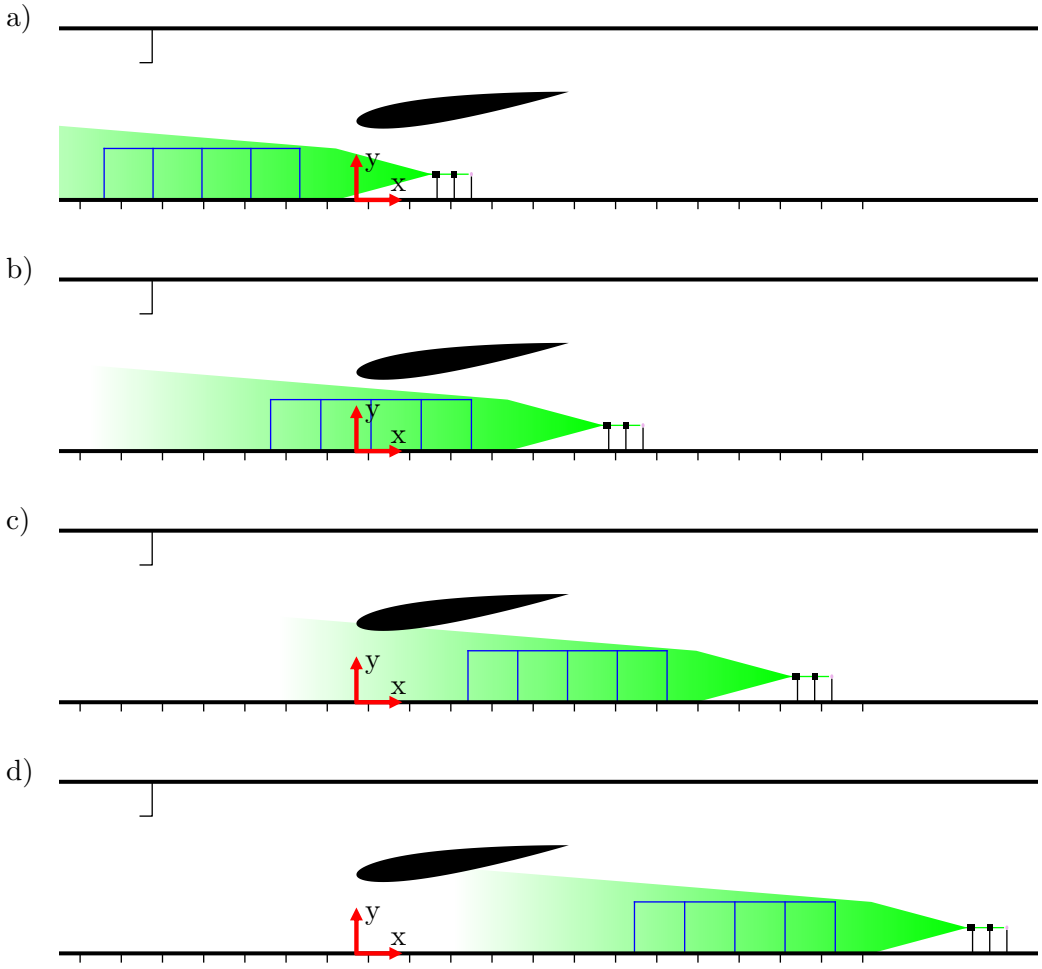

FIGURE 3.8: Experimental setup schematic of the Southampton Boundary Layer Wind Tunnel for non-equilibrium PIV measurements from 4.8 m to 10.2 m view, with camera views shown by blue squares and laser location for smooth wall shown for (*a*) Position 1, (*b*) Position 2, (*c*) Position 3 and (*d*) Position 4. The vertical lines below the floor show the position of the pressure taps.

3.5.2 Image processing

This section will look at the image processing carried out using in-house code known as PIVTOOLS (Lawson et al., 2024). Two different types of pre-processing are used depending on the surface. The classical pre-processing techniques of subtracting sliding minimum (SSMin) followed by min-max normalisation (Norm) are used for the smooth wall cases. For the rough wall, it was found that the roughness beyond the laser sheet affects the result of the processing. Therefore, a different method was implemented using a subtracting time minimum (Time) followed by POD-based background removal (POD) as defined by Mendez et al. (2017). The subtract time minimum filter takes a subgroup of the images, nominally 500. The minimum value across this subgroup at

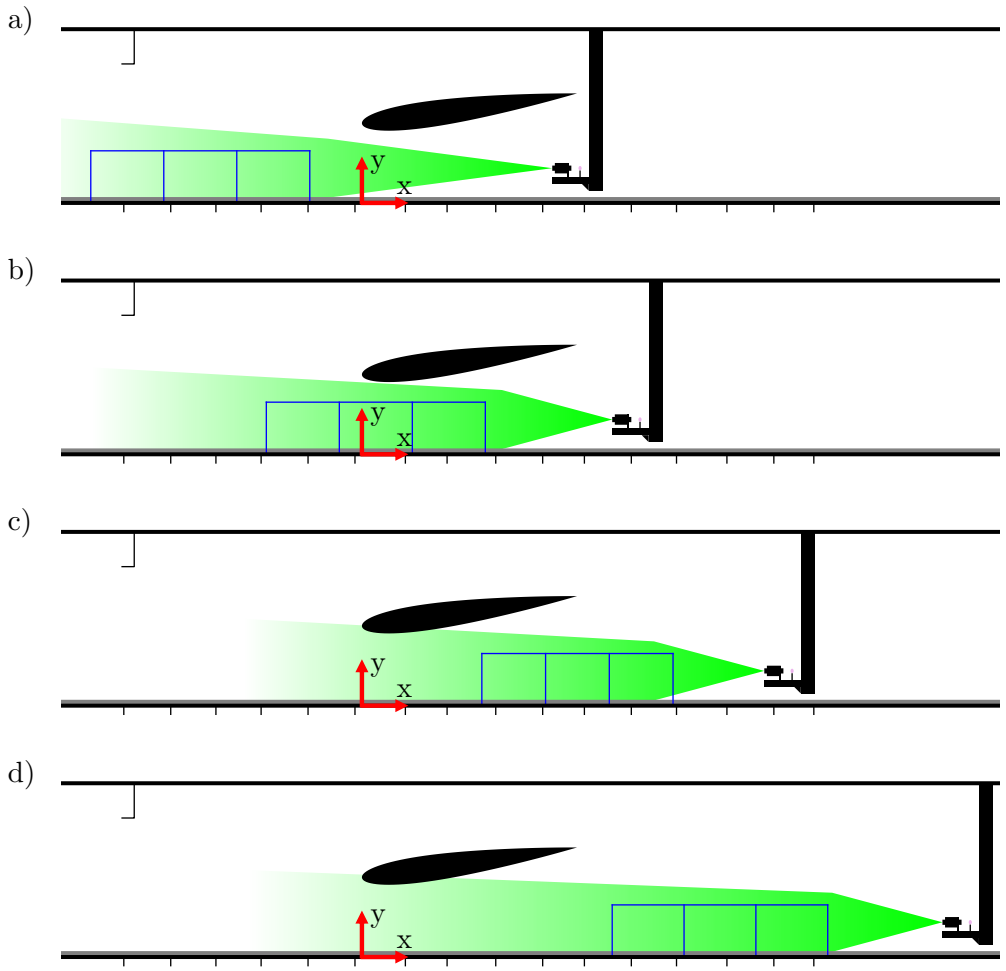

FIGURE 3.9: Experimental setup schematic of the Southampton Boundary Layer Wind Tunnel for non-equilibrium PIV measurements from 4.8 m to 10.5 m view, with camera views shown by blue squares and laser location for rough wall shown for (*a*) Position 1, (*b*) Position 2, (*c*) Position 3 and (*d*) Position 4. The vertical lines below the floor show the position of the pressure taps.

each pixel location is subtracted from the corresponding pixel in each image. The POD-based filtering removes the background by automatically removing the minimum number of modes corresponding to the background. The results of this are shown in figure 3.9*b*, where it can be seen that the Time-POD filter combination improves the accuracy of the PIV data with respect to the HWA reference data compared to using SSmin-Norm filtering. Figure 3.9*a* shows the SSmin-Norm pre-processing along with Time-POD filtering compared to the reference HWA data and shows no noticeable effect between the two pre-processing schemes.

The cross-correlation of the image pairs is carried out using a square window with five passes starting at 128x128 and ending with two passes of 16x16. The cross-correlation window has a 50% overlap such that the vector spacing in the final flow fields of the smooth wall is 0.46 mm and 0.73 mm for the rough wall. The final pass has an invalid

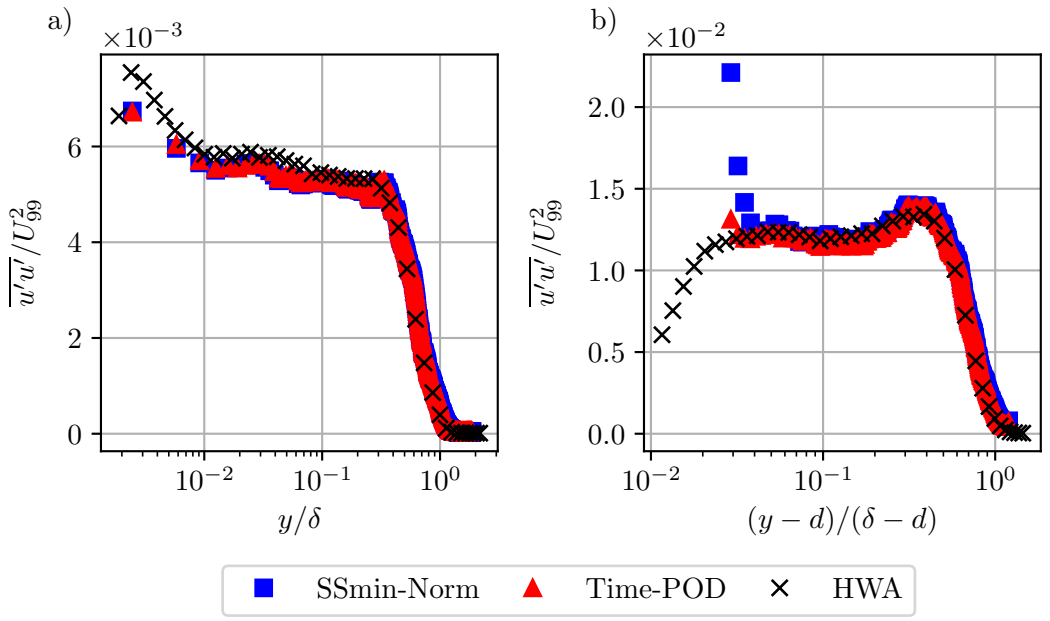

FIGURE 3.10: Comparison of the image pre-processing methods using streamwise Reynolds stress profiles at the HWA measurement station, 9.03 m from the tunnel inlet. Data is shown for (*a*) smooth wall and (*b*) rough wall. The different methods shown are subtracting sliding minimum followed by min-max normalisation, denoted by SSmin-Norm, and the second method is subtracting sliding minimum followed by POD-background removal, denoted by Time-POD.

vector rate of 4.7% for the rough wall cases and 3.9% for the smooth wall cases. These invalid vectors are typically located in the corners of the vector fields, where the lens distortion and lower illumination reduce the correlation in this region. Once vector fields are obtained, a polynomial calibration function is applied. Finally, images obtained simultaneously are stitched together to obtain the final flow fields from which statistics can be taken.

3.5.3 Uncertainty

When considering the uncertainty of the flow, the first assumption is that the tracer particles follow the flow. To access this, the particle Stokes' Number, Stk, is used, given by

$$Stk = \frac{\tau_p}{\tau_f}, \tag{3.14}$$

where τ_p is the response of the particle and τ_f is the response time of the flow usally given as δ / U_{99} for a boundary layer flow (Raffel et al. 2018). For smoke-based particles, the response time of the flow is around 2 μs (Ragni et al. 2011). For the flows presented

Variable	Typ. value	Accuracy Value	Unit	p.d.f	Sensitivty Coefficent	Standard Uncertainty Value (m/s)
Δx	13.4	0.2	pix	rect.	$M/\Delta t$	0.19
M	$0.003U$	0.037	m/s	norm.	1	0.038
σ_U	0.65	0.015	m/s	norm.	1	0.015
					Combined Expanded Uncertainty:	0.383 m/s

TABLE 3.9: Uncertainty budget for a velocity point taken from the rough wall velocity PIV field at $-8°$ at 9.03 m. The data point is taken in the freestream region where $U = 22.3$ m/s.

in this work, the maximum Stokes' number is 0.001, which satisfies $Stk < 0.1$ for which particles can be said to follow the flow well Ragni et al. (2011).

The work of Sciacchitano (2019) states that the error in a PIV measurement can be broken down into three main sources of error. They show the Taylor's expansion for the error of a PIV measurement.

$$\underbrace{\left(\frac{\sigma_U}{U}\right)^2}_{\text{Combined Uncertainty}} = \underbrace{\left(\frac{\sigma_{\Delta x}}{\Delta x}\right)^2}_{\text{Displacement Uncertainty}} + \underbrace{\left(\frac{\sigma_{\Delta t}}{\Delta t}\right)^2}_{\text{Timing Uncertainty}} + \underbrace{\left(\frac{\sigma_{\Delta M}}{\Delta M}\right)^2}_{\text{Calibration Uncertainty}}, \quad (3.15)$$

where u is the measured velocity, Δx is the displacement of the particle, Δt is the time between pluses and M is the magnification. The error due to the timing is often neglected since the $\sigma_{\Delta t} << \Delta t$ (Sciacchitano 2019). The error due to the calibration is typically negligible, especially for planar PIV as conducted for this work (Sciacchitano 2019). The error due to the calibration target manufacture shall be included in the uncertainty budget, but is seen to be small (see table 3.9). The error due to calibration comes from errors in the magnification ratio. Adrian and Westerweel (2011) states that the error due to calibration is typically 0.3% of U, which shall be used when calculating the error. The mean error in the calibration mapping function also results in an error in the vector position, which for the rough wall is 0.14 mm and for the smooth wall is 0.11 mm.

The largest sources of error in the mean velocity measurement are the interrogation and statistical errors. The interrogation error comes from the error in estimating the subpixel displacement. Adrian and Westerweel (2011) states these errors range from 0.1 to 0.2 pixels; the upper estimate is used in future calculations, giving the worst-case error. The statistical error is again calculated using the standard error of the mean in equation 3.2. Table 3.9 estimates the combined expanded uncertainty for a velocity point in the freestream with a mean speed of 22.3 m/s.

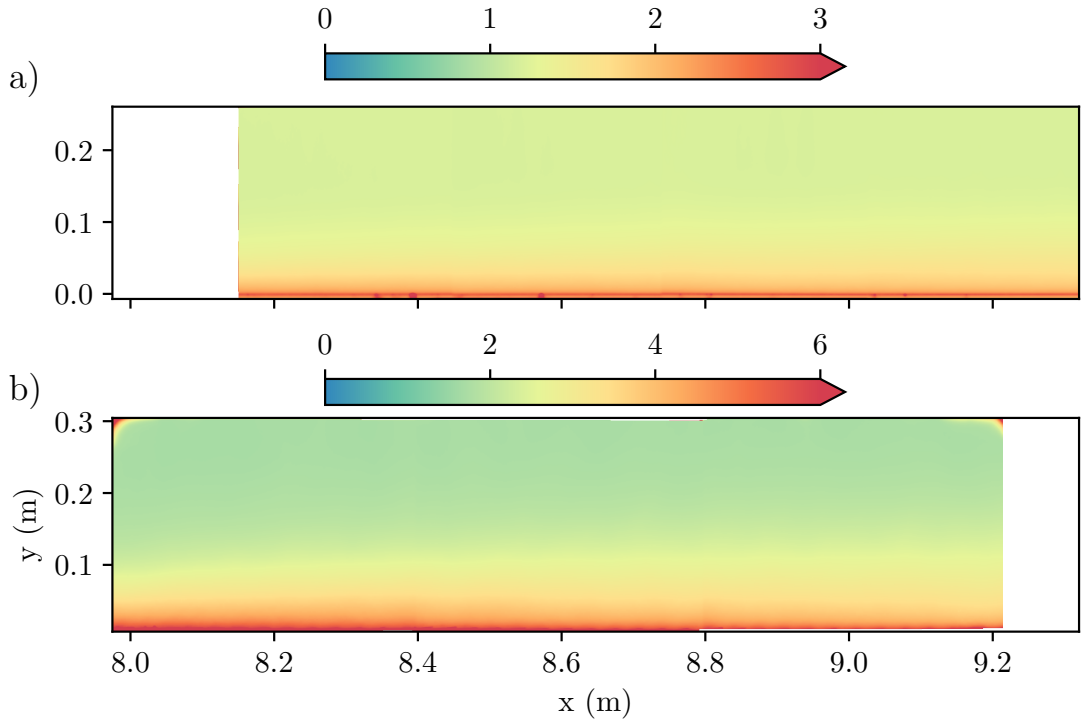

FIGURE 3.11: Uncertainty calculated using the method outlined in table 3.9 for position four. (*a*) uncertainty for the smooth wall data and (*b*) uncertainty for the rough wall data.

This uncertainty is small (1.7%) for a given mean velocity point since it lies in the freestream where the variation in the mean is very small. Figure 3.11 shows the uncertainty for both the smooth and rough wall when the cameras are in position four (see figure 3.8 and 3.9). It can be seen that the uncertainty for the smooth wall is less than that for the rough wall cases. This is to be expected since the camera used for the smooth wall measurements has a higher resolution and thus reduces the impact of the sub-pixel displacement. Furthermore, the smooth wall cases have lower variation statistical error due to lower turbulence intensities within the flow. The error near the wall is seen to be higher for the rough wall cases; this is due to the background reflections caused by the roughness elements. To estimate the uncertainty in the variance from PIV, it is possible to assume the uncertainty in $\overline{u'u'}$ is given by $2(\sigma_U^2)$ if the uncertainty in u and U are assumed to be the same. This results in an uncertainty in $\overline{u'u'}$ between 5 and 10% throughout the boundary layer. Although this is larger than the uncertainty in the mean velocity, it remains reasonable for a second-order statistic.

3.6 Wall Shear Stress Measurements

When studying boundary layers, one necessary quantity is the skin friction. The magnitude of skin friction means that it is difficult to take direct measurements accurately.

Taking a drag balance with an area of 0.04 m^2 the magnitude of the forces acting on the plate is of the order of 0.1 N. There are several different methods to measure the wall shear stress required to find the skin friction coefficient. Oil film interferometry (OFI) is used for smooth wall measurements based on the thinning rate of oil. For rough wall measurements, this is not possible since the roughness blocks the oil, so a direct drag balance is required.

3.6.1 Oil Film Interferometry (OFI)

Large-scale oil film interferometry (OFI) is used to obtain skin friction measurements throughout the region of interest. This region is the 3.75 m (3c) region that the PIV measurements focus on. OFI is based on the thinning rate of oil measured using the interference pattern at the oil-surface interface. The equation for calculating the wall shear stress is given by

$$\tau_0 = \mu_{oil}(\frac{\Delta x}{\Delta t})^2 \frac{2\sqrt{n_{oil}^2 - n_{air}^2 sin^2(\theta)}}{\lambda} \tag{3.16}$$

In this equation, μ_{oil} is the viscosity of the oil at the recording temperature, Δx is the difference in fringe space, Δt is the time over which the difference in fringe spacing occurs, θ is the angle of inclination of the light source and n_{air} and n_{oil} are the reflective indices of air and oil and λ is the wavelength of the light source. It can be seen that the wavelength of the light source needs to be known, and therefore, a monochromatic light source is used. A sodium bulb (Phillips 35W SOX-E bulb) is used for these experiments. Sodium has two spectral wavelengths at 589 and 589.6 nm, which using the coherence length given by $L_c = \lambda^2/\Delta\lambda$ gives $L_c \approx 0.6$ mm. This is orders of magnitude higher than the thickness of the oil film and hence suitable for achieving well-defined fringe patterns. An aluminium sheet is used behind the lamp to reflect light and increase the scattering of light. Two LaVision Imager ProLX 16MP cameras, with Scheimpflug adaptors and Sigma 105 mm F2.8 lenses, are used. Scheimflug adaptors are required to ensure the entire field of view is focused. This is because the cameras must be placed at an angle to capture the interference pattern; for this experiment, they are at $\approx 45^\circ$. The light source and cameras are mounted underneath the tunnel, imaging the wind tunnel glass floor as shown in figure 3.12. The oil used is Polycraft Dow Corning 200/50 Silicone Fluid with a well-defined viscosity at a given temperature. The two cameras result in a field of view of approximately 30 cm, and this is repeated at 16 different positions to obtain measurements at all streamwise positions. In each camera FOV, three oil lines are drawn in a staggered pattern to ensure good measurement density. Each run results in 200 images for each camera acquired at 1 Hz. The acquisition frequency is reduced to 0.5 Hz for cases where little change is seen to ensure a suitable signal. To

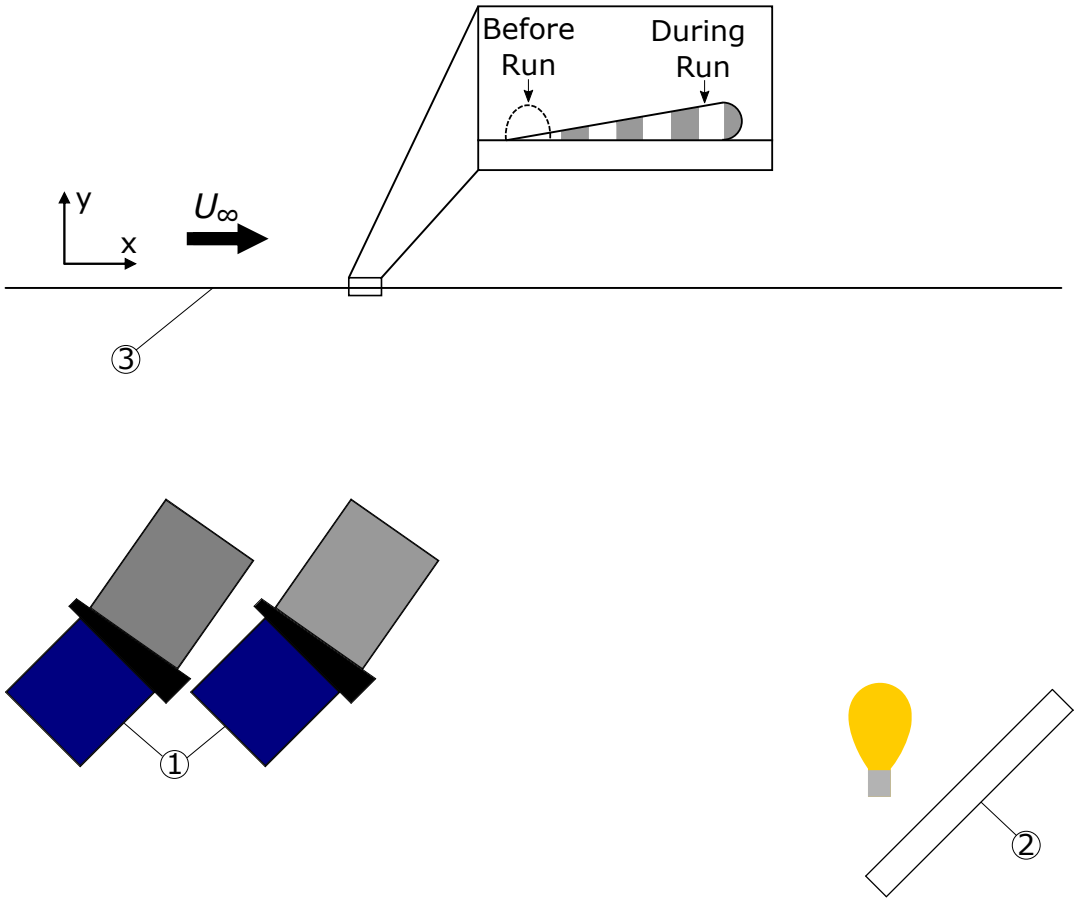

FIGURE 3.12: Simplified diagram showing the imaging setup for photographing the interference patterns on the oil-glass interface. ① LaVision Imager ProLX 16MP, Scheimpflug adaptor and Sigma 105 mm F2.8 lens. ② Monochromatic light source and aluminium panel to scatter light. ③ Shows the glass surface through which the camera images the interference pattern. The zoomed-in section shows oil before and during the measurement.

ensure a thin film and clear fringe patterns, the oil is allowed to thin, and it is checked that there are clear fringe patterns before image acquisition takes place.

Marco Virgillo (Post Doctoral Researcher) post-processed the experimental data as part of a collaboration. Details of the post-processing can be found in Virgilio et al. (2025). The uncertainty of Oil film measurements is typically assumed to be $< \pm 3\%$ (Pailhas et al. 2009; Thibault and Poitras 2017; Rezaeiravesh et al. 2018).

3.6.2 Floating element drag balance

The drag balance used to measure the skin friction of a rough wall independently consists of 0.20x0.20 m floating element located in the tunnel floor. The balance contains a floating element consisting of a flat plate mounted on a floating element hung from the outer casing with four thin flexures in the corners. The smooth, flat metal plate sits level with the outer casing, which is level with the wind tunnel floor; the roughness is

FIGURE 3.13: Simplified diagram of floating element drag balance used to measure a rough wall's shear stress. The outer structure is shown in black. The floating element is shown in red, which is supported by the blue flexures. The magnet shown in green is mounted on the floating element, and the electromagnet is shown in purple. The distance sensor is shown in yellow.

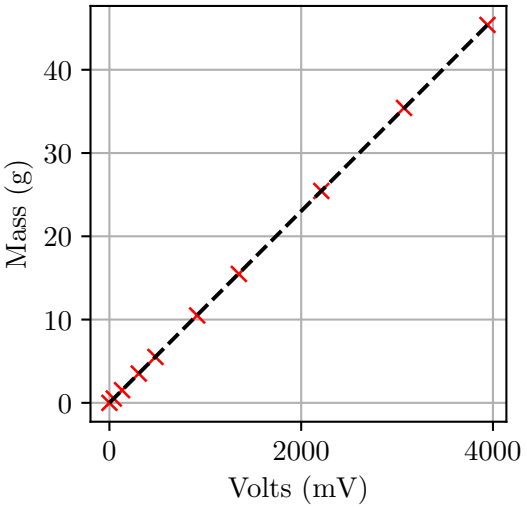

FIGURE 3.14: Calibration plot of applied load (g) vs measured voltage (mV) used for rough wall cases taken at h = 0.5 m.

then mounted onto the flat plate. An electromagnet and distance sensor with a range of $\pm 250 \mu m$ keeps the displacement at $0 \mu m$ when a force is applied. Figure 3.13 shows a simplified diagram of the balance used, showing the different components. More details of the construction and sensors can be found in Aguiar Ferreira et al. (2024).

Calibration involves applying known loads from 0 to 45 g to the floating element and measuring the mean voltage. An example calibration is shown from the rough wall cases at h = 0.5 m, as shown in figure 3.14. It should also be noted that the calibration process considers the pulley wheel's friction to ensure a linear fit. Since there will be a pressure gradient across the balance, which will act on the balance itself, since there is a 0.5 mm gap between the element and frame, the force is corrected to account for this force acting on the balance. This pressure correction is only applied from the 3 mm floating element, not the roughness elements and is given by

$$F_{actual} = F_{measured} + \frac{dp}{dx} \cdot t \cdot A \tag{3.17}$$

In this equation, F_{actual} is the corrected force (N), $F_{measured}$ is the measured force (N), $\frac{dp}{dx}$ is the streamwise pressure gradient, t is the thickness of the floating element and A is the top area if the balance. The correction for the pressure acting on the floating element is typically 2% of the measured load from the floating element. The initial distance is set as close to $0\mu m$ as possible using a fine thread traverse inside the balance, allowing the distance sensor to be traversed, setting the initial position. A PID control loop is then used to control the electromagnet to keep the distance at $0\mu m$. However, this has some limitations, for example, with a static load, such as during calibration, it is possible to obtain a steady voltage and, hence, a steady distance. However, when measuring wall shear stress, as is the nature of turbulence, there are fluctuations in the flow. This means the balance oscillates, resulting in a noisy signal. Hence, only a mean voltage can be taken, which is then converted to a force using the calibration.

The uncertainty with a 95% confidence interval is found not typically to exceed 1% (Aguiar Ferreira et al. 2024). The uncertainty introduced by the correction for the pressure acting on the floating element is negligible compared to the measured load on the floating element. This uncertainty is much smaller than that expected from fitting methods, which can be off by as much as 10% for strong PGs (Monty et al. 2011). Aguiar Ferreira et al. (2024) reports that calibration and repeatability errors are negligible for high Reynolds number flows. The leading sources of error are the streamwise pressure gradient and the balance's inclination. For rough wall measurements, these errors are reduced since the shear stress measured is much higher than that of a smooth wall.

3.7 Incoming Boundary Layer

The experiments carried out during this work aim to explore the impact of different PG histories on the boundary layer. Therefore, to quantify the effect of PG, it is important to know the boundary layer before experiencing the PG. The traverse is placed upstream of the leading edge so that the sensing wire is located at 5.28 m from the start of the test section. The rest of the setup is as per the setup for downstream HWA measurements as shown in figure 3.6. Rough wall profiles are taken for -8° and 8° at h = 0.5 m at 10, 20 and 30 m/s. The same speeds and angles of attack are obtained from Agathangelou (2024) for the smooth wall. These speeds equate to Reynolds numbers of $3.3 \times 10^6 < Re_L < 10.4 \times 10^6$.

Figure 3.15*a* shows the mean velocity profiles of both the smooth and rough walls at $13800 < Re_\theta < 16800$. The value of d for the rough wall is taken to be half the roughness height as in Squire et al. (2016) for ZPG measurements. The mean velocity profiles show that for a given surface, there is a collapse between the different angles of attack. This is to be expected since panel method simulations suggest the effect of the

Case	Surface	Symbol	U_∞ (m/s)	U_{99} (m/s)	δ (m)	δ^* (m)	θ (m)	H	Re_θ
$-8°$	SW		9.7	9.6	0.08	0.011	0.009	1.31	5612
$-8°$	SW		19.7	18.9	0.08	0.010	0.008	1.29	10205
$-8°$	SW		29.6	29.6	0.08	0.010	0.008	1.28	15864
$-8°$	RW		9.9	10.0	0.16	0.033	0.021	1.58	13843
$-8°$	RW		19.9	20.1	0.16	0.034	0.022	1.55	29026
$-8°$	RW		29.6	29.7	0.16	0.032	0.021	1.56	40332
$8°$	SW		9.6	9.3	0.08	0.013	0.009	1.32	5902
$8°$	SW		19.4	18.7	0.08	0.011	0.009	1.30	10959
$8°$	SW		29.0	28.7	0.08	0.011	0.009	1.29	16832
$8°$	RW		9.9	9.6	0.16	0.036	0.022	1.60	14102
$8°$	RW		19.9	19.9	0.17	0.036	0.023	1.57	30397
$8°$	RW		29.3	29.3	0.17	0.036	0.023	1.56	44975

TABLE 3.10: Summary of key boundary layer properties for two angles of attack, one chord upstream of the aerofoil. Surface given as SW for smooth wall and RW for rough wall.

aerofoil is limited to approximately one chord upstream of the leading edge. The rough wall results in a lower velocity at a given wall normal location compared to the smooth wall. Figure 3.15*b* shows the mean streamwise Reynolds stress. Again, there is good collapse across the different angles of attack for a given surface. Roughness results in much higher turbulence throughout the boundary layer.

Table 3.10 gives the key boundary layer properties of the different test cases. It is seen that the incoming boundary layer for the smooth wall at x=5.28 m is approximately 0.08 m. This means that the incoming boundary layer is $\approx 68\delta_0$ from the start of the test section. For the rough wall, the boundary layer is twice as thick at 0.16 m, which is $\approx 32\delta_0$ from the start of the test section. Table 3.10 shows that the rough wall boundary layer is 23% higher than the smooth wall. It is also seen that the shape factor can be considered constant for both the smooth and rough walls with Reynolds number.

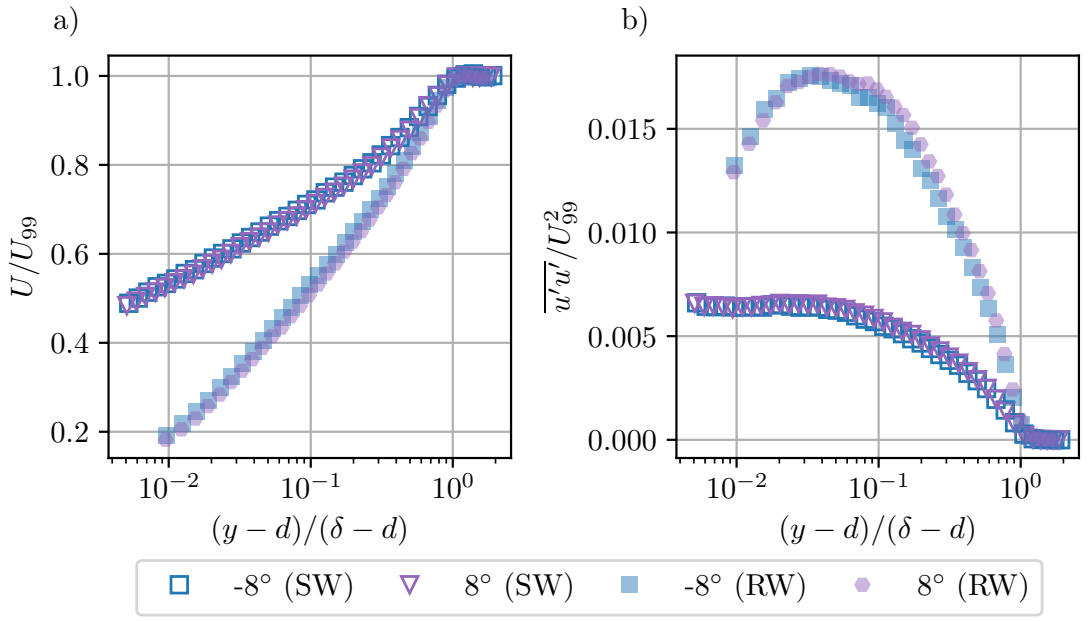

FIGURE 3.15: Comparison of mean profiles at similar $Re_\theta \approx 13800 - 16800$ for smooth and rough wall. The smooth wall data is taken at 30 m/s, and the rough wall data at 10 m/s. For the rough wall d is assumed to be $k/2$, while for the smooth wall d is 0. (*a*) Comparison of mean velocity profiles with outer scaling. (*b*) Comparison of mean streamwise Reynolds stress with outer scaling.

Chapter 4

Pressure Gradient History Effects on Skin Friction and Mean Flow

This chapter considers the effect of PG history on the mean flow at a fixed measurement location. Experiments are carried out using hot wire anemometry over both a smooth and rough wall as set out in section 3.4.2. Independent skin friction measurements are conducted using OFI and drag balance measurements as outlined in sections 3.6.1 and 3.6.2. First, the PG history is presented for the different test cases. This is followed by an examination of the mean flow, before looking at the prediction of PG flows. [1]

4.1 Parameters

This chapter focuses on the effects of PGs on skin friction and mean flow, with particular attention to five core angles of attack: -8° , -4° , 0° , 4° , and 8° . Measurements are taken one chord downstream of the trailing edge to assess these effects. For the smooth wall case, this corresponds to $116.1\delta_0$ from the test section inlet, while for the rough wall case, it is $55.4\delta_0$, where δ_0 is the boundary layer thickness one chord upstream of the aerofoil (see section 3.7).

For the smooth wall, measurements are conducted at freestream velocities of 10, 20, and 30 m/s. For the rough wall, measurements span 10–30 m/s in 5 m/s increments, covering a Reynolds number range of $6.0 \times 10^6 < Re_L < 19.6 \times 10^6$. The quarter chord is positioned 0.5 m above the wind tunnel floor for most cases, except for rough wall measurements at -10° , -8° , and -4° , where it is lowered to 0.4 m for tests at 20, 25, and 30 m/s. Smooth wall data at this height is only collected for -10° and -8° to expand the range of pressure gradient histories and strengths.

[1] The work in the chapter is published in the Journal of Fluid Mechanics as Preskett et al. (2025).

For the smooth wall ZPG cases, skin friction and velocity profiles from Wangsawijaya et al. (2023) and Aguiar Ferreira et al. (2024) are used, obtained at the same measurement station as the present data. Additionally, Aguiar Ferreira et al. (2024) provides direct skin friction measurements using OFI. To enhance clarity when comparing different velocities, transparency is adjusted in plots with increasing Reynolds numbers. The dataset spans an extended Reynolds number range, ensuring sufficient scale separation.

4.2 Pressure distribution

This section first compares the panel method distributions calculated as outlined in Appendix A for the smooth wall data with $h = 0.5$ m. This is followed by a comparison of the smooth and rough wall data at both $h = 0.5$ m and $h = 0.4$ m. Throughout this work, the pressure coefficient is given by equation 3.3; here, P_s is taken to be the static pressure at $x/c = -1$.

4.2.1 Comparison of panel method and experimental data

In section 3.4.2, it was explained that the HWA probe was placed at $x/c = 2$ based on the panel method simulations in Appendix A. In order to compare the panel method simulations and the smooth wall experimental data figure 4.1*a* presents the C_p distributions obtained from both. The experimental data shown is taken during the OFI experiments, and as such, the only influences on the PG are the aerofoil and boundary layer growth. The panel method simulation is inviscid, and as such, C_p recovers to zero downstream of the aerofoil. The experimental data doesn't recover due to the momentum loss caused by the drag of the surface. The experimental data reflects the shape and trends of the panel methods; however, the peak values of C_p in the experiments are lower. Looking at $dCp/d(x/c)$ as shown in figure 4.1*b*, the shape and trends agree between the panel method and experiments. For smaller pressure gradients, the agreement is good; for example, the 0° cases agree with each other. However, for the -8° case, the error in the first peak is 76%. One reason for these differences is that the simulation is inviscid and hence does not model the TBL development. For a wind tunnel, there are two boundary layers on the top and bottom of the tunnel, which will affect the velocity of the freestream of the tunnel, along with the boundary layer on the aerofoil. Panel method simulations in the planning stage showed that the effect of the aerofoil is limited to approximately one chord upstream and one chord downstream of the aerofoil. This result is also evident in the experimental data, which confirm that the aerofoil's effect is limited to this region.

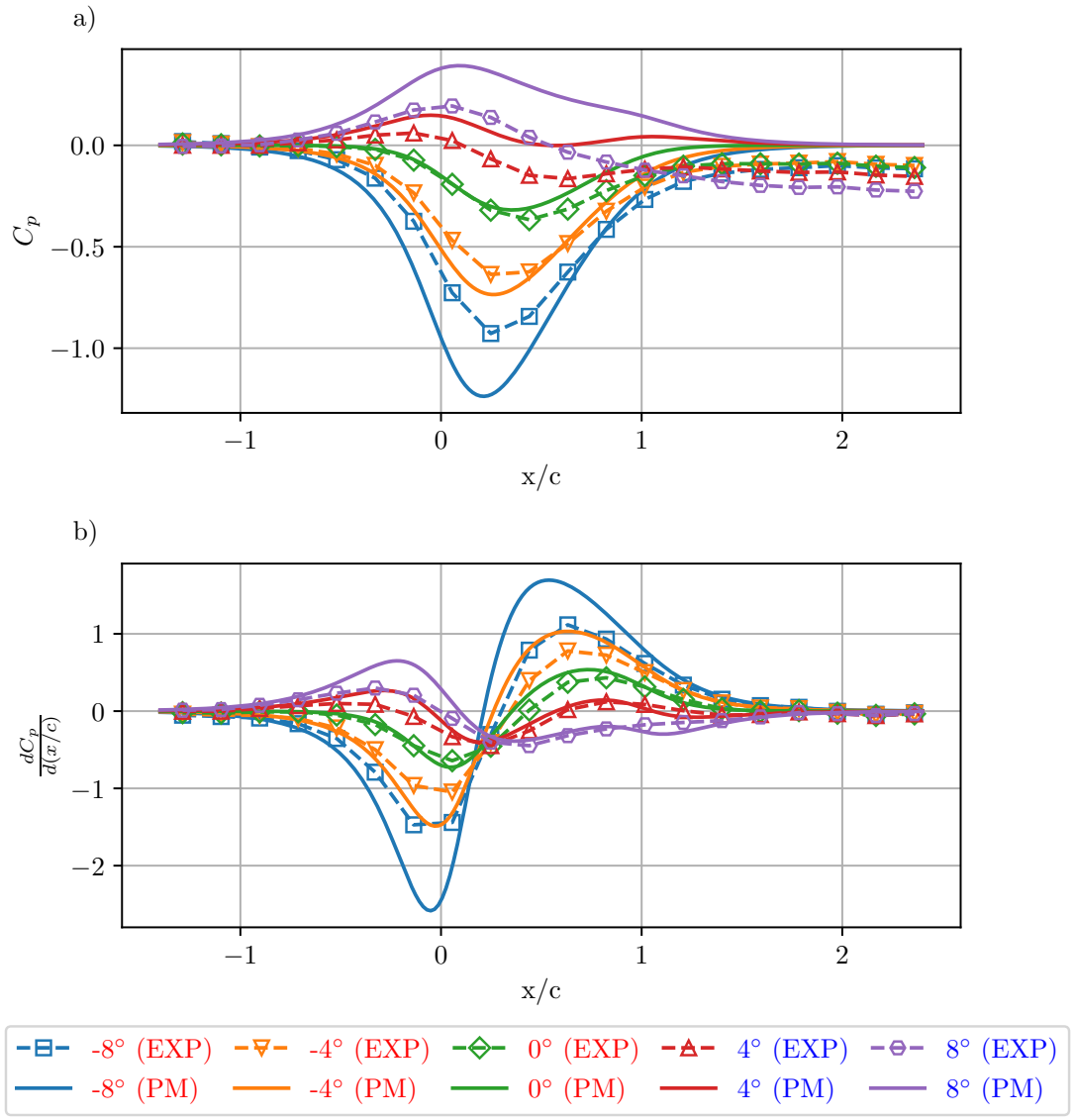

FIGURE 4.1: Comparison of panel method simulation and experimental data for different angles of attack at h = 0.5 m. (a) shows the mean pressure coefficient, C_p.(b) shows the mean pressure gradient with respect to x/c, $\frac{dC_p}{d(x/c)}$. F-APG cases have a red legend label, while A-FPG cases are blue.

For the 0.5 m cases, there are two distinct history types. The first are those that have an FPG followed by an APG ($-8°$, $-4°$, $0°$). Secondly, those with an APG followed by an FPG ($4°$ $8°$). All 0.4 m cases fall into the first category. They have greater strength than the 0.5 m cases due to the aerofoil being closer to the wall. The first group of cases will be called F-APG cases throughout this work, and shown with a red legend label. While the second group will be the A-FPG cases, shown with a blue legend label. This is because it is assumed that the pressure gradient type experience second will be more dominant in the resulting boundary layer one chord downstream.

4.2.2 Comparison of smooth and rough wall data

The mean pressure distribution from all speeds is presented for smooth and rough walls at the five angles of attack for h of 0.5 m height in figure 4.2*a*. Also presented are the cases with h of 0.4 m. It can be seen that both the smooth and rough wall datasets have very similar shapes. Furthermore, the maximum pressure coefficient is located at the same streamwise location. There are slight differences in the pressure coefficient between the rough and smooth walls. The smooth wall for strong negative angles of attack has higher magnitude peak values than the rough wall. The reason for this is likely due to the proximity of the taps to the roughness elements. This results in a lower pressure coefficient than for taps, which are further from roughness elements.

Figure 4.2*b* shows the pressure distribution for 10, 20 and 30 m/s for the -8° , 0° and 8° cases. This shows an important result that the C_p distribution is invariant to the Reynolds numbers. The small variations across the different speeds are due to minor differences in the boundary layer thicknesses, changing the tunnel's effective cross-section. The same result is seen for the rough wall data with Reynolds number.

The pressure gradient histories show good agreement between the smooth and rough wall cases. There is some variation in the pressure gradient around the hot wire measurement station. In some cases, the small FPG comes from the acceleration around the hot wire traverse. In other cases, pressure distribution was taken when the traverse was removed, such as when carrying out OFI or PIV. The effect of the traverse on the different boundary layers is assumed to be minimal and equal in all cases. Measurements were also taken in a nominal ZPG case, with the wing removed from the wind tunnel. This data was seen to have a slight FPG. The flow accelerates due to the boundary layer growing and the tunnel being a fixed cross-section.

The cases presented are non-equilibrium pressure distributions since $\beta = (\delta^*/\tau_0) \cdot (dP/dx)$ is not constant. The boundary layers one chord upstream are the same since they have had the same pressure gradient history, as shown in section 3.7. The hot wire is, therefore, placed one chord downstream of the aerofoil so that the local pressure gradient is the same for all cases. Thus, any difference can be attributed to the upstream pressure gradient history.

4.3 Mean Flow - After experiencing pressure gradient history

The velocity profiles of the rough and smooth wall TBLs are inner scaled using the directly measured friction velocity. Figure 4.4*a* shows the inner scaled profiles at $Re_\tau \approx 8000$, i.e. freestream speeds of 30 m/s for the smooth wall and 10 m/s for the rough wall cases. Table 4.1 gives the variation of the main boundary layer parameters used throughout the investigation. For the smooth wall case, Re_τ ranges from 8310 for the

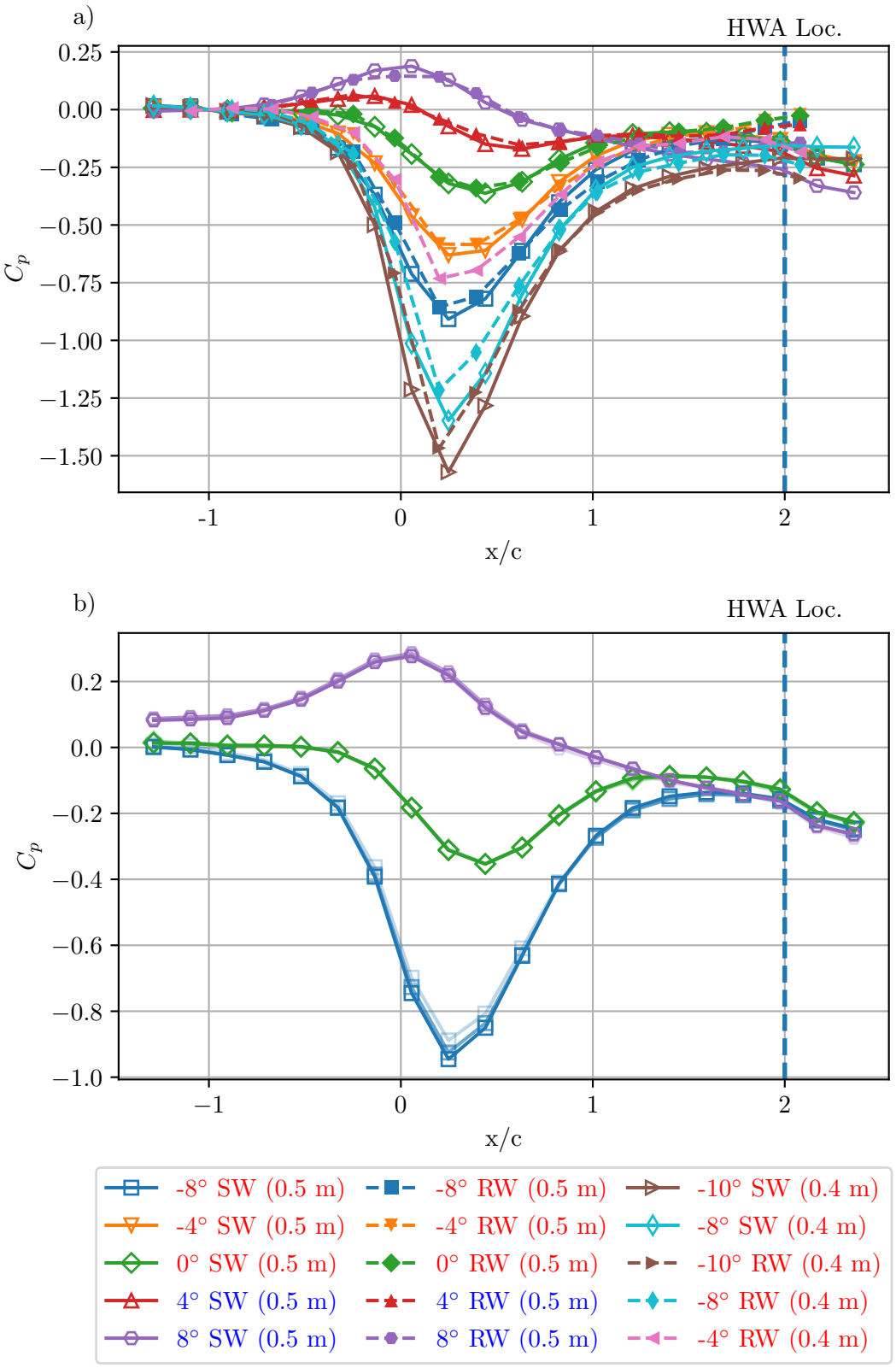

FIGURE 4.2: (*a*) Mean pressure coefficient, C_p, for smooth and rough wall cases. The quarter chord height is given in parentheses. (*b*) Variation in pressure coefficient with Reynolds number for the smooth wall at $-8°$, $0°$ and $8°$. 10, 20 and 30 m/s cases are shown, and the opacity of the symbols increased with velocity. The quarter chord height (h) is given in parentheses in the legend.

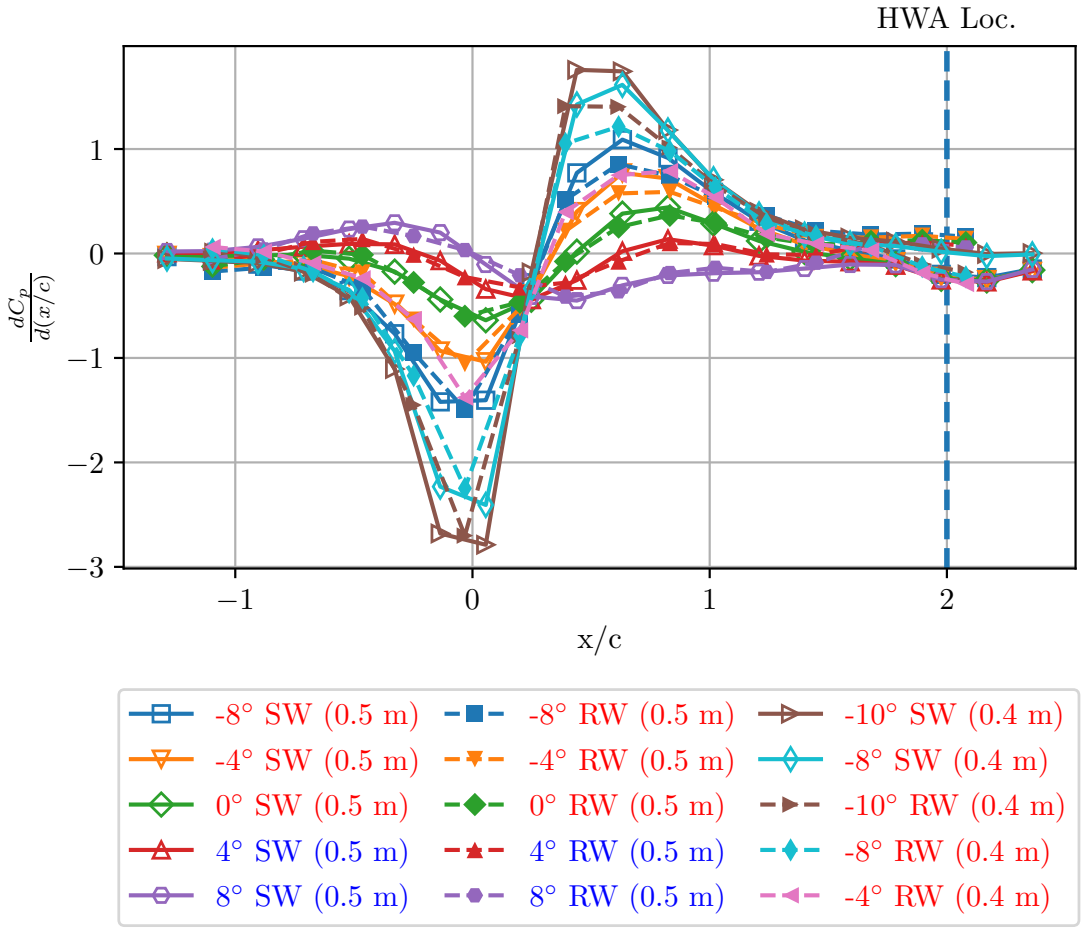

FIGURE 4.3: Mean pressure coefficient gradient with respect to x/c for smooth and rough wall cases. The quarter chord height (h) is given in parentheses in the legend.

$-8°$ to 6900 for the 8°. The variation in Re_τ is much lower for the rough wall, with values varying from 7830 to 8330 for the $-8°$ and 4°, respectively.

The boundary layer profiles of the flow over the smooth wall collapse into the log region. It is seen that the F-APG cases, which have an APG just upstream of the measurement location, have a larger wake region (i.e. larger Π) and earlier deviation from the log law region. As the angle of attack increases, the resulting pressure gradient just upstream of the measurement location becomes more favourable, the wake becomes smaller (i.e. smaller Π) and the log region extends further away from the wall. The rough wall cases show the same wake and log region trends. In figure 4.4*a*, there is a clear downward shift of the profiles from the smooth wall cases due to the roughness effects. As explained in section 2.2, this is because of the extra momentum loss and increased drag which depends on the type of roughened surface.

The roughness length scale chosen throughout this work is y_0. It was chosen since all the flow measurements were taken within the fully-rough regime, as was shown by the skin friction measurements. In equation 2.16, the two unknowns in the log region

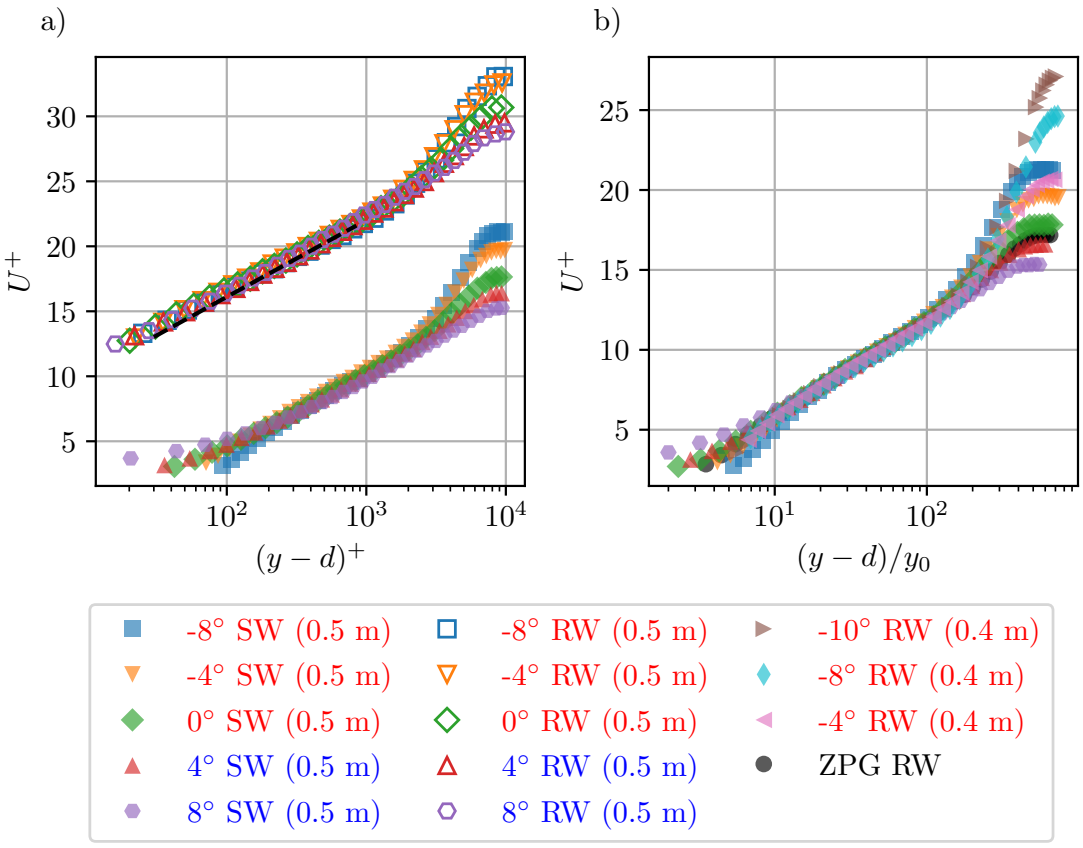

FIGURE 4.4: (*a*) Inner scaled velocity profiles at $Re_\tau \approx 6800 - 8300$ for both smooth and rough wall cases at 0.5 m. The dashed black line shows the log region from 2.7. (*b*) Rough wall velocity profiles for 20 m/s for the 0.4 m, 0.5 m and ZPG cases. In both plots, d is the zero plane displacement, which for a smooth wall is zero. The x axis is scaled using y_0, this results in the collapse of the log region of the profiles. The quarter chord height (h) is given in parentheses in the legend.

are d (the zero plane displacement) and y_0 (the roughness length scale). Using the measurement value of skin friction, we first fit the zero plane displacement while ensuring d should be less than the roughness height, k (Castro and Vanderwel 2021). The value of d is fitted using the diagnostic function, $\Xi = \frac{1}{U_\tau}\frac{dU}{dy}(y-d)$, which is equal to $1/\kappa$ in the log region. The value of d is chosen to give the longest log region possible within the acceptable error range. The acceptable error range is defined such that the average deviation of the points chosen to be in the log region is less than $\pm 5\%$ from $1/\kappa$. Further details, including example diagnostic plots, can be found in appendix C. The resultant values of zero plane displacement are shown in table 4.2. The results show APG just upstream of the measurement location reduces the value of the zero plane displacement, and FPG increases it. For the strong F-APG cases, the value of zero plane displacement is approximately zero. This suggests that the bounds set for d may be limiting and that d could well be negative; however, this would be inconsistent with the recommendations from previous work. Further work may be necessary to examine the influence of pressure gradients on this quantity. It is noted that the rough wall data

Case (h)	Surface	Symbol	U_∞ (m/s)	U_{99} (m/s)	U_τ (m/s)	δ (m)	δ^* (m)	θ (m)	H	Re_τ	Re_θ	Π	$\frac{TU_{99}}{\delta}$	l^+
ZPG	SW	○	9.8	9.7	0.35	0.12	0.018	0.013	1.31	2758	8617	0.51	24917	24
ZPG	SW	○	19.9	19.9	0.68	0.12	0.016	0.013	1.28	5508	17270	0.51	24773	46
ZPG	SW	○	29.5	29.5	0.98	0.12	0.016	0.012	1.27	7640	24202	0.51	25323	66
ZPG	RW	●	19.9	19.8	1.15	0.22	0.044	0.029	1.51	17001	38146	0.29	19622	77
ZPG	RW	●	29.9	29.7	1.72	0.23	0.044	0.029	1.50	26074	57530	0.29	19061	115
−8° (0.5 m)	SW	□	9.5	10.0	0.31	0.14	0.025	0.018	1.43	2904	12087	1.24	26329	21
−8° (0.5 m)	SW	□	19.3	20.3	0.62	0.14	0.024	0.017	1.38	5831	23763	1.24	26480	42
−8° (0.5 m)	SW	□	28.7	30.2	0.91	0.13	0.023	0.017	1.36	8328	34541	1.24	26848	62
−8° (0.5 m)	RW	■	9.9	10.4	0.50	0.23	0.063	0.037	1.72	7830	25177	1.18	23493	32
−8° (0.5 m)	RW	■	20.1	21.7	1.02	0.25	0.065	0.038	1.71	16592	53984	1.18	22988	67
−8° (0.5 m)	RW	■	30.1	32.5	1.51	0.26	0.065	0.038	1.71	25452	81527	1.18	22184	99
−4° (0.5 m)	SW	▽	9.6	10.0	0.33	0.13	0.022	0.016	1.38	2811	10803	1.02	26391	22
−4° (0.5 m)	SW	▽	19.5	20.3	0.65	0.13	0.021	0.016	1.35	5659	21607	1.02	26326	44
−4° (0.5 m)	SW	▽	28.9	30.5	0.94	0.13	0.020	0.015	1.34	7894	30056	1.02	27319	63
−4° (0.5 m)	RW	▼	9.9	10.4	0.53	0.22	0.053	0.032	1.63	7787	21991	0.81	24853	35
−4° (0.5 m)	RW	▼	20.2	21.6	1.10	0.25	0.055	0.034	1.63	17446	47442	0.81	23254	72
−4° (0.5 m)	RW	▼	29.9	31.8	1.61	0.24	0.056	0.034	1.64	25484	71023	0.81	23454	106
0° (0.5 m)	SW	◇	9.6	10.1	0.35	0.12	0.019	0.014	1.35	2775	9486	0.71	25458	23
0° (0.5 m)	SW	◇	19.5	20.1	0.67	0.12	0.017	0.013	1.32	5310	18061	0.71	25898	46
0° (0.5 m)	SW	◇	28.9	30.1	0.98	0.11	0.016	0.012	1.30	7517	25481	0.71	26680	67
0° (0.5 m)	RW	◆	10.0	10.3	0.59	0.21	0.045	0.029	1.57	8049	19063	0.47	26362	38
0° (0.5 m)	RW	◆	20.0	21.1	1.19	0.21	0.045	0.029	1.57	16974	40024	0.47	25974	78

Case (h)	Surface	Symbol	U_∞ (m/s)	U_{99} (m/s)	U_τ (m/s)	δ (m)	δ^* (m)	θ (m)	H	Re_τ	Re_θ	Π	$\frac{TU_{99}}{\delta}$	l^+
0° (0.5 m)	RW	◆	29.9	31.7	1.77	0.22	0.046	0.029	1.58	25672	61189	0.47	25580	117
4° (0.5 m)	SW	△	9.5	10.1	0.37	0.11	0.015	0.012	1.31	2739	8008	0.47	27832	25
4° (0.5 m)	SW	△	19.3	20.5	0.71	0.11	0.014	0.011	1.29	5093	15487	0.47	29101	48
4° (0.5 m)	SW	△	28.8	30.4	1.03	0.10	0.014	0.011	1.27	7294	21953	0.47	29254	70
4° (0.5 m)	RW	▲	9.9	10.3	0.63	0.20	0.038	0.025	1.52	8335	16839	0.22	27753	41
4° (0.5 m)	RW	▲	20.2	21.6	1.30	0.21	0.039	0.026	1.52	17447	36034	0.22	27748	85
4° (0.5 m)	RW	▲	29.9	31.8	1.91	0.20	0.039	0.025	1.54	26131	53378	0.22	27378	126
8° (0.5 m)	SW	⬡	9.5	10.5	0.40	0.10	0.013	0.010	1.29	2676	7047	0.26	29613	27
8° (0.5 m)	SW	⬡	19.2	20.9	0.76	0.10	0.012	0.009	1.26	5071	13500	0.26	30026	51
8° (0.5 m)	SW	⬡	28.7	30.9	1.08	0.09	0.011	0.009	1.25	6842	18228	0.26	31353	74
8° (0.5 m)	RW	⬢	10.1	10.7	0.70	0.18	0.032	0.021	1.50	8090	14607	0.03	31870	45
8° (0.5 m)	RW	⬢	20.1	22.2	1.44	0.19	0.034	0.023	1.50	17803	32851	0.03	30305	94
8° (0.5 m)	RW	⬢	30.0	32.9	2.12	0.20	0.035	0.023	1.50	27423	50254	0.03	29052	140
−10° (0.4 m)	SW	▷	9.5	10.3	0.30	0.15	0.034	0.022	1.54	3145	15440	1.83	44846	20
−10° (0.4 m)	SW	▷	19.6	21.4	0.61	0.16	0.032	0.022	1.47	6411	31030	1.83	45887	41
−10° (0.4 m)	SW	▷	29.5	32.4	0.89	0.16	0.030	0.021	1.44	9437	44517	1.83	35742	59
−10° (0.4 m)	RW	▶	20.0	22.2	0.82	0.29	0.092	0.049	1.89	15761	71538	2.32	24568	54
−10° (0.4 m)	RW	▶	30.2	33.6	1.22	0.30	0.093	0.049	1.90	23646	107286	2.32	24398	79
−8° (0.4 m)	SW	◊	9.5	10.1	0.30	0.14	0.029	0.019	1.48	2937	13292	1.54	42171	20
−8° (0.4 m)	SW	◊	19.3	20.8	0.61	0.15	0.028	0.019	1.44	6126	27394	1.54	38849	42
−8° (0.4 m)	SW	◊	28.7	30.8	0.89	0.15	0.025	0.018	1.40	8838	38246	1.54	42312	61
−8° (0.4 m)	RW	◆	19.9	21.4	0.87	0.28	0.081	0.045	1.78	16068	64203	1.78	24732	58

Case (h)	Surface	Symbol	U_∞ (m/s)	U_{99} (m/s)	U_τ (m/s)	δ (m)	δ^* (m)	θ (m)	H	Re_τ	Re_θ	Π	$\frac{TU_{99}}{\delta}$	l^+
$-8°$ (0.4 m)	RW	♦	30.3	32.9	1.33	0.28	0.080	0.045	1.76	24052	95654	1.78	20611	86
$-4°$ (0.4 m)	RW	◀	19.9	21.1	1.02	0.25	0.058	0.036	1.61	16494	50287	0.98	23636	67
$-4°$ (0.4 m)	RW	◀	30.1	31.9	1.54	0.25	0.061	0.037	1.65	24989	76944	0.98	26578	100

TABLE 4.1: Summary of hot wire data taken 9.03 m from the inlet of the wind tunnel for different pressure gradient histories.

	-10°	-8°	-4°	0°	4°	8°
d (mm) (0.5 m cases)		0.12	0.95	1.89	2.14	3.00
d (mm) (0.4 m cases)	0.474	0.00	0.00			
$y_0/y_{0_{ZPG}}$ (0.5 m cases)		1.16	1.06	1.04	1.02	1.04
$y_0/y_{0_{ZPG}}$ (0.4 m cases)	0.98	0.94	0.97			

TABLE 4.2: Values of d (mm) and $y_0/y_{0_{ZPG}}$ for different pressure gradient histories with $y_{0_{ZPG}} = 0.462$ mm.

here has not been corrected for the HWA probe deflection, and this may have an influence on the value of d. It is difficult to quantify the effect of this deflection; however, the overall trend in the values should remain the same. Furthermore, it is noted that since all velocities are fitted together, the overall effect should be minimised. Since most of our work involves high Reynolds numbers, the exact choice of d has minimal impact on the results in the following sections, so we opt to leave it unchanged. The value of d_{ZPG} was found to be $0.46k$ ($d_{ZPG} = 1.37$ mm) and this is consistent with the work of Squire et al. (2016), who, for ZPG flows, suggested choosing d as $k/2$.

The method for finding d defines the bounds of the log region where the error remains within an acceptable range. Within this region, we obtain y_0 as an offset from the smooth wall. Details on the fitting of y_0 and examples of the resulting fit can be found in appendix C. The results are shown in table 4.2. While for the zero plane displacement, there is a trend shown with pressure gradient history, for the roughness length scale, there is no clear trend. The $-8°$ case shows a small increase in the roughness length scale compared to the ZPG value. However, the cases at 0.4 m have roughness length scale values lower than the ZPG case. The absence of a clear trend with the pressure gradient history, along with the minimal variation in values, suggests that y_0, and hence k_s through equation 2.15, is unaffected by the flow history. Any differences are attributed to the fitting process and the selected boundary layer region. Especially for strong F-APG cases where the log region is small. This means that some of the wake region will likely be fitted to the log region, thus affecting the value of y_0. Regardless, the maximum deviation in y_0 across the different cases is less than 20% and, in fact, less than 10% for the majority of cases examined here. This is much smaller than the deviations reported in Vishwanathan et al. (2023) and is presumably because of the scale separation that was achieved in this study where a considerable log region can be identified across all profiles. Moreover, an independent measure of U_τ limits the uncertainty in fitting leading to better estimates of y_0.

The inner scale velocity profiles as a function $(y - d)/y_0$ is shown in figure 4.4*b*. Scaling of the x-axis with y_0 results in the collapse of the log regions of the profiles due to the fitting of y_0. All profiles also exhibit a clear wake region that changes with the nature of the pressure gradient just upstream of the measurement location. However, it should be noted that this local wake is an integral effect of the entire pressure gradient

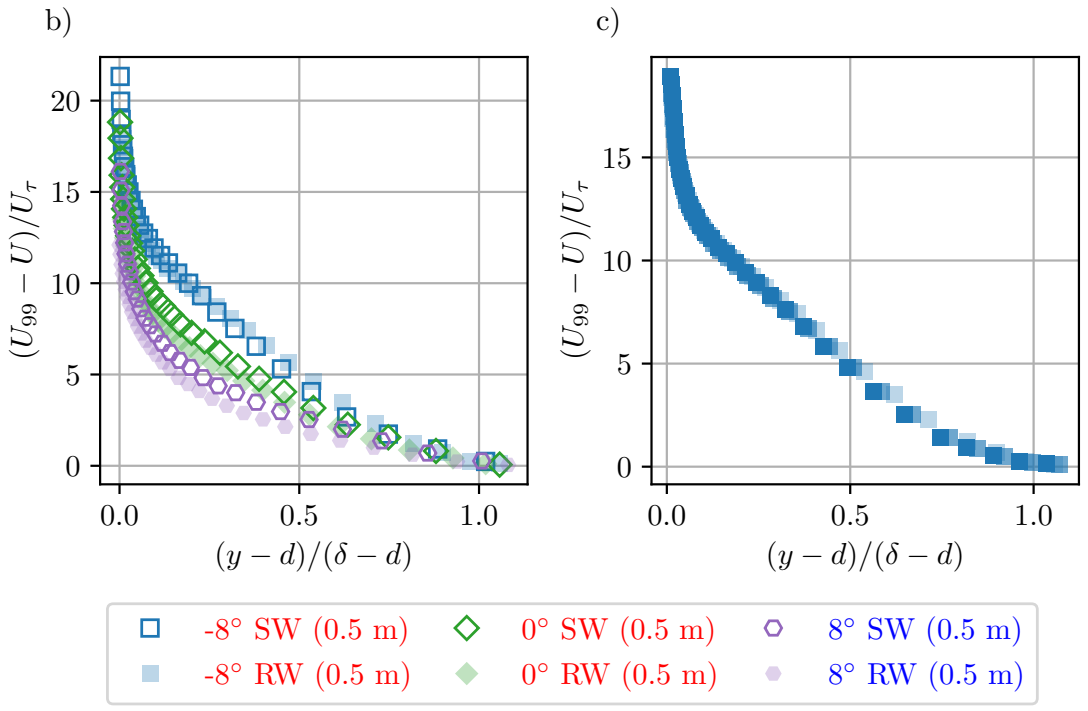

FIGURE 4.5: (*a*) Comparison of the velocity deficit profiles for $-8°$, $0°$ and $8°$ at 0.5 m for both smooth and rough walls. (*b*) shows the variation in velocity deficit profile for rough wall with Reynolds number for $-8°$ at a height of 0.5 m for 10, 20 and 30 m/s. In both plots, d is the zero plane displacement, which is zero for a smooth wall. The quarter chord height (h) is given in parentheses in the legend.

history experienced by the flow. It is shown that the profile of the ZPG case has a wake between those at $0°$ and $4°$ at 0.5 m. This is expected because the type of pressure gradients reverses order between these two cases. It can be seen that the $-4°$ at 0.4 m causes a larger wake than at 0.5 m but it is smaller than that is seen at $-8°$ case at 0.5 m. This pattern in the velocity profiles follows the same order seen in figure 4.3 between different cases. There is clearly a complex relationship between the wake profile and the imposed pressure gradient history. Be that as it may, the correlation between C_f and wake is consistent regardless of the history for both smooth and rough walls.

The velocity deficit profiles enable the examination of the outer wake in more detail. The results for three angles of attack are shown in figure 4.5*a*. For the $-8°$ case, there is a good collapse of the profiles between the smooth and rough wall cases. This would suggest that the integral effect of the pressure gradient and roughness on the outer region is similar to that of the smooth wall for this combination of pressure gradient history. However, no collapse occurs as the pressure gradient becomes more favourable immediately upstream of the measurement location. There is no outer layer similarity because the boundary layer growth of the rough wall is larger than that of the smooth wall. Therefore, the integral effect of roughness and pressure gradient between the smooth and rough walls are not consistent. As a result, the rough wall in the presence of an FPG just upstream of the measurement location has smaller wake strengths

	-10°	-8°	-4°	0°	4°	8°
Π SW (0.5 m cases)		1.24	1.02	0.71	0.47	0.26
Π SW (0.4 m cases)	1.83	1.54				
Π RW (0.5 m cases)		1.18	0.81	0.47	0.22	0.03
Π RW (0.4 m cases)	2.32	1.78	0.98			

TABLE 4.3: Values of Π for the different PG histories, for reference Π_{ZPG} is equal to 0.51 for the smooth wall and 0.29 for the rough wall.

(lower Π) than that of a smooth wall. Therefore, it may not be trivial to have information for a smooth wall with a given pressure gradient history (even at similar Re_τ and identical local β) and use that to infer properties of a rough wall.As suggested by Volino and Schultz (2023) and Vishwanathan et al. (2023) it appears important to match the β history to obtain complete similarity but that is almost impossible to devise in experiments (since β is an output while dP/dx is the only input). Therefore, we need new relationships that will allow us to infer information about these flows based on local measurements.

Figure 4.5*b* shows that deficit profiles (for $-8°$) collapse across different Reynolds numbers, and similar trends are observed for the other angles of attacks across smooth and rough wall cases. Based on this observation, the wake parameter, Π for each case is calculated using all available velocities for a given angle of attack. The fitting is carried out using equation 2.17, which only depends on directly measured values. The results of this fit are seen in table 4.3 for the different PG histories. The values of Π obtained with the fitting process confirm that TBLs under APG just upstream of the measurement location have larger wake strengths compared to ZPG flows. In contrast, FPGs reduce the wake strength. As shown in the deficit profiles, the wake values of the F-APG cases are similar. The variation in Π shows some interesting trends. Firstly, for 0.5 m cases, the smooth wall wake strength is always greater than the rough wall. This is despite the similar pressure gradient histories shown in figure 4.3. As explained previously, this is due to the difference in boundary layer thicknesses and the resulting acceleration of the flow. Further evidence of this is that for the ZPG TBLs, the wake strength is much higher for the smooth wall, suggesting an FPG effect.

The trends observed for the case where the wing is mounted at a distance of 0.5 m far from the wall do not occur at 0.4 m. With the aerofoil mounted closer to the wall, and so with stronger APG conditions, the smooth wall TBL exhibits a lower wake strength if compared to the rough wall velocity profiles. As shown in figure 4.3, the match between smooth and rough wall cases worsens as the pressure gradient strength increases. However, the difference suggests that the smooth wall has stronger peak pressure gradients. Therefore, one might expect the smooth wall to have a larger wake due to the APG; however, this is not what is observed. One possible explanation is that a thicker boundary layer is more susceptible to APG rather than FPG and thus results in

stronger wake strength. A Comparison of the measured skin friction compared to that predicted using the correlations of Castro (2007) is given in appendix E. These models predict the skin friction based on the roughness function, wake strength and boundary layer shape factor.

4.3.1 Skin Friction - After experiencing pressure gradient history

Most of the previous experimental studies on pressure gradient effects on TBLs over both smooth and rough walls had inferred skin friction from the velocity profiles. These methods introduce uncertainty into the measurements. Therefore, in this presented work, we aim to improve the experimental investigation by directly measuring the wall shear stress, as outlined in section 3.6. The skin friction coefficient for the smooth wall is shown in figure 4.6*a*. As expected for the ZPG smooth wall, the skin friction coefficient reduces as the Reynolds number increases (Schultz and Flack 2013). The 8° angle exhibits the strongest favourable pressure gradient just upstream of the measurement location and therefore exhibits the highest skin friction. Conversely, the -8° angle is characterised by the strongest APG just upstream of the measurement location and hence the lowest skin friction. The other angles are arranged in order of increasing angle of attack between these two cases. The ZPG case lies between the 0° and 4° cases. From figure 4.3 this might be expected since these are the mildest two cases. 0° case experiences a mild APG upstream of the hot wire while the 4° experiences an FPG region. Therefore, it makes sense that the ZPG cases fit between these two cases. These results indicate that the immediate upstream pressure gradient is more critical than those further upstream. This would indicate that any model that includes history effects should account for this variation in importance.

The rough wall skin friction coefficients, in figure 4.6*b*, do not depend on Re_x, meaning that the flow is in the fully-rough regime. For the smooth wall, the average range, defined as the average of the range-to-mean ratio was 12%, while for the rough wall, it was nearly constant at 2.4%. The order of cases observed with the smooth wall is replicated with the rough wall at the 0.5 m height for the angles tested. The ZPG case follows this trend, positioning between the 0° and 4° cases. The rough wall cases at 0.4 m show similar trends with decreasing skin friction as the angle of attack becomes increasingly negative. As expected, the -4° and -8° cases at 0.4 m have lower skin friction than the equivalents at 0.5 m since the aerofoil is closer to the surface and thus has a stronger pressure gradient history. The local skin friction measurement clearly retains the history of the PG type and strength. Furthermore, the PG type in the second half of the domain is more dominant in overall local skin friction than the PG type in the first half of the domain.

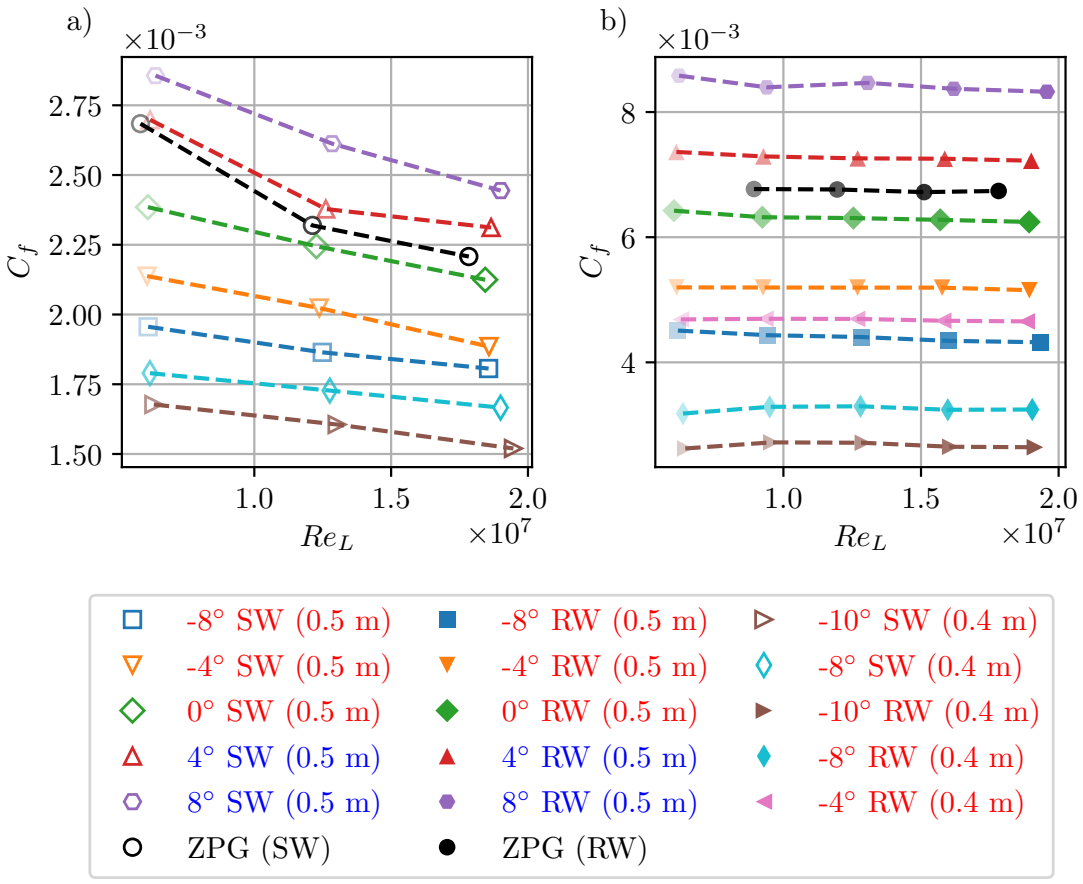

FIGURE 4.6: Skin friction coefficient one chord downstream of the trailing edge of the aerofoil for both 0.4 m and 0.5 m cases. (*a*) Skin friction coefficient for a smooth wall and (*b*) skin friction coefficient for a rough wall. The quarter chord height (h) is given in parentheses in the legend.

4.3.2 Skin friction estimation from mean flow

Direct skin friction measurements are rare, with a majority of previous studies relying on the mean velocity profile to estimate the friction velocity and, therefore, the skin friction coefficient. With the data presented in the previous sections, it is possible to discern the difference between skin friction estimation using mean flow and direct skin friction measurements. The log law fitting method for the smooth wall is a simple problem using log region in equation 2.7, where the only unknown from the raw data is U_τ. For the rough wall cases, we will use the log region in equation 2.16 assuming $y_{0_{ZPG}}$ to be the y_0 for all cases due to the very small variation. Therefore, when fitting the log law to this section, the zero-plane displacement was fixed at half the roughness height ($0.5k = 1.5$ mm), following the method used by Squire et al. (2016). This approach leaves only one unknown parameter, U_τ, which can be determined through curve fitting. Figure 4.7*a* shows the diagnostic function, defined as $\Xi = (y - d) \cdot (dU^+/dy)$. The black dashed line represents $1/\kappa$, as Ξ is equal to this value in the log region, as indicated by

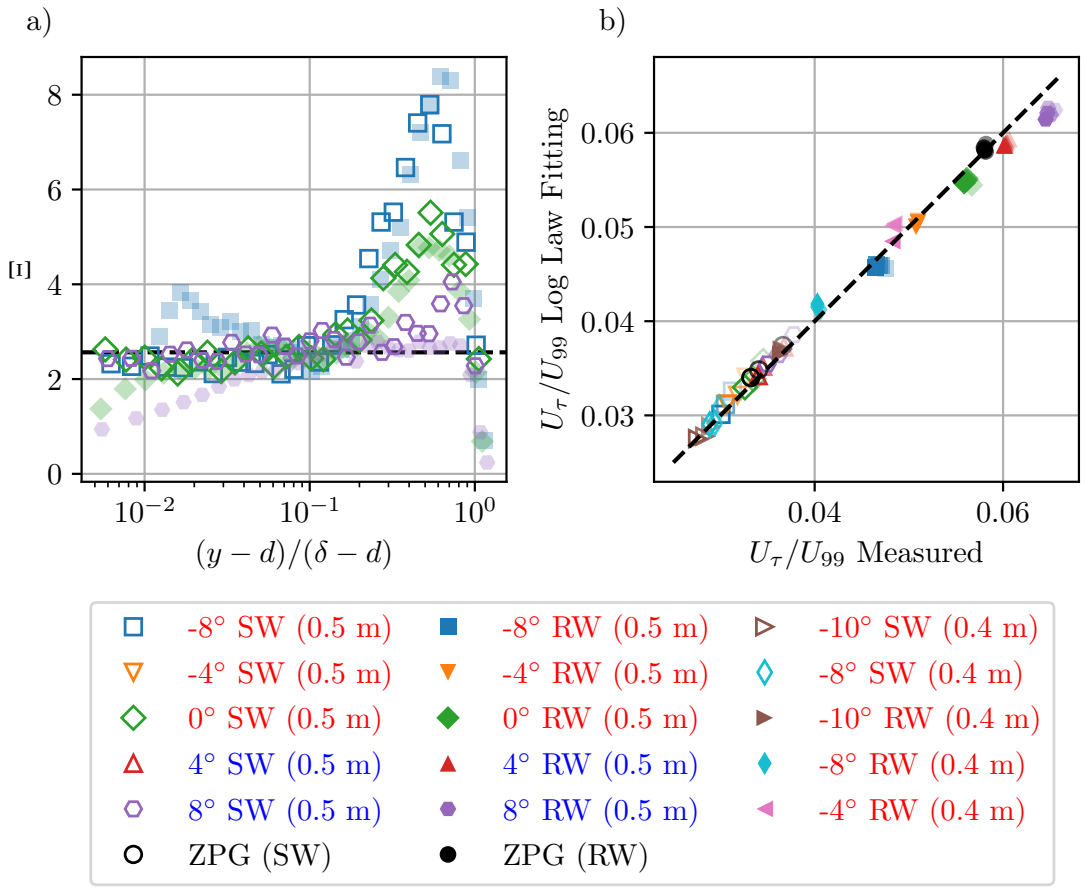

FIGURE 4.7: (*a*) Diagnostic plot showing $\Xi = (y-d)\cdot(dU^+/dy)$ for $-8°$, $0°$ and $8°$, both smooth (30 m/s) and rough wall (10 m/s) are shown at matched $Re_\tau \approx 6800-8300$. The black dashed line shows $1/\kappa$. (*b*) Comparison of U_τ/U_{99} from log law fitting vs U_τ/U_{99} from direct measurement techniques for both smooth and rough walls. The black dashed line is that of $y = x$, which would be true for a perfect prediction from indirect methods. The quarter chord height (h) is given in parentheses in the legend.

equations 2.7 and 2.16. This allows the extent of the log law to be assessed by examining deviations from $1/\kappa$. It can be seen that the smooth wall has an earlier departure from the log than the rough wall cases. Therefore, for the smooth wall cases, the log law is fitted with a minimum of seven points up to 0.15δ, while for the rough wall cases, this is extended up to 0.2δ.

Overall, figure 4.7*b* shows good agreement between the direct measurement techniques and the predicted value from the mean flow profiles. For the smooth wall cases, the error varies between 0.1% and 4.2%, while for rough wall cases, the error is between 0.6% and 4.8%. The largest percentage error for the smooth wall cases is seen for the 10 m/s cases. This was expected since the values of U_τ are the smallest. The largest error for the rough wall cases is seen in the A-FPG cases where the log law fitting method underpredicts the skin friction. These boundary layers have the longest log region and highest skin friction. Despite having a longer log region the error can be attributed to the fitting process. For consistency, the log region is assumed to end at 0.2δ; however,

as seen in figure 4.7*a*, the log region can be said to extend well into the outer region of the flow. Smooth wall data is expected to show good agreement since there is only one unknown in the fitting problem. For rough walls, the scatter is minimal since the y_0 is assumed a priori for a given surface. Otherwise, the scatter would be significantly greater as both y_0 and U_τ would need to be fitted simultaneously and are interdependent. We note that the work here shows that fitting methods do indeed work where the flow has locally reached a zero pressure gradient (i.e. relaxing flows). However, it is unclear if this is still the case when the flow is locally subjected to a pressure gradient and that requires further work.

4.4 Development of a correlation model for skin friction

Examination of mean flow characteristics indicated that the pressure gradient just upstream of the measurement location was important. The data showed the wake strength of smooth and rough walls with the same input pressure gradients are not similar. However, the roughness length in the measurement location did not exhibit any history effects and that suggests that any changes previously reported would have been due to a lack of scale separation or direct skin friction measurements. Finally, the data also showed that there is a clear correlation between local skin friction and local wake strength regardless of pressure gradient history. Therefore, it may be possible to develop a correlation model for skin friction and wake strength with some further modelling assumptions. This is explored further in this section.

We take inspiration from work of Vinuesa et al. (2017) who showed that for APG flows, the local skin friction can be predicted based on the skin friction and shape factor of ZPG flows, and the streamwise-averaged pressure gradient parameter ($\overline{\beta}$). The equations for these are given in equations 2.24 and 2.25 on just APG smooth wall flows at relatively low Reynolds numbers. It is unclear if this $\overline{\beta}$ will be feasible for flows that experience both APG and FPG (or vice versa) in succession as well as for flows with surface roughness. For experiments, it is often impracticable to obtain complete β history due to the need for many streamwise measurement stations (either for smooth or rough walls). Moreover, it is unclear if the streamwise average as proposed in equation 2.24 is sufficient to capture history effects. The previous section showed that the locations just upstream of a given point are more important than locations further upstream. Therefore, we need to revise the approach to get better skin friction models for arbitrary pressure gradient histories. To tackle this challenge, we evaluate the mean velocity profile relationships in 2.7 and 2.16 at $y = \delta$, to get U^+_{99} and this is directly related to C_f ($= 2/{U^+_{99}}^2$). The difference in C_f can then be written as follows between a PG and ZPG cases for a given surface,

$$\sqrt{\frac{2}{C_f^{PG}}} - \sqrt{\frac{2}{C_f^{ZPG}}} = \frac{1}{\kappa} ln\left(\frac{y_0^{ZPG}}{y_0^{PG}}\right) + \frac{2}{\kappa}(\Pi^{PG} - \Pi^{ZPG}) + \frac{1}{\kappa} ln\left(\frac{\delta^+_{PG}}{\delta^+_{ZPG}}\right) \tag{4.1}$$

Here, the superscript PG refers to an arbitrary pressure gradient case and ZPG is the zero-pressure-gradient case. The final term will be zero if we match the Reynolds numbers between PG and ZPG cases. This equation only depends on y_0 and Π for matched Re_τ cases. If y_0 does not change with pressure gradient as established in section 4.3, then the change in C_f is entirely due to changes in Π. It should be noted that the work of Castro (2007) developed similar correlations to obtain the skin friction of rough walls flows at ZPG conditions where he showed that $C_f = f(\theta/y_0, H, \Pi)$. In fact, the variation in local Π accounts for flows that do not satisfy outer-layer similarity. However, it is possible to interpret the relationship to be an effect of external pressure gradient history. In that case, the correlations in Castro (2007) are analogous to the relationship in 4.1. Both require knowledge of the local value of Π (in addition to the value of H and y_0) to determine the local skin friction.

The difference in skin friction from equation 4.1 is plotted against the true difference in skin friction obtained from direct measurements in figure 4.8*a* for all cases. It can be seen that there is an excellent agreement with all of the points lying along the diagonal line. Figure 4.8*b* shows the relative contribution of each term of equation 4.1 to the skin friction difference. As to be expected from the data presented in table 4.1, for a given freestream speed, the δ^+ term is negligible and is seen to only have a marginal contribution to the overall skin friction. The contribution of the y_0 difference is also very small since any difference between them is negligible. The dominant contribution is from the Π term as shown in figure 4.8*b*. Equation 4.1 therefore provides a solution to predict the skin friction increase due to an unknown pressure gradient history, if the wake strength (Π) is known.

We need to be able to predict Π from a known flow history of pressure gradients in order to determine the skin friction. Following Perry et al. (2002), the obvious parameter that can be used in this correlation is the pressure gradient parameter β. For our current problem, we cannot use β since we only have data at a single streamwise location and β at this location is zero (since local $dP/dx \approx 0$). Moreover, it will not be possible for us to evaluate $\overline{\beta}$ as proposed by Vinuesa et al. (2017) as the streamwise distribution of δ^* and τ_w is not available either (and it will not be for most studies as they are both outputs for a given dP/dx history). Therefore, we introduce a new parameter, $\Delta\beta$ that can account for the pressure gradient history. This parameter is defined as,

$$\Delta\beta = \left(\frac{\delta^*}{\tau_w}\right)_{DS} \left[\frac{1}{x_{DS} - x_{US}} \int_{x_{US}}^{x_{DS}} \left(\frac{dP}{dx}\right) w(x) dx\right] \quad \text{where } w(x) = \frac{x - x_{US}}{x_{DS} - x_{US}}, \tag{4.2}$$

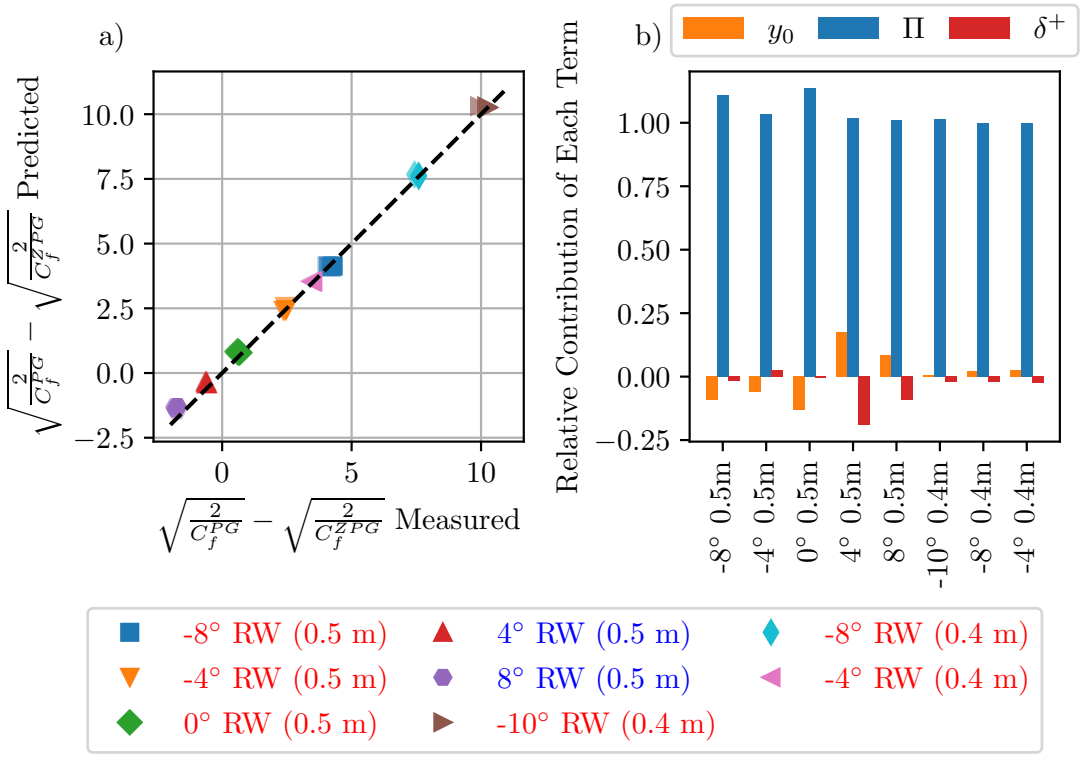

FIGURE 4.8: *a)* Predicted difference in skin friction from equation 4.1 against the measured skin friction difference for the rough wall from the drag balance for 15, 20, 25 and 30 m/s for all pressure gradient histories. The value of Π is taken from fitting the velocity profile to equation 2.7 and 2.16. The black dashed line is that of $y = x$, which would be true for a perfect prediction. *b)* Relative contribution of each term in equation 4.1 to the overall drag of the surface at 20 m/s. The quarter chord height (h) is given in parentheses in the legend.

where, $(\delta^*/\tau_w)_{DS}$ is the ratio of displacement thickness to the wall shear stress at the downstream measurement location, the integral term within $[\cdot]$ that includes dP/dx distribution and a weighting function $w(x)$ is the weighted integral of streamwise pressure gradient history between the two streamwise locations. We hypothesise that local values of δ^* and τ_w at the measurement location already have history effects incorporated in them, and it may not be necessary to include them in the integral. Since the pressure gradient history closer to the measurement station has a greater influence compared to the upstream regions, some weighting should be applied to obtain a weighted pressure gradient history. For simplicity, a linear weighting as shown in equation 4.2 is applied.

Using our experimental data for smooth walls, we develop a correlation between $\Delta\beta$ and Π for the measurement location. Figure 4.9 shows $\Pi^{PG} - \Pi^{ZPG}$ as a function of $\Delta\beta$ just for the smooth wall case. Only the 20 m/s case is plotted here while the trend appears to hold for other freestream speeds as well. The black dashed line gives the best fit linear relationship given by

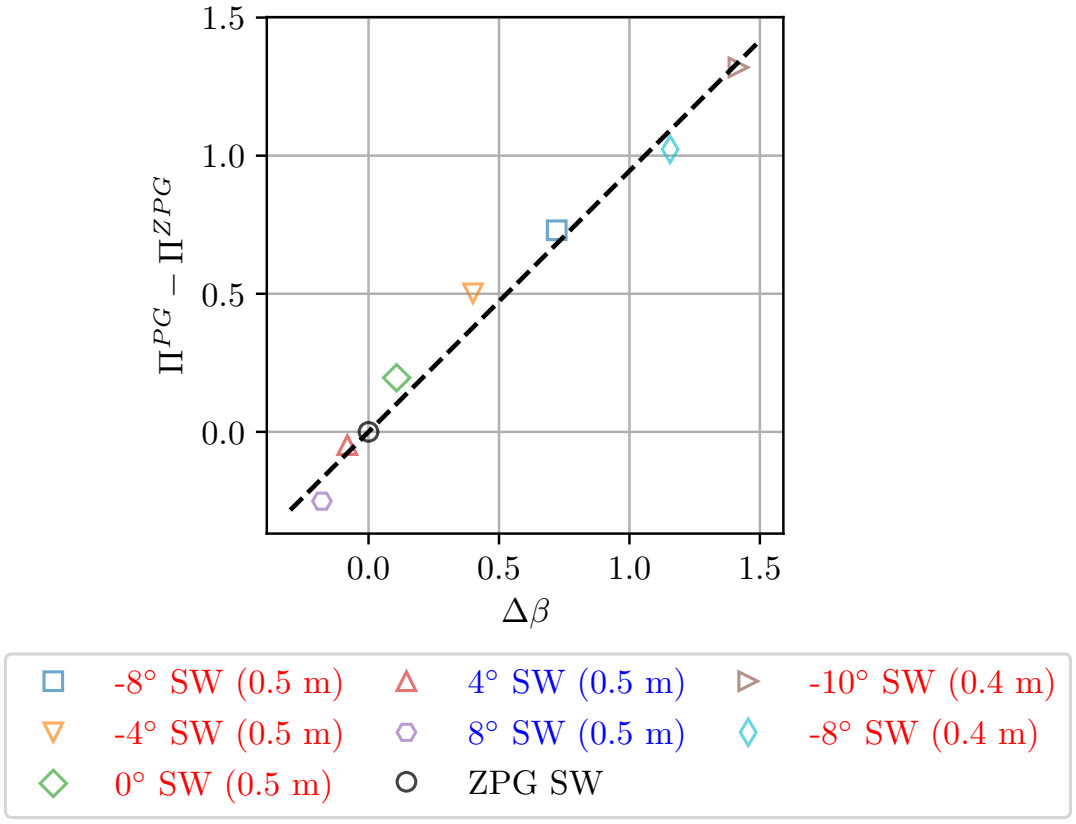

FIGURE 4.9: Difference between Π^{PG} and Π^{ZPG} for smooth wall as a function of $\Delta\beta$. Only the 20 m/s data is shown. Here the δ^* is calculated from the estimated profile with the near wall based on the Musker profile (Musker 1979) and outer wake as given in equation 2.7. The black dashed line is the best fit to the data. The quarter chord height (h) is given in parentheses in the legend.

$$\Pi^{PG} - \Pi^{ZPG} = 0.94\Delta\beta \tag{4.3}$$

This suggests that once the weighted integral of the pressure gradient history (which can be provided as an input) is known, we can infer the local value of δ^*, τ_w, and Π^{PG}. This form is different to what previous works have found such as Das (1987) who showed that local β varies as Π^2. However, this would not appear to be case for the flows considered in the current study as local $\beta \approx 0$. The work of Perry et al. (2002) gave a different functional form using a theoretical relationship, $\beta = 0.5 + A\Pi^{4/3}$ based on the attached eddy hypothesis (where the A is a constant derived from data). This relationship underpredicts the value of Π as it does not fully capture the non-equilibrium effects. In fact, Perry et al. (2002) included history effects, especially strong streamwise changes in β, through a gradient parameter ζ that captures $d\Pi/dx$. This gradient parameter, together with the evolution equations (momentum integral), can be used to predict the streamwise evolution, which can be further calibrated using experimental

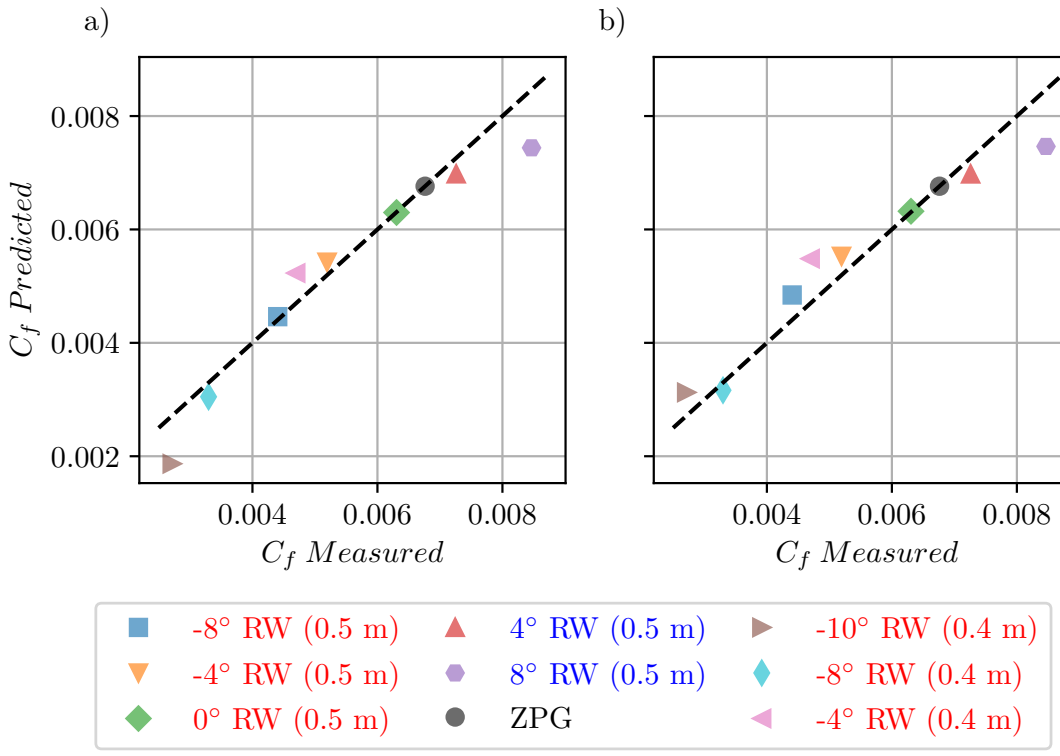

FIGURE 4.10: (*a*) Predicted value of C_f using minimisation function of equation 4.3 and the predicted fit of the velocity profile. δ^* here is provided as calculated from the hot wire velocity profile. This is compared to the measured value of C_f with the black dashed line showing $y = x$, a perfect prediction. Data shown for the 20 m/s cases. (*b*) The predicted value of C_f using the minimisation function of equation 4.3 and the predicted fit of the velocity profile. δ^* here is calculated using the velocity profile in 2.16 where the value of Π is implicitly included. The black dashed line shows $y = x$, which would be true for a perfect prediction, while the ZPG data point shows the null hypothesis. Data shown for the 20 m/s cases. The quarter chord height (h) is given in parentheses in the legend.

data. In the current work, the history effects are captured with $\Delta\beta$ through integration of dP/dx weighted by a function, $w(x)$, over a fixed streamwise distance where the pressure gradient effects are present. Changing this weighting function will result in an altered relationship between $\Delta\beta$ and Π. For example, an error function (rather than linear) that goes from 0 at x_{US} to 1 at x_{DS} (with 0.5 at the midpoint between x_{US} and x_{DS}) lead to approximately half the slope (i.e. $\Pi^{PG} - \Pi^{ZPG} = 0.45\Delta\beta$). However, it does not take away from the nature of the relationship between the two quantities. Comparing the current approach with that of Perry et al. (2002) is more involved, but the first steps towards this comparison is presented in Appendix D. Further work is required to reconcile the similarities/differences between equation 4.3 (and various different weighting functions) and the work of Perry et al. (2002) which is beyond the scope of this study.

We can test the predictive capability of the above relationship on flow over rough walls experiencing arbitrary pressure gradients, as it is clear from figure 4.8*b* that most

of the skin friction comes from the changes in the wake parameter, especially if roughness length is not altered by the pressure gradient history. Given the weighted integral of the upstream pressure gradient history (as depicted in equation 4.2), we solve equations 4.1 and 4.3 simultaneously to obtain C_f^{PG} and Π^{PG} provided C_f^{ZPG}, y_0, and Π^{ZPG} are known. Solving these equations also requires an input of δ^* or the velocity profile data at the location of prediction. Figure 4.10*a* shows the prediction of skin friction of rough walls experiencing different pressure gradients from this minimisation. The figure shows good agreement between prediction and data, demonstrating the suitability of the derived correlations for both smooth and rough walls. In fact, we can go a step further and include the calculation of δ^* as part of the minimisation process. In this case, the value of δ^* can be calculated from casting the mean velocity profile in equation 2.16 in the appropriate form for displacement thickness, and therefore it depends only on input values for ZPG case (at matched Re_τ). It is therefore possible to implicitly solve for C_f, Π and δ^* again using equations 4.1 and 4.3. Figure 4.10*b* shows that the agreement between measured and predicted skin friction using this approach and it appears to be just as good as the former (where δ^* was given as an input). Overall, this shows the merit of the derived correlation-based method for predicting skin friction of smooth and rough wall flows experiencing arbitrary pressure gradient histories. As such, this method does have some limitations. Although the local values of β over the pressure gradient history can attain large values (β up to 5 in these flows), the range of integrated pressure gradient strengths is limited (i.e $0 < \Delta\beta < 1.5$). We note that this integrated value is still higher than the local β achieved in some previous studies (Vishwanathan et al. 2023). It is also unclear if the shape of the pressure gradient history is critical for this correlation.

4.5 Summary

Single-point HWA measurements, taken one chord downstream of the trailing edge of the aerofoil with various different PG histories, have been used to assess the variation in the mean flow. Since the local conditions are approximately zero for all cases, and therefore any changes to the incoming boundary layer are due to the different PG histories. It was hypothesised that the PG type closer to the measurement location would dominate compared to the flow history further upstream. Both the skin friction measurements and the mean velocity profiles support this conclusion. They showed that cases experiencing a favourable pressure gradient followed by an APG have lower skin friction compared to cases experiencing them in the reverse order.

The velocity profiles show a clear downward shift due to the additional drag of the rough wall. There is also a larger wake for APG immediately upstream, while an upstream FPG is found to suppress the wake. A key result was that the variation in the roughness length scale y_0 is not significant. The observed difference is assumed to

be attributable to the fitting process and is thus considered invariant. Furthermore, it was seen that if y_0 is known from ZPG measurements, it is possible to predict the skin friction for the rough wall within 5%. This error is comparable to the error observed in smooth wall log law fitting. Building upon previous models from past literature, a method for the prediction of the skin friction based on a correlation between the wake strength and a weighted-averaged pressure gradient parameter, $\Delta\beta$. A linear relationship between $\Delta\beta$ and Π was seen, which, based on the smooth wall prediction, allowed prediction of the rough wall data.

Chapter 5

Pressure Gradient History Effects on Turbulence Characteristics

This chapter examines the effect of PG history on the turbulence within the flow at fixed measurement locations. The data used is from the same experiments as those presented in chapter 4, but only cases with $h = 0.5$ m are considered. First, the mean streamwise Reynolds stresses are presented for different PG histories, followed by an analysis of the pre-multiplied energy spectra for the ZPG smooth and rough wall cases. The chapter then explores the effect of PG on the different smooth wall cases. The final section compares the flow response to PG between smooth and rough walls. The chapter concludes with a discussion of the scaling of the smooth wall spectra and whether it can be used to predict rough wall flows for different PG histories. [1]

5.1 Turbulence Profiles

The influence of pressure gradient histories on mean streamwise Reynolds stress ($\overline{u'u'}$) is depicted in figure 5.1*a*. When scaled in outer units (U_∞ and δ), the FPG results in higher turbulence levels in the inner layer while the APG results in lower levels. This trend is seen for both the smooth and rough wall data sets. However, there is much more spread in the rough wall data than in the smooth wall cases. Furthermore, the rough wall has higher turbulence levels than the equivalent smooth wall case. In the outer region of the flows, the APG results in higher levels than those compared to the A-FPG cases. Previous works have shown distinct peaks in the outer region caused by APGs over both smooth and rough walls (Monty et al. 2011; Harun et al. 2013; Volino and Schultz 2023). It is seen in figure 5.1*a* that the outer peak in the rough wall is much higher than the inner peak for the -8° case. In the smooth wall case, however, the outer

[1] The work in the chapter is published in Physical Review of Fluids as Preskett et al. (2026).

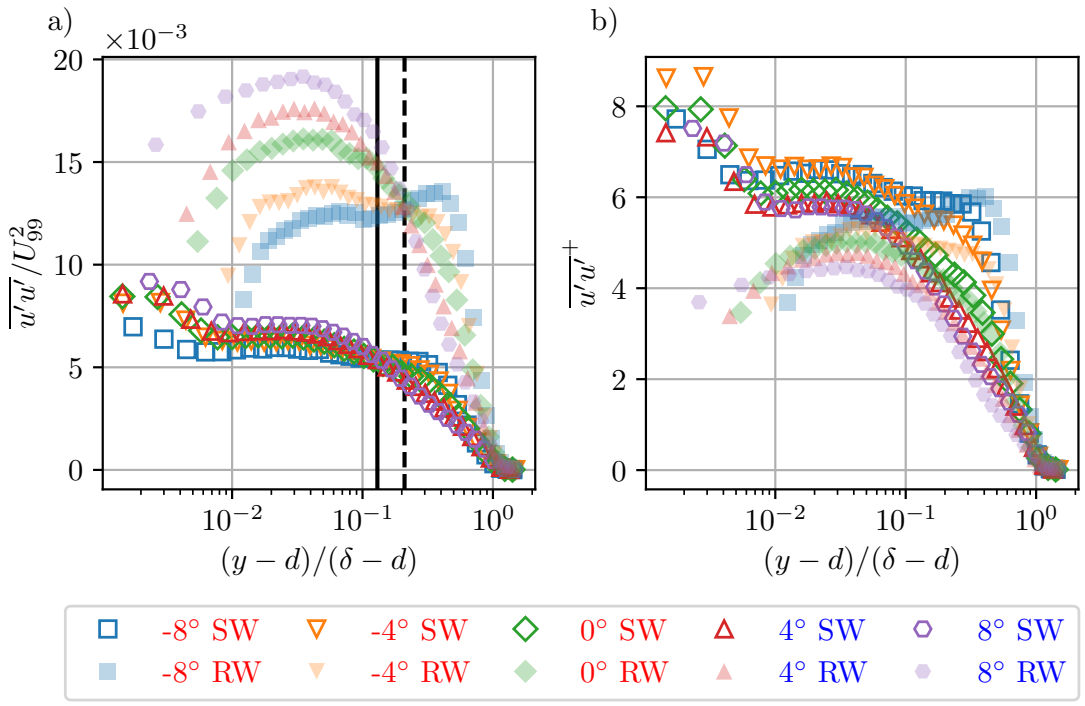

FIGURE 5.1: Variation in streamwise Reynolds stress measured at $x/c = 2$, at $Re_\tau \approx 6900 - 8300$ with *a)* outer scaling and *b)* inner scaling. Smooth wall data is taken at 30 m/s and rough wall data at 10 m/s. d is the zero plane displacement of the surface; for a smooth wall, this is zero. The black solid line is at 0.13δ and the dashed black line is at 0.21δ.

peak is less than the inner peak despite having the same pressure gradient histories. This suggests that roughness may enhance the effects of APG; this is consistent with the conclusions of previous studies (Tachie 2007).

Figure 5.1*a* shows a clear crossover point of different turbulence intensities in both the smooth and rough wall cases, shown by the solid and dashed lines, respectively. While both cases have this crossover point, they occur at significantly different positions in the boundary layer, 0.13δ and 0.21δ for the smooth and rough walls. Interestingly, the crossover is not seen with inner scaling as shown in figure 5.1*b*. This crossover has been seen on the smooth wall work of Monty et al. (2011) and Ghanadi and Djenidi (2022). In Monty et al. (2011), the crossover point is at 0.14δ, very close to the crossover found in the present study, although at a much lower $Re_\tau \approx 1900$. Monty et al. (2011) used a diverging test section to give different APG, while the present study uses rapidly changing non-equilibrium pressure gradients of both APG and FPG. This suggests that this crossover point is independent of a Reynolds number. Further evidence of this is found in this work, where the crossover point is found to be in the same place, independent of the Reynolds number, for both the smooth and rough wall cases. While the crossover point appears independent of the pressure gradient history, it is not surface independent since it lies further away from the way for the rough wall cases compared

to the smooth wall cases. The crossover point for the smooth wall lies close to the classical limit of the log region, typically defined as 0.15δ (Jiménez 2004). In appendix F, the diagnostic function shows that the smooth and rough wall crossover points lie at the end of the log region. The log region is typically used to define the limit between the inner and outer regions of the flow. The inner region of the flow is dominated by the viscous forces within the flow, while the outer region is dominated by the inertial forces within the flow. These two different regions suggest two different mechanisms present within the flow. In the outer region of the flow, the PG directly affects the structures present in this region. In the inner region, the PG history indirectly affects the structures since the PG changes the wall shear stress, which in turn changes the near-wall structures and production cycle.

Figure 5.1*b* shows that scaling is important since the conclusions made with outer scaling do not hold with inner scaling. Generally, such as in Volino and Schultz (2023), conclusions about turbulence levels are made with inner scaling. As seen in Volino and Schultz (2023) with inner scaling, FPG reduces the turbulence levels throughout the boundary layer compared to F-APG cases. With both inner and outer scaling, it is seen that within the limits imposed by l^+, the inner peak of the smooth walls is constant irrespective of pressure gradient history. With outer scaling, it was seen that roughness had higher turbulence levels; meanwhile, with the inner scaling, the opposite is seen. This means that U_τ increases more due to the roughness than the turbulence levels do. With inner scaling, it is possible to see evidence of outer layer similarity, which states that the turbulent motions in the outer region should be independent of the surface type. The degree to which outer similarity is seen varies depending on the PG history. The -4° and 0° cases show good collapse in the outer region. However, despite the -8° case being an APG case, the outer peak occurs further away from the wall for the rough wall case. The A-FPG cases show reasonable collapse in the outer region; however, this agreement reduces with PG strength.

5.2 Pre-Multiplied Energy Spectra

We now examine the pre-multiplied energy spectra where Taylor's hypothesis is used to convert time series into length scales (as per previous studies Deshpande et al. 2023 and Sanmiguel Vila et al. 2020). The wavelength, λ_x, for a given frequency, f, is given by $\lambda_x = U_c/f$. At each wall-normal location, the mean local velocity is used as the mean convection velocity, U_c, for all scales. The wavelength is related to the wavenumber, k_x, by $k_x = 2\pi/\lambda_x$. The energy for a given frequency at a given wall-normal location is calculated using the signal's fast Fourier transform (FFT). This is done using the Welch method with Hann windowing of length f_{daq}, where f_{daq} is the frequency of acquisition. A 50% overlap between adjacent windows is used when calculating the FFT. The output of the FFT results in a frequency output between 0 and $f_{daq}/2$.

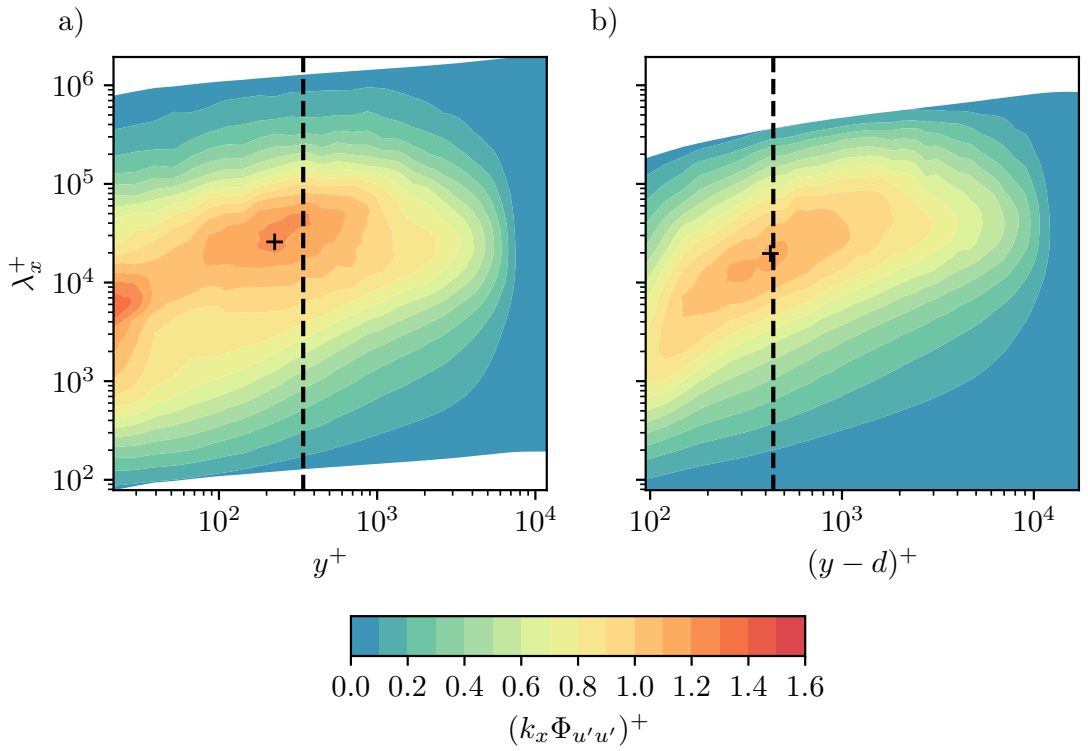

FIGURE 5.2: Zero pressure gradient pre-multiplied energy spectra for (*a*) smooth wall at 30 m/s and (*b*) rough wall at 15 m/s. The black dashed line shows the predicted VLSM peak of $3.9Re_\tau^{1/2}$ from Marusic et al. (2010a). The + shows the measured peak calculated from the pre-multiplied energy spectra.

5.2.1 Zero Pressure Gradient Spectra

Before examining the effects of roughness and pressure gradients, the ZPG spectra of a smooth wall TBL are considered first. This will serve as the baseline for the proceeding analysis. Figure 5.2*a* presents the smooth-wall pre-multiplied energy spectra for the ZPG case at 30 m/s. The spectra show clear peaks, the first being the classic inner peak around $y^+ \approx 15$. The second peak is the VLSM peak around $y^+ \approx 0.032Re_\tau$. Comparing this to figure 5.2*b* for the rough wall, where the VLSM peak occurs at a similar location of $y^+ \approx 0.028Re_\tau$. It should be noted that rough wall data is taken at 15 m/s, corresponding to an Re_τ of 12640 compared to the 7640 of the smooth wall case. While ideally Re_τ would match, this is not possible due to the lack of a 10 m/s rough wall ZPG case. The rough wall case is, however, in the fully rough regime, meaning comparisons can be made. The VLSMs seen in the rough wall flow occur at a smaller wavelength of $\lambda^+ \approx 1.3Re_\tau$, compared to $\lambda^+ \approx 4.5Re_\tau$ for the smooth wall. One factor contributing to this is that the freestream speed for the rough wall is half that of the smooth wall. This leads to a reduced convection speed and, therefore, wavelength. It is seen that the VLSMs are less energised for the rough wall flow compared to the smooth wall flow. Similar results are seen in Volino et al. (2007) and Squire et al. (2016). The roughness reduces the energy in the large-scale regions near the wall compared to that

in the smooth wall. This is due to the roughness breaking up the large-scale structures into smaller scales. This results in a curved shape to the energy distribution compared to an inclined elliptical shape for the smooth wall. It is noted that, when comparing flow spectra in this work, inner scaling is used to compare the energy between the different cases, as in Squire et al. (2016). As seen here, the inner scaling results in an energy reduction for the rough wall cases compared to the smooth wall equivalent. In absolute terms, the energy of the rough wall flows is much higher when scaled with U_{99} as seen in figure 5.1*a*, since rough wall flows have higher turbulent kinetic energy.

The work of Marusic et al. (2010a) suggested the VLSM peak should occur around $3.9Re_\tau^{1/2}$, shown by the black dashed lines in figure 5.2. The $+$ indicates the location of maximum energy as found from the pre-multiplied energy spectra. For the smooth wall case in figure 5.2*a*, there is reasonable agreement with the location of the peak. The maximum energy at the y^+ closest to the that predicted by $3.9Re_\tau^{1/2}$ is within 1% of the value of the peak shown in figure 5.2*a*. This means there is a plateau in the pre-multiplied energy spectra, and therefore accounts for the error in the measured and predicted peaks. The highest energy contour of the log region, which contains the energy peak, is bisected by the predicted from Marusic et al. (2010a). For the rough wall case shown in figure 5.2*b* shows excellent agreement between the predicted peak location and the measured peak location.

5.2.2 Effect of Pressure Gradient History

Figure 5.3 illustrates the effect of the pressure gradient history on spectral content. The first column shows the different pre-multiplied energy spectra for the five angles of attack. The second column shows the difference between the PG and ZPG cases. Throughout this work, inner scaling is used to show the effect of PG history on the pre-multiplied energy spectra. When presenting subtracted spectra throughout this work, the cases are at matched Re_τ, removing any Reynolds number effects. This means any changes are due only to the PG history. The subtraction spectra show the same effects whether plotted in inner or outer scaling; hence, inner scaling is used for consistency. Subtraction of two spectra will inherently introduce some uncertainty into the results shown. The signal has a low-pass filter applied at 10 kHz, which for the SW cases equates to $f^+ = f\nu/U_\tau^2$ between 0.13 and 0.18. The noise within the pre-multiplied spectra can be estimated based on the mean energy outside of the boundary layer, which for the ZPG is $(k_x\Phi_{u'u'})^+ \approx 0.01$. Therefore, assuming this to be a reasonable estimate for the noise level in a single pre-multiplied spectrum, the noise level in the subtracted spectra is assumed to be $(k_x\Phi_{u'u'})^+ < 0.05$. This is contained within the white contour when showing the subtracted spectra, and anything within this white region is assumed to be unaffected by the PG history. In an overall sense, it is seen

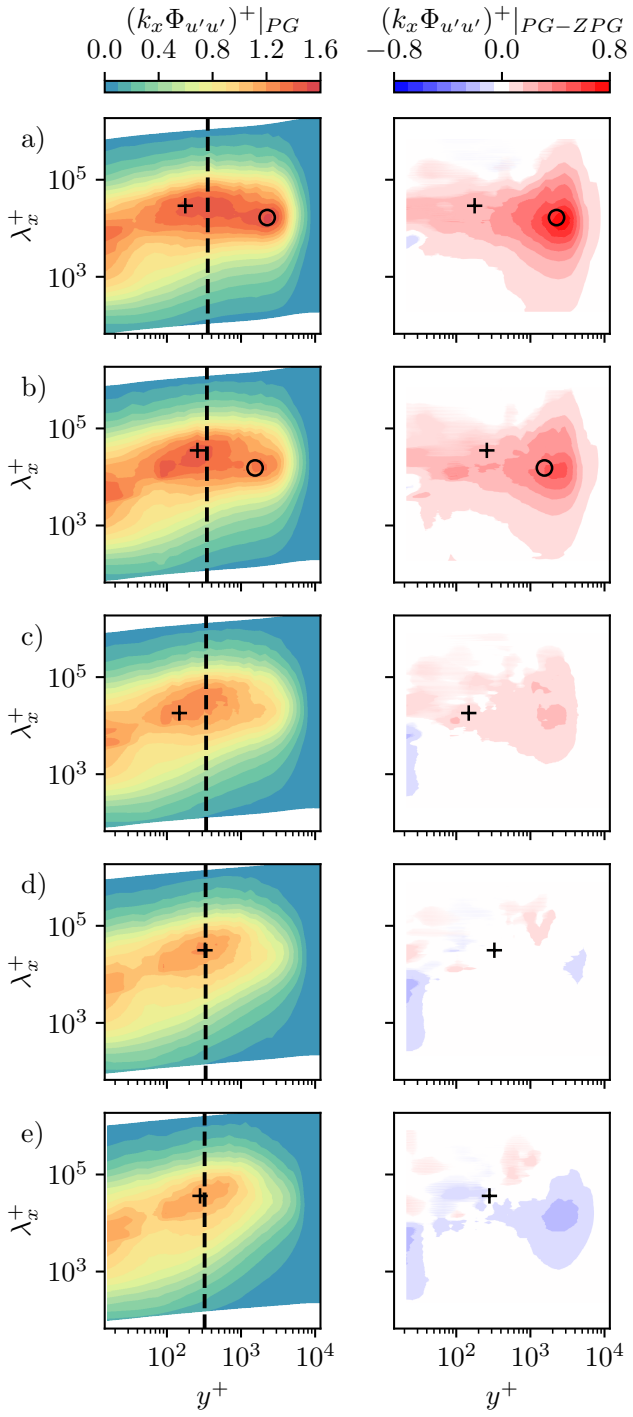

FIGURE 5.3: Smooth wall pre-multiplied energy spectra for the five different pressure gradient cases: (*a*) $-8°$, (*b*) $-4°$, (*c*) $0°$, (*d*) $4°$ and (*e*) $8°$ at 30 m/s. The first column shows the inner scaled spectra, and the second column shows the difference between the pressure gradient and the ZPG cases. The black dashed lines show $3.9Re_\tau^{1/2}$ from Marusic et al. (2010a) while the + shows the measured peak from the pre-multiplied energy spectra in the log region and o shows the measured peak in the outer region due to PG. The symbols in the second column are taken from column one to show the location of the peaks.

that APG results in higher energy in the outer region compared to the ZPG case. Furthermore, the FPG results in a deficit in the outer region compared to the ZPG case. The 4° case shows the smallest difference from the ZPG case. From figure 4.3, it can be seen that from $x/c \approx 0.6$, the PG is approximately zero. This results in the 4° case pre-multiplied energy spectra recovering to near ZPG conditions.

The ZPG showed a clear peak within the log region due to the VLSMs. Starting with the $-8°$ in figure 5.3*a*, there are three distinct peaks in the pre-multiplied energy spectra. The first two peaks are the same as those seen for the ZPG, the inner peak and the VLSM peak. The third peak is responsible for a large increase in energy seen in the outer region compared to the ZPG case. This is caused by the energisation of the large scales in the outer region as seen in Monty et al. (2011). This outermost peak occurs around $\lambda^+ \approx 2Re_\tau$ at $y^+ \approx 0.3Re_\tau$. As the APG reduces in strength by the 0° case, the outer peak has disappeared. As the PG becomes an FPG, the peak within the log region is flatter and less energetic. This results in a deficit compared to the ZPG case within the log region.

The ZPG cases showed good agreement with the results from Marusic et al. (2010a) concerning the location of the energy peak within the log region. The F-APG cases all have measured peaks, which are slightly less than the prediction of $3.9Re_\tau^{1/2}$. There is, however, no clear trend with APG strength; they are all at a lower predicted peak. In the two A-FPG cases, the prediction of the VLSM peak lies very close to the prediction, the stronger FPG being slightly less than the prediction; however, the difference is not significant. The percentage difference in the position of the peak in the FPG region is less than 15%. In contrast, in the APG region the difference is between 32% and 124%. For all cases, the maximum energy at the wall normal position closest to the predicted maximum position is within 3.1% of the actual peak value. The maximum energy along the predicted line being so close to the actual maximum suggests that prediction from Marusic et al. (2010a) holds true even with PGs.

The small scales in the inner region of the flow ($y^+ \leq 0.15Re_\tau$) are unaffected by the PG history. The limits of this region, however, do depend on both the PG type and the strength of the PG history. For the strong F-APG cases ($-8°$ and $-4°$), the wavelength below which is unaffected by the PG is $\lambda^+ \approx 0.3Re_\tau$. For the remaining three cases, the wavelength below which the inner region is unaffected is significantly higher at $\lambda^+ \approx Re_\tau$. Above these wavelengths, the difference in energy and range of wavelengths affected depends on the PG strength. In all cases, however, the peak difference in this inner region is seen around $\lambda^+ \approx 3Re_\tau$. In the outer region, the range of wavelengths affected is much larger than seen in the inner region. For the $-8°$ case, all wavelengths show differences from the ZPG case, similarly in the $-4°$ case. The 0° case has a smaller range of wavelengths which are affected since the peak APG strength is reduced. The 8° case, which is the strongest FPG case, has a much more limited range of wavelengths affected than that of the $-8°$ case.

The largest wavelengths seen in figure 5.3 is $\lambda^+ \approx 10^5$, which is at least 12δ. When constructing the pre-multiplied energy spectra, Taylor's hypothesis is used to convert from the time domain to the spatial domain. This hypothesis assumes that the turbulence fluctuations are small compared to the freestream speed at the measurement points. That assumption holds at the measurement location since locally it is ZPG. However, the resulting structures of 12δ will be developing over at least one chord of the aerofoil and therefore responding to the changes in PG history. Over this distance, the freestream speed will vary due to changes in the PG history; however, Taylor's hypothesis assumes a constant speed at a given wall normal location throughout the structure's development. Therefore, while Taylor's hypothesis provides an estimate of the wavelengths of the flow structures, their exact lengths may be affected by varying PG.

5.2.3 Effect of Roughness

The pressure gradient histories for smooth and rough walls are set to be similar for a given wing angle. Therefore, it is possible to see how roughness changes the flow response to a given PG history at approximately matched Re_τ. Building on the pre-multiplied energy spectra shown in the previous section, figure 5.4 shows both the smooth and rough wall pre-multiplied energy spectra along with the difference. The first column shows the smooth wall pre-multiplied energy spectra for the smooth, same as in figure 5.3.

The rough wall pre-multiplied energy spectra are shown in the second column of figure 5.4. The data is shown for $Re_\tau \approx 8000$ (10 m/s), which is similar to smooth wall data. It can be seen that the smallest $(y-d)^+$ varies due to the variation in zero plane displacement as shown in section 4.3. The lower freestream velocity of the rough wall results in lower wavelengths when Taylor's hypothesis is used compared to that of the smooth wall. When comparing the differences, this results in a reduced overlap area between the two cases. Looking at the rough wall overall, the effects seen with PG are the same as those on the smooth wall. There is a clear peak in the outer region in the rough wall -8° case in figure 5.4*a*. As with the smooth wall, this is the energisation of the large scales. Likewise, the smooth wall, the energy in the outer region is reduced by the presence of an FPG, as seen in figure 5.4*e* for the 8° case.

The third column of figure 5.4 shows the difference between the smooth and rough walls. Starting with the mild PG cases 0° and 4° cases, the outer region ($y/\delta > 0.15$) shows very little difference between the surfaces. As expected, the roughness changes the structure of the inner region. There is more energy on small scales for the rough wall cases. In contrast, the larger scales in the rough wall case are much less energised. This is because the roughness elements break up the large coherent structures within the flow, explaining the increase in energy of the small scales. These trends in the

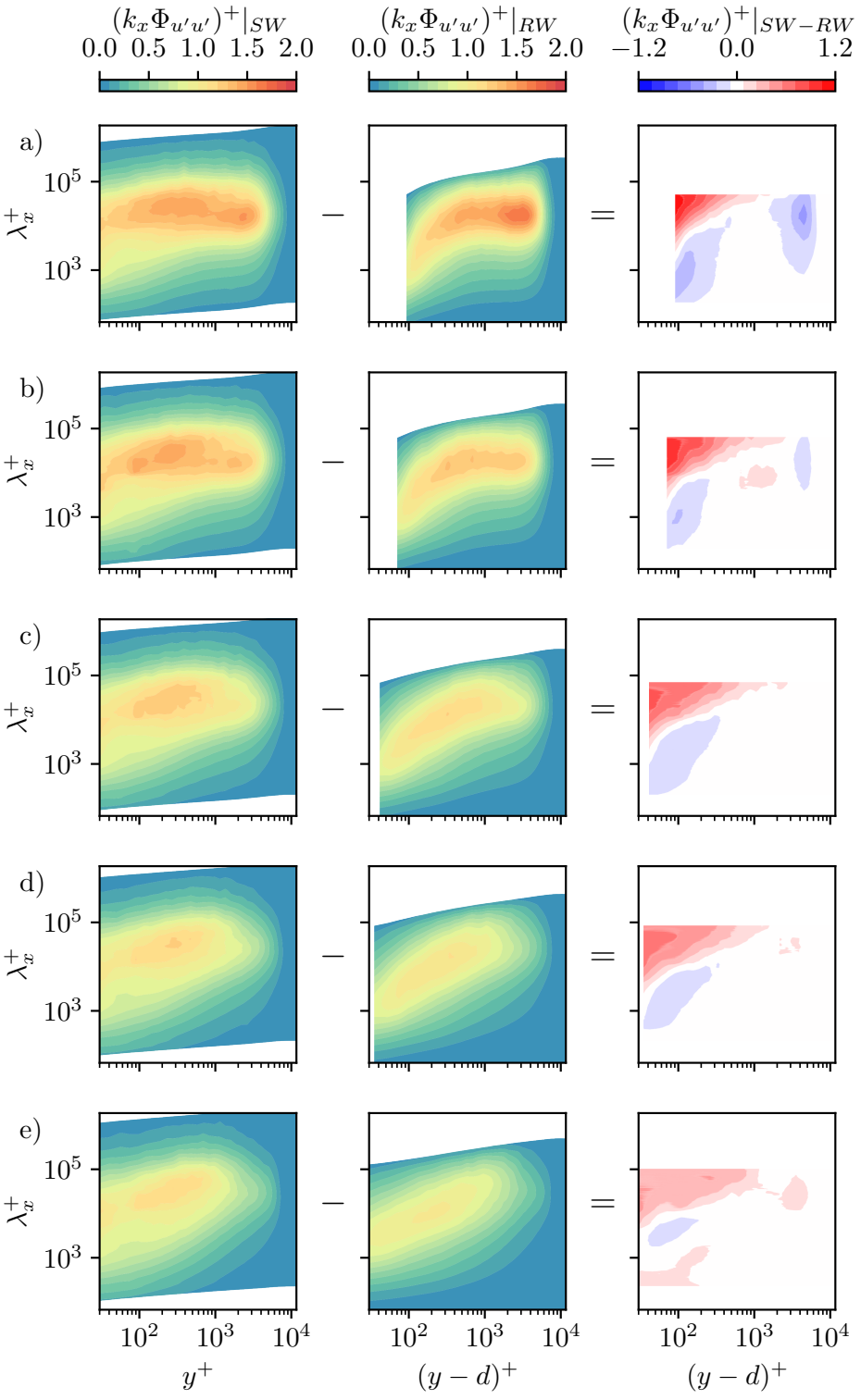

FIGURE 5.4: Smooth and rough wall pre-multiplied energy spectra for the five pressure gradient cases at similar Re_τ ($Re_\tau \approx 6800 - 8300$): (*a*) -8° , (*b*) -4° , (*c*) 0° , (*d*) 4° and (*e*) 8° . The first column shows the smooth wall pre-multiplied energy spectra at 30 m/s, the second column shows the rough wall pre-multiplied energy spectra at 10 m/s, and the third column shows the difference between the smooth and rough wall pre-multiplied energy spectra.

inner region are seen in all the cases. For a strong APG, the differences for large scales increase. As the PG becomes an FPG, the difference reduces, suggesting that APGs increase the effect of the roughness. For the small scales, the extent of the region of differences reduces in size and strength as the PG switches from APG to FPG.

The strong F-APG cases, -8° and -4° , shown in figure 5.4*a* and *b* show differences in the outer region. These cases show that the rough wall cases have more energy in the outer region at high wavelengths than smooth wall cases. This difference increases as the adverse pressure gradient increases in strength. Furthermore, the range of wavelengths affected increases, meaning smaller wavelengths are affected as the APG increases. Around $\lambda^+ \approx Re_\tau$ at $y^+ \approx 0.15Re_\tau$ for the -4° case, there is a region where the smooth wall has more energy than the rough wall. This is not seen in the other cases and is likely the result of experimental noise. This deficit is not, however, seen in the -8° case. The 8° case, which has a strong FPG, shows the smooth wall to be more energised in the outer region. This again indicates that the FPG affects the rough wall case more strongly than the smooth wall case. The centre of this deficit is centred around $\lambda^+ \approx 3Re_\tau$ at $y^+ \approx 0.4Re_\tau$. Similar trends are also seen, to a much lesser extent, in the 4° case, showing it is a function of the FPG strength.

5.3 Trends in Pressure Gradient Influence on Pre-Multiplied Spectra

This section explores the possible predictive correlations that can capture the effect of pressure gradient history on the position of the peaks within the pre-multiplied energy spectra. We first consider the location of the peak energy for different pressure gradient histories. Then, we look at the peak energy at these locations and the differences between smooth and rough wall flows.

5.3.1 Effect of Pressure Gradient History on Pre-Multiplied Spectra Peaks

We consider three regions in the pre-multiplied spectra for more detailed examination. The first of these is $y^+ \leq 50$ for the near-wall inner peak, only seen in the smooth wall cases. The second region is bounded by $y^+ > 50$ and $y/\delta \leq 0.15$ to capture the VLSM within the log region. The final region is the outer region $y/\delta > 0.15$. Figure 5.5*a* illustrates the trends for a given surface and PG history with outer scaling. The outer peak is approximately constant with the Reynolds number. The rough wall outer peak occurs further away from the wall than is seen in the smooth wall cases for a given PG history. For the strong F-APG cases, -4° and -8° cases, the outer peak moves further away from the wall as the PG strength increases. For the remaining three cases, the position of the outermost peak is approximately constant. In these cases, the location

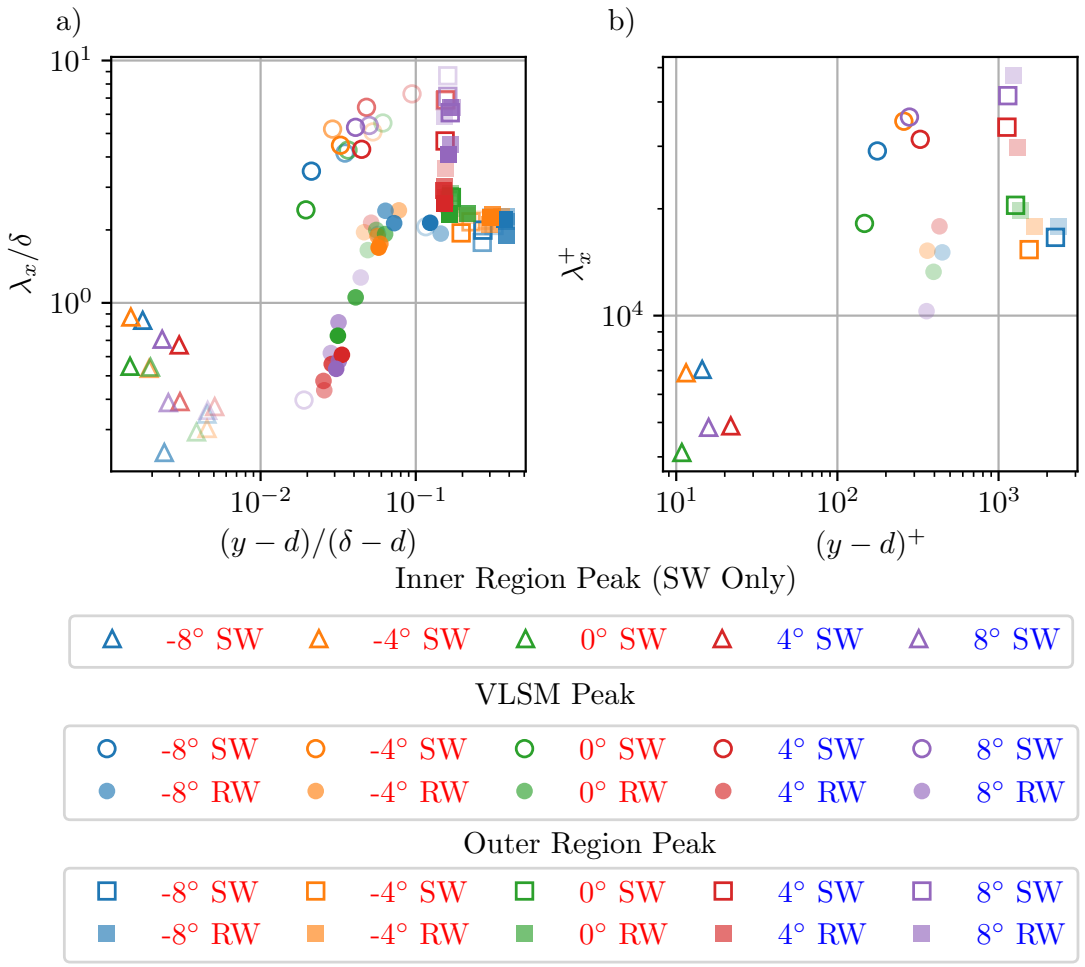

FIGURE 5.5: Variation in both the wall-normal position, y, and the wavelength, λ, of different peaks given by △: inner peak ($y^+ \leq 50$), ○: VLSM peak ($y^+ > 50$ and $y/\delta \leq 0.15$) and □: outer region peak ($y/\delta > 0.15$). (*a*) Shows the variation in the various peak positions with outer scaling for all available angles of attack and Reynolds numbers. (*b*) Shows the variation in the various peak positions with inner scaling for all angles of attack at 30 m/s for the smooth wall and 10 m/s for the rough wall ($Re_\tau \approx 6800 - 8300$). Higher opacity is used to represent a higher Reynolds number.

corresponds to the edge of the log region since there is no clear outer region peak. For the A-FPG cases, there is a much larger variation in the wavelength at which the peak occurs. The wavelength reduces as the Reynolds number increases. The cause of this is likely due to the lack of a well-defined peak in the outer region. The spread in wavelengths is much smaller for the F-APG cases, with no clear trend.

The smooth wall VLSMs occur at a higher wavelength, as seen in the ZPG pre-multiplied energy spectra. This is seen in all the PG histories. When outer scaling is used, there is a trend for the rough wall that FPG results in the VLSM peak being closer to the wall. Furthermore, the wavelength at which the peak occurs reduces with an FPG compared to an APG. This trend is not seen in the smooth wall data, where there is no clear trend. Figure 5.5*b* shows the peak locations at approximately match Re_τ,

$Re_\tau \approx 6800 - 8300$, with inner scaling. The trends in the outer region are the same as seen with outer scaling. For the rough wall, the VLSM peaks all occur around the same location, $y^+ \approx 400$. The smooth wall shows more variation in the position, although there is more variation in the Re_τ. When energy from all wavelengths is integrated, the near-wall peak value occurs around $y^+ = 15$ as shown in figure 5.1*b*. However, the peak energy location varies with PG histories. For the A-FPG cases, the peak energy occurs farther away from the wall than in the F-APG cases.

The preceding analysis focuses on the different peak locations; we move on to look at the energy at these locations. In section 4.4, we have shown that the variation in wake strength is linearly proportional to $\Delta\beta$ as given by equation 4.2. This gives a numerical way of quantifying the PG history, which can be used to compare different PG histories. As with all methods, it has limitations; for example, there is a situation where an FPG and APG follow each other such that, with weighting, the resulting value is zero. In this case, the boundary layer properties may not necessarily have recovered to the ZPG state. The previous work allowed for the prediction of a mean velocity profile; however, it does not provide any details of the turbulence within the flow. We can now look at how the energy scales with $\Delta\beta$.

The trends in the near-wall peak for the smooth wall are shown in figure 5.6*a*. There is a trend where the near-wall peak energy is enhanced by APGs and reduced by FPGs. While this trend is clear, the exact values should be taken cautiously since the l^+ values vary between 62 and 74. A higher l^+ value will result in greater spatial resolution effects, reducing the near-wall peak energy. Similar trends with peak energy are seen in both the smooth and rough wall datasets in figure 5.6*b*. It is seen that the smooth wall datasets have a systematically higher peak energy than those of the rough wall. This is expected from figure 5.1*b*, which shows the total energy at each wall-normal position being higher for the smooth wall than the rough wall. In the outer region, which is the region most affected by the pressure gradient history once again, there is a clear trend with $\Delta\beta$.

For all the peaks, the trends are approximately linear with $\Delta\beta$ within measurement uncertainty. We now focus on the outer peak since this region is dominated by PG effects compared to the near wall, which has some PG effects but mainly surface effects. In this region, it is seen that the response to a given PG history is greater for a rough wall than a smooth wall. This is based on the larger change for a given $\Delta\beta$ value for a rough wall than for a smooth wall. The rough wall has a gradient over 25% steeper than the smooth wall value. The peak energy for the smooth and rough wall cases is very similar for the median values of $\Delta\beta$.

Figure 5.3 shows the differences in the pre-multiplied spectra between PG and ZPG cases over a smooth. Section 4.4 showed that the difference in the wake strength between a PG and ZPG case can be directly modelled using $\Delta\beta$. To examine this in more

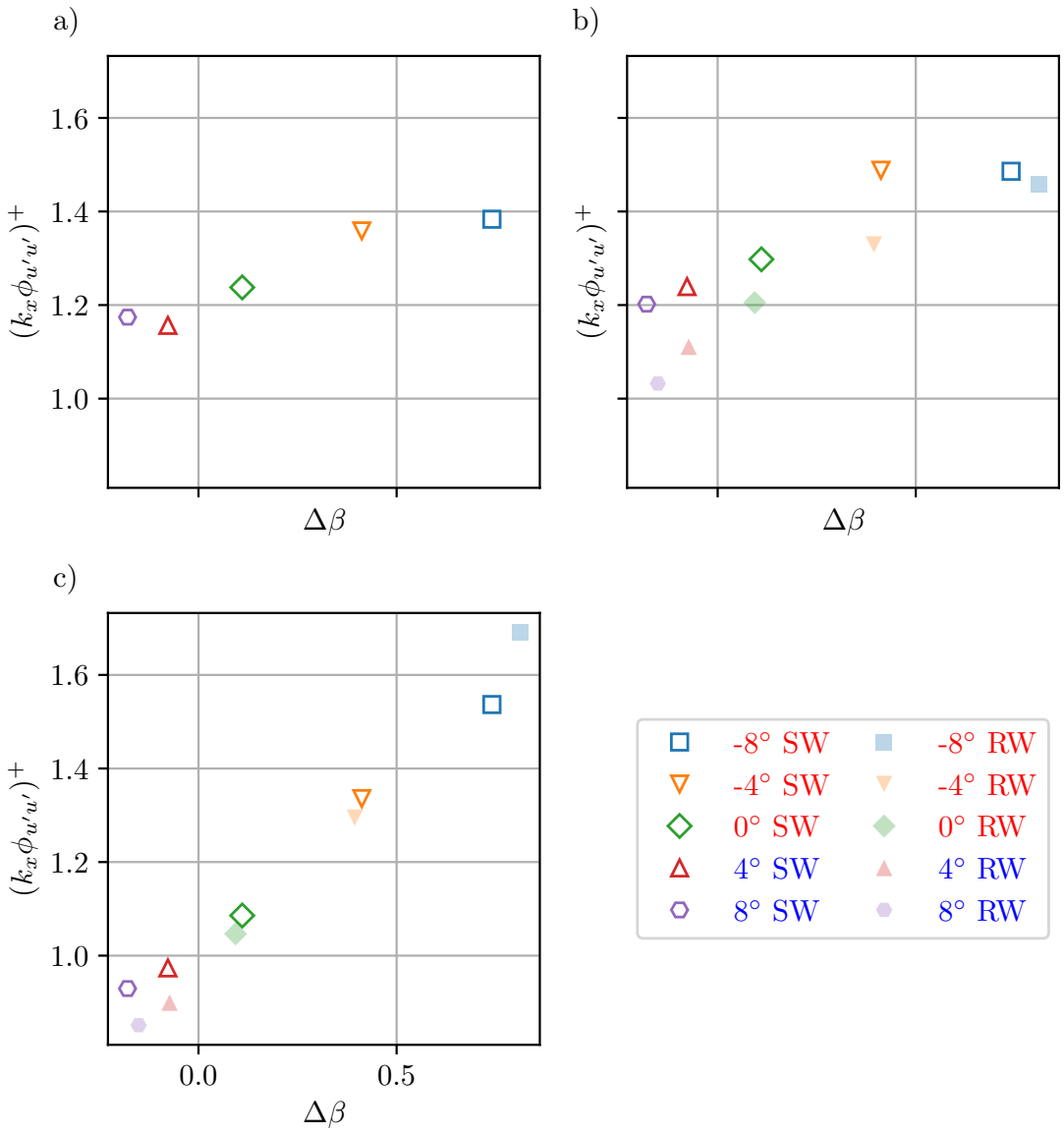

FIGURE 5.6: Variation in peak energy for peaks with inner scaling for all angles of attack at 30 m/s for the smooth wall and 10 m/s for the rough wall ($Re_\tau \approx 6800 - 8300$) for peaks shown in figure 5.5*b*. (*a*) Smooth wall near wall ($y^+ < 50$) peak energy. (*b*) Smooth and rough wall log region ($y^+ > 50$ and $y/\delta \leq 0.15$) peak energy. (*c*) Smooth and rough wall outer region ($y/\delta > 0.15$) peak energy.

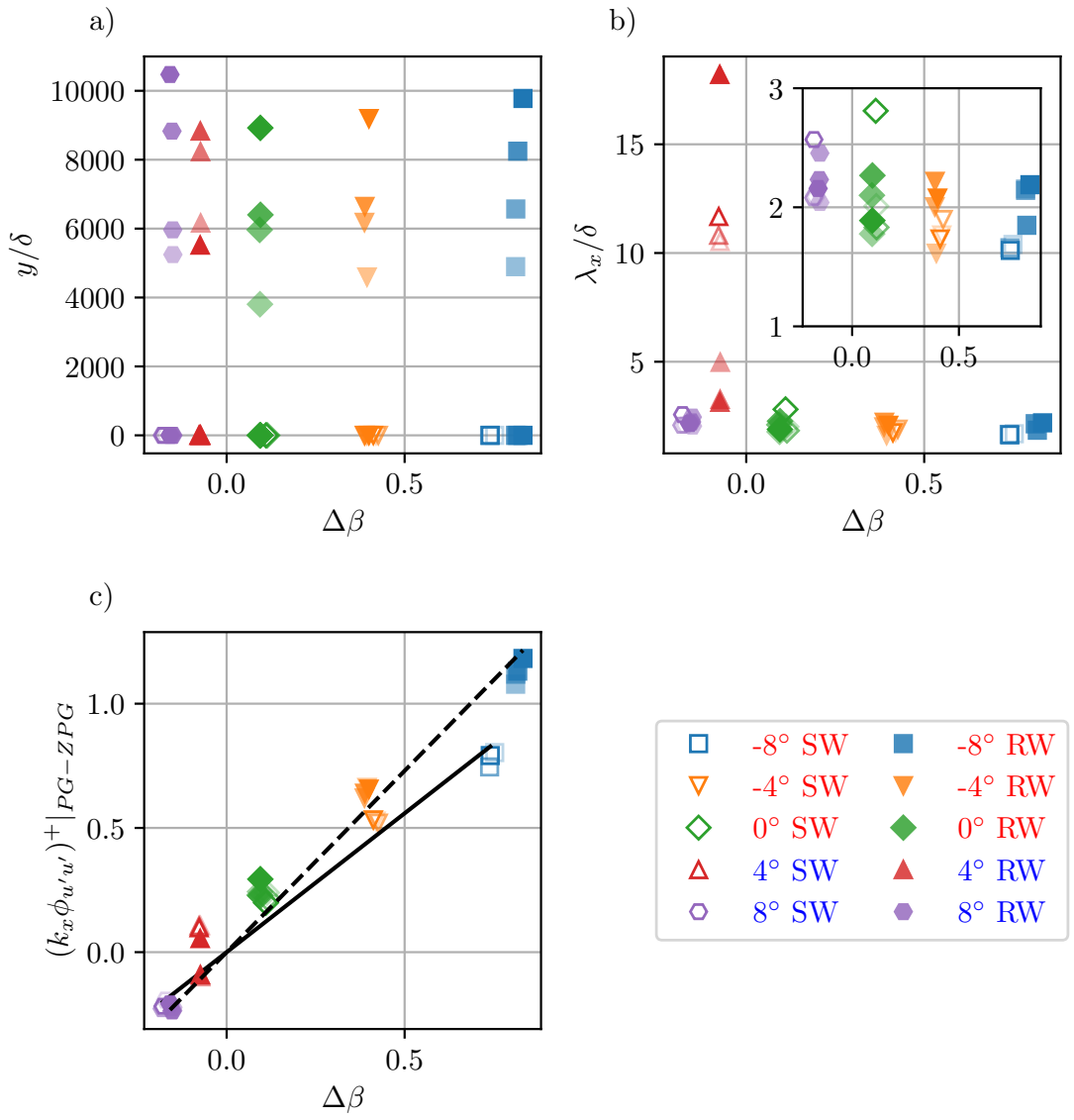

FIGURE 5.7: Variation in outer peak from $(k_x\phi_{xx})^+|_{PG-ZPG}$ for all Reynolds numbers and PG histories over both smooth and rough walls. (*a*) Variation in y/δ for outer peak, (*b*) variation in λ/δ for outer peak and (*c*) variation in $(k_x\phi_{xx})|^+_{PG-ZPG}$ for outer peak. The solid black line gives the best fit of the smooth wall data as given by equation 5.1 and the black dashed line the rough wall data as given by equation 5.2.

detail, in particular the turbulence statistics behind these variations, we shall consider the maximum difference within the outer region from $(k_x\phi_{xx})^+|_{PG-ZPG}$. First, considering the wall-normal position of maximum change in figure 5.7*a*. The majority of the cases show maximum variation between 0.3δ and 0.4δ. There are a couple of exceptions, the first being the $-4°$ case for both the smooth and rough wall. This case has a very weak PG history as shown by the small $\Delta\beta$ value and in figure 5.3*d* where the difference is seen to be minimal compared to the ZPG case. The only other major outlier is the $0°$ case, where the 10 and 30 m/s cases lie around 0.2δ.

Figure 5.7*b* considers the wavelength at which the maximum energy is affected.

There is a clear trend with the smooth and rough wall cases showing good agreement. All cases except for the 4° cases have maximum variation at $\lambda/\delta \approx 2$. There is a weak trend that the wavelength decreases slightly with APGs and increases with FPG although there is some scatter in the data points. The differences seen in the 4° cases are due to the very small differences seen between the PG and ZPG cases, see figure 5.3*d*. This is because the PG history, which in the second half of the domain, is very weak and close to ZPG, hence the recovery of the pre-multiplied spectra. Works such as Monty et al. (2011) and Harun et al. (2013) have previously noted that under APGs, the large scales increasing in energy are responsible for changes in turbulence intensity seen in APG flows. While Harun et al. (2013) showed that the energy of both the small and large scales is reduced under FPG conditions. Here, we see that the most affected wavelength is the same under both APG and FPG conditions and is surface-independent.

The final variable to consider is the trends in the peak pre-multiplied energy in figure 5.7*c*. As seen in figure 5.3, the APGs increase the outer region energy, and FPGs cause a reduction. Equations 5.1 and 5.2 show the resulting linear fit. Note that the intercept is forced to zero since for a ZPG flow, $\Delta\beta$ is zero; therefore, the energy difference should also be zero.

$$(k_x\phi_{xx})^+|^{SW}_{PG-ZPG} = 1.12 \cdot \Delta\beta \tag{5.1}$$

$$(k_x\phi_{xx})^+|^{RW}_{PG-ZPG} = 1.46 \cdot \Delta\beta \tag{5.2}$$

As can be seen, the SW data has a lower gradient than the rough wall data with a difference of 30%. The key result here is that the peak energy difference appears to be Reynolds number independent over the range of the Reynolds number tested for both the smooth and rough wall cases. Comparing the gradient of the smooth wall peak to that seen between $\Delta\beta$ and $\Delta\Pi$ from section 4.4. Section 4.4 had a gradient of 0.94 for the variation of the wake strength, which is about 15% less than the value seen here for the peak energy. While there are some differences, they are similar, which one might expect since the maximum energy change is seen in the large-scale structures.

5.4 Summary

This chapter extends the analysis of the mean flow seen previously in chapter 4 utilising the same single-point HWA measurements. Initially, the mean streamwise Reynolds stress was examined, which, with outer scaling, showed a distinct crossover point. On further examination, the diagnostic function suggests that these crossover points occur at the end of the log region. The crossover point can be thought of as the balance

between the inner and outer regions, where two different mechanisms are seen in response to the PG.

Utilising the HWA measurements over the smooth wall, it has been possible to look at the effect different PG histories have on the turbulence statistics. Examination of the streamwise pre-multiplied energy spectra shows that APG energises scales throughout the boundary layer when inner scaling is used. The largest increase compared to the ZPG is seen in the outer region of the flow. The opposite effect is seen for an FPG flow, leading to a deficit in the outer region. The effect on the near wall was seen to be less for the FPG flows than APG. Using both the smooth and rough wall pre-multiplied energy spectra at matched Re_τ allowed examination of how roughness changes as the flow responds to a given PG history. The APG was seen to have a greater effect on the outer region of the rough wall, resulting in higher energy in the outer region. Similarly, in the FPG cases, the rough wall has less energy than the smooth wall, and these effects are a function of the PG strength. Differences were also seen in the inner region, where the breakup of large-scale structures by the roughness is greater under APG than FPG flows. Differences were also seen in the inner region, where the breakup of large-scale structures by the roughness is greater under APG than FPG flows. Further analysis of the peak energy position in the outer region showed the rough wall flows' peak energy to occur further from the wall than for a smooth wall flow, independent of the PG. This outer peak was seen to move further away from the way as the APG strength increases. The VLSM peak location appears to be independent of the PG history since its position remains approximately constant when inner scaling is used.

Extending the previously seen correlations between $\Delta\beta$ and the wake strength, scaling of the outer region of the pre-multiplied energy spectra was considered. The peak energy of the outer was seen to scale linearly with $\Delta\beta$. Comparing the differences between the PG and ZPG cases, the rough wall was seen to respond more to a given PG history. When outer scaling is used, the position and wavelength at which the maximum change within the outer region is seen to be approximately constant.

Chapter 6

Pressure Gradient History Effects on Smooth Wall Flow Structures

The previous sections have focused on the mean flow and temporal response at a single streamwise location using hot wire measurements. This chapter moves on to look at the effect of PG history over a large region of interest from $x/c = -1$ to $x/c = 2$. PIV measurements were obtained using the setup given in section 3.5.1. Independent skin friction measurements over the whole domain were obtained using OFI as outlined in sections 3.6.1. First, the effect of different PG histories is considered, focusing on the mean flow. Following this, the effect of PG histories on the turbulence statistics and flow structures is explored.

6.1 Parameters

This chapter focuses on the effects of PGs on the development of a smooth wall turbulent boundary layer. Five PG histories are considered: -8° , -4° , 0° , 4° , and 8° . The quarter chord height is maintained at $h = 0.5$ m for all cases. All cases are taken at a nominal inlet speed of 20 m/s with the unit Reynolds number matched to those in chapter 4. This equates to Reynolds numbers between $6.9 \times 10^6 < Re_x < 13.1 \times 10^6$.

6.2 Effect of pressure gradient history on the mean flow

In chapter 4, velocity profiles were presented at $x/c = 2$. Using PIV measurements, it is possible to look at the development of the mean velocity field. Figure 6.1 shows the variation it U from $x/c = -1$ to $x/c = 2$. When considering boundary layer flows, the boundary layer thickness and edge velocity are often required to normalise properties.

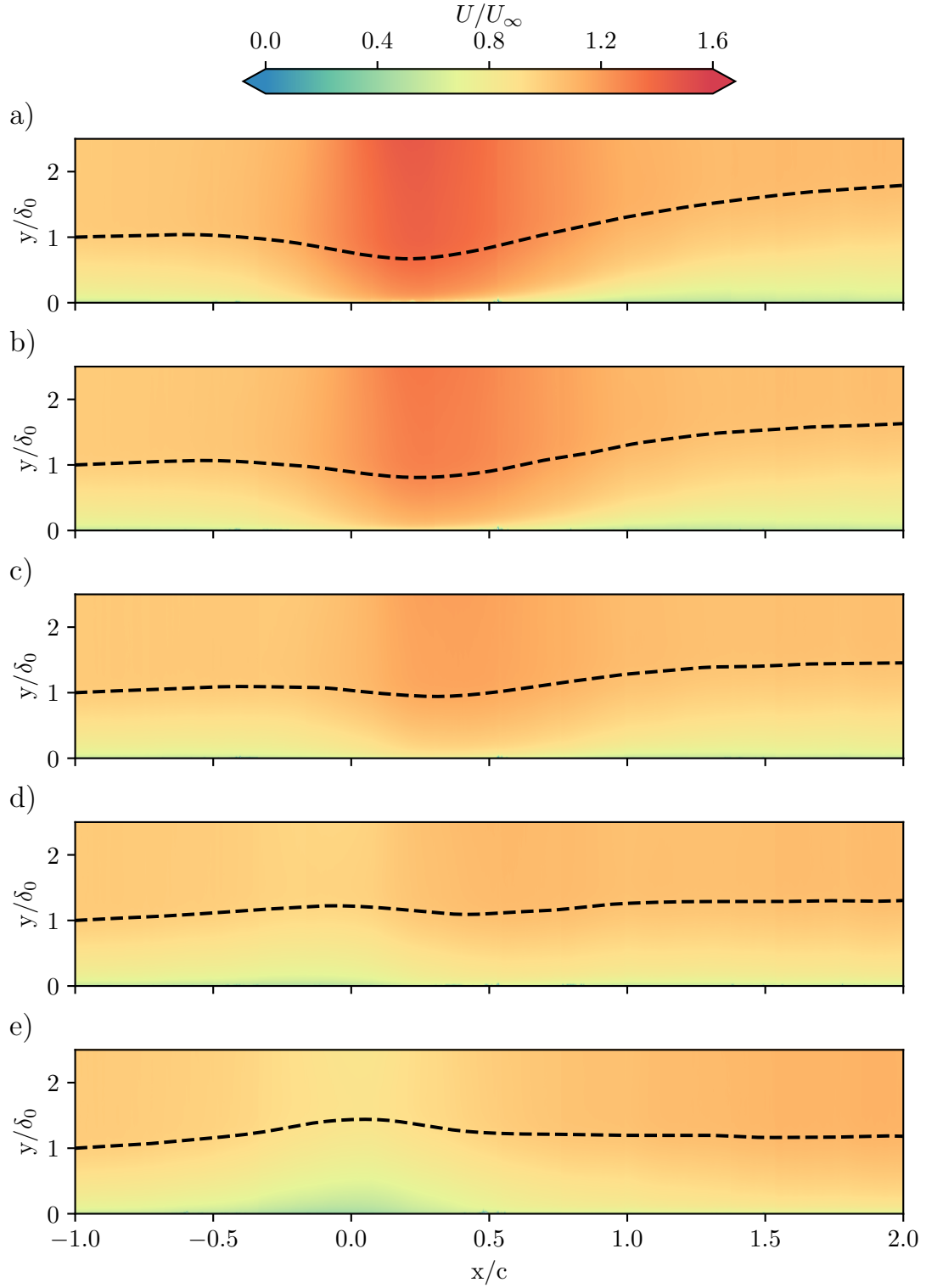

FIGURE 6.1: Smooth wall velocity field plots of the mean streamwise velocity, U/U_∞, from $x/c = -1$ to 2. U_∞ is the velocity from the pitot at $x/c = -1$. The black dashed line shows the edge of the boundary layer, δ, determined using the method described in Vinuesa et al. (2016). The five sub figures correspond to: (*a*) -8° , (*b*) 4° , (*c*) 0° , (*d*) 4° , and (*e*) 8°

	$x/c = -1$		$x/c = 2$				
	-8°	8°	-8°	-4°	0°	4°	8°
HWA δ (m)	0.075	0.078	0.138	0.130	0.117	0.106	0.099
PIV δ (m)	0.078	0.079	0.139	0.126	0.114	0.102	0.093

TABLE 6.1: Boundary layer thickness at $x/c = -1$ and $x/c = 2$ for both the HWA data, as given in chapter 4, calcualted using the point at which the $U = U_{99}$ and the PIV data as calculated using the method of Vinuesa et al. (2016).

The classical method for calculating the boundary layer thickness involves calculating the position at which the velocity reaches 99% of the freestream velocity. This is the method employed in the previous two chapters. The limitation of this method is that it requires a well-defined freestream in which the velocity can be considered constant with increasing wall normal position at a given streamwise location. As seen in figure 6.1 in regions of strong pressure gradient, such as for the -8° case in figure 6.1*a* between $x/c = 0$ and $x/c = 0.5$, there is a clear region with no well-defined freestream. Therefore, the method proposed by Vinuesa et al. (2016) is used for PIV data. This method uses the local root mean square of the streamwise velocity normalised with the local streamwise velocity and shape factor. As in Vinuesa et al. (2016), a threshold of 0.02 is used to define the edge of the boundary layer as given by

$$\frac{u_{rms}}{U\sqrt{H}} \leq 0.02, \tag{6.1}$$

where u_{rms} is the local root mean square of the streamwise velocity, U is the local mean streamwise velocity, and H is the local shape factor. The results of this process are shown in figure 6.1 by the black dashed line. As expected, it is seen that FPGs result in the suppression of the boundary layer while APGs lead to growth in the boundary layer thickness. Table 6.1 compares the classical method and that of Vinuesa et al. (2016). As can be seen, there is very good agreement between the two methods at the two points at which they are both available. The largest difference is 0.006 m, which is negligible compared to the overall thickness of the boundary layer. The average deviation with respect to the HWA values is 3%. If the threshold used in equation 6.1 is changed to either 0.01 or 0.03, the average change in boundary layer thickness is 16%. This supports the use of 0.02 as the threshold for determi the boundary layer. ning

Figure 6.2 shows the variation in U_τ/U_∞ through the domain for the OFI data taken with $U_\infty = 20$ m/s. As one would expect from the results in chapter 4, U_τ increases under FPG conditions and reduces under APG conditions. To interpolate data between the OFI data points, modified bell curves are used. These are chosen since they asymptotically approach a given value, which is required in the ZPG regions of the curve where U_τ is approximately constant.

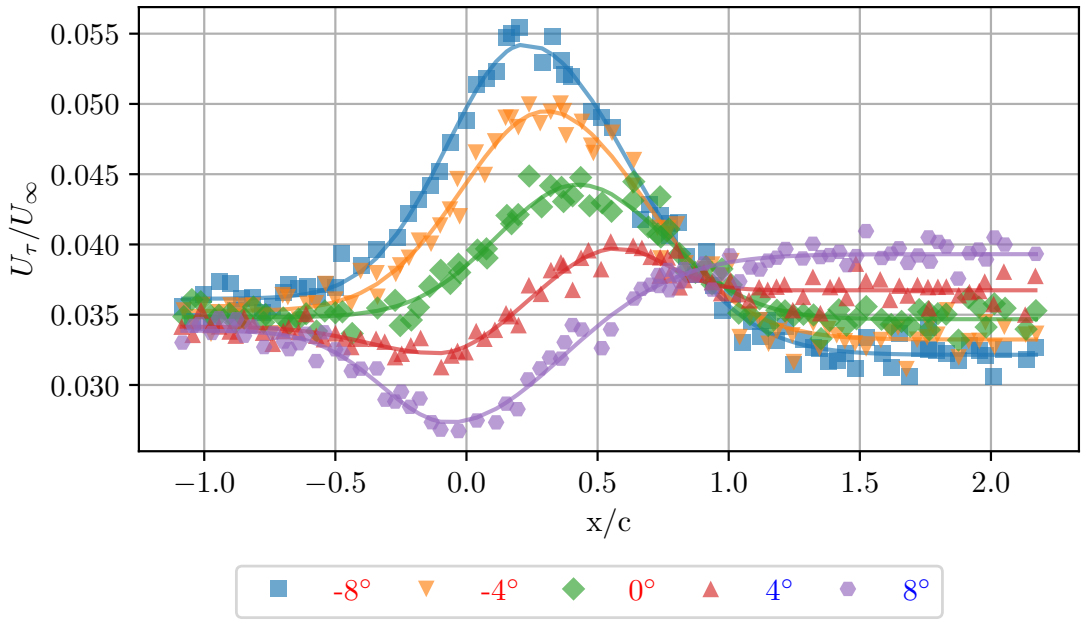

FIGURE 6.2: Variation in U_τ/U_∞ obtained using OFI at 20 m/s. The data points show the data as measured from the OFI, while the solid lines show the best fit used to interpolate the data.

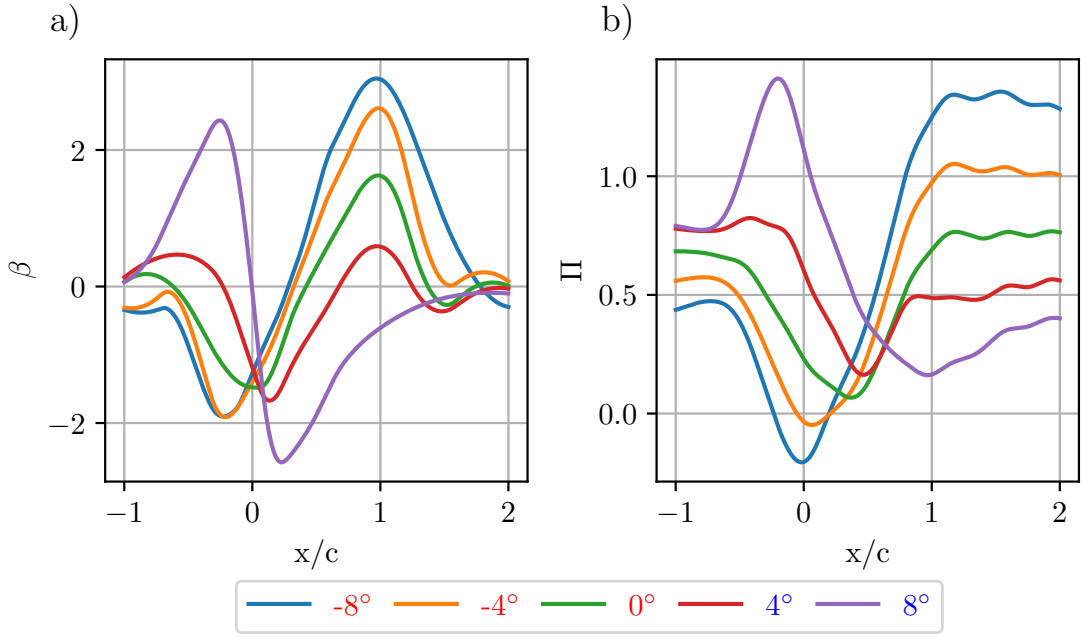

FIGURE 6.3: (*a*) Variation in β calculated from PIV and OFI data along with the PG from figure 4.3. (*b*) Variation in Π as calculated from the PIV velocity fields.

The flow history can be represented by the parameter β as was seen in equation 2.18. An estimate of the β history is presented in figure 6.3*a* using U_τ obtained from OFI from figure 6.2, along with the directly measured pressure gradient and δ^* obtained from the PIV flow fields. β is seen to vary between -2.6 and 3 over the five PG cases. All the cases start at approximately zero, as expected, since the pressure gradient history at this point is approximately zero. The shape of the β distributions follows the shape of the $dP/d(x/c)$ distribution. There are some differences, for example, there is a crossover point in $dP/d(x/c)$ seen at $x/c = 0.25$, while the crossover point in β distributions occurs at $x/c = 0$. The β history will be used to explain the trends seen in the subsequent analysis.

The first variable to consider is the variation in the wake strength at different streamwise stations. In chapter 4, the wake strength was calculated using the polynomial wake distribution as given by equation 2.8. This wake function has a drawback; the polynomial fails to capture the wake region shape for strong PG histories adequately. Therefore, as given in Volino (2020), the maximum deviation from the log law is used defined as

$$\Pi = \frac{\kappa}{2}\left(U_{99}^{+} - \frac{1}{\kappa} ln\left(\delta^{+}\right) - B\right) \tag{6.2}$$

Figure 6.3*b* shows the variation in Π for the different PG histories. Overall, as seen in chapter 4, FPGs suppress the wake strength while APGs increase the wake strength. Using a Monte-Carlo type simulation, it is possible to estimate the uncertainty in Π due to the uncertainty in the mean velocity and U_τ (estimated at 3%), which is the main contributor. The mean uncertainty is estimated at ± 0.21 for a confidence interval of 95%. This uncertainty explains the scatter seen at $x/c = -1$, where it would be expected that all cases have similar Π values since they have only experienced ZPG conditions up to this point. For the first 0.4c, there is little change in the value of Π, while changes in both $dCp/d(x/c)$ and β are seen in this region. It is also seen that after $x/c \approx 1$, there is little change in the value of Π for the cases experiencing an APG in this region (-8° , -4° and 0°). In this region, $d\beta/dx < 0$, suggesting that the energisation of the outer region structures due to the APG is large enough to resist any changes due to a reduction in APG strength. In the FPG region, after $x/c \approx 1$, some recovery of wake strength towards the ZPG value is seen, likely because the outer region structures are not as energised. It is noted that the -8° and -4° cases have similar β histories up to $x/c = 0.4$; however, the Π distributions in this region differ. The first reason is the uncertainty in U_τ, which is relatively small. The second is that the uncertainty in Π is relatively high, despite the small uncertainty in U_τ. However, it is noted that if the initial value difference is accounted for, the actual change in Π in this region between the two cases is very similar.

6.3 Examination of the $\Delta\beta$ model to predict change in wake strength

In section 4.4, a model for determining the skin friction based on wake strength was presented. This section examines the applicability of this model to the full development of the wake strength. Figure 6.4*a* shows the smooth wall variation in $\Delta\Pi$ as measured from the PIV along with the prediction based on equation 4.3, which has an integration length of L/c = 3. As can be seen, the prediction is poor with an average error of 0.20 between the measured and predicted values. This original model was based on measurements at a single streamwise location, hence the whole history was accounted for ($L/C = 3$). When developing a universal model, it is more useful to have this integration length based on a non-dimensional length. For this work, we shall choose that distance to be based on the local boundary length thickness at the point of interest. To find the distance over which the PG history needs to be accounted for, L/δ is varied to find the minimum average error over the domain. This optimisation is done simultaneously over all the smooth wall data sets. Since only the pressure gradient history from approximately $x/c = -1$ is known, and based on figure 4.3, it is assumed that $dP/dx = 0$ upstream of this point. This results in a value of $L/\delta = 21.4$ with $\Delta\Pi$ given by

$$\Delta\Pi = 0.85\Delta\beta \tag{6.3}$$

The fit coefficient is reduced from 0.94 in equation 4.3 to 0.85. The average error using this method is reduced to 0.12.

The main source of error is from regions of strong PG, and therefore the functional form of the equation is modified to include a quadratic term in the form of $\Delta\Pi = A\Delta\beta^2 + B\Delta\beta$. Using the method reduces the error to 0.09, with the optimum integration length found to be $L/\delta = 16.4$. The fit is given by

$$\Delta\Pi = -0.28\Delta\beta^2 + 0.93\Delta\beta, \tag{6.4}$$

with coefficients of -0.28 and 0.93. The results using equation 6.4 are shown in figure 6.4*b*. In regions of strong PG history, especially FPG regions, the fit still is not at an acceptable level and is seen to be larger than the uncertainty in $\Delta\Pi$. Inspiration is taken from Virgilio et al. (2025) to further reduce the model's error, and a proportional term is added. The non-dimensional PG is β, which results in a value of $L/\delta = 25.2$ with a fit equation as given by

$$\Delta\Pi = 0.02\beta^2 - 0.32\Delta\beta^2 - 0.06\beta\Delta\beta + 0.10\beta + 1.132\Delta\beta \tag{6.5}$$

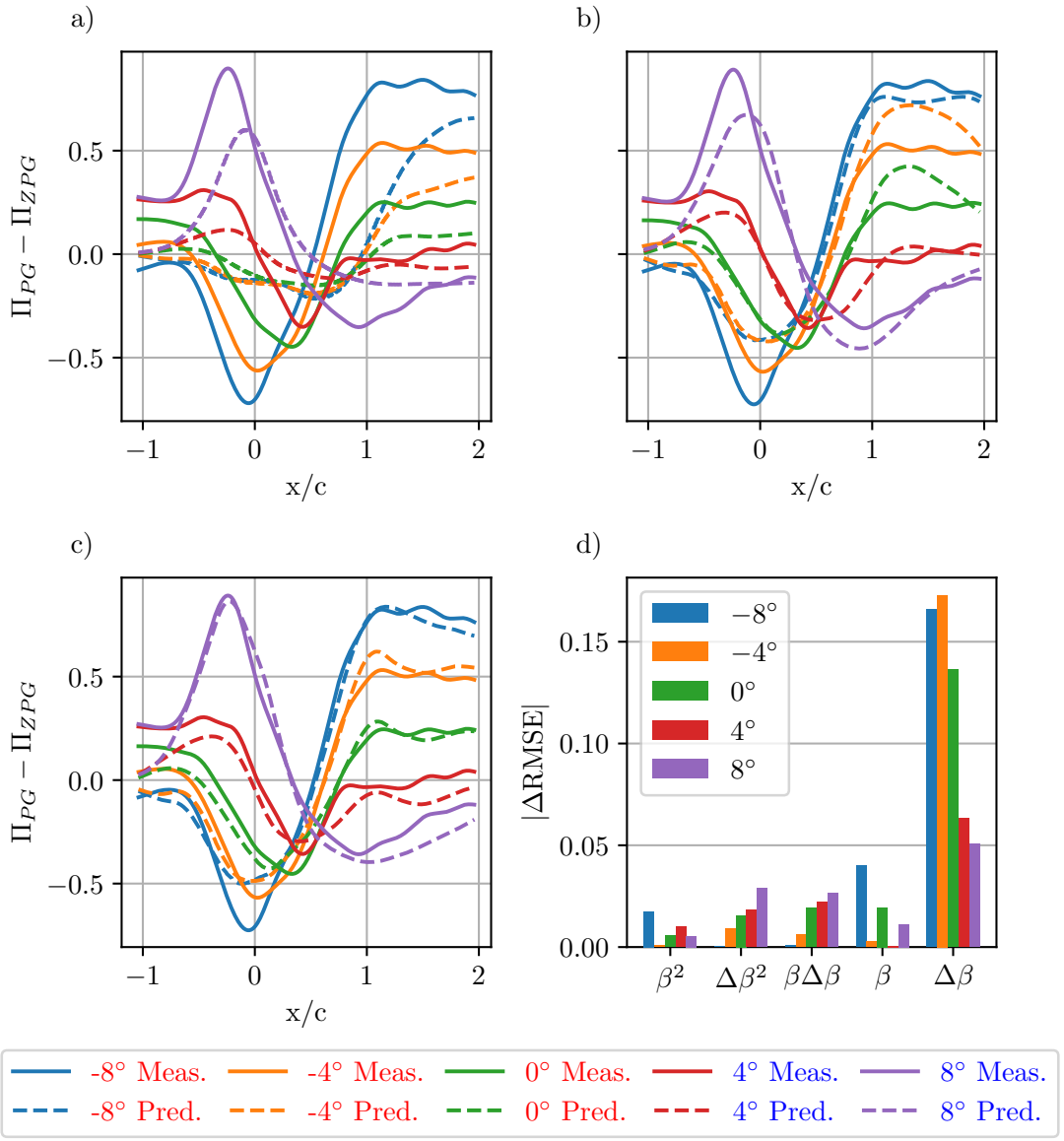

FIGURE 6.4: Variation in measured and predicted values of $\Delta\Pi$ for the five PIV smooth wall cases from different predicted models. (*a*) Prediction using equation 4.3 from chapter 4, (*b*) prediction using equation 6.4, (*c*) prediction using equation 6.5. (*d*) shows the absolute change in error based on removing and refitting equation 6.5.

The predicted values of $\Delta\Pi$ are shown in figure 6.4*c*. As can be seen, overall, there is very good agreement with the average error reduced to just 0.07. The region of largest error lies in the FPG region of the $-8°$ case being 0.23, which is similar to the uncertainty estimate in Π. Figure 6.4*d* explores the importance of each term by considering the change in the mean error when each term is removed from the equation. The integration length is kept constant at the optimum value of $L/\delta = 25.2$ found using all terms. The most important term is the $\Delta\beta$ term for all five cases since this term results in the largest change in the mean error with an average change of 0.11. This is to be expected from the work in section 4.4, which showed good agreement between the prediction and measured values using $\Delta\beta$. The least important term is the β^2, with its

removal only resulting in a change in error of 0.008. The remaining three terms have very similar mean changes in error at 0.015, an order of magnitude smaller than the change in error due to $\Delta\beta$.

6.4 Influence of pressure gradient history on turbulence statistics

In chapter 5, the effect on the streamwise turbulence statistics at a single location is discussed. This section uses both u' and v' fluctuations to explore the different events present in the TBL. Quadrant analysis is used to examine the different types of events. The method of Lu and Willmarth (1973) examines the contribution of the most significant effects present within the flow. The contribution from each region is defined, as given in Lu and Willmarth (1973), as

$$\widetilde{u'v'}_i = \frac{1}{\overline{u'v'}} \frac{1}{T} \lim_{T\to\infty} \int_0^T u'v'(t) S_i(t,H) dt, \tag{6.6}$$

where $\widetilde{u'v'}_i$ is the Reynolds shear stress contribution from the ith quadrant, $\overline{u'v'}$ is the local mean Reynolds shear stress, H is the hyperbolic hole size used to set the threshold of events, and

$$S_i(t,H) = \begin{cases} 1 & \text{if } |u'v'(t)| > H u_{rms} v_{rms} \text{ and } (u',v') \text{ is within the ith quadrant} \\ 0 & \text{otherwise} \end{cases} \tag{6.7}$$

The hyperbolic hole size H is adjusted to provide the threshold to which events are considered significant. For this work, $H = 1$ is used to set the threshold for events as in Gul and Ganapathisubramani (2021). Figure 6.5*a* shows an example $u'v'$ space for the $-8°$ case at $x/c = 2$ and $y/\delta = 0.2$. The black dashed lines show the hyperbolic hole as defined by equation 6.6. As can be seen, the two quadrants with the largest number of events in figure 6.5*a* are Q2 and Q4, the ejections and sweep events.

Figure 6.5*b* shows the variation in $\widetilde{u'v'}_2$ and $\widetilde{u'v'}_4$ across the boundary layer at $x/c = 2$. At the wall $\widetilde{u'v'}_2$ and $\widetilde{u'v'}_4$ are seen to be the same at approximately 0.5 for all cases. Higher up in the boundary layer $\widetilde{u'v'}_2$ is seen to increase. In contrast, $\widetilde{u'v'}_4$ decreases as you move further away from the wall. It can be seen that different PG histories result in different $\widetilde{u'v'}_2$ and $\widetilde{u'v'}_4$ distributions. To explore this in more detail, we shall look at $\widetilde{u'v'}_2$ and $\widetilde{u'v'}_4$ at $y/\delta = 0.2$ and $y/\delta = 0.6$ at all points in the domain.

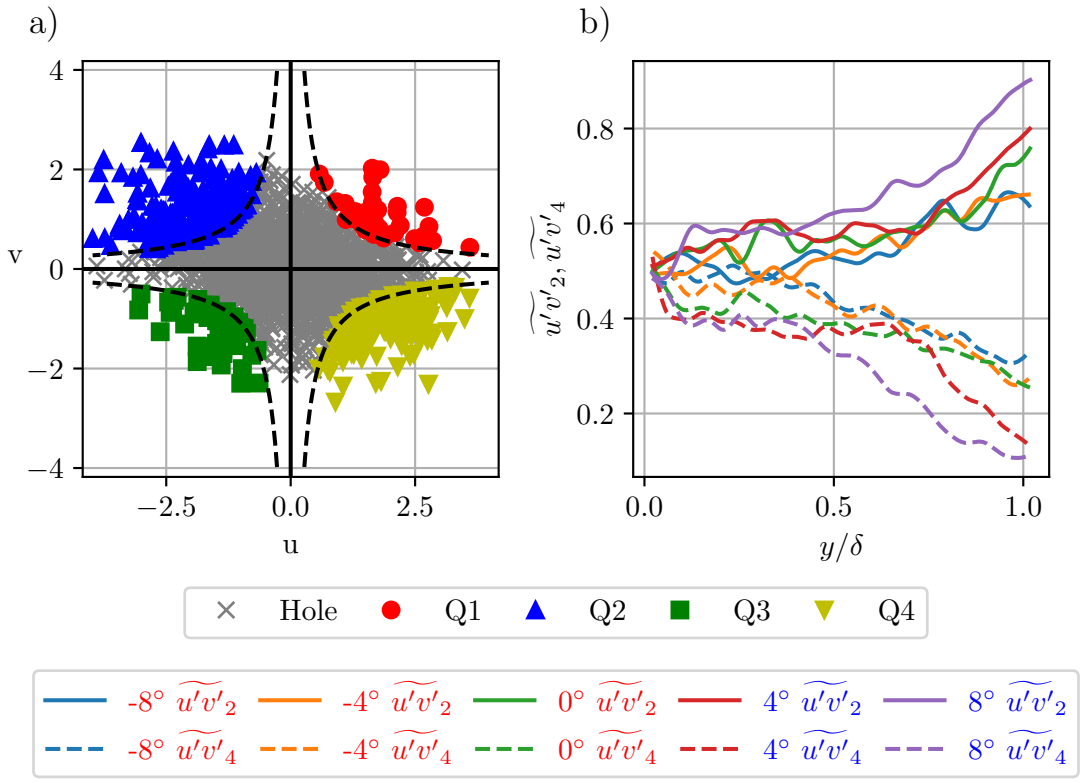

FIGURE 6.5: (*a*) Example plot of quadrant analysis using the method of Lu and Willmarth (1973) at $x/c = 2$ at $y/\delta = 0.2$, the black dashed lines show the limit of the hole as given by equation 6.7. (*b*) Shows the variation in $\widetilde{u'v'}_2$ and $\widetilde{u'v'}_4$ with distance from the wall for the five smooth wall cases at $x/c = 2$.

Figure 6.6*a* shows the streamwise variation in $\widetilde{u'v'}_2$ and $\widetilde{u'v'}_4$ evaluated at $y/\delta = 0.2$. The first observation is that there is no effect due to PG up to $x/c = -0.2$ for $\widetilde{u'v'}_2$, while for $\widetilde{u'v'}_4$, variation is seen from $x/c = -0.5$. This is the same for all cases, suggesting that sweep events are more susceptible to PG effects than ejection events. This result is independent of the PG type. At $y/\delta = 0.2$, FPGs lead to an increase in the importance of ejection events ($\widetilde{u'v'}_2$) and a reduction in the contribution of sweep events ($\widetilde{u'v'}_4$). APGs have the opposite effect, reducing $\widetilde{u'v'}_2$ and increasing $\widetilde{u'v'}_4$. At $x/c = 1.7$ for the -8° case in the region of strong APG, it is seen that the contribution of sweep events overtakes that of ejections.

Figure 6.6*b* shows the streamwise variation in $\widetilde{u'v'}_2$ and $\widetilde{u'v'}_4$ further away from the wall at $y/\delta = 0.6$. As expected from the preceding analysis, sweep events' contribution is reduced and ejections' contribution increased compared to $y/\delta = 0.2$. Overall, it is seen that the response of the flow to PGs differs from that seen at $y/\delta = 0.2$. First, considering the contribution of ejection events, it is seen that an FPG leads to a reduction, while an APG leads to an increase. The contribution of sweep events is approximately constant for all PG histories. There is a very weak trend with PG around $x/c = 1$; however, the variation is less than 10%

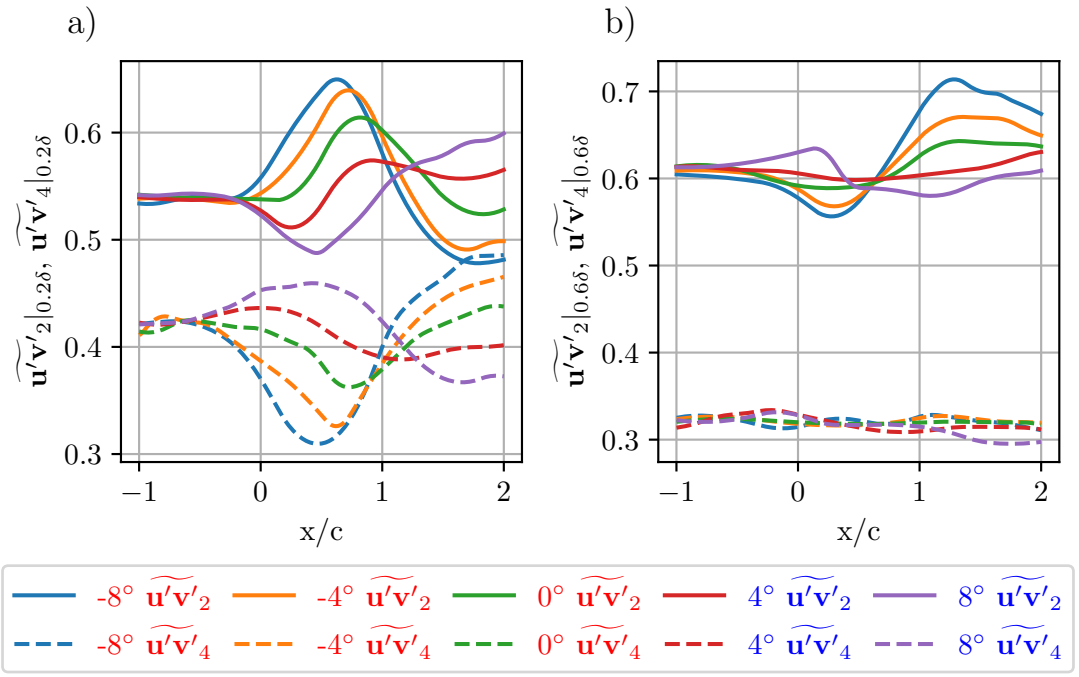

FIGURE 6.6: Streamwise variation of $\widetilde{u'v'}_2$ and $\widetilde{u'v'}_4$ for the five smooth wall cases at y/δ: (*a*) 0.2 and (*b*) 0.6.

6.5 Behaviour of internal layers in the presence of pressure gradients

Internal layers have been seen to form when the flow responds to changes in PG type. The edge of the IL is typically identified from an inflection point within the velocity profiles. The work of Antonia and Luxton (1971) identified this inflection point by plotting $y^{1/2}$ vs U. This method was taken by Parthasarathy and Saxton-Fox (2023) to calculate the edge of the IL based on the partitioning point, Δ_p. Δ_p is the point at which there is a maximum difference between the two linear slopes in fitting the U/U_{99} vs $\sqrt{y/\delta_0}$ profile. Taking this method as the basis for calculating the edge of the internal layer, the following equation is fitted between $y = 0.07\delta$ and $y = 0.3\delta$.

$$\frac{U}{U_{99}} = \begin{cases} m_1\sqrt{\frac{y}{\delta_0}} + c_1, & \text{if } \sqrt{\frac{y}{\delta_0}} \leq \Delta_p \\ m_2\sqrt{\frac{y}{\delta_0}} + (m_1 - m_2)\Delta_p + c_1, & \text{if } \sqrt{\frac{y}{\delta_0}} > \Delta_p \end{cases} \tag{6.8}$$

where m_1 is the gradient of the lower fit, m_2 is the gradient of the upper fit, and c_1 is the intercept of the lower fit with the y axis. Example plots of this fitting are shown for all cases at $x/c = 1.5$ in figure 6.7*a*. The inflection point is highlighted with a circle showing the position at which the gradient switches (Δ_p). At the edge of the IL, one would expect high Reynolds stresses due to the interaction of the two layers. Figure 6.7*b* shows the Reynolds shear stress, $\overline{u'v'}$, at $x/c = 1.5$ with the peak location

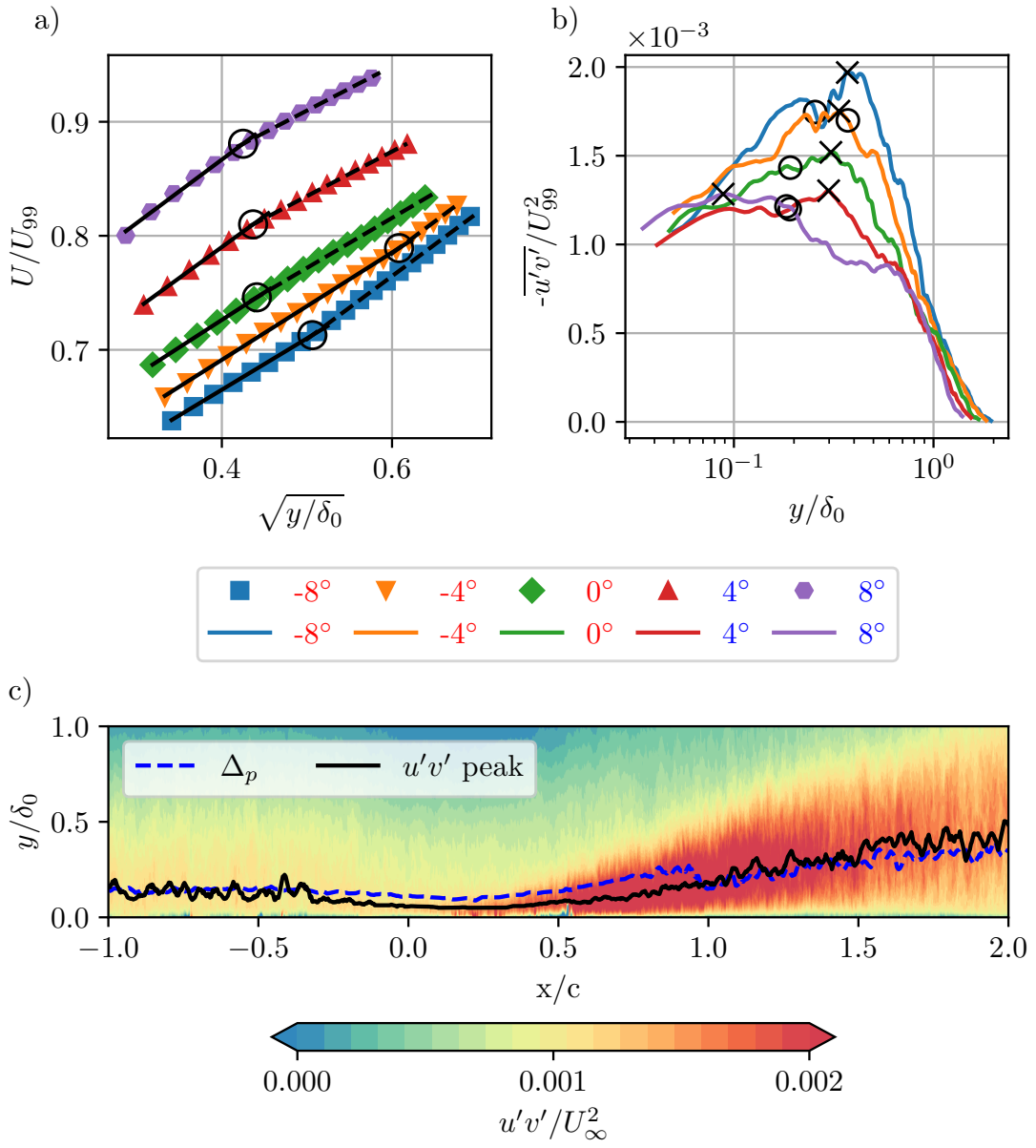

FIGURE 6.7: (*a*) Example plots used to identify the limit of the internal layer using equations 6.8, ○ identifying the inflexion point, for the five smooth wall cases at $x/c = 1.5$. (*b*) Plots of $-\overline{u'v'}/U_{99}^2$ at $x/c = 1.5$ for the five smooth wall cases with the maximum $|\overline{u'v'}/U_{99}^2|$ marked using a × and ○ using equations 6.8. (*c*) Streamwise variation in the edge of the internal layer, the black dashed line using the method from equations 6.8 and the solid black line the maximum of $|\overline{u'v'}/U_{99}^2|$ for the $-8°$ smooth wall case.

identified by the black crosses for each case. There is reasonable agreement between the two methods at this position, with an average difference of less than 10% of δ_0 between the two methods at the given point.

Figure 6.7*c* shows the variation in the edge of the IL as identified by both methods. There is good agreement between the two methods across the domain, especially in the IL from $x/c > 1$. The mean difference between the two methods is $0.05\delta_0$, which is

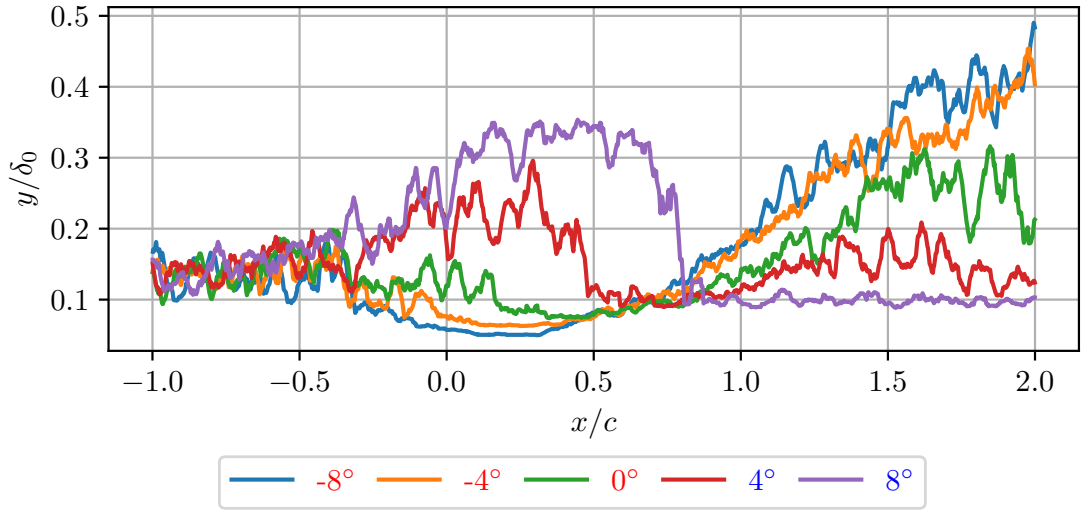

FIGURE 6.8: The variation in the edge of the internal layer as defined using the position of maximum $|\overline{u'v'}|$ for the five smooth wall cases.

negligible. The IL is only present in the APG region of the flow from $x/c > 0.5$ since the FPG suppresses the IL. To extend this analysis to the other cases, only the peak $|\overline{u'v'}|$ position shall be used to explore the development of the IL.

Figure 6.8 shows the edge of the IL and how it varies with streamwise position. In FPG regions, the boundary layer suppression means the y/δ_0 of the peak location of $\overline{u'v'}$ is approximately constant. In regions of strong FPG, the $-8°$ and $-4°$ cases show some reduction in the y/δ_0 at which the peak location occurs. In APG regions, independent of whether it follows a ZPG or an FPG region, clear growth of the IL is observed. The $4°$ and $8°$ cases are the first two cases to experience an APG, and the growth rate depends on the APG strength. A stronger APG results in a faster growth rate of the internal layer. This trend is also seen in the $-8°$, $-4°$ and $0°$ cases. This result supports the conclusion of Parthasarathy and Saxton-Fox (2023), who showed that the growth rate is linearly proportional to the average PG strength.

The $4°$ and $8°$ cases both show clear regions in which the IL is seen to collapse. In both cases, the collapse happens over approximately $\Delta x/c \approx 0.2$, for the $4°$ case it starts at $x/c \approx 0.3$ and for the $8°$ case at $x/c \approx 0.65$. The $8°$ case collapses to a constant value of $y/\delta_0 = 0.1$ since the FPG suppresses the boundary layer. The $4°$ case shows some small growth of a second IL due to a secondary weak APG region between $x/c = 0.6$ and $x/c = 1.2$. The $4°$ case collapses first since the PG type switches at $x/c \approx -0.2$ while the $8°$ case switches at $x/c \approx 0$. The lag from the PG switching to the IL collapse is slightly higher for the $8°$ case. One possible reason is that the thicker boundary layer contains larger, more energised structures, which take longer to respond to the change in the PG. This results in a thicker boundary layer for the $8°$ case, likely contributing to IL surviving longer than the $4°$ case.

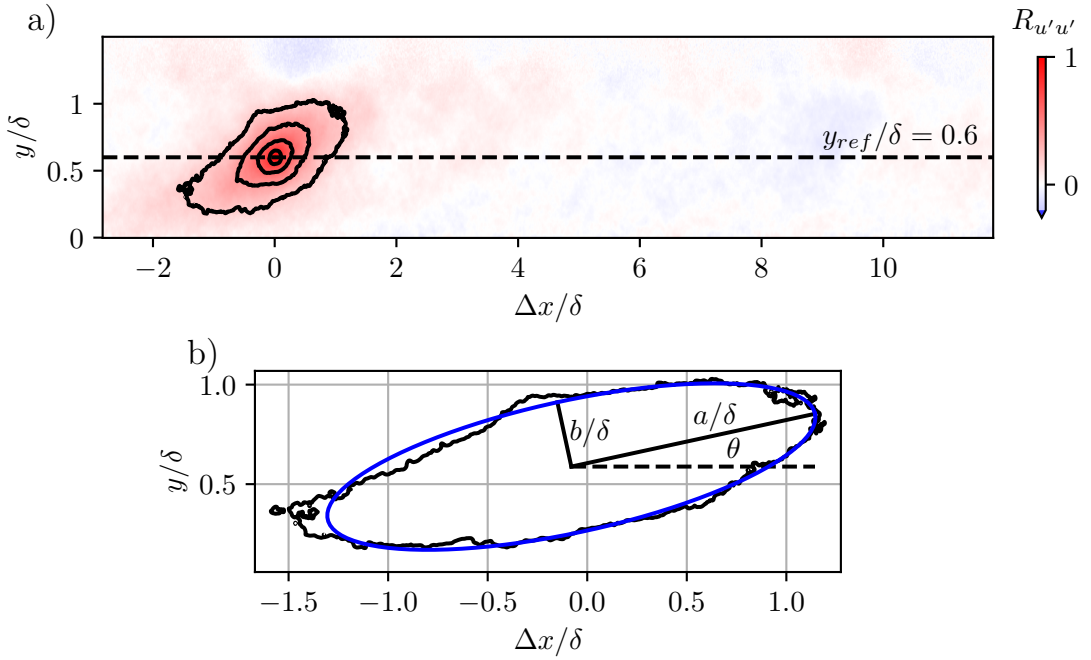

FIGURE 6.9: (*a*) Example $R_{u'u'}$ correlation field with contours of level 0.2, 0.4, 0.6 and 0.8 shown with $x_{ref}/c = -1$ and $y_{ref}/\delta = 0.6$. *b* 0.2 level contour from (*a*) with ellipse fitted using equations 6.10 and 6.11 with the major axis (a/δ), minor axis (b/δ) and inclination θ shown.

6.6 Evolution of flow structures in response to pressure gradients

The review of previous literature in section 2.5 highlighted the variation of structures due to both surface and PG history. When considering flow structures, two-point spatial correlation is often used to look at the shape of these structures (Volino et al. 2007; Volino 2020; Gul and Ganapathisubramani 2021). Two-point spatial correlation coefficient, $R_{u_1'u_2'}$, is defined by

$$R_{u_1'u_2'} = \frac{\overline{u_1'(x_{ref}, y_{ref}) u_2'(x_{ref} + \Delta x, y_{ref} + \Delta y)}}{\sqrt{\overline{u_1'^2(x_{ref}, y_{ref})}\ \overline{u_2'^2(x_{ref} + \Delta x, y_{ref} + \Delta y)}}}, \tag{6.9}$$

where u_1' and u_2' are the velocity fluctuation components at the point of interest, x_{ref} and y_{ref} are the reference coordinates from which the correlations are computed, and Δx and Δy are the spatial offsets from the reference point to the location where the correlation coefficient is evaluated.

Figure 6.9*a* shows an example correlation field for the $-8°$ case with the reference point taken at $x_{ref}/c = -1$ and $y_{ref}/\delta = 0.6$. The correlation coefficients are calculated over the stitch FOV, consisting of four cameras, approximately 1.2 m long for the

smooth wall cases. Contours levels of 0.2 to 0.8 in steps of 0.2 are shown in figure 6.9*a*. It can be seen that a contour level of 0.2 encloses a relatively large area, whereas a level of 0.8 corresponds to a much smaller enclosed region. Therefore, in this work, we shall use a contour level of 0.2 to represent the large-scale coherent structures present within the flow. A contour level of 0.6 is chosen to represent the small-scale coherent structures. This was selected from over 0.8 since very high correlation levels result in small, near-circular structures, making determining their properties difficult with acceptable uncertainty. The large-scale structure in figure 6.9*a* extends 1.6δ upstream of the reference point and -1.2δ downstream. In contrast, the small-scale structure extends only 0.3δ upstream and downstream of the reference point.

Figure 6.9*b* shows the 0.2 level contour as shown in figure 6.9*a* but plotted on scaled axes. As can be seen, the contour has an approximately elliptical shape. Taking each contour of interest, it is possible to fit an ellipse as described by equations 6.10 and 6.11.

$$x = x_0 + a\cos(t)\cos(\theta) - b\sin(t)\sin(\theta) \tag{6.10}$$

$$y = y_0 + a\cos(t)\sin(\theta) + b\sin(t)\cos(\theta) \tag{6.11}$$

$$\text{where } t \in [0, 2\pi]$$

where x_0 and y_0 are the ellipse's centre as determined by fitting, a is the major axis, b is the minor axis and θ is the inclination of the ellipse. These three parameters can be used to estimate the variation in flow structures due to the PG history. The major axis shall represent the streamwise extent of the flow structures, while the minor axis represents the wall-normal extent of the structures. It is noted that other works, such as Christensen and Wu (2005), have calculated the streamwise extent as twice the distance from the reference point to the most downstream point of the given contour. For the wall normal extent, the distance is calculated based on the difference between the point nearest and farthest away from the wall. However, as noted by Volino et al. (2007), this method is limited to reference points greater than $y_{ref}/\delta > 0.2$ due to the contour merging with the wall. Therefore, the ellipse is fitted to estimate both these dimensions and the inclination in one simplified shape.

Figure 6.10 show example correlation fields for three angles of attack (-8° , 0° , 8°) at four streamwise positions ($x_{ref}/c = -1$, $x_{ref}/c = 0$, $x_{ref}/c = 1$ and $x_{ref}/c = 2$). It is observed that at $x_{ref}/c = -1$, the contours are similar, as the flow has only experienced ZPG conditions up to this point. This is true across both contour levels plotted, representing the small and large-scale structures. Moving downstream to $x/c = 0$ there are clear differences seen in the contours as expected from section 2.5. It is observed that an FPG leads to elongated structures, as shown in the -8° case. In the 8° case at

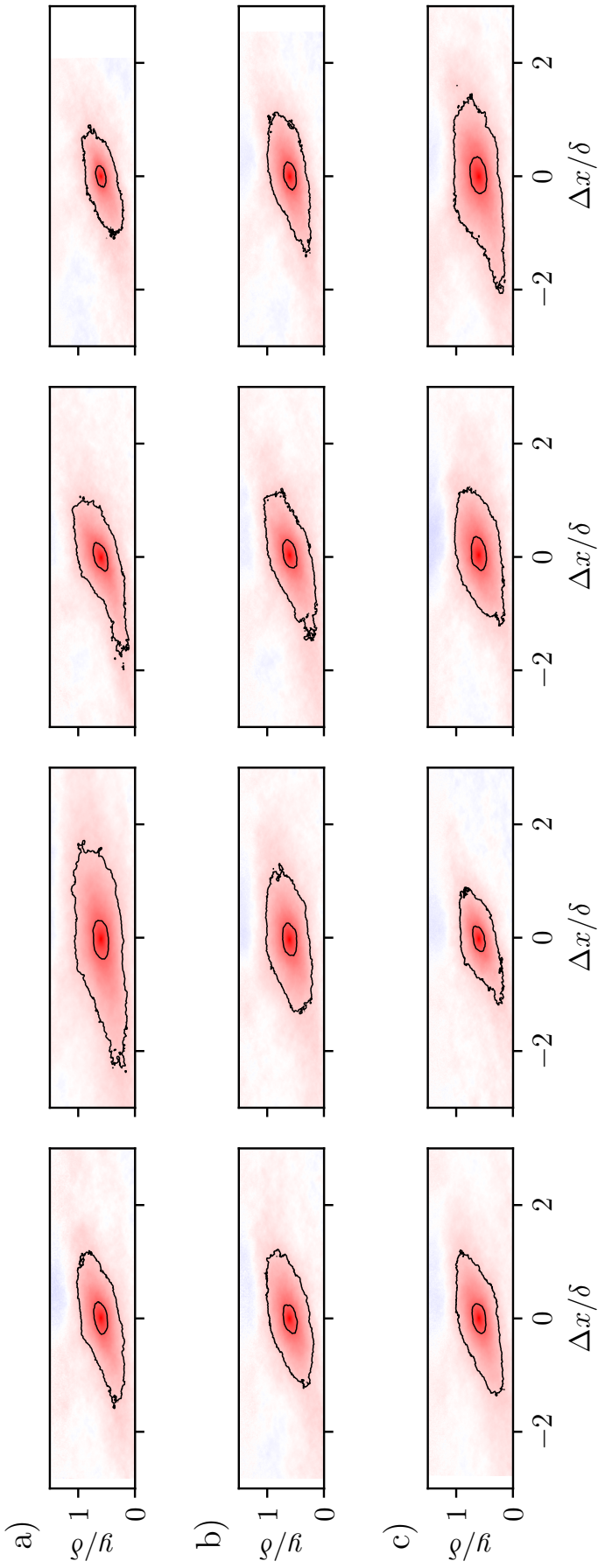

FIGURE 6.10: Example $R_{u'u'}$ correlation field with contours of level 0.2 and 0.6. Rows (*a*), (*b*) and (*c*) correspond to the -8° , 0° and 8° case. The columns correspond to $x_{ref}/c = -1$, $x_{ref}/c = 0$, $x_{ref}/c = 1$ and $x_{ref}/c = 2$.

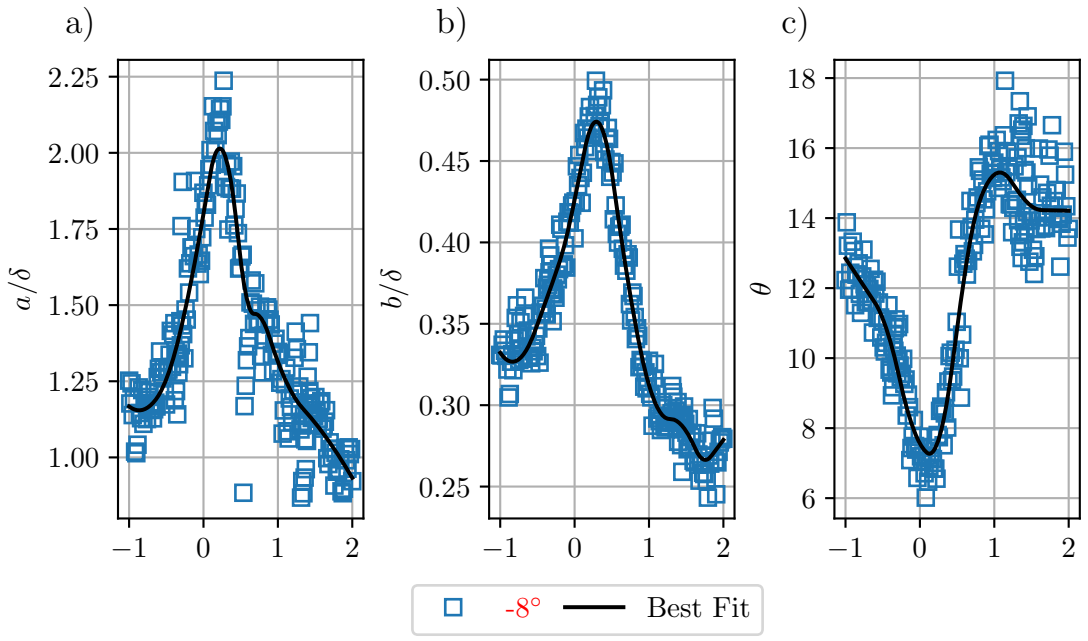

FIGURE 6.11: Streamwise variation in the coherent structure properties for the $-8°$, the large-scale structures are represented by a contour level of 0.2, in all cases $y_{ref}/\delta = 0.6$. Sub figure (*a*) shows the major axis variation, (*b*) shows the minor axis variation, and (*c*) shows the inclination variation. The black line shows the resulting fit from the smooth polynomial.

$x_{ref}/c = 0$, where there is an APG, results in the suppression of the structures compared to the initial ZPG value. At $x_{ref}/c = 1$ and $x_{ref}/c = 2$, the opposite is true, as the PG type has switched, despite the local PG being zero at the reference point.

Figure 6.11 uses the ellipse fitting method to quantify the variation of the large-scale coherent structures for the $-8°$ case with $y_{ref}/\delta = 0.6$. Starting with the large-scale structures, figure 6.11*a* shows the variation in the major axis for a contour level of 0.2. As expected from figure 6.10, it is seen that an FPG increases the major axis length while an APG reduces it. Similar trends are seen in the minor axis in figure 6.11*b*, where an APG leads the shorter minor axis while an FPG extends the minor axis. The inclination of the coherent structures is also affected, as expected from previous works of Lee (2017) and Volino and Schultz (2023), among others. An FPG reduces the inclination of the structures, causing them to become more aligned with the wall, as seen in figure 6.11*c*. Meanwhile, an APG has the opposite effect, lifting the structures away from the wall and increasing their inclination.

Figure 6.11 shows the raw data points as found from the ellipse fitting along with the trend line obtained from smoothing the data. These curves are constrained to have no more than five turning points. This limit is based on the PG histories in figure 4.3, which exhibit fewer than five turning points. As noted by Volino (2020), fitting methods of this type introduce scatter due to the contour-fitting process. This analysis of the large-scale structures is extended to the $0°$ and $8°$ cases in figure 6.12*a-c*. For

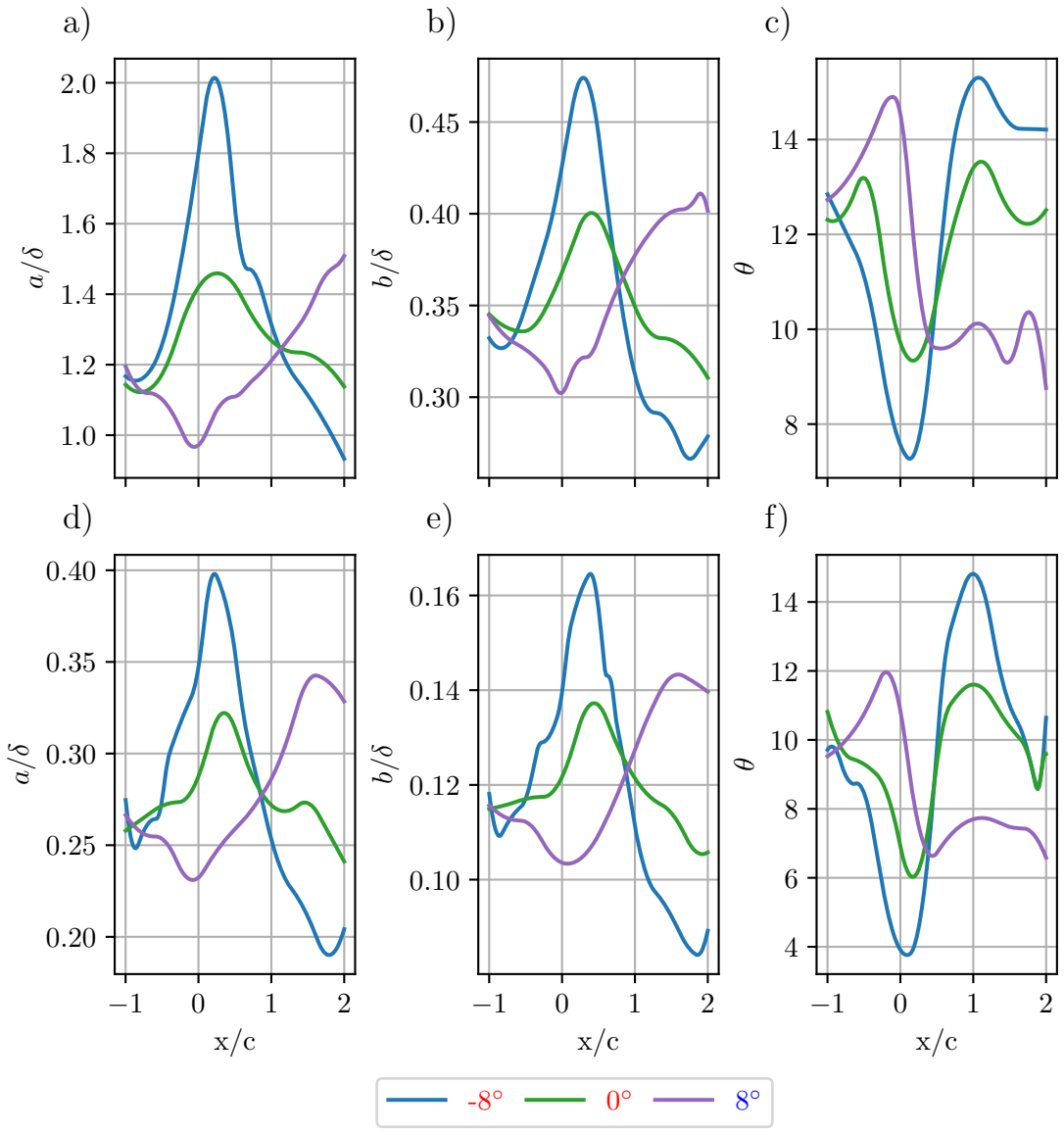

FIGURE 6.12: Streamwise variation in the coherent structure properties for the $-8°$, $0°$ and $8°$ cases, the large-scale structures are represented by a contour level of 0.2 in (*a-c*) and the small scales are represented by a contour level of 0.6 in (*d-f*), in all cases $y_{ref}/\delta = 0.6$. Sub figures (*a*) and (*d*) show the major axis variation, (*b*) and (*e*) show the minor axis variation, and (*c*) and (*f*) show the inclination variation.

large-scale structures, the major axis exhibits an average deviation from the trend line shown in figure 6.12*a* of $\pm 5.5\%$. The average deviation from the mean value of the minor axis and inclination is less than 6.5%.

Figures 6.12*d-f* show the variation in the small-scale structures represented by a contour level 0.6 a $y_{ref}/\delta = 0.6$. The overall trends in the small scales are the same as those in the large-scale structures in response to different PG histories. While one would expect both the major and minor axes to be reduced for small scales, the eccentricity of the flow structures also changes between the scales. The eccentricity, e,

describes how elongated the flow structures are and is defined using

$$e = \sqrt{1 - \frac{b^2}{a^2}} \tag{6.12}$$

Calculating the eccentricity in the upstream region around $x/c \approx -1$ leads to the value of $e \approx 0.96$ for the large scales. For the small scales, the value of $e \approx 0.90$ is found in the ZPG region. While this difference does not appear large, the non-linear nature of equation 6.12 means this change is more significant than the difference suggests. Across both the small and large scales, it is seen that an FPG elongate the structures as shown by an increase in eccentricity. In contrast, an APG compresses the flow structures, reducing the eccentricity of the flow structures. The variation in the eccentricity is larger for the small scales than for the large scales. Over the region of interest shown in figure 6.12 from $x/c = -1$ to $x/c = 2$, the maximum variation for the large scales from the initial ZPG value is 1.5%. While for the small scales, there is a maximum variation of around 2% from the initial value. In both cases, the maximum variation occurs in the -8° case.

The initial inclination of both the small and large-scale structures is similar at around $\theta \approx 12.5^\circ$. This is similar to the angle noted in the ZPG region of Volino (2020) and Adrian et al. (2000) of 12°. The inclination of the flow structure property to respond to the PG history before the structures are either stretched or compressed. This conclusion is based on the turning points of the inclination distribution occurring before those of the major and minor axes for all cases and structure sizes.

The preceding analysis has focused on the contours at $y_{ref}/\delta = 0.6$; we now move on to look at the variation in properties at different reference heights. This will focus on only the -8° case; however, similar results are seen across the other cases. Figure 6.13 looks at differences in the major and minor axes plus the inclination at $y_{ref}/\delta =$ 0.2, 0.4, 0.6 and 0.8. Figure 6.13*a* looks at the major axis for the large-scale structures. The overall trends are the same as those seen at $y_{ref}/\delta = 0.6$. Within experimental uncertainty, the peak location in the FPG region occurs at similar locations at all y_{ref}/δ locations. It is also seen that the major axis reduces in length as the reference point moves further away from the wall. The opposite effect is seen in the minor axis, which increases in length as the reference point is moved further from the wall. This means that the eccentricity of the structures decreases further away from the wall, meaning they are less elongated. Figure 6.13*c* shows the effect of varying y_{ref} for the -8° case. The inclination for y_{ref}/δ between 0.4 and 0.8 is found to be between 10° and 13°. It is seen that the $y_{ref}/\delta = 0.2$ case is much lower than those further away from the wall. This is likely due to the wall, which limits the inclination of the structure due to physical limitations on the rotation of the structure. The maximum inclination reached in the APG region is $\approx 16^\circ$ from the average trend line, slightly less than the suggested inclination limit of 18° seen in Lee and Sung (2009). However, the maximum measured

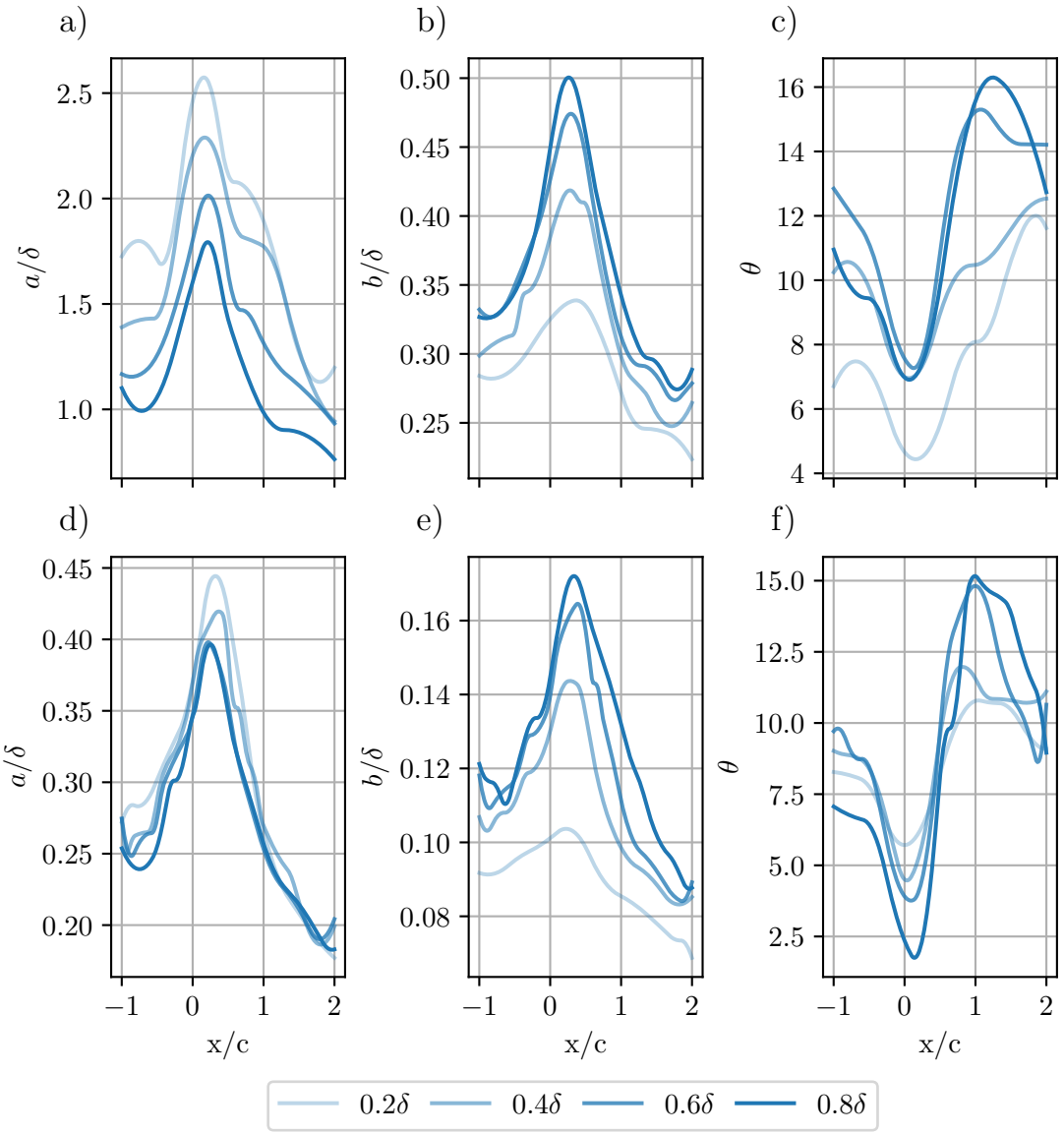

FIGURE 6.13: Streamwise variation in coherent structure properties at different y_{ref}/δ heights for the -8° case. The large-scale structures are represented by a contour level of 0.2 in (*a-c*) and the small scales are represented by a contour level of 0.6 in (*d-f*). Sub figures (*a*) and (*d*) show the major axis variation, (*b*) and (*e*) show the minor axis variation, and (*c*) and (*f*) show the inclination variation.

value is 17.8° seen for $y_{ref}/\delta = 0.8$, which is very similar to the suggested limit of previous works.

Figure 6.13*d–f* shows the major axis, minor axis, and inclination of the small-scale structures at different y_{ref} locations. The trends for the small scales are broadly similar to those observed for the large-scale structures. Focusing on the major axis in figure 6.13*d*, its variation across y_{ref} is notably smaller than that of the large scales. The major axis length is approximately constant within experimental uncertainty from $y_{ref} = 0.4\delta$ to 0.8δ. While this collapse is not observed in the 0° and 8° cases (not shown), a consistent reduction in the spread between different y_{ref} locations is seen when comparing small and large scales.

6.7 Summary

This chapter moves on from looking at single-point measurements to flow field measurements using PIV to understand the development of the flow over a smooth wall. The flow domain considered is from $-1 \leq x/c \leq 2$ for the five angles of attack with $h = 0.5$ m. The first part of this chapter looks at an extension to the $\Delta\beta$ model proposed in chapter 4 using Π calculated from the maximum deviation from the log law throughout the region of interest. To improve the initially proposed model 2^{nd} order terms are found to be needed for both $\Delta\beta$ and β. The β term is added to give a term which accounts for the local PG, while the $\Delta\beta$ term accounts for the upstream history. It has been seen that the most important term remains the linear $\Delta\beta$ term.

The effect of PG history on the turbulent events was examined using quadrant analysis, focusing on sweep and ejection events. Near the edge of the log region at $y/\delta = 0.2$, the contribution of ejection events to the overall shear stress is seen to increase with FPG. The opposite effect is seen for APG, where the contribution of ejection events is reduced. For sweep events, the opposite trends are seen with FPG reducing its contribution and APG increasing it. Further away from the wall at $y/\delta = 0.6$, there is seen to be no effect on the sweep events, while ejection events are seen to increase in importance with APG and reduce under FPG conditions. This is the opposite of what was seen nearer the wall. Utilising the peak Reynolds shear stress allowed examination of the IL and their development. ILs are seen to form under APG conditions independent of the upstream history. The IL is seen to collapse rapidly when the FPG changes to an APG, while there growth rate is dependent on the FPG strength.

The final part of this chapter looked at the response of the coherent structures within the flow using the contours from the two-point correlation fields. It has been seen that an FPG increases the streamwise length of the coherent structures while an APG reduces it. It was also seen that the inclination increases with APG and reduces with FPG. These trends are seen for both the large and small-scale structures. Examination

of the structures at different positions within the boundary layer showed that for the large scales, the streamwise length of the structures reduces as you move further away from the wall. However, this trend was not seen for the small-scale structures.

Chapter 7

Surface Effects on Flow Structures with Pressure Gradients

Building on the previous chapter, which considered the effect of PG on the development of a smooth wall turbulent boundary layer under different conditions, this chapter compares the response of the smooth and rough walls. The region of interest is the same as that used in chapter 6 with the experimental setup given in section 3.5.1. Firstly, the universality of the previously developed model to predict Π is examined. The effect of PG history on the turbulence statistics and IL is compared between smooth and rough walls. The final section looks at quantifying the changes in the coherent structures and comparing the differences between smooth and rough walls. [1]

7.1 Parameters

This chapter focuses on the effects of pressure gradients (PGs) on skin friction and mean flow for five angles of attack: -8° , -4° , 0° , 4° , and 8° . The quarter chord height is maintained at $h = 0.5$ m for all cases. All cases are taken at a nominal inlet speed of 20 m/s with the Reynolds number matched to those in chapter 4. This equates to Reynolds numbers between $6.9 \times 10^6 < Re_x < 13.1 \times 10^6$.

7.2 Effect of pressure gradient history on the mean flow

The mean flow development of a TBL over the rough wall is first examined to assess the impact of surface roughness under pressure gradient conditions. Figure 7.1 shows

[1] Parts of this chapter are published in the International Journal of Heat and Fluid Flow as Preskett and Ganapathisubramani (2025).

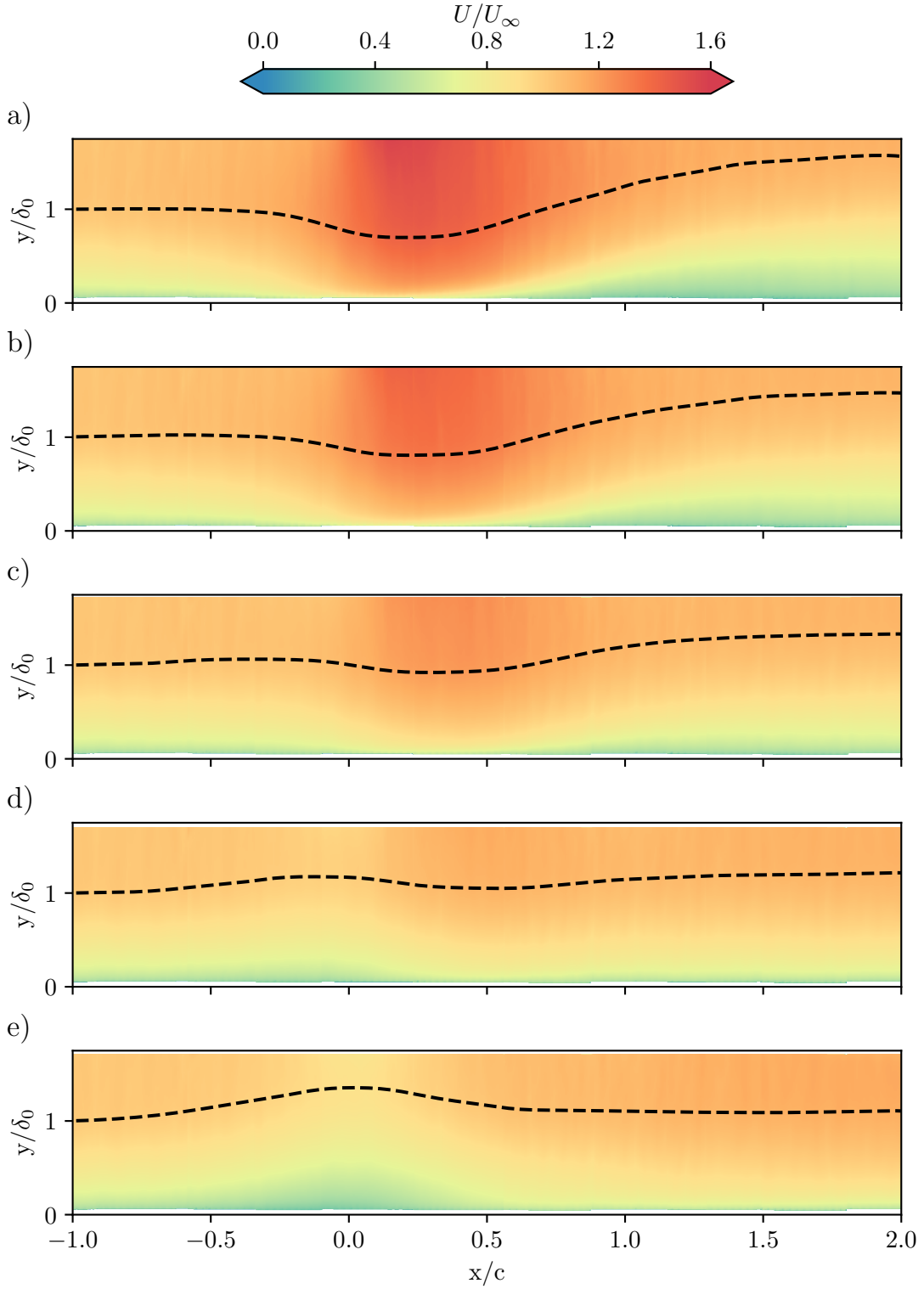

FIGURE 7.1: Rough wall velocity field plots of the mean streamwise velocity, U/U_∞, from $x/c = -1$ to 2. U_∞ is the velocity from the pitot at $x/c = -1$. The black dashed line shows the edge of the boundary layer, δ, determined using the method described in Vinuesa et al. (2016). The five sub figures correspond to: (*a*) -8° , (*b*) 4° , (*c*) 0° , (*d*) 4° , and (*e*) 8°

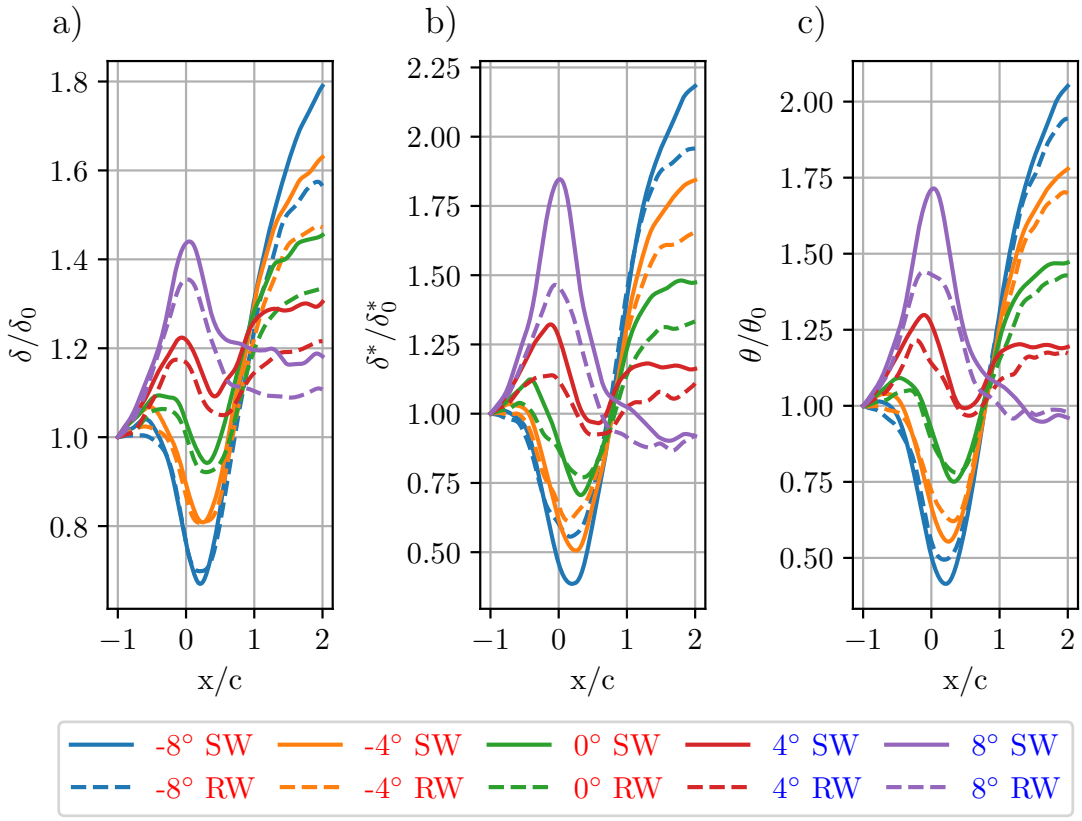

FIGURE 7.2: Rough wall velocity field for the mean streamwise velocity, U, normalised by U_∞ from the pitot at $x/c = -1$ for (a) $-8°$, (b) $-4°$, (c) $0°$, (d) $4°$, and (e) $8°$. The black dashed line shows the variation in the boundary layer thickness, δ normalised by the δ_0 at $x/c = -1$

the mean velocity fields and the boundary layer thickness variation for the five rough wall cases. The boundary layer thickness is again calculated using equation 6.1 as in the smooth wall PIV cases. As seen in the near wall region, there is missing data due to the reflections of the roughness as explained in section 3.5.1. Where needed linear velocity distribution from the first data point in the log region to the zero slip condition at the wall accounts for missing data in this region. Using this method on the HWA data in chapter 4 results in an error of less than 3% in δ^*. This suggests it is a reasonable method, data in the absence of data, to estimate the near-wall velocity distribution.

The mean PIV fields of the smooth and rough walls allow exploration of the differences between the boundary layer thicknesses (δ, δ^* and θ). We shall consider the evolution of the boundary layer property compared to its initial value (δ_0, etc) at $x/c = -1$. Figure 7.2*a* looks at the change of δ/δ_0 for the smooth and rough wall cases. The cases that initially experience an FPG ($-8°$, $-4°$ and $0°$) show good agreement up to $x/c \approx 1$. After this point, there are clear differences in the flow response depending on the surface due to the APG that the flow experiences. The smooth wall in these regions shows a higher growth rate than the rough wall. This is also seen in the cases with which experience APG first ($4°$ and $8°$), where the smooth wall growth rate exceeds

that of the rough wall in the APG region. The offset introduced between the surfaces in the APG region is not recovered in the following FPG. This indicates different flow responses to APG for smooth and rough walls, even for weak A-FPG cases such as 4° . It is noted that these cases are taken at different Re_τ values. However, it was seen in table 4.1 that the boundary layer thicknesses are approximately constant for the rough wall cases with Reynolds number.

The next parameter to consider is δ^* and how the response differs for smooth and rough walls. The smooth and rough wall agreement for δ^* is not as good as that seen with δ. The effect of the PG is always greater on the smooth wall flow than on the equivalent rough wall flow. Better agreement is seen for θ between the smooth and rough wall cases, with all cases except for the 8° case showing excellent agreement through the domain. For the 8° case, the smooth wall responds more to the APG's PG history than the rough wall. However, unlike with δ, for θ, the smooth and rough wall recover to the same ratio in the following FPG region.

The preceding analysis used independent measurements of skin friction. It was impractical for the rough wall PIV section due to the need to constantly move the drag balance, along with the associated calibration. The log region from equation 2.16 is fitted to the data to estimate the skin friction. For the value of y_0, 0.462 mm is used, which is the $y_{0_{ZPG}}$ value from table 4.2. This method's accuracy is compared in section 4.3.2. The uncertainty in U_τ is at least 5% based on the error from section 4.3.2. This aligns with the uncertainty estimate from Monty et al. (2011).

Figure 7.3*a* uses this estimate of the skin friction along with δ^* from the PIV to estimate the distribution of β for the RW cases. The smooth β is given in figure 6.3*a*. The 4° and 8° cases show excellent agreement in β history between the smooth and rough wall cases. For the $-4°$ and 0° cases, there is good agreement between the smooth and rough walls in the FPG region. The APG region of the 0° case has similar peak values of β between the smooth and rough walls. However, the smooth wall β recovers to zero faster than the rough wall case in the APG region ($x/c > 1$). The rough wall peak in the APG region of the $-4°$ case is 25% larger for the rough wall compared to the smooth wall case. The difference for the $-8°$ case is even larger at 83%. As with other FPG regions, excellent agreement between smooth and rough wall β distributions has been seen in the preceding FPG region. A similar trend is seen in the Volino and Schultz (2023) which only considered FPG - ZPG - APG distributions.

The preceding analysis in section 4.4 and 6.3 showed that it is possible to relate $\Delta\beta$ and $\Delta\Pi$. $\Delta\Pi$ is used to access the change in Π since wall similarity is not seen in the ZPG cases and therefore would not be expected for the PG cases due to the roughness effects. Figure 7.3*b* shows the variation in $\Delta\Pi$ which is again defined as $\Pi_{PG} - \Pi_{ZPG}$. Π_{ZPG} is taken from table 4.1 for the ZPG case of the corresponding surface. Π_{PG}, as in

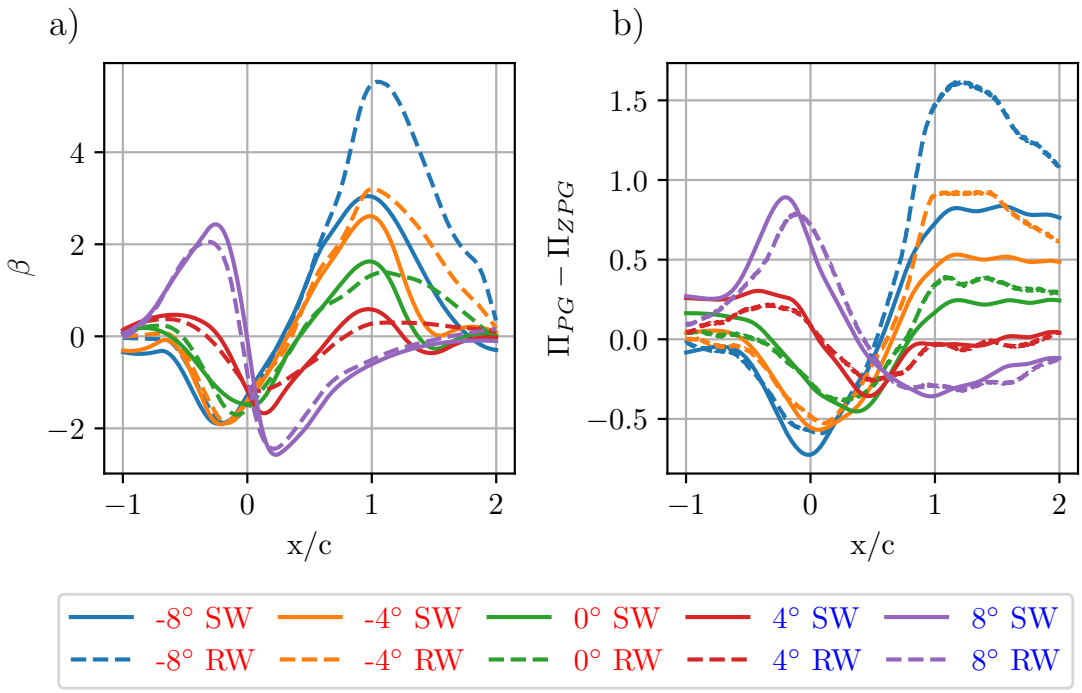

FIGURE 7.3: (*a*) Variation in β with streamwise position for both the smooth and rough wall cases at $h = 0.5$ m. Variation of $\Pi_{PG} - \Pi_{ZPG}$ where Π_{PG} is the local value of Π and Π_{ZPG} is taken from table 4.1 for the ZPG cases for the corresponding surface.

section 6.2, is calculated using the maximum deviation from the log law, which for a rough wall is given by

$$\Pi = \frac{\kappa}{2}\left(U^+_{99} - \frac{1}{\kappa} ln\left(\frac{\delta - d}{y_0}\right)\right) \tag{7.1}$$

Again, y_0 is taken to be $y_{0_{ZPG}}$ value from table 4.2 and d is taken to be $k/2$ as in Squire et al. (2016). This method is estimated to give an uncertainty of ± 0.3 for a confidence interval of 95%. This uncertainty is higher than that seen in the smooth wall cases since the uncertainty in U_τ is higher, since it is estimated from the mean profile and not directly measured.

In figure 7.3*a*, it was seen that for the 8° case, the smooth and rough wall β values match throughout the domain. Figure 7.3*b* shows that $\Delta\Pi$ match for these cases. The 4° case shows similar agreement, which is to be expected since the magnitude of the PG history is much weaker. For the cases which first experience an FPG ($-8°$, $-4°$ and $0°$), the β histories were seen to match in the FPG region but not in the APG region. As might be expected based on β history, there is good agreement in the FPG region. For the rough wall case, $\Delta\Pi$ is seen to be 20% less than the smooth wall at $x/c \approx 0$ for the $-8°$ case. This difference, however, is limited to the peak region, and the flows recover the same value quickly. In the APG region, clear differences are seen in these cases, with the rough wall having a much larger increase in $\Delta\Pi$ than the smooth wall.

This difference in the APG region following an FPG was also seen in the work Volino and Schultz (2023) and was suggested to be due to the faster boundary layer growth under APG conditions for a rough wall flow. It is therefore interesting that for an APG following only a ZPG, as in 8° case, does not show large differences in $\Delta\Pi$. This, despite a difference in the growth rate of the boundary layer in this region in figure 7.2*a*. The peak β in this region is around two, similar to that seen in the $-4°$ case, which exhibits a significant difference in $\Delta\Pi$.

7.3 Steps towards a universal model for change in wake strength

In section 6.3, an extended model for predicting $\Delta\Pi$ based on the PG history is presented, based on the smooth wall data. The previously defined model from the smooth wall data is given by equation 6.5 with the integration length calculated for the smooth wall of $L/\delta = 25.2$. Using this with the rough wall data results in the prediction shown in figure 7.4*a*. The mean error is 0.18, much larger than the value seen when the same equation was applied to the smooth wall data. The reason for this is that the rough wall requires a different value of L/δ compared to that of the smooth wall. For both the smooth and rough wall, we want the equation to find $\Delta\Pi$ to be universal between surfaces, with any differences being accounted for in the integration length used to find $\Delta\beta$. Therefore, the pair of L/δ values is found, resulting in the minimum error across smooth and rough wall cases. The result of the optimisation is shown in figure 7.4*b*, which for the smooth wall gives an optimum value of $L/\delta = 26.9$ and for the rough wall $L/\delta = 12.7$. The equation for $\Delta\Pi$ is given by

$$\Delta\Pi = 0.03\beta^2 - 0.16\Delta\beta^2 - 0.12\beta\Delta\beta + 0.12\beta + 1.11\Delta\beta \tag{7.2}$$

The coefficients are similar to those found from the smooth wall dataset, which is to be expected since the L/δ value is very similar. The value in terms of δ is double for the rough wall compared to the smooth wall. It is, however, noted that if you take the average boundary layer thickness through the domain of both smooth and rough walls, the physical distances for both the smooth and rough walls are very similar at 2.55 m. The fit is shown in figures 7.4*c* and *d* for smooth and rough walls, respectively. Using this method, the average error across both surfaces is 0.07, similar to that of the smooth wall. It should be noted that the number of points used to calculate the error for a given surface is the same to ensure one surface does not dominate the error calculation.

While the above model is reasonable, the value of L/δ being surface dependent is not ideal when creating a universal model. Therefore, a method which accounts for the surface parameters would be useful for future uses; however, the exact form of the equation is unknown. The momentum integral equation (equation 2.20) suggests that

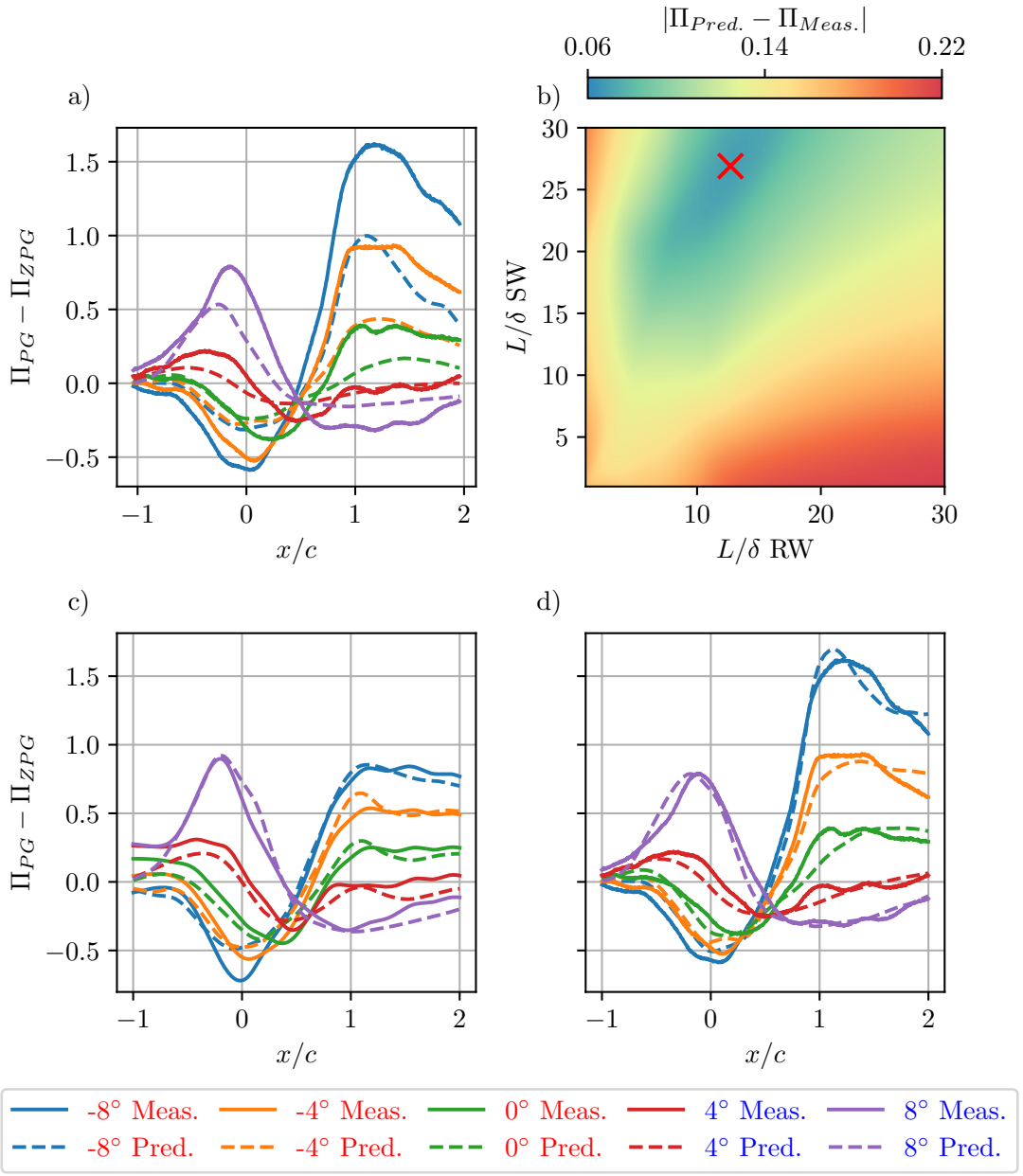

FIGURE 7.4: (*a*) Measured and predicted values of $\Delta\Pi$ for the five rough wall cases from equation 6.5 using $L/\delta = 25.2$ from chapter 6. (*b*) Shows the average error between the measured and predicted value of $\Delta\Pi$ for different values of L/δ for the smooth and rough wall cases, the X showing the optimum value. (*c*) and (*d*) shows the smooth and rough wall cases respectively using the optimum values of L/δ from (*b*) and the curve defined by equation 7.2.

A	a	b	c	d
23.4	0.51	-2.11	2.59	0.53

TABLE 7.1: Optimum fit values found from fitting process for equation 7.3

the parameters for normalisation will be δ, δ^*, θ, U_{99} and U_τ. Therefore, we require an equation for L in the form of

$$L = A\delta^a \delta^{*b} \theta^c U_\tau^d U_{99}^{-d} \tag{7.3}$$

To ensure dimensional consistency, the power for U_τ and U_{99} must be equal and opposite. Similarly, the sum of a, b, and c must equal one to ensure L has m units.

All cases are used to find the values of the constants, and once again, the mean error is minimised to find their values. The optimisation values are given in table 7.1. The exponents obtained from fitting (e.g. -2.11) were rounded to the nearest fractional power to facilitate comparison with classical scaling laws, and the coefficient of A is refitted. The result of this is given by

$$L = 25.4\delta^{\frac{1}{2}}\theta^{\frac{5}{2}}\delta^{*-2}U_{99}^{\frac{1}{2}}U_\tau^{-\frac{1}{2}} = 25.4\frac{1}{H^2}\sqrt{\theta\delta}\sqrt[4]{\frac{2}{C_f}} \tag{7.4}$$

where it is also seen that it can be written in terms of H, θ, δ and C_f. This can further simplified as,

$$\frac{L}{\delta} = L^* \approx \frac{25}{H^2}\sqrt{\frac{Re_\theta}{Re_\tau}} \tag{7.5}$$

The above relationship for integration length to compute $\Delta\beta$ together with the following equation to relate $\Delta\beta$, β and $\Delta\Pi$ provides the necessary universal closure for smooth and rough walls.

$$\Delta\Pi = 0.02\beta^2 - 0.08\Delta\beta^2 - 0.10\beta\Delta\beta + 0.11\beta + 1.05\Delta\beta \tag{7.6}$$

The final prediction of $\Delta\Pi$ for the smooth and rough wall, using equations 7.4 and 7.6, is shown in figure 7.5*a* and *b* respectively. The final fit is very similar to that seen with the different L/δ values, and the mean error is the same at 0.07. This model can be used in the same way as shown in section 4.4 to estimate the flow development based on the pressure gradient history.

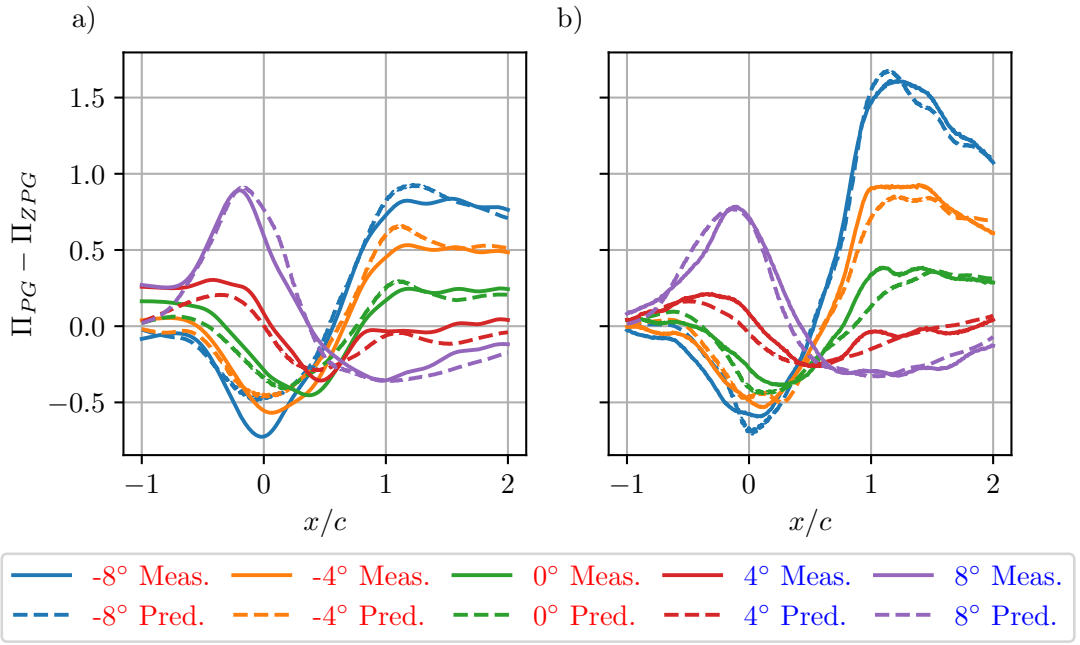

FIGURE 7.5: Measured and predicted values of $\Delta\Pi$ for the five PG histories using L/δ from equation 7.4 and $\Delta\Pi$ from equation 7.6 for: (*a*) smooth wall cases and (*b*) rough wall cases.

7.3.1 Application of model to other datasets

The analysis in this work has developed a model based on data collected using a NACA 0012 aerofoil to generate different PG histories. This part moves on to apply the derived model to other datasets over smooth and rough walls and examine the strengths and weaknesses of the model. For smooth and rough wall cases, data is obtained from Volino (2020) and Volino and Schultz (2023). Their setup consists of an FPG-ZPG-APG imposed by a ramp mounted in the freestream, with three different configurations giving strong, medium and weak PG histories. The highest available Reynolds number case for each ramp configuration is chosen. Data is taken from table 1 in Volino (2020) and table 2 in Volino and Schultz (2023). These being the strong PG case *Case 2* for both surfaces, the medium PG strength *Case 5* is used and finally for the weak PG history *Case 8*. Their experiments are conducted in water, with the strong PG cases taken at 1 m/s and the others at 2 m/s. These correspond to a $590 \leq Re_\tau \leq 1901$ for the smooth wall cases and $960 \leq Re_\tau \leq 4084$ for the rough wall cases.

Taking equations 7.4 and 7.6, it is possible to predict the change in Π and compare it to the measured values given in Volino (2020) and Volino and Schultz (2023). Figure 7.6 shows the measured and predicted values at different streamwise stations. Continuing the trend seen in figure 7.5, the model performs reasonably well in the APG region, the region with the red background. The model, however, struggles in the FPG region, denoted by the blue background. For these datasets, the model tends to under-predict the reduction in Π due to a given PG history. This prediction then recovers through

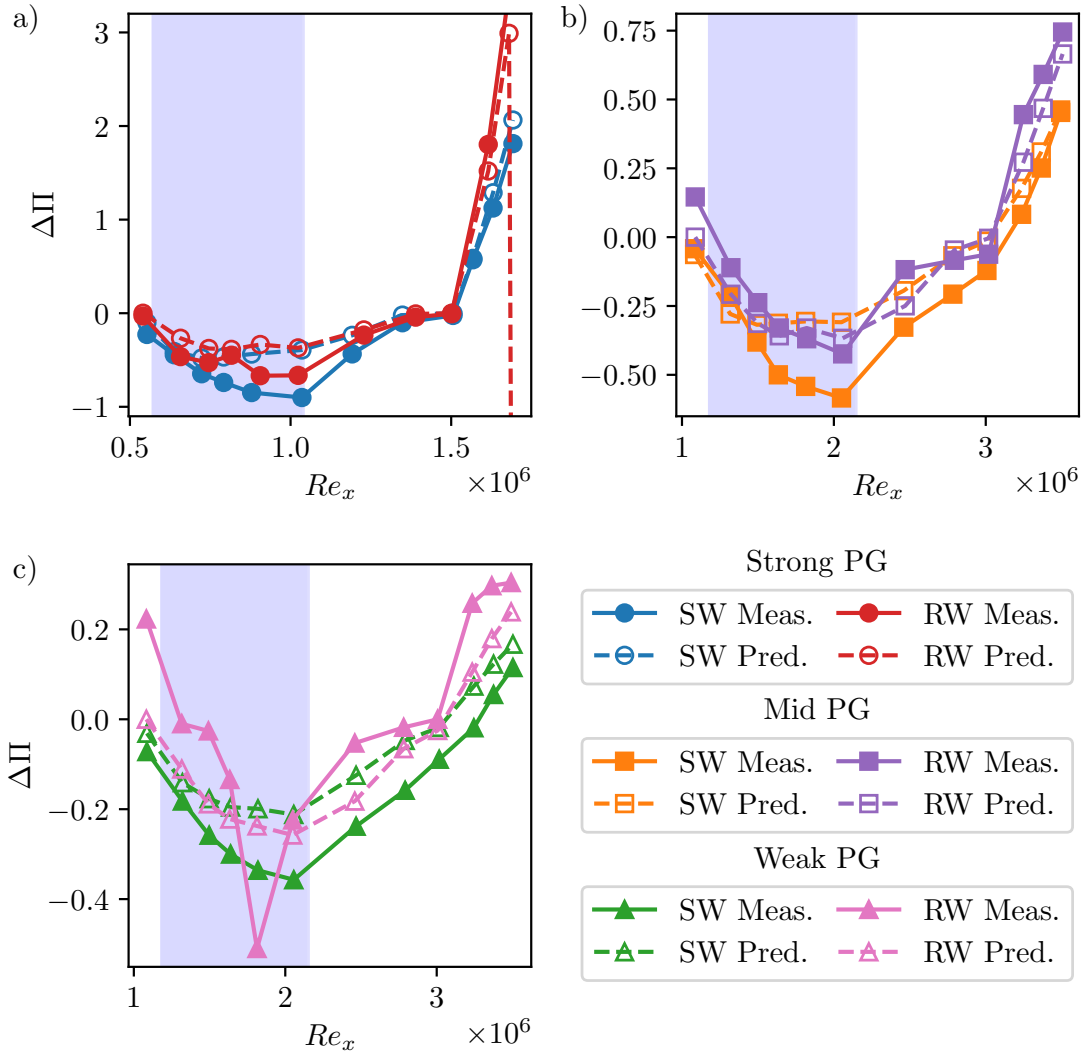

FIGURE 7.6: Measured and predicted values of ΔΠ as a function of Re_x, defined based on the initial conditions in the initial ZPG region, using data from Volino (2020) and Volino and Schultz (2023) for the smooth and rough wall, respectively. (*a*) Shows the strongest PG histories (Corresponding to *Case 2* in Volino (2020) and Volino and Schultz (2023)), (*b*) shows the medium PG histories (Corresponding to *Case 5* in Volino (2020) and Volino and Schultz (2023)) and (*c*) shows the weakest PG histories (Corresponding to *Case 8* in Volino (2020) and Volino and Schultz (2023)). The white background regions are ZPG, the blue are FPG and the red APG.

the ZPG before giving good agreement in the APG region. For the mid-strength PG history, the change in Π is similar to the experiments given in the current work. The rough wall case shows excellent agreement between the prediction and the measured value. However, the smooth wall cases do not have such good agreement, especially in the FPG and ZPG regions. For extreme values of Π ($\Delta\Pi > 3$) under strong APG, the model fails to capture the trend; however, this is to be expected since this is well outside the range of data on which the model was developed. Furthermore, for these extreme values of Π, classical boundary layer shape profiles such as those given by equation 2.7 fail due to the lack of a classical logarithmic region.

7.4 Comparison of turbulence statistics between smooth and rough wall flows

Section 6.4 explored the contribution of Q2 and Q4 events to the overall Reynolds shear stress and how PG history affects the flow response for a smooth wall. This section extends this analysis and considers how the flow turbulence response differs between a smooth and a rough wall. Figure 7.7*a* and *b* show the variation in the $\widetilde{u'v'}_2$ and $\widetilde{u'v'}_4$ at $y/\delta = 0.2$ respectively. Once again, the contributions of sweeps and ejections are calculated using the hole method previously outlined, with a hole size of $H = 1$ for both the smooth and rough walls. The overall trends in response to the PG history are the same as seen in the smooth wall for $\widetilde{u'v'}_2$ and $\widetilde{u'v'}_4$. The largest difference between the smooth and rough walls is that the flow is seen to respond faster for the rough wall flows compared to the smooth wall cases. It is noted that the Re_τ of flow between the smooth and rough walls is different; however, we assume the rough wall is invariant to Reynolds number. This decision is supported by the mean flow in chapter 4, where invariance to Reynolds number is seen for the flows presented. For the smooth and rough wall cases, $\widetilde{u'v'}_2$ and $\widetilde{u'v'}_4$ are initially constant before any PG effects. The contribution of sweeps and ejections is the same for the smooth and rough walls in this ZPG region. For $\widetilde{u'v'}_2$, this is seen to be 0.54, while for $\widetilde{u'v'}_4$, the value is around 0.41. For the smooth wall, it was seen that deviation from the constant value occurs at $x/c = -0.2$ and $x/c = -0.5$ for $\widetilde{u'v'}_2$ and $\widetilde{u'v'}_4$ respectively. For the rough wall deviation occurs around $x/c = -0.8$ for both $\widetilde{u'v'}_2$ and $\widetilde{u'v'}_4$. This value is much earlier than that seen for the smooth wall, despite having very similar beta histories in this region between the smooth and rough wall cases.

Moving on to look at the response of $\widetilde{u'v'}_2$ to the initial PG history, it is seen that the change due to the PG history is always less for the rough wall than the smooth wall. The opposite effect is true $\widetilde{u'v'}_4$, where the rough wall change from the initial value is greater than that of the smooth wall. The trends are less clear-cut for the second half of the PG history for $\widetilde{u'v'}_2$. In this region, it was seen in figure 7.3*a* that in the

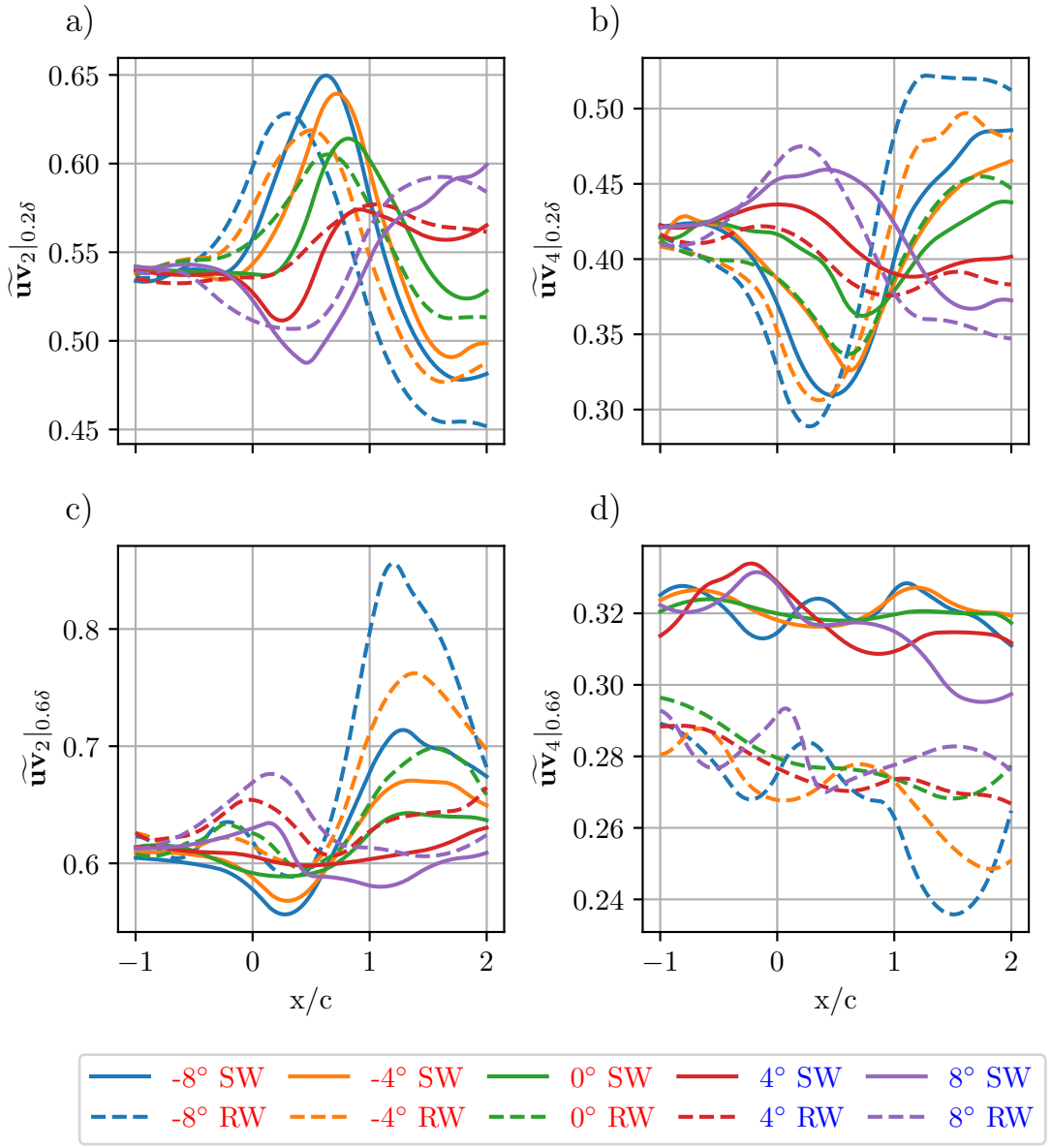

FIGURE 7.7: Comparison of streamwise variation of $\widetilde{u'v'}_i$ for the smooth and rough wall cases. (*a*) $\widetilde{u'v'}_2$ with $y_{ref}/\delta = 0.2$, (*b*) $\widetilde{u'v'}_4$ with $y_{ref}/\delta = 0.2$, (*c*) $\widetilde{u'v'}_2$ with $y_{ref}/\delta = 0.6$ and (*d*) $\widetilde{u'v'}_4$ with $y_{ref}/\delta = 0.6$

APG, the rough wall β significantly exceeds that of the smooth wall. This explains the trends seen in $\widetilde{u'v'}_2$ in figure 7.7*a*, where for the cases which experience FPG then APG ($-8°$, $-4°$ and $0°$), the minimum value reached is less than that of the smooth wall. The actual change from the peak value in the initial PG to the minimum in the second half of the PG history is similar for the $-4°$ and $0°$ cases. While for the $-8°$ case, the difference between the rough and smooth wall is significant, with a difference of 0.1 between the values. For the cases which experience an APG then FPG, there is no significant difference between the two surfaces for the final values of $\widetilde{u'v'}_2$ in the FPG region. Similar trends are seen in $\widetilde{u'v'}_4$ with the rough wall values having greater

change than the equivalent smooth wall case.

After experiencing the different PG histories, all cases appear to reach plateaus for $\widetilde{u'v'}_2$ and $\widetilde{u'v'}_4$. This is particularly true for the rough wall cases, which show no clear sign of recovery. The smooth wall values only just reach a plateau towards the end of the domain of interest. This is despite the PG history recovering to a ZPG and is seen for smooth and rough surfaces, and follows the behaviours seen in the boundary layer thickness and $\Delta\Pi$.

The smooth wall analysis showed that the response to the PG history at $y/\delta = 0.6$ is the inverse of that seen at $y/\delta = 0.2$ for $\widetilde{u'v'}_2$. The same is seen in figure 7.7*c* for the rough wall cases. This is clear in the second half of the PG history; the initial PG history shows little variation from the initial value. As was seen at $y/\delta = 0.2$, the initial value of $\widetilde{u'v'}_2$ in the ZPG region is the same between the smooth and rough wall cases. The response to the PG history is much stronger for the rough wall than for the smooth wall. Unlike the values at $y/\delta = 0.2$, there is a clear recovery of $\widetilde{u'v'}_2$ with all cases tending towards a new equilibrium value. For the -8° , -4° and 0° cases, this new equilibrium sits higher than the initial ZPG value seen before experiencing the different PG histories. Figure 7.7*d* shows the variation in $\widetilde{u'v'}_4$ at $y/\delta = 0.6$. There is a systematic offset between the smooth and rough wall cases not seen in $\widetilde{u'v'}_2$ at either height or $\widetilde{u'v'}_4$ at $y/\delta = 0.2$. The initial value for the smooth wall case is around 0.32; for the rough wall, this is reduced to 0.29. Once again, there is no clear trend with PG history, with the variation from the initial ZPG value for the rough wall. The variation for the smooth wall from the initial value is less than 10% of the initial value for all cases. For the rough wall cases, the 0° , 4° and 8° cases all have less than 10% variation from the initial value. The -8° and -4° cases show slightly higher variation, but it is less than 20%, and there is no clear trend between the rough and smooth wall, and it is likely caused by noise in the PIV datasets.

7.5 Comparison of internal layer development in smooth and rough wall flow

In section 6.5, we considered the effect of PG history on the formation of IL within the boundary layer over a smooth wall. Figure 7.8*a* shows the edge of the IL again, determined using the peak of $\overline{u'v'}$ for both the smooth and rough wall. Overall, the behaviour of the IL between smooth and rough walls shows similar trends; however, there are some differences in the behaviour of the flows. It was noted for the smooth wall flows that there is a clear collapse of the IL for the 4° and 8° cases when the PG becomes an FPG. The same is also seen for these rough wall cases, although the collapse occurs earlier in the domain. For the 4° case, the collapse for the rough wall starts around $x/c \approx 0.1$ compared to 0.3 for the smooth wall. Similar differences in the 8° case

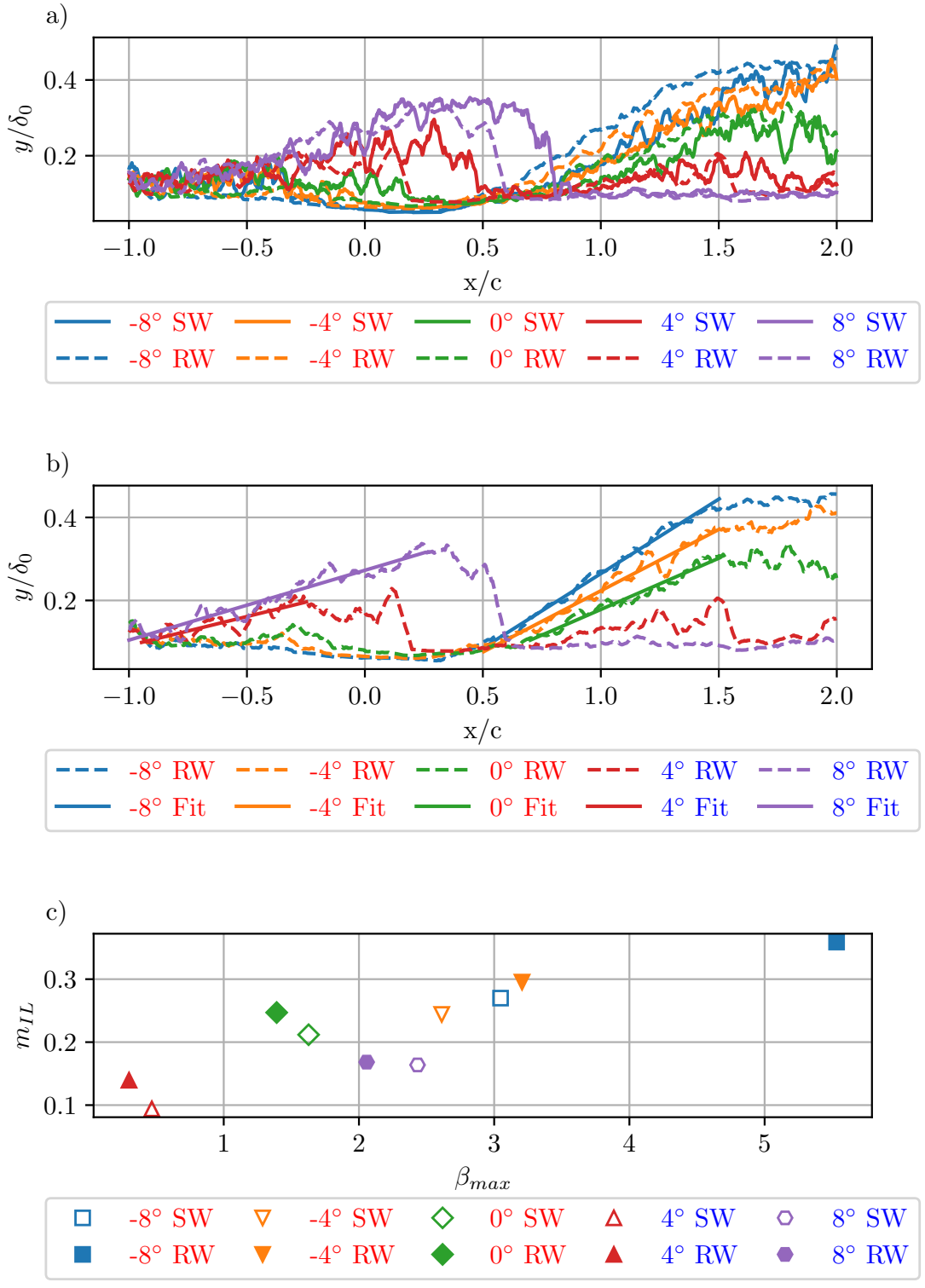

FIGURE 7.8: (*a*) Streamwise development of internal layers for five smooth and rough wall cases. (*a*) Streamwise development of internal layers for the five rough wall cases, along with the best fit of the APG region used to measure the growth rate of IBL. (*c*) Average growth rate of the internal layer for the smooth and rough wall cases, as a function of the maximum β which occurs in the region of the internal layer.

were that the collapse occurs at $x/c \approx 0.5$ for the rough wall compared to $x/c \approx 0.65$ for the smooth wall. This earlier behaviour of the rough wall is also seen in the IL for the -8° , -4° and 0° cases, all of which begin growing earlier than the corresponding smooth wall.

The IL growth rate was noted to increase with APG strength for the smooth wall flow. We shall now quantify this growth rate and examine the differences between smooth and rough walls. Taking only the area in which the boundary layer is growing, meaning the plateau regions seen in the 4° and 8° cases are excluded. A linear fit is fitted to the region of interest in the y/δ_0 vs x/c space to give a non-dimensional gradient, m_{IL}. The fit for the five rough wall cases can be seen in figure 7.8*b*, denoted by the solid lines. To compare the gradient to the strength of the PG history, we shall use β_{max}. This is the maximum β in the APG region where the IL occurs. This is chosen over an integral parameter due to a sign change in β seen in the regions of growth, and we are interested in only the APG region. Figure 7.8*c* shows the variation in the growth rate with the variation of β_{max}. The 4° and 8° cases, which only experience ZPG before the APG responsible for the IL, show good agreement in the growth rate between the smooth and rough walls. For these cases, the β_{max} value of the smooth and rough walls is similar since the β histories in 7.3*a* are similar for both a smooth and rough wall. Some differences exist between the cases that first experienced an FPG before the APG. For the 0° case, there is less than 15% difference between the smooth and rough wall values, and therefore can be said to be similar. In the -8° and -4° cases, the β_{max} values differ due to the different β histories between the smooth and rough wall flows. Despite these differences in β_{max}, the smooth and rough wall cases seem to lie along the same trend line. Similar behaviour is seen between $\Delta\beta$ and $\Delta\Pi$, where the smooth and rough walls lie along the same trend line (see appendix G). The smooth wall -8° case and the rough wall -4° case are particularly interesting since these have very similar β_{max} values despite the different PG histories. Having the same β_{max} value results in similar growth rates of the internal layer. The 8° smooth and rough wall cases have a β_{max} value between the 0° cases and the smooth wall 4° case. It is, however, seen that the growth rate lies below all of these cases. This is likely due to the order in which PG history and the fact that the 8° case has only experienced a ZPG and an APG, whereas the others have experienced a ZPG, FPG and an APG.

7.6 Comparison of flow structures in smooth and rough wall flows

In section 6.6, the effect of PG history on flow structures was considered. This section will compare how the response differs between a smooth and a rough wall. In Figure 7.9 the first column shows the variation in the large-scale flow structures at $x/c = -1$

for both a smooth and rough wall under ZPG conditions at $y_{ref}/\delta = 0.6$. Three angles of attack are shown (-8° , 0° and 8°) to represent the ZPG condition. All the structures in this position are expected to be similar, as the PG histories are approximately ZPG up to this point. As with the smooth wall, a contour level of 0.2 represents the large scales and 0.6 the small scales. Comparing the smooth and rough wall contours, it is clear that the smooth wall structures have a larger major axis than the rough wall structures. At $y_{ref}/\delta = 0.6$, the rough wall structures are on average 22% smaller than the smooth wall structures. This trend is seen at all y_{ref}/δ values, with the difference always being greater than 20%. This difference is larger than that reported by Volino et al. (2007), which suggested the difference was between 10 and 20% under ZPG conditions. This difference is likely due to the roughness used by Volino et al. (2007) being much thinner than that used in the current experiments. The extent to which the coherent structure extends downstream from the reference point is similar for smooth and rough walls. However, for the smooth case, the coherence extends further upstream than the rough wall.

The variation in the minor axis is much smaller, with the rough wall being less than 10% smaller than the smooth wall. At $y_{ref}/\delta = 0.6$, the inclination of the rough wall cases is within 7% of that of the smooth wall cases. This result agrees with the conclusion of Volino et al. (2007) that the inclination is independent of the surface. It is noted that near the wall at $y_{ref}/\delta = 0.2$, the rough wall has a 50% higher inclination than the smooth wall. One reason for this is the lack of near-wall data for the rough wall compared to the smooth wall data, affecting the ellipse's fitting.

Figure 7.9 also shows the smooth and rough wall contours at $x_{ref}/c = 0$, $x_{ref}/c = 1$ and $x_{ref}/c = 2$. It should be noted that at $x_{ref}/c = 2$ the rough wall contours are not complete since the PIV does not extend far enough downstream from the reference point. Overall, as with the ZPG contours, the smooth wall's large-scale coherent structures are larger than those in the corresponding rough wall case. Furthermore, the shape of the resulting large-scale structures are similar between the smooth and rough walls, despite the difference in the overall size of the structure. The size of the small-scale coherent structures shows little difference between the smooth and rough wall cases.

The impact of PG history on flow structures can be quantified by looking at the change in the structure's shape compared to its initial values at $x/c = -1$. Figure 7.10 shows the effect of PG history for both the large and small scales over smooth and rough walls with $y_{ref}/\delta = 0.6$. In this position, the inclinations at this point in the ZPG region are similar, reducing the effect of the surface. This means the effect of no data in the near-wall region for the rough wall is reduced. Overall, the trends seen in section 6.6 hold for a rough wall; however, the extent of the response has some differences. To account for the scatter in the data, the initial value has been calculated as the average of

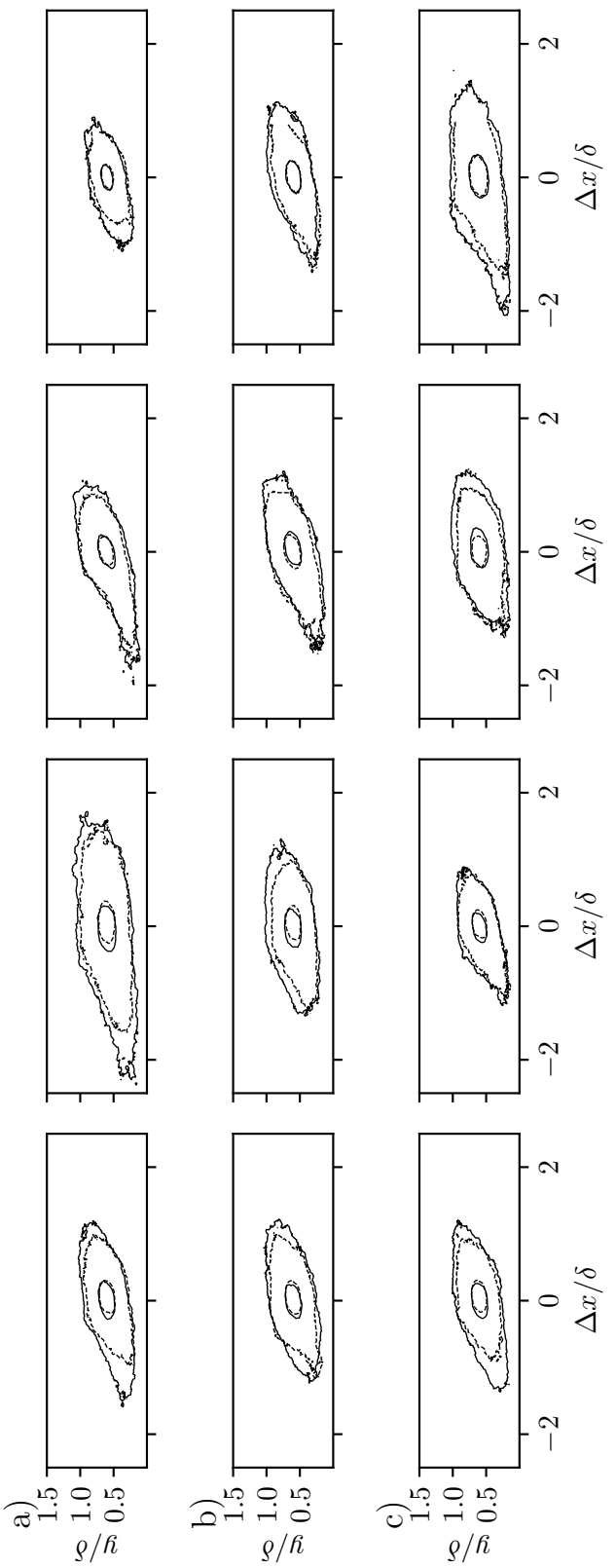

FIGURE 7.9: Contours of $R_{u'u'}$ at levels 0.2 and 0.6 for smooth (**——**) and rough wall (**- - -**) flows. Rows (*a*), (*b*) and (*c*) correspond to the -8° , 0° and 8° case. The columns correspond to $x_{ref}/c = -1$, $x_{ref}/c = 0$, $x_{ref}/c = 1$ and $x_{ref}/c = 2$.

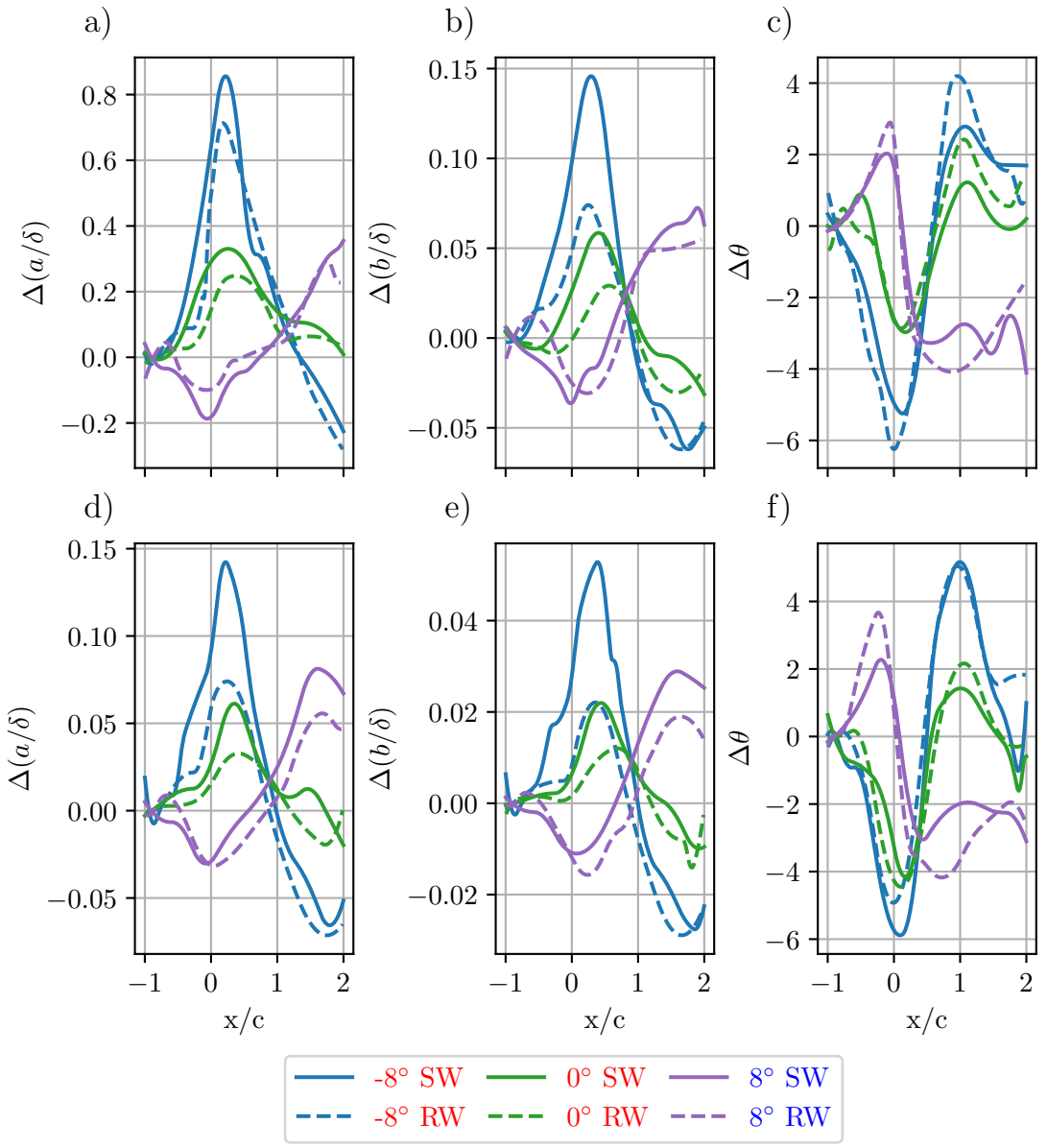

FIGURE 7.10: Comparison of streamwise development of coherent structures between the smooth and rough wall cases for the $-8°$, $0°$ and $8°$ cases, the large-scale structures are represented by a contour level of 0.2 in (*a-c*) and the small scales are represented by a contour level of 0.6 in (*d-f*), in all cases $y_{ref}/\delta = 0.6$. Sub figures (*a*) and (*d*) show the major axis variation, (*b*) and (*e*) show the minor axis variation, and (*c*) and (*f*) show the inclination variation.

the first 0.2 m of the domain. In this region, there is little variation due to the upstream ZPG history.

The effect of PG history on both the major axis of both the large and small scales is shown in figure 7.10*a* and *d*, respectively. Starting with the large-scale structures, there is good agreement between the smooth and rough walls in their response to a given PG history. The small scales show reasonable agreement for the $0°$ and $8°$ cases within the uncertainty of the method. The $-8°$ case in the FPG region, however, shows

a significant increase in the small-scale major axis compared to the rough wall case. In the APG region of the -8° case, the smooth wall recovers to the rough wall values and shows good agreement in this region. Similar trends are seen in the minor axis for both the small and large-scale axes in figure 7.10*b* and *e*. Overall, there is reasonable agreement between the smooth and rough wall structures. The largest difference is seen in the FPG region of the -8° cases, which shows significant differences. The inclination similarly shows no clear trends or differences between the smooth and rough walls. This trend is seen for both the large and small-scale structures. The response time of the flow is seen to be similar between the rough and smooth wall cases. This is based upon the turning points of the mean curve lying in the same position, within the uncertainty of the measurement, for the smooth and rough wall cases. Overall, this happens for all the variables, and it is also seen that the response time of the small and large scales is similar.

7.7 Quantitative variation in coherent structures

The preceding analysis showed significant variation in the structures due to the PG history. The trends in properties have been shown in figure 7.10. This section will look at quantifying the variation in the coherent structure properties. Figure 7.11*a* shows the variation in $\Delta(a/\delta)$, which again is defined as $\Delta(a/\delta) = (a/\delta)_{PG} - (a/\delta)_{ZPG}$, as a function of β. Only the large-scale structures are considered in the outer region with the reference point at $y_{ref}/\delta = 0.6$. There is no trend between the streamwise length of the coherent structure and the local value of β. As with previous variables, such as Π, the local PG history does not instantly affect the coherent structure; as such, there is a delay in responding to the local condition. There is also the cumulative effect due to the upstream PG history, which, as seen with previous analysis, is not accounted for using β.

The preceding analysis has shown that PG history can be quantified using the variable $\Delta\beta$ to account for changes in both Π and pre-multiplied energy from the turbulent spectra. Here $\Delta\beta$ is calculated using L from equation 7.4 developed using the PIV data. Figure 7.11*b* shows the variation $\Delta(a/\delta)$ with $\Delta\beta$, again at $y_{ref}/\delta = 0.6$ for the large scale coherent structures. There is an overall trend when plotted in such a way; however, there is a large scatter in the results. The overall trend is that as $\Delta\beta$ increases, the length of the coherent structure reduces. As could be expected from figure 7.10, there is reasonable agreement between the smooth and rough wall cases for a given value of $\Delta\beta$, supporting the agreement seen in section 7.6. The trend can be described using $\Delta\beta \propto 1/(x - x_0)$, although the constants are unimportant to the analysis. Using the trend line, the average deviation from measured data is found to be 0.08, which is a similar level of scatter to that seen from the moving average curve to variation in a/δ for figures 6.12 and 7.10. The deviation from the curve fit being similar to the scatter

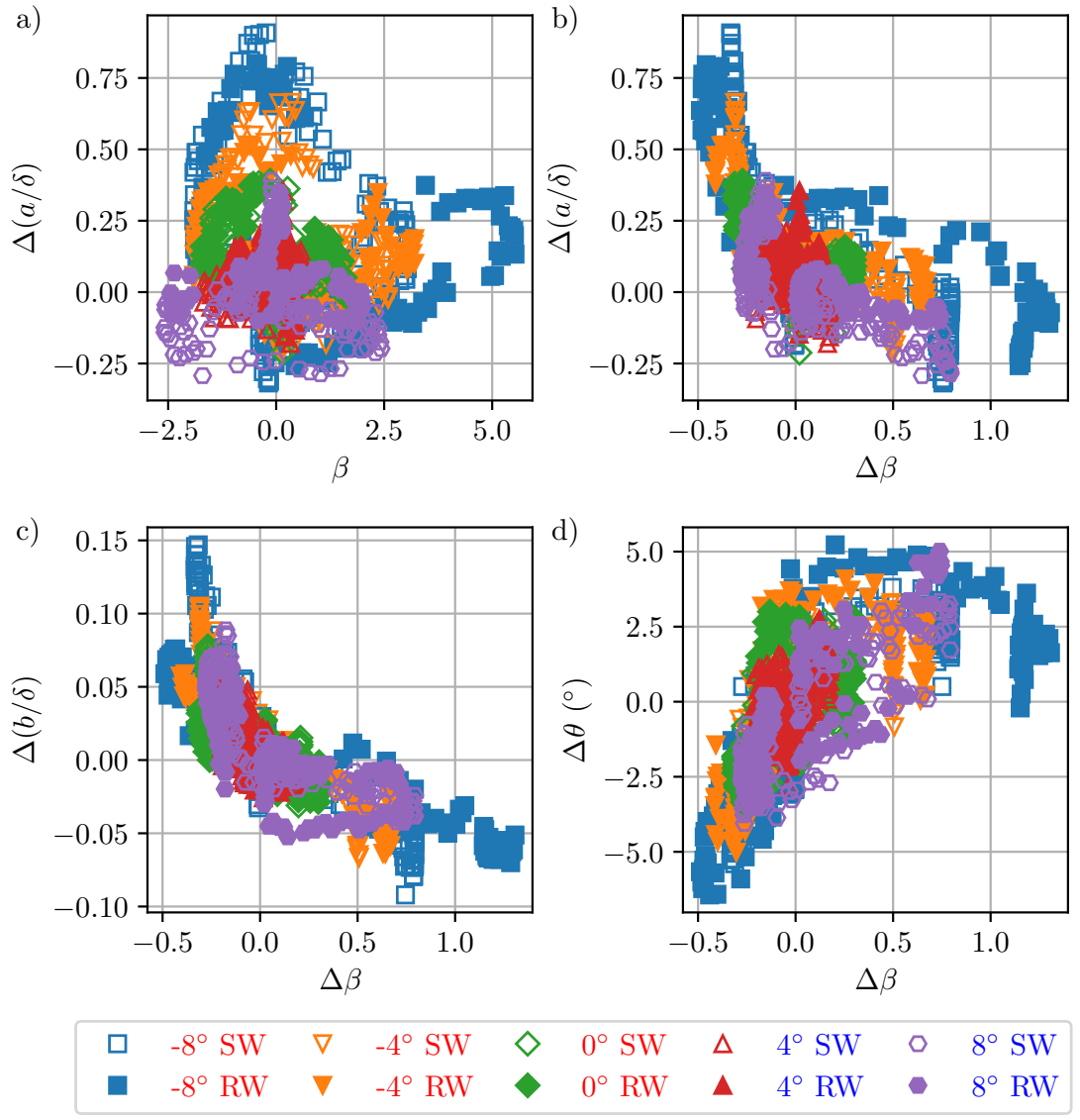

FIGURE 7.11: (*a*) Variation in large-scale coherent structure major axis, a/δ with β. (*b*) Variation in large-scale coherent structure major axis, a/δ with $\Delta\beta$. (*c*) Variation in large-scale coherent structure minor axis, b/δ with $\Delta\beta$. (*d*) Variation in large-scale coherent structure inclination, θ, with $\Delta\beta$. All cases use a contour level of 0.2 to represent the large-scale structures with $y_{ref}/\delta = 0.6$

seen in the data suggests that it is possible to account, at least partially, for the variation in the coherent structures using $\Delta\beta$. In regions of strong FPG, there are limitations in using $\Delta\beta$, as was seen when modelling Π. This is because there is a rapid increase in the length of the coherent structures, which means modelling in this region is difficult.

Figure 7.11*c* show the variation in $\Delta(b/\delta)$ with $\Delta\beta$. The collapse in the minor axis is better than that seen for the major axis. Once again, it is seen in the FPG region that $\Delta\beta$ fails to capture the change in minor axis, due to the rapid change in the minor axis with $\Delta\beta$. The relationship between $\Delta\beta$ and $\Delta(b/\delta)$ is approximately linear in the APG region. Similar behaviour can be seen in $\Delta(a/\delta)$; however, the scatter in the data is much

larger, making more detailed conclusions difficult. The final variable to consider is $\Delta\theta$ with $\Delta\beta$ shown in figure 7.11*d*. The results clearly show that the inclination reaches a maximum change of 5° at which no further increase is seen with increasing $\Delta\beta$. This supports the conclusion drawn by Lee and Sung (2009), which showed that as APG strength increases, the inclination reaches a maximum of 18°. The scatter seen in the inclination for a given value of $\Delta\beta$ is significant, reaching as much as 5°. There is, however, a clear trend where the inclination increases with increasing $\Delta\beta$, with the scatter being reduced in the FPG region. Overall, unlike when looking at the variation in Π, $\Delta\beta$ fails to adequately collapse the variation in the shape of the structures. This means that a different method is needed to capture the variation in structures; however, that is beyond the scope of this work.

7.8 Summary

Comparing the response of the smooth and rough wall cases to the same pressure gradient histories showed clear differences in the response of the flow through the domain. Despite having the same PG histories in regions of strong APG, the smooth wall TBL is seen to grow faster than that of a rough wall. When considering the β history between the smooth and rough walls, they have very similar histories except in regions of strong APG where the rough wall β is seen to be higher. This difference translates to a greater increase in the wake strength for the rough wall in regions of strong APG compared to the smooth wall. The $\Delta\beta$ model is extended to rough walls, normalising the length over which the PG history is accounted for. Testing of this result on datasets from Volino (2020) and Volino and Schultz (2023), reasonable agreement is seen in the APG region; however, the FPG region has significant errors.

The trends seen in the turbulence events are seen to be the same between the smooth and rough walls. The rough wall, however, is seen to respond faster than the corresponding smooth wall case. The same trend is seen in the response of the ILs, with the rough wall responding faster to changes in the PG compared to the smooth wall. There is a clear trend of the IL growth rate increasing as β_{max} increases, with smooth and rough wall cases appearing to lie on the same curve. When looking at the coherent structures within the flow, the rough wall structures are seen to be smaller; however, they have similar inclinations under ZPG conditions. When comparing the effect of PG histories on the structures for the large-scale structures, the change in the size of the structure was seen to be very similar between smooth and rough wall cases. Some difference was seen in regions of strong FPG for the small scales when looking at the streamwise length; however, the change in inclination of both the small and large scales is similar between rough and smooth walls.

Chapter 8

Conclusions

This thesis has examined the complex topic of turbulent pressure gradients with non-equilibrium PGs over smooth and rough walls. In chapter 2, it was seen that past research on non-equilibrium boundary layers is limited and carried out at relatively low Reynolds numbers. This results in a summary of the open questions from previous research. These open questions resulted in the aim of this work, which is "*to investigate the influence of non-equilibrium pressure gradient history on high Reynolds number turbulent boundary layers over smooth and rough walls, with a focus on the evolution of mean flow properties, turbulence statistics, and coherent flow structures.*"

To explore the aim, high Reynolds number experiments were carried out to explore the effect of PG history on the mean flow, turbulence, and structures within the flow. Chapter 3 describes the experimental setup used throughout this work. A NACA 0012 aerofoil with a chord of 1.25 m is mounted in a 12 m boundary layer to allow different PG histories to be imposed on the flow. Measurements are carried out using HWA to obtain the time-resolved single-point measurements, while PIV is used to obtain a large field of view to examine variation in structures and the flow development. Independent skin friction measurements are used, something not often seen in past research, resulting in lower uncertainty in the skin friction measurements. Examination of the PG histories imposed on the flow showed that one chord upstream and one chord downstream of the aerofoil, there was a ZPG, meaning any changes to the incoming boundary layer are due to the PG between these two points. In all cases seen throughout this work, the flow experiences both an APG and an FPG; however, the strength and order differ.

Chapter 4 examined the effect of PG history on the mean flow using single-point measurements from HWA mounted one chord downstream of the aerofoil. Independent skin friction measurements are used throughout this chapter, resulting in lower uncertainty than if conventional fitting methods were used. The skin friction measurements showed that the PG type closer to the measurement point is more important in

the final value of the skin friction. These skin friction measurements allowed the effect of PG history on the roughness length scale, y_0, to be examined. Fitting the log-law to the mean velocity profiles showed no significant variation in y_0, suggesting that y_0 is independent of the PG history.

One of the objectives of this work was to develop models which can be used to predict key boundary layer properties based on the PG history and limited measurements. This was first explored in chapter 4, introducing the parameter, $\Delta\beta$, which is used to capture the variation in pressure gradient history. This variable is a weighted integral of the PG history, which accounts for the history directly upstream of the point of interest being more important than that further upstream. It was seen that the change in the wake strength, $\Delta\Pi$, is linearly proportional to $\Delta\beta$. This relationship was similar between smooth and rough walls, meaning that the change in Π is similar for a given PG despite the ZPG values of Π being different. Utilising the PIV data, obtaining the streamwise development in $\Delta\Pi$ for different PG histories was possible. For the smooth wall data, it was seen that the distance over which the PG had to be accounted for was approximately 25δ. Using classical boundary layer properties, it was also possible to derive a relationship to normalise the distance over which the integral is calculated, independent of the surface. Applying this model to datasets from previous work showed reasonable results in the APG region; however, in the FPG region, there were significant errors.

Chapter 5 focused on the effect of PG history on the pre-multiplied energy spectra. Under APG conditions, three distinct peaks were seen in the pre-multiplied energy spectra for the smooth wall and two for the rough wall cases. The common peaks are the VLSM peak and a peak in the outer region due to the APG, along with the classical inner peak for the smooth wall. The position of the VLSM peak is seen to be independent of the PG history with inner scaling, which, with the roughness length scale also being unaffected, supports the conclusion that the PG effects are limited to the outer region. As was seen with $\Delta\Pi$, the change in the maximum outer region energy was seen to vary linearly with $\Delta\beta$. Outer layer similarity is seen to hold for weak PG histories between the smooth and rough wall cases. For stronger PG histories, however, there are differences seen in the mean turbulence, especially for the APG, where the outer peak in $\overline{u'u'}^+$ occurs further from the wall for the rough wall compared to the smooth wall.

Outer layer similarity is seen to be valid for a given non-equilibrium PG history between the smooth and rough wall cases. This is despite the upstream β histories seen to differ in the APG, which was seen to result in large changes in Π for the rough wall cases.

The effect of PG histories of the structures within the flow was explored in chapters 6 and 7. When considering the contribution of sweeps and ejections and the internal layer growth within the flow, the rough wall cases responded faster than the corresponding smooth wall cases. In the mean flow, this trend is much weaker, although it can be seen in the response of the wake strength. When considering the large-scale structures, the addition of roughness results in smaller coherent structures due to roughness breaking up structures within the flow. The major axis and inclination of the coherent structures are seen to respond similarly between smooth and rough walls. The variation in the structures shows trends with $\Delta\beta$ which were not seen with β; however, further work is required on the variation in structures due to the large scatter in the results.

Overall, this thesis has experimentally examined the effect of non-equilibrium PG histories on smooth and rough wall TBLs at high Reynolds numbers. This has included looking at the mean flow, the turbulence statistics and the flow structures to explain the variations seen from the canonical ZPG case. Within this analysis, a method for capturing the accumulated PG history has been developed and used to develop a model for the prediction of variation in Π and therefore C_f.

8.1 Future work

This thesis has experimentally explored the effect of different PG histories on high Reynolds number TBLs over smooth and rough walls. This section gives areas which can extend the findings of this thesis in future work. One of the key themes of this work is the integral pressure gradient parameter $\Delta\beta$, utilising it to develop a model for predicting the wake strength. The integration length is based on a single set of experiments in which the PG is applied over the same distance. High Reynolds number experiments with PG histories applied over different distances are required to improve these. Furthermore, a range of different roughnesses would improve the model's reliability on unknown surfaces. These would help build on the correlations given in this work, developing a model which can be used to estimate the boundary layer properties based only on the PG histories without the need for simulations or experiments.

This work considered extensively the pre-multiplied energy spectra and the scaling of the maximum energy with $\Delta\beta$. This work could not find a universal pre-multiplied energy spectrum which could be scaled based on the PG history. This is due to the complex relationships with the outer peak growing in size and position. The nature of this problem would likely require the use of machine learning, which is beyond the scope of this work; however, the trends seen in this work suggest there are methods for scaling a ZPG spectra into a PG spectra.

The PIV measurements in this work were carried out at the same unit Reynolds number based on the freestream speed and not at a matched Re_τ. While this work has shown both $\Delta\beta$ and Π to be independent of the Reynolds number, and as such can be used together to develop the predictive models in this work. A range of matched Re_τ cases would allow the effect of Reynolds number on the structures to be examined. Furthermore, it would allow the response time of the flow and how it differs with surface and Reynolds number to be examined. Due to the high uncertainty when obtaining the size of the coherent structures, more data will enable more reliable trends to be seen in the structures. It was seen in this work that the inclination reaches a maximum; it is also seen that the major axis variation starts to level off. It is currently unknown whether this tends towards an asymptote since higher APG strengths are required.

Appendix A

Linearly Varying Vortex Panel Method

Panel methods are computational techniques used to predict the flow around a body by approximating its surface with discrete panels. Based on potential flow theory, these methods provide an inviscid flow solution. Figure A.1 illustrates a discretised aerofoil represented by ten panels. Cosine spacing is employed to increase panel density near the leading and trailing edges, thereby enhancing accuracy in these critical regions.

A.1 Numerical methods

The panel method used in this study is a linearly varying vortex panel method, adapted from the work of Wang (2015) and Barba and Mesnard (2019). This method is specifically developed for modelling ground effect. It operates by calculating the vortex strength at the start and end of each panel, assuming a linear variation between these points. This approach classifies it as a second-order panel method, in contrast to the more common first-order methods often encountered during undergraduate studies. In first-order methods, a source is placed at the centre of each panel, with its strength varying between panels, while a vortex of constant strength is also positioned at the panel centre.

The general equation for linearly varying vortex panels is given by

$$\phi(x_{ci}, y_{ci}) = V_\infty x_{ci} \cos(\alpha) + V_\infty y_{ci} \sin(\alpha) - \sum_{j=1}^{N} \int_0^{s_i} \frac{\gamma(s_j)}{2\pi} \arctan\left(\frac{y_{ci} - y_j(s_j)}{x_{ci} - x_j(s_j)}\right) ds_j, \tag{A.1}$$

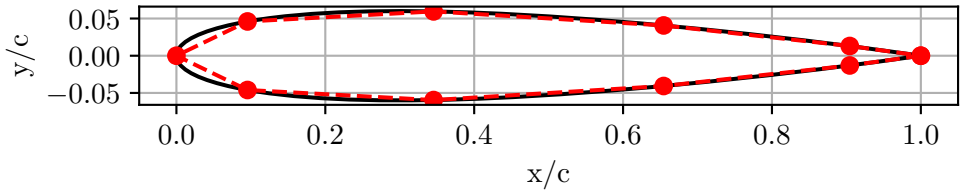

FIGURE A.1: Plot showing NACA 0012 aerofoil (——) with discretisation for ten panels (- - -).

where i is the control point number and j is the panel number (Wang 2015; Liu 2018). A control point is typically located at the centre of each panel, with s_j representing the distance along the panel. Here, ϕ is the flow potential, V_∞ is the freestream velocity, x_{ci} and y_{ci} are the coordinates of the ith control point, α is the angle of attack, $\gamma(s_j)$ is the panel strength as a function of the position along the jth panel, and $x_j(s_j)$ and $y_j(s_j)$ are the corresponding coordinates along the panel.

To solve equation A.1, a boundary condition must be applied given by

$$\frac{\partial}{\partial n_i}\phi(x_{ci}, y_{ci}) = 0, \tag{A.2}$$

which enforces zero flow normal to the panels (Wang 2015). Additionally, the Kutta condition ensures that the flow leaves the trailing edge parallel to the chord line, maintaining equal pressure. This condition is implemented via

$$\gamma_1 = -\gamma_{N+1}, \tag{A.3}$$

which equates the vortex strengths of the two trailing-edge panels to equal and opposite values (Liu 2018).

The methodology described above serves as the basis for analysing an aerofoil in a freestream. For ground effect simulations, the method of images is employed. In this approach, vortexes are reflected across the wall, maintaining equal strength but opposite direction, ensuring no flow perpendicular to the wall. In wind tunnel scenarios, the aerofoil is reflected in both the top and bottom walls. These reflections, in turn, reflect in the opposing wall, theoretically requiring infinite reflections. However, after a certain number of reflections, further iterations have a negligible impact on accuracy, thus making additional reflections unnecessary.

To account for the aerofoil and its reflections, a matrix of influence coefficients is defined. This matrix facilitates solving for the vortex strengths on each panel while ensuring the Kutta condition is satisfied (Wang 2015). Once the vortex strengths are

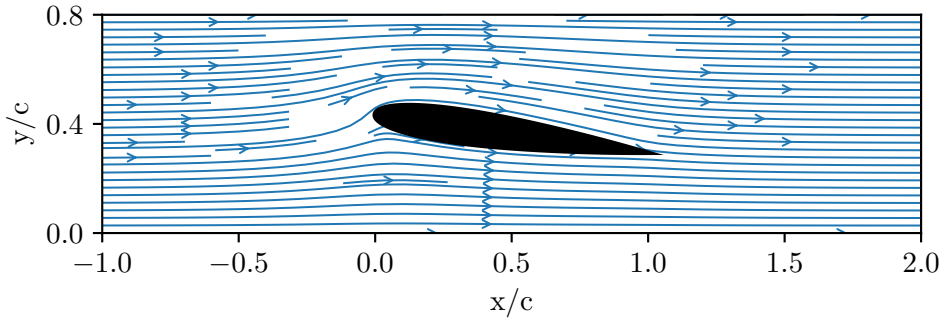

FIGURE A.2: Streamline plot of a wind tunnel setup with the aerofoil quarter chord positioned 0.5 m above the floor.

determined, velocities and pressure coefficients over the flow domain are computed using the stream function. The stream function is given by

$$\psi(x_{ci}, y_{ci}) = \underbrace{U_\infty(y_{ci} - x_{ci})}_{\textit{Uniform Freestream}} + \underbrace{\sum_{j}^{N} \int_0^{s_j} \frac{\gamma(s_j)}{2\pi} \arctan\left(\frac{y_{ci} - y_j(s_j)}{x_{ci} - x_j(s_j)}\right) ds_j}_{\textit{Aerofoil}}$$
$$+ \underbrace{\sum_{R}^{N_{reflection}} \sum_{j}^{N} (-1)^R \int_0^{s_j} \frac{\gamma(s_j)}{2\pi} \arctan\left(\frac{y_{ci} - y_{uj}(s_j)}{x_{ci} - x_{uj}(s_j)}\right) ds_j}_{\textit{Aerofoils reflected in the upper wall}}$$
$$+ \underbrace{\sum_{R}^{N_{reflection}} \sum_{j}^{N} (-1)^R \int_0^{s_j} \frac{\gamma(s_j)}{2\pi} \arctan\left(\frac{y_{ci} - y_{lj}(s_j)}{x_{ci} - x_{lj}(s_j)}\right) ds_j}_{\textit{Aerofoils reflected in the lower wall}}, \quad \text{(A.4)}$$

where $N_{reflection}$ denotes the number of reflections. The u and v velocity components can then be derived from

$$u = \frac{1}{\rho} \frac{\partial \psi}{\partial y} \quad \text{(A.5)}$$

$$v = -\frac{1}{\rho} \frac{\partial \psi}{\partial x} \quad \text{(A.6)}$$

Figure A.2 shows the resulting flow field for a NACA 0012 aerofoil positioned in a wind tunnel. The aerofoil's quarter chord is mounted 500at an angle of attack of 8°. To determine the number of reflections required for a converged solution, a sensitivity study was conducted. The final stage of the panel method was to carry out a convergence study. This was done by varying the number of panels as well as the number of reflections. The result of this is shown in figure A.3. Its clear that after 200 panels

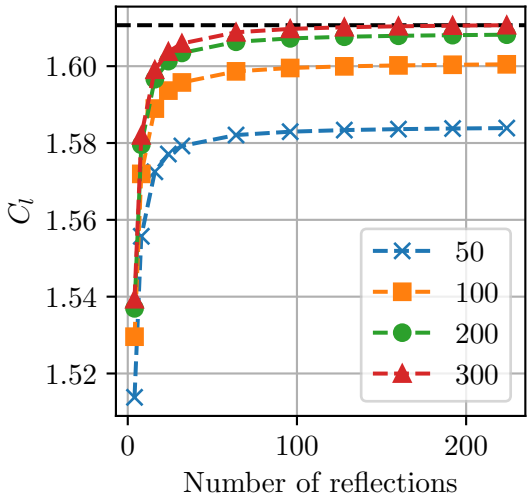

FIGURE A.3: Variation of C_l with the number of reflections for a NACA 0012 aerofoil at 5° and for different number of panels. The black dashed line shows the final value of C_l for 300 panels.

the variation the final C_l is minimal however the solution time increases. After 100 reflections, there is minimal change in the value of C_l. It was therefore chosen to use 200 panels with 100 reflections to obtain the predicted wall pressure distribution.

Figure A.4*a* shows the C_p distributions from the panel method simulations for five angles of attack at $h/c = 0.4$. This is the equivalent of the $h = 0.5$ m cases that are used throughout this thesis. Varying the angle of attack leads to different pressure distributions along the bottom wall. Figure A.4*b* shows the distribution of $dCp/d(x/c)$ along the bottom wall. It can be seen that the region of influence for the aerofoil is limited to one chord upstream of the leading edge and one chord downstream of the trailing edge. The order of the APG and FPGs depends on the angle of attack, as does the strength.

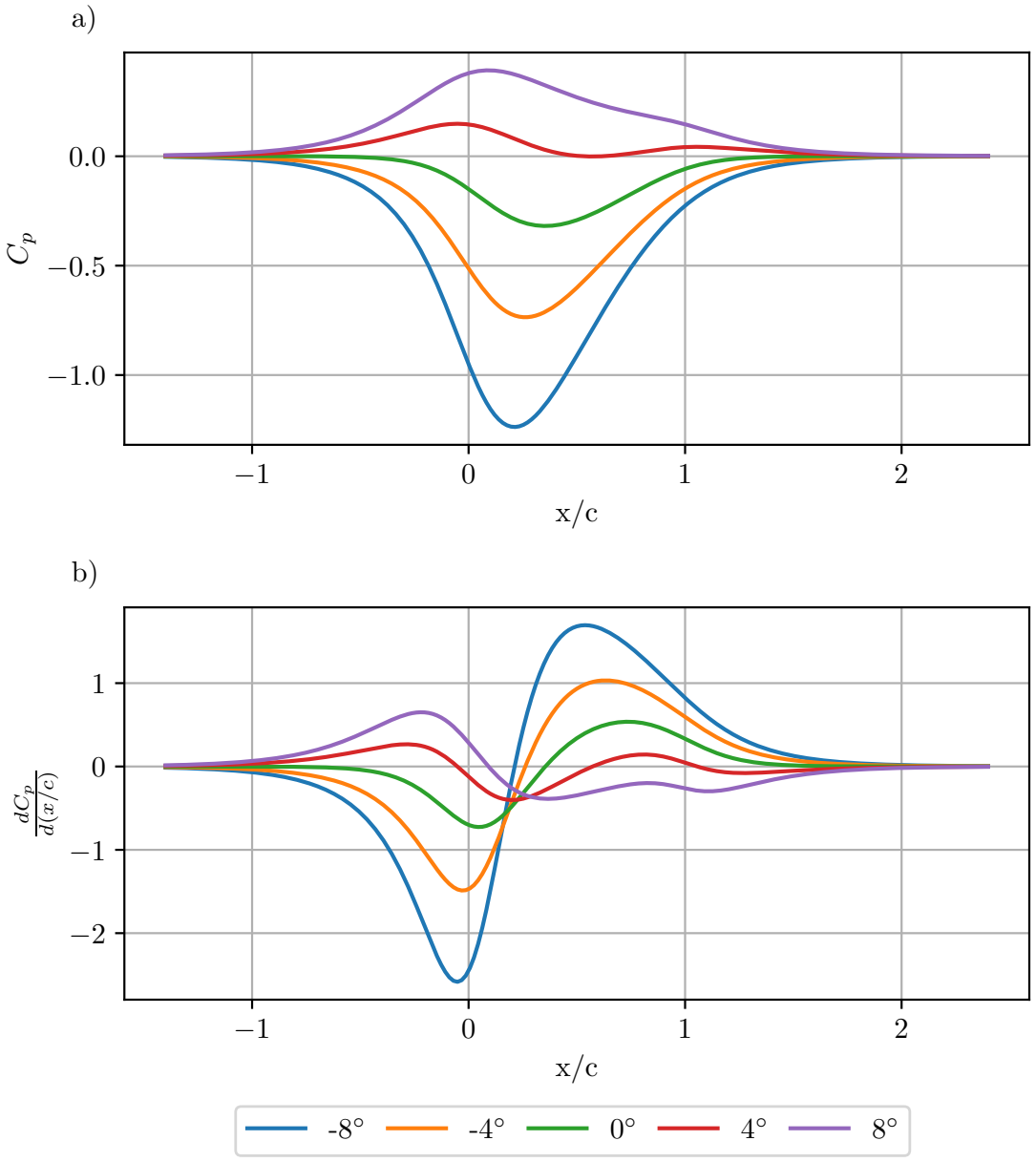

FIGURE A.4: Results of panel method simulation for different angles of attack at h = 0.5 m. (a) shows the mean pressure coefficient, C_p. (b) shows the mean pressure gradient with respect to x/c, $\frac{dC_p}{d(x/c)}$

Appendix B

Correction of Wall Position - HWA

The hot wire probe holder was found to deflect meaning the initial wall position was incorrect since the probe is deflected towards the wall. This deflection is varies with speed and therefore needs to be corrected for. For a high enough speed this deflection means the first couple of data points are obtained with the probed pushed against the wall. In section 2.4 it was noted that the inner scaled peak of the streamwise Reynolds stress is always located at $y^+ = 15$ independent of Reynolds number and PG history. Using the independently measured skin friction the wall position is corrected to ensure the peak occurs at $y^+ = 15$. This is done by fitting a quadratic curve through the inner peak points from which the maximum peak location be obtained. This correction is calculated for all data sets individually and applied to the data set. Table B.1 gives the correction values for all the cases.

It is seen in table B.1 that the maximum deflection is 0.76 mm seen for the 30 m/s cases and the deflection increases non linearly with speed. Figure B.1*c* and *b* shows the corrected inner scaled velocity profiles and streamwise turbulence profiles. Figures B.1*c* and *d* are used to remove erroneous data points from from the final datasets. The main tool used is the diagnostic plot as defined by Alfredsson and Örlü (2010) which has no dependence on the wall position. Therefore it is possible to remove erogenous data points based on the just the velocity signal. The 10 m/s was used as the baseline dataset since the there is least deflection in these cases and therefore not pressed into the wall. For the 20 and 30 m/s any points deviating from the path of the 10 m/s were

	$-8°$	$-4°$	$0°$	$4°$	$8°$	Avg. (mm)
10 m/s	-0.16	0.01	-0.20	-0.11	-0.10	-0.11
20 m/s	-0.15	-0.31	-0.32	-0.34	-0.30	-0.29
30 m/s	-0.69	-0.74	-0.61	-0.76	-0.68	-0.70

TABLE B.1: Correction of hot wire probe position in mm for the different PG cases with $h = 0.5$ m, negative value means the wall position is shifted downwards from the initial position.

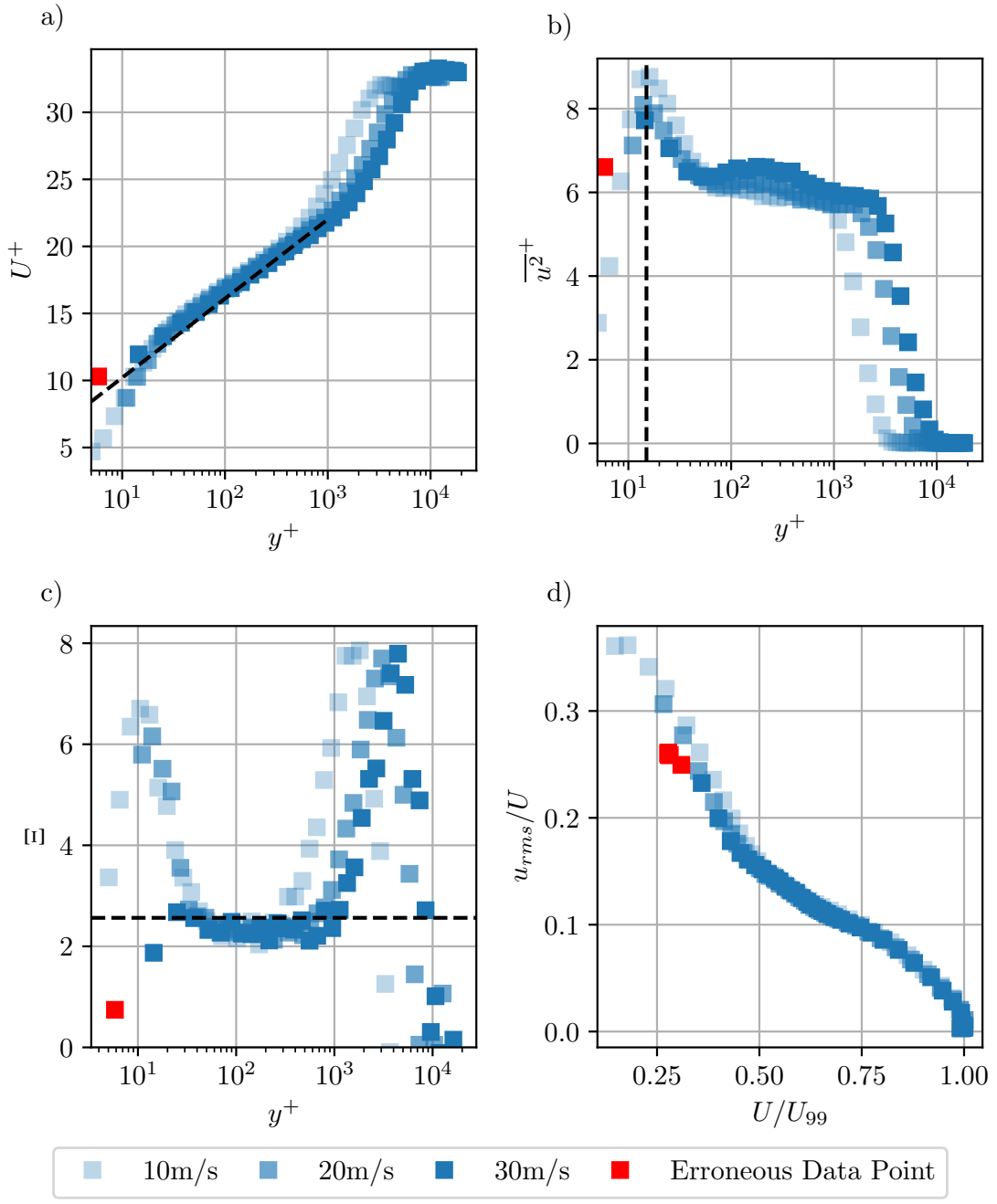

FIGURE B.1: Plots used when correcting the wall position for the smooth wall cases, shown for the $-8°$ case. (*a*) shows inner scaled velocity profile with the back dashed line showing the classical smooth wall log law given by equation 2.6. (*b*) Shows the inner scaled streamwise Reynolds stress with the vertical dashed black line at $y^+ = 15$. (*c*) The diagnostic function as defined by equation B.1 with the black dashed line showing $\Xi = 1/\kappa$. (*d*) The diagnostic plot as defined by Alfredsson and Örlü (2010) showing outer scaled root mean square of the velocity signal as a function of the mean velocity.

discounted as shown in figure B.1 by the red data points. The diagnostic function, Ξ, as defined by

$$\Xi = y^+ \frac{dU^+}{dy^+}, \tag{B.1}$$

is used in figure B.1*c* to confirm which data points need to be removed.

Appendix C

Fitting of the logarithmic region constants

The log law of a rough wall TBL, as shown by equation 2.16, is requires known of the zero plane displacement (d) and the roughness length (y_0). When fitting d it was chosen to pick a value which maximises the length of the log region while keeping the error within the acceptable bounds. For both d and y_0, all Reynolds numbers are used together to find the constants for a given PG history. In order to find d and initial

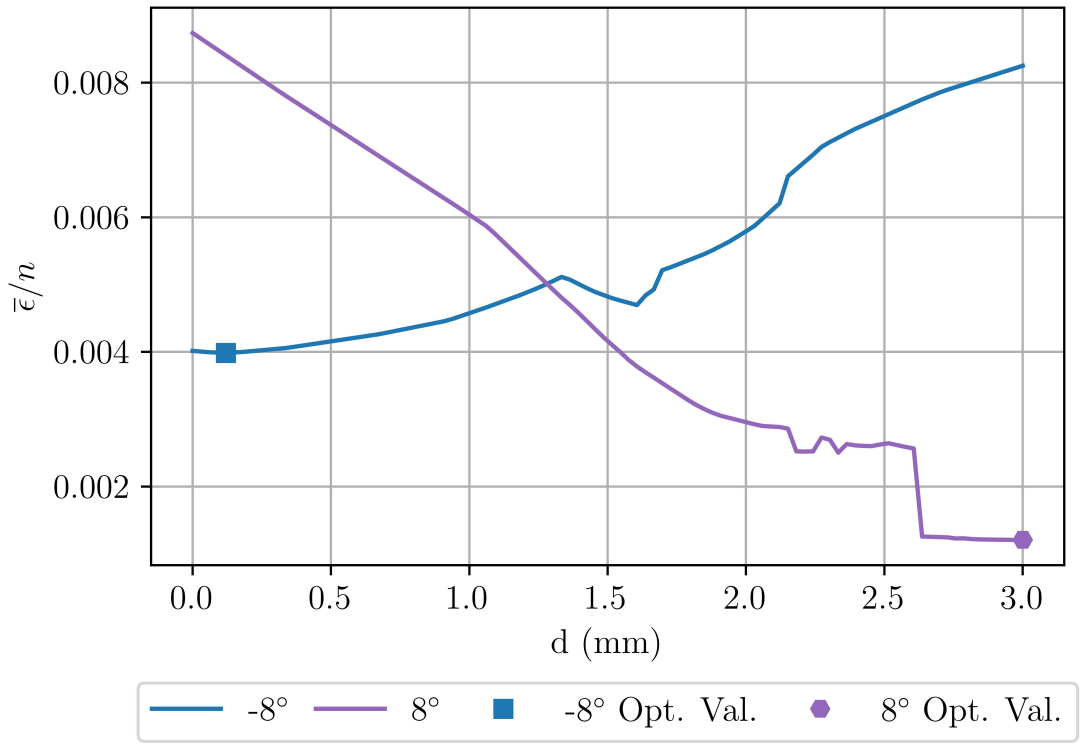

FIGURE C.1: Variation in average error, $\bar{\epsilon}$, normalised with the number of points within the log region as a function of zero plane displacement, d.

array of d values are test from 0 to 3mm, the top of the roughness elements. The log region bounds for a given value of d are defined to find the longest length of log region. The log region is calculated using the diagnostic function, $\Xi = \frac{1}{U_\tau}\frac{dU}{dy}(y-d)$, which in the log law is equal to $1/\kappa$. The longest log region for a given value of d is defined such that the average error, $\overline{\epsilon}$, of all points within the region lies within $\pm 5\%$ of $1/\kappa$. The minimum length of the log region is restricted to seven points to ensure a sufficient number of samples for fitting the constants. This is repeated for each test value of d and the result shown in figure C.1, however here the average error has been normalised with the number of points in the log region again to favour longer log regions. The optimum value of d is then found which as shown by the markers in figure figure C.1.

Example plots of the diagnostic function, Ξ, are given in figures C.2*a* and *b* for the -8° and 8° cases. These are plotted with the optimised value of d founds using the above method. The red lines on each plot show the limits of the log region from the d was fitted, this being the region in which the error is within the acceptable range.

Taking all Reynolds numbers together with all points that lie within the log region bounds, it is possible to find the value of y_0. This is done by the fitting of the log region, defined for a rough wall as

$$U^+ = \frac{1}{\kappa} ln\left(\frac{y-d}{y_0}\right) \tag{C.1}$$

Figure C.3*a* and *b* shows two example boundary layer plots for -8° and 8°, with the best fit of the log region show by the dashed black line.

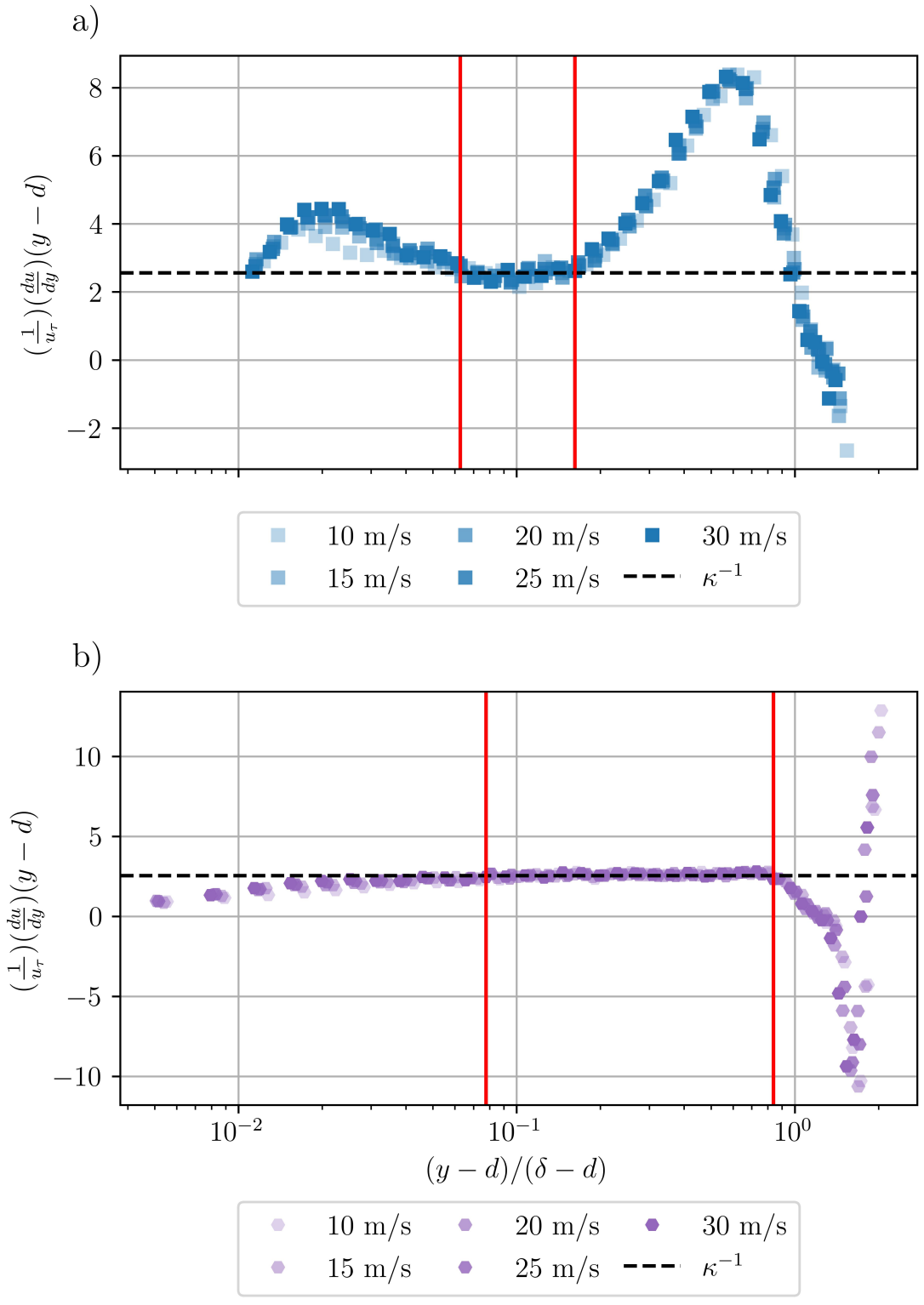

FIGURE C.2: Diagnostic plot for *a* −8° and *b* 8° for the five Reynolds numbers tested. The black dashed line shows the theoretical value of the diagnostic function in the log region, defined by $1/\kappa$. The vertical red lines shows the limits of the log region where the error is within ±5% of $1/\kappa$.

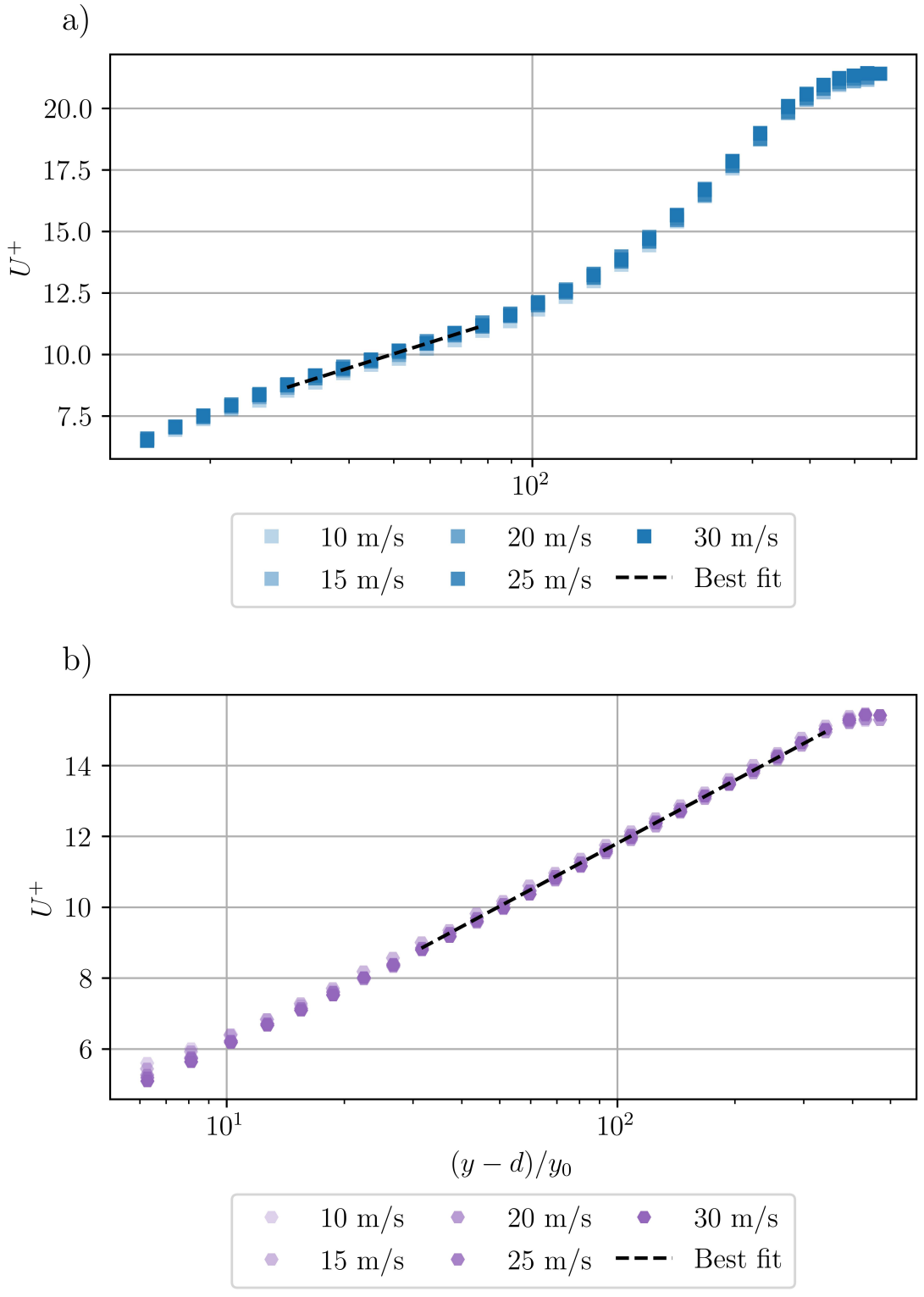

FIGURE C.3: Example boundary layers plots of U^+ vs $(y-d)/y_0$ which are used for the fitting of y_0. Shown for *a* $-8°$ and *b* $8°$ for the five Reynolds numbers tested. The black dashed line shows the log region fit as calculated from

Appendix D

First Steps Towards Reconciling the Model Presented in Perry et al. (2002) with the Current Work

The work of Perry et al. 2002 presented a model which incorporates pressure gradient history effects into calculating Π. The key parameter for their work is ζ, which is given by equation 2.22. Using this parameter, they define a relationship for β, which is shown in equation 2.23. This gives $\beta = f(\Pi, d\Pi/dx)$ that, for many flows, presents a problem since knowing $d\Pi/dx$ is often not practical or possible to predict. It requires measurements at regular intervals with skin friction and boundary layer measurements at each station.

Using the definition of β it is possible to rewrite equation 2.23 in the form of equation 4.2 as

$$\frac{1}{x_{DS} - x_{US}} \int_{x_{US}}^{x_{DS}} \frac{dP}{dx} w(x) dx = \frac{1}{x_{DS} - x_{US}} \int_{x_{US}}^{x_{DS}} \frac{\tau_w}{\delta^*} f\left(\Pi, \frac{d\Pi}{dx}\right) w(x) dx, \tag{D.1}$$

where $f(\Pi, d\Pi/dx)$ is given by equation 2.23. The left hand side is the weighted integral of the pressure gradient and the right hand side comes from equation 2.23.

Figure D.1 shows contours of Π and β from Perry et al. (2002) for various values of ζ. A flow with a given pressure gradient history will trace out a path in this space. However, the $\Delta\beta$ term in the current study is a weighted integral of the pressure gradient term, and this will take on a value that can only be obtained through the integration of the function in this space. Figure D.1 also shows the curve that relates $\Delta\beta$ against Π from equation 4.3. It is clear that the relationship in equation 4.3 jumps from across different ζ curves for different pressure gradient histories. This can also be seen

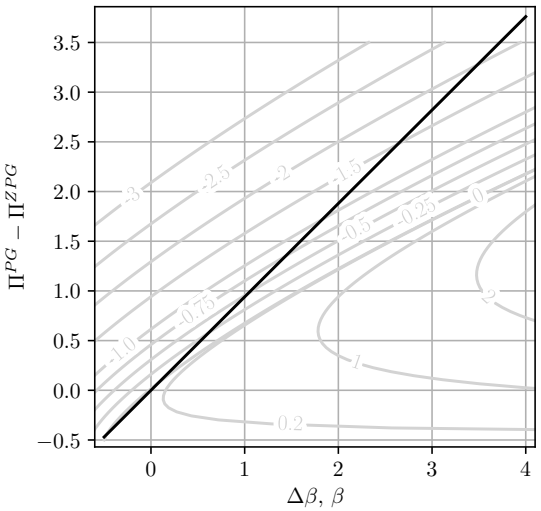

FIGURE D.1: Comparison of variation $\Pi^{PG} - \Pi^{ZPG}$ with $\Delta\beta$ as given by equation 4.3 and variation in $\Pi^{PG} - \Pi^{ZPG}$ with β from the model of Perry et al. (2002). The black line is showing the fit of 4.3 and the labelled lines show variation of $\Pi_{PG} - \Pi_{ZPG}$ for different ζ values from equation 2.23.

from equation D.1 where $\Delta\beta$ is indeed an integral across different curves. The effect of this space is, in fact, captured through the weighting function, and at this stage, linear weighting appears to capture the trends reasonably well. However, further work is required to tune the weighting function for different pressure gradient histories and to reconcile the similarities/differences with Perry et al. (2002).

Appendix E

Comparison of Current Work with Castro (2007)

Castro (2007) provided a three parameter model for skin friction $C_f = f(\frac{\theta}{y_0}, H, \Pi)$ over rough walls in ZPG conditions (where H is the shape factor of the boundary layer and θ is the momentum thickness). This work showed that for a given value of Π and H the variation in C_f with θ/y_0 can be calculated using

$$\sqrt{\frac{2}{C_f}} = -\frac{1}{\kappa} ln\left(\frac{1}{H}\sqrt{\frac{C_f}{2}}\right) + \frac{1}{\kappa} ln\left(\frac{\theta}{y_0}\right) + \frac{2\Pi}{\kappa} - \frac{1}{\kappa} ln\left(\frac{1+\Pi}{\kappa}\right) \tag{E.1}$$

Alternatively, it is also possible to obtain a variation of C_f with H for different values of Π using

$$\sqrt{\frac{2}{C_f}} = \left(\frac{H}{H-1}\right)\left[\frac{2.009 + 3.018\Pi + 1.486\Pi^2}{\kappa(0.983+\Pi)}\right] \tag{E.2}$$

Note that the constants in equation E.2 are taken directly from Castro (2007) and they depend on the type of wake profile fitted to the velocity data. This is consistent with the use of Lewkowicz (1982) polynomial wake profile, which is also used in the current study.

This analysis can be extended to flows with pressure gradients. Figure E.1*a* and E.1*b* shows the predictions of C_f as a function of θ/y_0 as well as C_f versus H for the different rough wall flows examined in this study. Lines of constant Π are shown in both figures and these lines are based on the value of Π from the new correlation developed in section 4.4 for different pressure gradient histories.

Both figures show very good agreement between trendlines for different Π and the skin friction measured. We also attempted to fit the wake function from Coles (1956)

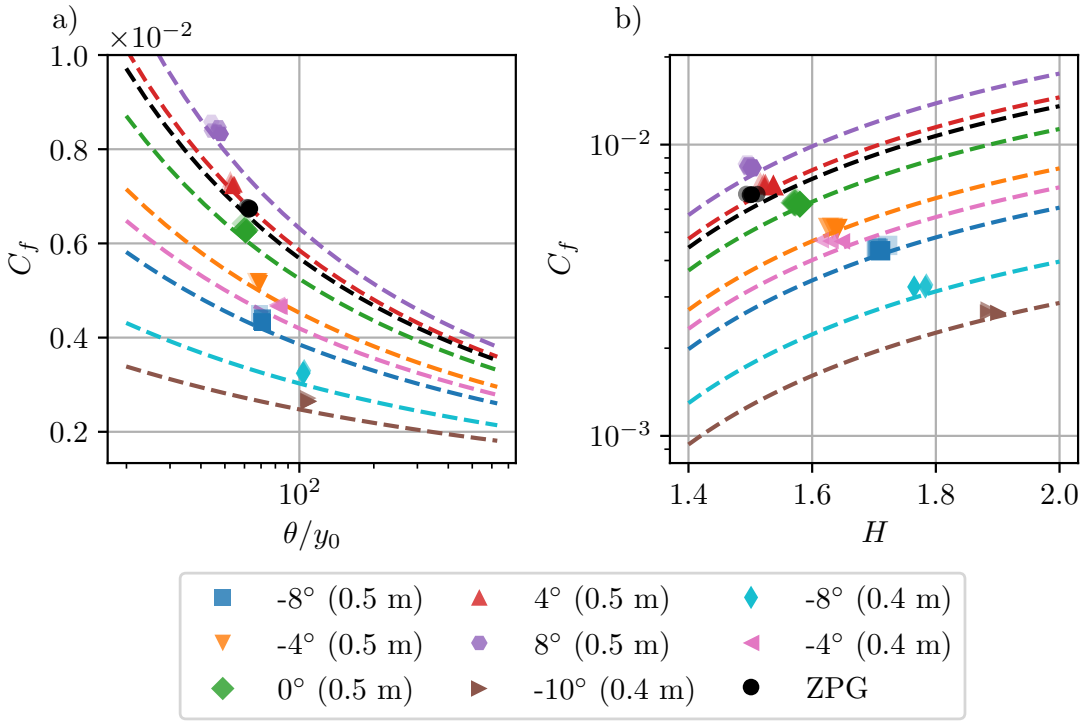

FIGURE E.1: Three parameter model based on Castro (2007) where it is assumed $C_f = f(\theta/y_0, H, \Pi)$. (*a*) Variation in C_f with θ/y_0 curves show predicted C_f variation for each cases Π from equation E.1. (*b*) Variation in C_f with H curves shows predicted C_f variation for each case Π from equation E.2.

wake function which does not seem to affect the fitted value of Π. However, in this case, the coefficients in equation E.2 have to be altered. Regardless, this agreement shows that the method proposed in the current work is consistent with the results of Castro (2007), provided a suitable value of Π as determined from $\Delta\beta$ is used.

Appendix F

Edge of the logarithmic region

Section 5.1 showed two clear crossover points when using outer scaling. The smooth wall crossover point occurs at 0.13δ and is very close to the limit of the log region of 0.15δ (Jiménez (2004); Smits et al. (2011)). Therefore, this crossover point could be interpreted as the end of the log region in which VLSMs are present. To explore the extent of the log region, the diagnostic function, $\Xi = y^+ dU^+/dy^+$, is used. Figure F.1*a* shows the diagnostic function for the smooth wall at 30 m/s. It is seen that there is a

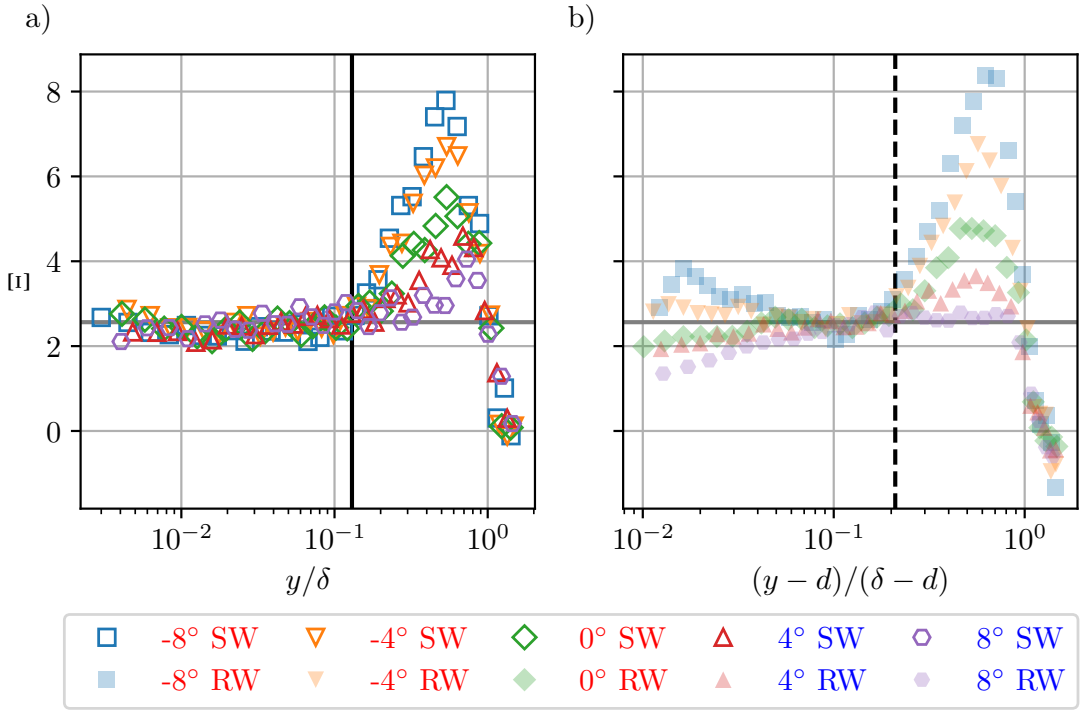

FIGURE F.1: Diagnostic function, Ξ, at $Re_\tau \approx 6800 - 8300$ for *a)* smooth wall and *b)* rough wall. Smooth wall data is taken at 30 m/s and rough wall data at 10 m/s. The black solid line is at 0.13δ and the dashed black line is at 0.21δ. The solid grey line shows the value of $1/\kappa$.

region of $\Xi = 1/\kappa$ sown by the horizontal grey line. The 0.13δ line is close to where the -8° case deviates from logarithmic behaviour. It can be seen that APGs lead to an earlier departure from the log region than FPGs. Therefore, the log region is extended as the pressure gradient switches from APG to FPG.

Figure F.1*b* presents the same analysis for a rough-wall flow at a similar Re_τ. The results indicate that the log region extends to approximately 0.2δ due to roughness, closely matching the crossover point of 0.21δ observed in the turbulence profiles. The trends with PG remain consistent regarding deviations from logarithmic behaviour.

Appendix G

Comparison of $\Delta\beta$ vs $\Delta\Pi$ for Smooth and Rough Walls

A comparison of the variation of $\Pi_{PG} - \Pi_{ZPG}$ with $\Delta\beta$ is provided in figure G.1. Here $\Delta\beta$ has been calculated using the δ^* from the HWA profiles. This differs from that

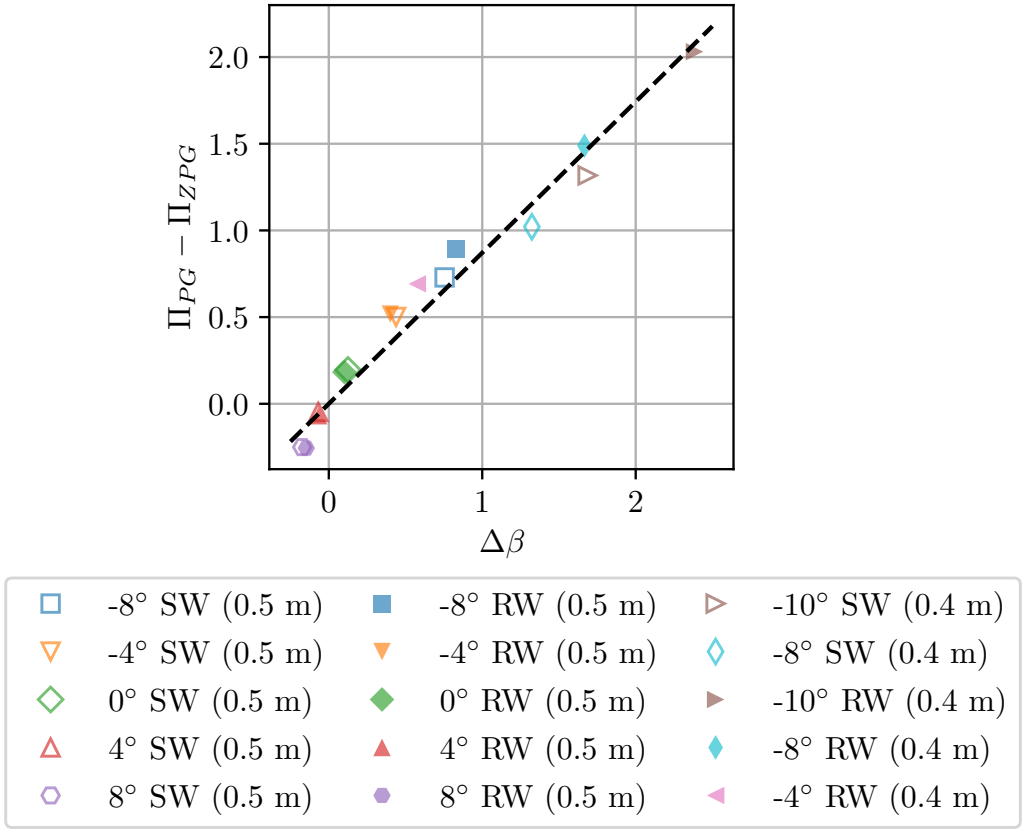

FIGURE G.1: Variation in $\Pi_{PG} - \Pi_{ZPG}$ with $\Delta\beta$ for the smooth and rough wall cases. Here $\Delta\beta$ is calculated using the measured δ^* from the corresponding HWA profiles, note this is different from figure 4.9.

shown in figure 4.9, which calculated δ^* from the composite profile. The variation in $\Pi_{PG} - \Pi_{ZPG}$ with $\Delta\beta$ is the same for the smooth and rough walls. The trend line shown has a gradient of 0.87, which is similar to the 0.94 found in equation 4.3.

References

R.J. Adrian. Hairpin vortex organization in wall turbulence. *Physics of Fluids*, 19(4): 041301, 2007.

R.J. Adrian and J. Westerweel. *Particle Image Velocimetry*. Cambridge University Press, 2011.

R.J. Adrian, C.D. Meinhart, and C.D. Tomkins. Vortex organization in the outer region of the turbulent boundary layer. *Journal of Fluid Mechanics*, 422:1–54, 2000.

N. Agathangelou. Velocity measurements of turbulent boundary layers subject to pressure gradients. Undergraduate thesis, University of Southampton, 2024.

M. Aguiar Ferreira, P. Costa, and B. Ganapathisubramani. Wall shear stress measurement using a zero-displacement floating-element balance. *Experiments in Fluids*, 65 (4):56, 2024.

P.H. Alfredsson and R. Örlü. The diagnostic plot — a litmus test for wall bounded turbulence data. *European Journal of Mechanics - B/Fluids*, 29(6):403–406, 2010.

R.A. Antonia and R.E. Luxton. The response of a turbulent boundary layer to a step change in surface roughness part 1. smooth to rough. *Journal of Fluid Mechanics*, 48 (4):721–761, 1971.

R.A. Antonia and R.E. Luxton. The response of a turbulent boundary layer to a step change in surface roughness. part 2. rough-to-smooth. *Journal of Fluid Mechanics*, 53 (4):737–757, 1972.

C.D. Aubertine and J.K. Eaton. Turbulence development in a non-equilibrium turbulent boundary layer with mild adverse pressure gradient. *Journal of Fluid Mechanics*, 532: 345–364, 2005.

R. Balin and K.E. Jansen. Direct numerical simulation of a turbulent boundary layer over a bump with strong pressure gradients. *Journal of Fluid Mechanics*, 918:A14, 2021.

L.A. Barba and O. Mesnard. Aero python: classical aerodynamics of potential flow using python. *Journal of Open Source Education*, 2(15), 2019.

V. Baskaran, A.J. Smits, and P.N. Joubert. A turbulent flow over a curved hill part 1. growth of an internal boundary layer. *Journal of Fluid Mechanics*, 182:47–83, 1987.

V. Baskaran, A.J. Smits, and P.N. Joubert. A turbulent flow over a curved hill. part 2. effects of streamline curvature and streamwise pressure gradient. *Journal of Fluid Mechanics*, 232:377–402, 1991.

L.H. Benedict and R.D. Gould. Towards better uncertainty estimates for turbulence statistics. *Experiments in Fluids*, 22(2):129–136, 1996.

R.F. Blackwelder and H. Eckelmann. Streamwise vortices associated with the bursting phenomenon. *Journal of Fluid Mechanics*, 94(3):577–594, 1979.

A. Bobke, R. Vinuesa, R. Örlü, and P. Schlatter. History effects and near equilibrium in adverse-pressure-gradient turbulent boundary layers. *Journal of Fluid Mechanics*, 820: 667–692, 2017.

G. Borrell, J.A. Sillero, and J. Jiménez. A code for direct numerical simulation of turbulent boundary layers at high reynolds numbers in bg/p supercomputers. *Computers & Fluids*, 80:37–43, 2013.

Cadisch Precision Meshes. Expanded metal, n.d. URL `www.cadischprecisionmeshes.co.uk/site_downloads/Expanded.pdf`. Accessed: 18-01-2025.

R.B. Cal, G. Johansson, and L. Castillo. Upstream condition effects on turbulent boundary layers subject to favorable pressure gradients. *AIAA Journal*, 44(11):2488–2499, 2006.

Y. Cao, Z. Wu, Y. Su, and Z. Xu. Aircraft flight characteristics in icing conditions. *Progress in Aerospace Sciences*, 74:62–80, 2015.

I.P. Castro. Rough-wall boundary layers: Mean flow universality. *Journal of Fluid Mechanics*, 585:469–485, 2007.

I.P. Castro and C. Vanderwel. Turbulent flows: an introduction, 2021.

K.T. Christensen and Y. Wu. Characteristics of vortex organization in the outer layer of wall turbulence. In *Fourth Intl Symp. on Turbulence and Shear Flow Phenomena*, volume 3, pages 1025–1030, 2005.

D. Chung, N. Hutchins, M.P. Schultz, and K.A. Flack. Predicting the drag of rough surfaces. *Annu. Rev. Fluid Mech. 2021*, 53:439–471, 2021.

F.H. Clauser. Turbulent boundary layers in adverse pressure gradients. *Journal of the Aeronautical Sciences*, 21(2):91–108, 1954.

D. Coles. The law of the wake in the turbulent boundary layer. *Journal of Fluid Mechanics*, 1(2):191–226, 1956.

E.R. Corino and R.S. Brodkey. A visual investigation of the wall region in turbulent flow. *Journal of Fluid Mechanics*, 37(1):1–30, 1969.

D. Das. A numerical study of turbulent separated flows. In *Forum on Turbulent Flow*, pages 85–90. American Society of Mechanical Engineers, 1987.

D.B. De Graaff and J.K. Eaton. Reynolds-number scaling of the flat-plate turbulent boundary layer. *Journal of Fluid Mechanics*, 422:319–346, 2000.

S. Deng and Z. Mi. A review on carbon emissions of global shipping. *Marine Development*, 1(1):4, 2023.

R. Deshpande, A. van den Bogaard, R. Vinuesa, L. Lindić, and I. Marusic. Reynolds-number effects on the outer region of adverse-pressure-gradient turbulent boundary layers. *Physical Review Fluids*, 8(12):124604, 2023.

Epri Journal. A new approach to predict life of corrosion-pitted turbine blades, 2015. URL https://eprijournal.com/epri-led-effort-helps-predict-life-of-corrosion-pitted-turbine-blades. Last accessed: 2025-07-05.

K.A. Flack and M.P. Schultz. Review of hydraulic roughness scales in the fully rough regime. *Journal of Fluids Engineering, Transactions of the ASME*, 132:041203, 2010.

K.A. Flack and M.P. Schultz. Roughness effects on wall-bounded turbulent flows. *Physics of Fluids*, 26(10):101305, 2014.

K.A. Flack, M.P. Schultz, and T.A. Shapiro. Experimental support for townsend's reynolds number similarity hypothesis on rough walls. *Physics of Fluids*, 17(3):035102, 2005.

K.A. Flack, M.P. Schultz, and J.S. Connelly. Examination of a critical roughness height for outer layer similarity. *Physics of Fluids*, 19(9):095104, 2007.

Flight Safety Foundation. Discoveries on ice, 2017. URL https://flightsafety.org/asw-article/discoveries-on-ice. Last accessed: 2025-07-05.

D.J. Fritsch, V. Vishwanathan, C.J. Roy, K.T. Lowe, and W.J. Devenport. Turbulence and pressure fluctuations in rough wall boundary layers in pressure gradients. *Experiments in Fluids*, 63(9):140, 2022.

B. Ganapathisubramani, E.K. Longmire, and I. Marusic. Characteristics of vortex packets in turbulent boundary layers. *Journal of Fluid Mechanics*, 478:35–46, 2003.

F. Ghanadi and L. Djenidi. Study of a rough-wall turbulent boundary layer under pressure gradient. *Journal of Fluid Mechanics*, 938:A17, 2022.

A.J. Grass. Structural features of turbulent flow over smooth and rough boundaries. *Journal of Fluid Mechanics*, 50(2):233–255, 1971.

M. Gul and B. Ganapathisubramani. Revisiting rough-wall turbulent boundary layers over sand-grain roughness. *Journal of Fluid Mechanics*, 911:A26, 2021.

GUNT Gerätebau GmbH . Windtunnel für grenzschichtuntersuchung 008.blwt, 2020a. Technical drawing, internal document.

GUNT Gerätebau GmbH . Blwt messstrecke, 2020b. CAD Drawing, internal document.

F.R. Hama. *Boundary-layer Characteristics for Smooth and Rough Surfaces*, volume 62. Transactions of the Society of Naval Architects and Marine Engineers, 1954.

Z. Harun, J.P. Monty, R. Mathis, and I. Marusic. Pressure gradient effects on the large-scale structure of turbulent boundary layers. *Journal of Fluid Mechanics*, 715:477–498, 2013.

M.R. Head and P. Bandyopadhyay. New aspects of turbulent boundary-layer structure. *Journal of Fluid Mechanics*, 107:297–338, 1981.

H.M. Goverment. Net zero strategy: Build back greener. Report, Department for Energy Security and Net Zero and Department for Business, Energy & Industrial Strategy, 2021.

N. Hutchins and I. Marusic. Large-scale influences in near-wall turbulence. *Philosophical Transactions of the Royal Society A: Mathematical, Physical and Engineering Sciences*, 365(1852):647–664, 2007a.

N. Hutchins and I. Marusic. Evidence of very long meandering features in the logarithmic region of turbulent boundary layers. *Journal of Fluid Mechanics*, 579:1–28, 2007b.

N. Hutchins, T.B. Nickels, I. Marusic, and M.S. Chong. Hot-wire spatial resolution issues in wall-bounded turbulence. *Journal of Fluid Mechanics*, 635:103–136, 2009.

J. Jiménez. Turbulent flows over rough walls. *Annual Review of Fluid Mechanics*, 36: 173–196, 2004.

F.E. Jørgensen. *How to measure turbulence with hot-wire anemometers: a practical guide*. Dantec dynamics, 2001.

H.T. Kim, S.J. Kline, and W.C. Reynolds. The production of turbulence near a smooth wall in a turbulent boundary layer. *Journal of Fluid Mechanics*, 50(1):133–160, 1971.

L. Kirkup and R.B. Frenkel. *An Introduction to Uncertainty in Measurement: Using the GUM (Guide to the Expression of Uncertainty in Measurement)*. Cambridge University Press, Cambridge, 2006.

S. Kline and P. Runstadler. Some preliminary results of visual studies of the flow model of the wall layers of the turbulent boundary layer. *Journal of Applied Mechanics*, 1959.

S.J. Kline, W.C. Reynolds, F.A. Schraub, and P.W. Runstadler. The structure of turbulent boundary layers. *Journal of Fluid Mechanics*, 30(4):741–773, 1967.

T. Knopp, N. Reuther, M. Novara, D. Schanz, E. Schülein, A. Schröder, and C.J. Kähler. Experimental analysis of the log law at adverse pressure gradient. *Journal of Fluid Mechanics*, 918:A17, 2021.

P.A. Krogstad, R.A. Antonia, and L.W.B. Browne. Comparison between rough and smooth-wall turbulent boundary layers. *Journal of Fluid Mechanics*, 245:599–617, 1992.

P.Å. Krogstad and P.E. Skåre. Influence of a strong adverse pressure gradient on the turbulent structure in a boundary layer. *Physics of Fluids*, 7(8):2014–2024, 1995.

B.E. Launder. Laminarization of the turbulent boundary layer in a severe acceleration. *Journal of Applied Mechanics*, 1964.

J. Lawson, B. Ganapathisubramani, and M. Taylor. Pivtools: A unified open-source platform for piv analysis. *University of Southampton*, 2024. Paper coming soon.

J.H. Lee. Large-scale motions in turbulent boundary layers subjected to adverse pressure gradients. *Journal of Fluid Mechanics*, 810:323–361, 2017.

J.H. Lee and H.J. Sung. Structures in turbulent boundary layers subjected to adverse pressure gradients. *Journal of Fluid Mechanics*, 639:101–131, 2009.

A. Lewkowicz. An improved universal wake function for turbulent boundary layers and some of its consequences. *Z. Flugwiss. Weltraumforsch*, 6:261–266, 1982.

P.M. Ligrani and P. Bradshaw. Spatial resolution and measurement of turbulence in the viscous sublayer using subminiature hot-wire probes. *Experiments in Fluids*, 5(6): 407–417, 1987.

H. Liu. Linear strength vortex panel method for naca 4412 airfoil. In *IOP Conference Series: Materials Science and Engineering*, volume 326, page 012016. IOP Publishing, 2018.

S.S. Lu and W.W. Willmarth. Measurements of the structure of the reynolds stress in a turbulent boundary layer. *Journal of Fluid Mechanics*, 60(3):481–511, 1973.

Martin Professional. Effect particle size, fluid density, and refractive index information, n.d. URL https://www.martin.com/en-US/site_elements/martin-hints_and_tips-particle-size-fluid-density-and-refractive-index-values.

I. Marusic and J.P. Monty. Attached eddy model of wall turbulence. *Annual Review of Fluid Mechanics*, 51(Volume 51, 2019):49–74, 2019.

I. Marusic, R. Mathis, and N. Hutchins. High reynolds number effects in wall turbulence. *International Journal of Heat and Fluid Flow*, 31(3):418–428, 2010a.

I. Marusic, B.J. McKeon, P.A. Monkewitz, H.M. Nagib, A.J. Smits, and K.R. Sreenivasan. Wall-bounded turbulent flows at high reynolds numbers: Recent advances and key issues. *Physics of Fluids*, 22(6):065103, 2010b.

I. Marusic, J.P. Monty, M. Hultmark, and A.J. Smits. On the logarithmic region in wall turbulence. *Journal of Fluid Mechanics*, 716:R3, 2013.

G.L. Mellor and D.M. Gibson. Equilibrium turbulent boundary layers. *Journal of Fluid Mechanics*, 24(2):225–253, 1966.

M.A. Mendez, M. Raiola, A. Masullo, S. Discetti, A. Ianiro, R. Theunissen, and J.M. Buchlin. Pod-based background removal for particle image velocimetry. *Experimental Thermal and Fluid Science*, 80:181–192, 2017.

J. Monty, E. Dogan, R. Hanson, A. Scardino, B. Ganapathisubramani, and N. Hutchins. An assessment of the ship drag penalty arising from light calcareous tubeworm fouling. *Biofouling*, 32(4):451–464, 2016.

J.P. Monty, Z. Harun, and I. Marusic. A parametric study of adverse pressure gradient turbulent boundary layers. *International Journal of Heat and Fluid Flow*, 32(3):575–585, 2011.

A.J. Musker. Explicit expression for the smooth wall velocity distribution in a turbulent boundary layer. *AIAA Journal*, 17(6):655–657, 1979.

Y. Nagano, T. Tsuji, and T. Houra. Structure of turbulent boundary layer subjected to adverse pressure gradient. *International Journal of Heat and Fluid Flow*, 19(5):563–572, 1998.

S. Nakagawa and T.J. Hanratty. Particle image velocimetry measurements of flow over a wavy wall. *Physics of Fluids*, 13(11):3504–3507, 2001.

J. Nikuradse. Stromungsgesetze in rauhen rohren. *vdi-forschungsheft*, 361:1, 1933.

G. Pailhas, Y. Touvet, and B. Aupoix. Effects of reynolds number and adverse pressure gradient on a turbulent boundary layer developing on a rough surface. *Journal of Turbulence*, 9:1–24, 2008.

G. Pailhas, P. Barricau, Y. Touvet, and L. Perret. Friction measurement in zero and adverse pressure gradient boundary layer using oil droplet interferometric method. *Experiments in Fluids*, 47(2):195–207, 2009.

A. Parthasarathy and T. Saxton-Fox. A family of adverse pressure gradient turbulent boundary layers with upstream favourable pressure gradients. *Journal of Fluid Mechanics*, 966:A11, 2023.

A.E. Perry and M.S. Chong. On the mechanism of wall turbulence. *Journal of Fluid Mechanics*, 119:173–217, 1982.

A.E. Perry and P.N. Joubert. Rough-wall boundary layers in adverse pressure gradients. *Journal of Fluid Mechanics*, 17(2):193–211, 1963.

A.E. Perry and I. Marušić. A wall-wake model for the turbulence structure of boundary layers. part 1. extension of the attached eddy hypothesis. *Journal of Fluid Mechanics*, 298:361–388, 1995.

A.E. Perry, S. Hafez, and M.S. Chong. A possible reinterpretation of the princeton superpipe data. *Journal of Fluid Mechanics*, 439:395–401, 2001.

A.E. Perry, I. Marusic, and M.B. Jones. On the streamwise evolution of turbulent boundary layers in arbitrary pressure gradients. *Journal of Fluid Mechanics*, 461:61–91, 2002.

U. Piomelli, E. Balaras, and A. Pascarelli. Turbulent structures in accelerating boundary layers. *Journal of Turbulence*, 1:N1, 2000.

S.B. Pope. *Turbulent Flows*. Cambridge University Press, Cambridge, 2000.

L. Prandtl. 7. bericht über untersuchungen zur ausgebildeten turbulenz. *ZAMM-Journal of Applied Mathematics and Mechanics/Zeitschrift für Angewandte Mathematik und Mechanik*, 5(2):136–139, 1925.

T. Preskett and B. Ganapathisubramani. The impact of pressure gradient history on flow structures in high reynolds number rough wall turbulence. *International Journal of Heat and Fluid Flow*, 116:109942, 2025.

T. Preskett, M. Virgilio, P. Jaiswal, and B. Ganapathisubramani. Effects of pressure-gradient histories on skin friction and mean flow of high reynolds number turbulent boundary layers over smooth and rough walls. *Journal of Fluid Mechanics*, 1010:A30, 2025.

T. Preskett, M. Virgilio, P. Jaiswal, and B. Ganapathisubramani. Effect of pressure gradient histories on turbulence characteristics of turbulent boundary layers over smooth and rough walls. *Physical Review Fluids*, 11(1):014603, 2026.

M. Raffel, C.E. Willert, F. Scarano, C.J. Kähler, S.T. Wereley, and J.r. Kompenhans. Particle image velocimetry : a practical guide, 2018.

D. Ragni, F. Schrijer, B.W. van Oudheusden, and F. Scarano. Particle tracer response across shocks measured by piv. *Experiments in Fluids*, 50(1):53–64, 2011.

S. Rahgozar and Y. Maciel. Low-and high-speed structures in the outer region of an adverse-pressure-gradient turbulent boundary layer. *Experimental thermal and fluid science*, 35(8):1575–1587, 2011.

M.R. Raupach, R.A. Antonia, and S. Rajagopalan. Rough-wall turbulent boundary layers. *Applied Mechanics Reviews*, 44(1):1–25, 1991.

S. Rezaeiravesh, R. Vinuesa, M. Liefvendahl, and P. Schlatter. Assessment of uncertainties in hot-wire anemometry and oil-film interferometry measurements for wall-bounded turbulent flows. *European Journal of Mechanics - B/Fluids*, 72:57–73, 2018.

S. Romero, S. Zimmerman, J. Philip, C. White, and J. Klewicki. Properties of the inertial sublayer in adverse pressure-gradient turbulent boundary layers. *Journal of Fluid Mechanics*, 937:A30, 2022.

J. Rotta. Turbulent boundary layers in incompressible flow. *Progress in aerospace sciences*, 2(1):1–95, 1962.

A. Samuel and P. Joubert. A boundary layer developing in an increasingly adverse pressure gradient. *Journal of Fluid Mechanics*, 66(3):481–505, 1974.

C. Sanmiguel Vila, R. Vinuesa, S. Discetti, A. Ianiro, P. Schlatter, and R. Örlü. Separating adverse-pressure-gradient and reynolds-number effects in turbulent boundary layers. *Physical Review Fluids*, 5(6):064609, 2020.

H. Schlichting. *Experimental investigation of the problem of surface roughness*. National Advisory Commitee for Aeronautics, 1937.

M.P. Schultz and K.A. Flack. The rough-wall turbulent boundary layer from the hydraulically smooth to the fully rough regime. *Journal of Fluid Mechanics*, 580:381–405, 2007.

M.P. Schultz and K.A. Flack. Reynolds-number scaling of turbulent channel flow. *Physics of Fluids*, 25(2):025104, 2013.

A. Sciacchitano. Uncertainty quantification in particle image velocimetry. *Measurement Science and Technology*, 30(9):092001, 2019.

J.H. Shin and S.J. Song. Pressure gradient effects on smooth-and rough-surface turbulent boundary layers-part ii: Adverse pressure gradient. *Journal of Fluids Engineering, Transactions of the ASME*, 137(1):011204, 2015a.

J.H. Shin and S.J. Song. Pressure gradient effects on smooth and rough surface turbulent boundary layers-part i: Favorable pressure gradient. *Journal of Fluids Engineering, Transactions of the ASME*, 137(1):011203, 2015b.

C.R. Smith and S.P. Metzler. The characteristics of low-speed streaks in the near-wall region of a turbulent boundary layer. *Journal of Fluid Mechanics*, 129:27–54, 1983.

A.J. Smits and D.H. Wood. The response of turbulent boundary layers to sudden perturbations. *Annual Review of Fluid Mechanics*, 17(Volume 17, 1985):321–358, 1985.

A.J. Smits, B.J. McKeon, and I. Marusic. High–reynolds number wall turbulence. *Annual Review of Fluid Mechanics*, 43:353–375, 2011.

P.R. Spalart. Numerical study of sink-flow boundary layers. *Journal of Fluid Mechanics*, 172:307–328, 1986.

P.R. Spalart and J.H. Watmuff. Experimental and numerical study of a turbulent boundary layer with pressure gradients. *Journal of Fluid Mechanics*, 249:337–371, 1993.

D. Squire, C. Morrill-Winter, N. Hutchins, M. Schultz, J. Klewicki, and I. Marusic. Comparison of turbulent boundary layers over smooth and rough surfaces up to high reynolds numbers. *Journal of Fluid Mechanics*, 795:210–240, 2016.

M.F. Tachie. Particle image velocimetry study of turbulent flow over transverse square ribs in an asymmetric diffuser. *Physics of Fluids*, 19(6):065106, 2007.

M.F. Tachie, D.J. Bergstrom, and R. Balachandar. *The effect of wall roughness on an open channel boundary layer*, pages 455–463. Elsevier Science Ltd, Oxford, 2002.

M.F. Tachie, M. Agelinchaab, and M.K. Shah. Turbulent flow over transverse ribs in open channel with converging side walls. *International Journal of Heat and Fluid Flow*, 28(4):683–707, 2007.

A. Tanarro, R. Vinuesa, and P. Schlatter. Effect of adverse pressure gradients on turbulent wing boundary layers. *Journal of Fluid Mechanics*, 883:A8, 2020.

G. Tay, D. Kuhn, and M. Tachie. Particle image velocimetry study of rough-wall turbulent flows in favorable pressure gradient. *Journal of fluids engineering*, 131(6):061205, 2009a.

G.F.K. Tay, D.C.S. Kuhn, and M.F. Tachie. Influence of adverse pressure gradient on rough-wall turbulent flows. *International Journal of Heat and Fluid Flow*, 30(2):249–265, 2009b.

G.I. Taylor. The spectrum of turbulence. *Proceedings of the Royal Society of London. Series A - Mathematical and Physical Sciences*, 164(919):476–490, 1938.

T. Theodorsen. Mechanisms of turbulence. In *Proceedings of the 2nd Midwestern Conference on Fluid Mechanics, 1952*, 1952.

R. Thibault and G.J. Poitras. Uncertainty evaluation of friction velocity measurements by oil-film interferometry. *Journal of Fluids Engineering*, 139(5):051401, 2017.

A.A. Townsend. The structure of the turbulent boundary layer. *Mathematical Proceedings of the Cambridge Philosophical Society*, 47(2):375–395, 1951.

A.A. Townsend. The properties of equilibrium boundary layers. *Journal of Fluid Mechanics*, 1(6):561–573, 1956.

A.A.R. Townsend. *The Structure of Turbulent Shear Flow*. Cambridge University Press, 1976.

C. Tropea, A.L. Yarin, and J.F. Foss. *Springer handbook of experimental fluid mechanics*, volume 1. Springer, 2007.

C. Tropea, A.L. Yarin, and J.F. Foss. *Springer handbook of experimental fluid mechanics*. Springer, Berlin, 2016.

J.M. Tsikata and M.F. Tachie. Adverse pressure gradient turbulent flows over rough walls. *International Journal of Heat and Fluid Flow*, 39:127–145, 2013.

Y. Tsuji and Y. Morikawa. Turbulent boundary layer with pressure gradient alternating in sign. *Aeronautical Quarterly*, 27(1):15–28, 1976.

R. Vinuesa, A. Bobke, R. Örlü, and P. Schlatter. On determining characteristic length scales in pressure-gradient turbulent boundary layers. *Physics of Fluids*, 28(5):055101, 2016.

R. Vinuesa, R. Örlü, C. Sanmiguel Vila, A. Ianiro, S. Discetti, and P. Schlatter. Revisiting history effects in adverse-pressure-gradient turbulent boundary layers. *Flow, Turbulence and Combustion*, 99(3):565–587, 2017.

M. Virgilio, T. Preskett, P. Jaiswal, and B. Ganapathisubramani. Pressure gradient history effects on integral quantities of turbulent boundary layers: experiments and data-driven models. *Journal of Fluid Mechanics*, 1014:A2, 2025.

V. Vishwanathan, D.J. Fritsch, K.T. Lowe, and W.J. Devenport. History effects and wall-similarity of non-equilibrium turbulent boundary layers in varying pressure gradient over rough and smooth surfaces. *International Journal of Heat and Fluid Flow*, 102: 109145, 2023.

R.J. Volino. Non-equilibrium development in turbulent boundary layers with changing pressure gradients. *Journal of Fluid Mechanics*, 897:A2, 2020.

R.J. Volino and M.P. Schultz. Comparison of smooth- and rough-wall non-equilibrium boundary layers with favourable and adverse pressure gradients. *Journal of Fluid Mechanics*, 959:A35, 2023.

R.J. Volino, M.P. Schultz, and K.A. Flack. Turbulence structure in rough- and smooth-wall boundary layers. *Journal of Fluid Mechanics*, 592:263–293, 2007.

T. Wang. Ground effect in vortex panel method, 2015. URL https://github.com/barbagroup/AeroPython-studentprojects2015/blob/master/Ground-Effect-in-Vortex-Panel-Method/Ground-Effect-in-Vortex-Panel-Method.ipynb.

D.D. Wangsawijaya, P. Jaiswal, and B. Ganapathisubramani. Towards decoupling the effects of permeability and roughness on turbulent boundary layers. *Journal of Fluid Mechanics*, 967:R2, 2023.

D. Warnack and H.H. Fernholz. The effects of a favourable pressure gradient and of the reynolds number on an incompressible axisymmetric turbulent boundary layer. part 2. the boundary layer with relaminarization. *Journal of Fluid Mechanics*, 359:357–381, 1998.

F.M. White and J. Majdalani. *Viscous Fluid Flow*. McGraw-Hill Education, 2021. URL https://books.google.co.uk/books?id=fNb-zQEACAAJ.

Wildlife and Welfare. Biofouling - what is it and why should we care?, n.d. URL https://www.wildlifeandwelfare.org/news-blog/biofouling-what-is-it-and-why-should-we-care. Last accessed: 2025-07-05.

W. Wu and U. Piomelli. Effects of surface roughness on a separating turbulent boundary layer. *Journal of Fluid Mechanics*, 841:552–580, 2018.

X. Wu and K.D. Squires. Numerical investigation of the turbulent boundary layer over a bump. *Journal of Fluid Mechanics*, 362:229–271, 1998.

Y. Wu and K.T. Christensen. Population trends of spanwise vortices in wall turbulence. *Journal of Fluid Mechanics*, 568:55–76, 2006.

Y.I. Yun, I.Y. Park, and S.J. Song. Performance degradation due to blade surface roughness in a single-stage axial turbine. *Journal of Turbomachinery*, 127(1):137–143, 2005.